

8-27-2009

Optimal spectral reconstructions from deterministic and stochastic sampling geometries using compressive sensing and spectral statistical models

Oliver Jeromin

Follow this and additional works at: https://digitalrepository.unm.edu/ece_etds

Recommended Citation

Jeromin, Oliver. "Optimal spectral reconstructions from deterministic and stochastic sampling geometries using compressive sensing and spectral statistical models." (2009). https://digitalrepository.unm.edu/ece_etds/126

This Dissertation is brought to you for free and open access by the Engineering ETDs at UNM Digital Repository. It has been accepted for inclusion in Electrical and Computer Engineering ETDs by an authorized administrator of UNM Digital Repository. For more information, please contact disc@unm.edu.

Oliver M. Jeromin

Candidate

Electrical and Computer Engineering

Department

This dissertation is approved, and it is acceptable in quality and form for publication:

Approved by the Dissertation Committee:

Mages Tatayus

, Chairperson

Isabel Horta

Jim Ball

V. D. C.

Ann W. Dwyer

Chris Smith

**Optimal Spectral Reconstructions from
Deterministic and Stochastic Sampling
Geometries Using Compressive Sensing and
Spectral Statistical Models**

BY

Oliver Max Jeromin

B.A., Liberal Arts Engineering, Wheaton College (IL), 2002
B.S., Electrical Engineering, Illinois Institute of Technology, 2002
M.S., Electrical Engineering, University of New Mexico, USA, 2005

DISSERTATION

Submitted in Partial Fulfillment of the
Requirements for the Degree of

**Doctor of Philosophy
Engineering**

The University of New Mexico
Albuquerque, New Mexico

August 2009

© 2009, Oliver Max Jeromin

DEDICATION

To my beautiful wife, Summer, and our two daughters, Heidi Anne and Elsa Joy.

ACKNOWLEDGEMENTS

I would like to first and foremost thank my adviser and committee chair, Dr. Marios Pattichis for the insight, guidance, patience, and friendship he has provided during the course of this work. He has spent the better part of five years advising and overseeing my work in applying geostatistics to image processing applications. During this time he was always been available to provide assistance when called upon. More recently, he has spent many hours helping me finalize this dissertation into a formal representation of our work together. For these things, I am very grateful.

I would like to thank Dr. Armin Doerry for being supportive of my professional and academic pursuits, as well as his willingness to be a member of my committee. His thoughtful feedback is greatly appreciated. My gratitude also extends to Dr. Vince Calhoun for providing the data in our fMRI study, providing guidance as we ventured into an application we were not familiar with, and for his willingness to serve on my committee. I would like to thank Dr. Christos Christodoulou for his willingness to serve on my committee and for his role as co-principle investigator, along with Dr. Pattichis, on the research grant¹ that provided the funding and motivation for our satellite image reconstruction techniques. I would like to thank the final two members of my committee, Dr. Gabriel Huerta and Dr. Thomas Caudell, for their helpful feedback

Lastly, but certainly not the least, I would like to thank the love of my life, Summer. Without her support and faith, I would not have been able to complete this work. The final months of this dissertation coincided with the expectation of a new arrival in our family, and because of her steadfastness and dedication to my academic pursuit, we have both made it through an exciting, yet challenging chapter of our lives together. As iron sharpens iron, Summer has provided an example of strength that has inspired me in my life as a husband, father, engineer, and student.

¹*Real-Time Reconfigurable Systems for Space Applications*, \$1,562,949. Lead PIs: C. Christodoulou, M.S. Pattichis. Co-PIs: P Zarkesh-Ha, S. K. Jayaweera, **AFRL Award #FA9453-09-C-0309**, 11/24/2008-11/24/2012.

Optimal Spectral Reconstructions from Deterministic and Stochastic Sampling Geometries using Compressive Sensing and Spectral Statistical Models

BY

Oliver Max Jeromin

B.A., Liberal Arts Engineering, Wheaton College (IL), 2002
B.S., Electrical Engineering, Illinois Institute of Technology, 2002
M.S., Electrical Engineering, University of New Mexico, USA, 2005
Ph.D., Engineering, University of New Mexico, USA, 2009

ABSTRACT OF DISSERTATION

Submitted in Partial Fulfillment of the
Requirements for the Degree of

**Doctor of Philosophy
Engineering**

The University of New Mexico
Albuquerque, New Mexico

August 2009

Optimal Spectral Reconstructions from Deterministic and Stochastic Sampling Geometries using Compressive Sensing and Spectral Statistical Models

by

Oliver Max Jeromin

B.A., Liberal Arts Engineering, Wheaton College (IL), 2002
B.S., Electrical Engineering, Illinois Institute of Technology, 2002
M.S., Electrical Engineering, University of New Mexico, USA, 2005
Ph.D., Engineering, University of New Mexico, USA, 2009

Abstract

This dissertation focuses on the development of high-quality image reconstruction methods from a limited number of Fourier samples using optimized, stochastic and deterministic sampling geometries. Two methodologies are developed: an optimal image reconstruction framework based on Compressive Sensing (CS) techniques and a new, Spectral Statistical approach based on the use of isotropic models over a dyadic partitioning of the spectrum. The proposed methods are demonstrated in applications in reconstructing fMRI and remote sensing imagery.

Typically, a reduction in MRI image acquisition time is achieved by sampling K-space at a rate below the Nyquist rate. Various methods using correlation between samples, sample averaging, and more recently, Compressive Sensing, are employed

to mitigate the aliasing effects of under-sampled Fourier data. The proposed solution utilizes an additional layer of optimization to enhance the performance of a previously published CS reconstruction algorithm.

Specifically, the new framework provides reconstructions of a desired image quality by jointly optimizing for the optimal K-space sampling geometry and CS model parameters. The effectiveness of each geometry is evaluated based on the required number of FFT samples that are available for image reconstructions of sufficient quality. A central result of this approach is that the fastest geometry, the spiral low-pass geometry has also provided the best (optimized) CS reconstructions. This geometry provided significantly better reconstructions than the stochastic sampling geometries recommended in the literature. An optimization framework for selecting appropriate CS model reconstruction parameters is also provided. Here, the term “appropriate CS parameters” is meant to infer that the estimated parameter ranges can provide some guarantee for a minimum level of image reconstruction performance. Utilizing the simplex search algorithm, the optimal TV-norm and Wavelet transform penalties are calculated for the CS reconstruction objective function. Collecting the functional evaluation values of the simplex search over a large data set allows for a range of objective function weighting parameters to be defined for the sampling geometries that were found to be effective. The results indicate that the CS parameter optimization framework is significant in that it can provide for large improvements over the standard use of non-optimized approaches.

The dissertation also develops the use of a new Spectral Statistical approach for spectral reconstruction of remote sensing imagery. The motivation for pursuing

this research includes potential applications that include, but are not limited to, the development of better image compression schemas based on a limited number of spectral coefficients. In addition, other applications include the use of spectral interpolation methods for remote sensing systems that directly sample the Fourier domain optically or electromagnetically, which may suffer from missing or degraded samples beyond and/or within the focal plane.

For these applications, a new spectral statistical methodology is proposed that reconstructs spectral data from uniformly spaced samples over a dyadic partition of the spectrum. Unlike the CS approach that solves for the 2D FFT coefficients directly, the statistical approach uses separate models for the magnitude and phase, allowing for separate control of the reconstruction quality of each one. A scalable solution that partitions the spectral domain into blocks of varying size allows for the determination of the appropriate covariance models of the magnitude and phase spectra bounded by the blocks. The individual spectral models are then applied to solving for the optimal linear estimate, which is referred to in literature as Kriging.

The use of spectral data transformations are also presented as a means for producing data that is better suited for statistical modeling and variogram estimation. A logarithmic transformation is applied to the magnitude spectra, as it has been shown to impart intrinsic stationarity over localized, bounded regions of the spectra. Phase spectra resulting from the 2D FFT can be best described as being uniformly distributed over the interval of $-\pi$ to π . In this original state, the spectral samples fail to produce appropriate spectral statistical models that exhibit inter-sample covariance. For phase spectra modeling, an unwrapping step is required to ensure

that individual blocks can be effectively modeled using appropriate variogram models. The transformed magnitude and unwrapped phase spectra result in unique statistical models that are optimal over individual frequency blocks, which produce accurate spectral reconstructions that account for localized variability in the spectral domain.

The Kriging spectral estimates are shown to produce higher quality magnitude and phase spectra reconstructions than the cubic spline, nearest neighbor, and bilinear interpolators that are widely used. Even when model assumptions, such as isotropy, violate the spectral data being modeled, excellent reconstructions are still obtained. Finally, both of the spectral estimation methods developed in this dissertation are compared against one another, revealing how each one of the methods developed here is appropriate for different classes of images. For satellite images that contain a large amount of detail, the new spectral statistical approach, reconstructing the spectrum much faster, from a fraction of the original high frequency content, provided significantly better reconstructions than the best reconstructions from the optimized CS geometries. This result is supported not only by comparing image quality metrics, but also by visual assessment.

Table of Contents

LIST OF FIGURES	xv
LIST OF TABLES	xxi
CHAPTER 1. INTRODUCTION	
1.1. Motivation.....	1
1.2 Thesis statement.....	3
1.3 Innovations and Contributions	5
1.4 Overview of the dissertation	7
CHAPTER 2. OPTIMAL COMPRESSED SENSING RECONSTRUCTIONS FROM FMRI USING DETERMINISTIC AND STOCHASTIC SAMPLING GEOMETRIES	
2.1. Introduction	11
2.2. Literature Review.....	16
2.3. Theoretical Background.....	20
2.3.1. Compressed Sensing Image Reconstruction Framework	20
2.3.2. Optimal TV Norm and Wavelet Transform Penalty	24
2.4. Methods.....	27
2.4.1. Data Set and fMRI Activity Detection.....	27
2.4.2. Partial K-Space Sampling Geometries.....	29
2.4.3. Optimization of CS Penalty Parameters	32
2.5. Results.....	37
2.6. Discussion.....	51

2.7. Conclusion	57
References	58

**CHAPTER 3. FOURIER SPECTRA RECONSTRUCTIONS OF
SATELLITE IMAGER PART I: STATISTICAL INTERPOLATION
MODELS OF THE MAGNITUDE AND PHASE**

3.1. Introduction.....	62
3.2. Literature Review.....	63
3.2.1 Data Set Description	66
3.3 Theoretical Background.....	72
3.3.1. Spectral Statistical Approach.....	72
3.3.2. A Magnitude Spectrum Model using the Logarithm	75
3.3.3. Two-Dimensional Phase Unwrapping	77
3.3.3.1. <i>Path Following Algorithms</i>	79
3.3.3.2 <i>Minimum-Norm Algorithms</i>	80
3.3.4. Optimal Interpolation using Kriging.....	86
3.4. Methods.....	90
3.4.1. Spectral Sampling Rates	90
3.4.2. Statistical Models for Magnitude and Phase Spectra.....	95
3.4.2.1. Isotropy Model Considerations.....	96
3.4.2.2. Variogram Range Selection	98
3.4.2.3. Variogram Model Selection and Fitting	98
3.4.3 Kriging Interpolation of Magnitude and Phase Spectra.....	100

3.4.3.1. Magnitude Spectra Estimation.....	100
3.4.3.2. Phase Spectra Estimation.....	104
3.5. Results.....	105
3.5.1. Variogram Isotropy.....	105
3.5.2. Variogram Range Selection, Estimation, and Model Fitting	111
3.5.3. Magnitude and Phase Kriging.....	128
3.5.3.1. <i>Parameter Optimization Results</i>	129
3.5.3.2. <i>Magnitude Reconstruction Results</i>	132
3.6 Discussion.....	138
3.6.1 Remarks on Spectral Statistical Models	138
3.6.2. Magnitude and Phase Kriging Remarks	140
3.7 Conclusion	143
References.....	145

**CHAPTER 4. FOURIER SPECTRA RECONSTRUCTIONS OF
SATELLITE IMAGERY PART II: RECONSTRUCTIONS FROM
STATISTICAL MODELS AND COMPRESSIVE SENSING**

4.1. Introduction.....	149
4.2. Sub Image Data Set Selection.....	154
4.3. Comparison of Reconstructed Image Quality.....	158
4.3.1. Kriged Magnitude Spectra and CS Reconstruction Comparison.....	158
4.3.2. Kriged Magnitude and Phase Spectra and CS	

Reconstruction Comparison.....	169
4.3.3. Original Satellite Image Comparison.....	181
4.4. Magnitude Spectrum Extrapolation	188
4.5. Comparison of Computational Complexity	191
4.6. Conclusion.	197
References.....	199
 CHAPTER 5. FINAL CONCLUSIONS AND FUTURE WORK	
5.1 Final Conclusions.....	201
5.2 Future Work	203

List of Figures

2.1. Example of a simple CS reconstruction problem.....	12
2.2. MRI image slices with the corresponding Fourier magnitude spectra	14
2.3. Parameter optimization flow chart.....	36
2.4 Optimal PSNR values for CS reconstructions for each sampling geometry for both ON and OFF images	39
2.5. Parameter optimization surface of an fMRI image pair.....	40
2.6. Individual parameter values at each simplex iteration for an fMRI image pair.....	41
2.7. Example of reconstruction quality for two sample images.....	43
2.8. Reconstruction image quality as a function of parameter optimization	44
2.9. Difference images obtained from four individual fMRI sample sets (I)	48
2.10. Difference images obtained from four individual fMRI sample sets (II)	49
2.11. Difference images obtained from four individual fMRI sample sets (III) ..	50
2.12. Optimal parameter regions over an entire fMRI image data	52
2.13. A comparison of results when either of the reconstruction parameters are zero	55
3.1. Rural scene satellite image data set and log-transformed magnitude Fourier spectrum	68
3.2. Full resolution satellite image of London, England depicting five urban sub regions. The third rural sub region is also indicated.....	69

3.3. Urban scene satellite image data set and log-transformed magnitude Fourier spectrum.....	70
3.4. Natural scene satellite image data set and log-transformed magnitude Fourier spectrum.....	71
3.5. Spectral partition map.....	74
3.6. Comparison of phase unwrapping methods.....	83
3.7. The wrapped phase image of a sample urban scene.....	84
3.8. The unwrapped phase image of a sample urban scene obtained by Flynn's minimum discontinuity method.....	85
3.9. Spectral modeling procedure flow chart.....	91
3.10. Fourier and spatial image reconstruction flow chart.....	92
3.11. A grid of FFT discrete frequency samples, where we only consider one of every four samples in each dimension.....	102
3.12. Anisotropic variograms of a high and medium frequency block from a rural image.....	106
3.13. Anisotropic variograms of a high and medium frequency block from an urban image.....	107
3.14. Anisotropic variograms of a high and medium frequency block from a natural image.....	108
3.15. Isotropic and anisotropic variogram estimates.....	110
3.16. Selected image for which we calculate all of the variogram estimates for each spectral block.....	111

3.17. The high frequency block variogram estimates and adaptively fitted models for the log-transformed magnitude spectra of the rural image depicted in Figure 3.16(a).	112
3.18. The medium frequency block variogram estimates and adaptively fitted models for the log-transformed magnitude spectra of the rural image depicted in Figure 3.16(a).	113
3.19. The high frequency block variogram estimates and adaptively fitted models for the unwrapped phase spectra using Flynn’s Minimum Discontinuity method of the rural image depicted in Figure 3.16(a).	114
3.20. The medium frequency block variogram estimates and adaptively fitted models for the unwrapped phase spectra using Flynn’s Minimum Discontinuity method of the rural image depicted in Figure 3.16(a).	115
3.21. The high frequency block variogram estimates and adaptively fitted models for the log-transformed magnitude spectra of the urban image depicted in Figure 3.16(a).	117
3.22. The medium frequency block variogram estimates and adaptively fitted models for the log-transformed magnitude spectra of the urban image depicted in Figure 3.16(b)	118
3.23. The high frequency block variogram estimates and adaptively fitted models for the unwrapped phase spectra of the urban image depicted in Figure 3.16(b)	119

3.24. The medium frequency block variogram estimates and adaptively fitted models for the unwrapped phase spectra of the urban image depicted in Figure 3.16(b)	120
3.25. The high frequency block variogram estimates and adaptively fitted models for the log-transformed magnitude spectra of the natural image depicted in Figure 3.16(c).....	122
3.26. The medium frequency block variogram estimates and adaptively fitted models for the log-transformed magnitude spectra of the natural image depicted in Figure 3.16(c).....	123
3.27. The high frequency block variogram estimates and adaptively fitted models for the unwrapped phase spectra of the natural image depicted in Figure 3.16(c).....	124
3.28. The medium frequency block variogram estimates and adaptively fitted models for the unwrapped phase spectra of the natural image depicted in Figure 3.16(c).....	125
3.29. Kriging parameter optimization example for the max-distance and max-samples parameters.....	130
3.30. Variogram model fitting for a medium-frequency block of an urban scene.....	131
3.31. High frequency and low frequency block magnitude reconstruction comparison of Kriging, splines, Nearest Neighbor and linear interpolators.....	133
3.32. High frequency and low frequency block unwrapped phase reconstruction using Kriging to compare unwrapping methods.....	137

3.33. Example of best and worst phase reconstructions	142
4.1. Images that comprise our sub image data set.....	155
4.2. Comparison of SLP and RSP2 CS sampling geometries.....	156
4.3. The mean PSNR and mean SSIM values for magnitude sample rates	162
4.4. Comparative example for a rural sub scene reconstruction using 11.97% of the original samples.....	164
4.5. Comparative example for an urban sub scene reconstruction using 18.75% of the original samples.....	165
4.6. Comparative example for a natural sub scene reconstruction using 11.97% of the original samples.....	166
4.7. Comparative example for a brain image reconstruction using 18.75% of the original samples.....	168
4.8. Magnitude and phase data reconstruction results	174
4.9. The mean PSNR values for each data sample rates based on magnitude and phase Kriging	175
4.10.. The mean SSIM Index values for each data sample rates based on magnitude and phase Kriging	176
4.11. Comparison of rural sub image reconstruction and related SSIM index maps using a 7.68% data sample rate	179
4.12. Comparison of natural sub image reconstruction and related SSIM index maps using a 18.75% data sample rate	180
4.13. Example of Kriging reconstructed magnitude and phase spectra of rural scene in Figure 4.11(a).....	181

4.14. Results of magnitude spectra interpolation using Kriging, SLP CS, and Zero Filling the SLP sampling geometry on a full sized image of the rural class	185
4.15. Results of magnitude spectra interpolation using Kriging, SLP CS, and Zero Filling the SLP sampling geometry on a full sized image of the urban class.....	186
4.16. Results of magnitude spectra interpolation using Kriging, SLP CS, and Zero Filling the SLP sampling geometry on a full sized image of the natural class.....	187
4.17. The magnitude spectra extrapolation	190

List of Tables

2.1. K-space sampling geometry class examples.....	34
2.2. Average Maximum PSNR per geometry class	39
2.3. Bounding box ratios for partial K-space geometries	46
2.4. Estimated parameter ranges for select bounding box regions	53
3.1. Spectral statistical data sample rates.....	95
3.2. Rural image variogram model parameters.....	116
3.3. Urban image variogram model parameters.....	121
3.4. Natural image variogram model parameters.....	126
3.5. High frequency block reconstruction PSNR, magnitude.....	133
3.6. Medium frequency block reconstruction PSNR, magnitude	134
3.7. High frequency block reconstruction PSNR, unwrapped phase.....	135
3.8. Medium frequency block reconstruction PRNS, unwrapped phase	135
4.1. Summary statistics of PSNR and SSIM for 18.75% effective sampling rate (Magnitude sampling rate is 9.375%)	160
4.2. Summary statistics of PSNR and SSIM for 11.97% effective sampling rate (Magnitude sampling rate 5.985%).....	160
4.3. Summary statistics of PSNR and SSIM for 10.17% effective sampling rate (Magnitude sampling rate is 5.085%)	161
4.4. Summary statistics of PSNR and SSIM for 9.91% effective sampling rate (Magnitude sampling rate is 4.955%)	161

4.5. Summary statistics of PSNR and SSIM for 17.26% total spectral sampling rates	171
4.6. Summary statistics of PSNR and SSIM for 15.572% total spectral sampling rates	171
4.7. Summary statistics of PSNR and SSIM for 15.12% total spectral sampling rates	171
4.8. Summary statistics of PSNR and SSIM for 9.38% total spectral sampling rates	172
4.9. Summary statistics of PSNR and SSIM for 7.68% total spectral sampling rates	172
4.10. Summary statistics of PSNR and SSIM for 7.23% total spectral sampling rates	172
4.11. Summary statistics of PSNR and SSIM for 5.99% total spectral sampling rates	173
4.12. Summary statistics of PSNR and SSIM for 5.54% total spectral sampling rates	173
4.13. Mean PSNR for magnitude sampling rates on full image reconstruction & visual image quality score.....	183
4.14. Mean SSIM index for magnitude sampling rates on full image reconstruction & visual image quality score.....	184
4.15. Computational cost, in seconds, of reconstruction methods in the above comparisons	193

Chapter 1

Introduction

1.1 Motivation

The 2D Discrete Fourier Transform (DFT) from discrete time signals has been used ubiquitously over the past forty years. The relationship between the spatial image and its spectral representation is utilized in various image processing techniques, including image filtering, image denoising, and image restoration.

It is important to recognize that the 2D FFT is just one of many possible discrete frequency sampling geometries of the continuous, periodic 2D Fourier representation of discretely sampled images. A central point in this dissertation is that we want to explore different Fourier-domain sampling geometries and explore if they can result in high-quality image reconstructions. We constrain our sampling geometries to subsets of the 2D FFT frequency samples to allow for both efficient sampling and fast reconstructions.

In certain applications, data is directly sampled in the frequency domain, and the Fourier transform allows the data to be represented in a way that we can visually understand. Examples of such applications include MRI and CT scanning in medicine; and radio telescopes and, more recently, synthetic aperture

radar (SAR) in remote sensing. Often times such systems operate under constraints where the spectral data is partially collected, resulting in an image of reduced quality. In such cases, a mechanism for spectral estimation over the missing frequencies (interpolation or extrapolation) would be useful to enhance the final image.

There are a number of specific open problems that have not been addressed in the image processing community pertaining to task of spectral estimation. For instance, fast MRI data acquisition based on limited K-space samples and subsequent high fidelity image reconstructions. Another problem which has been explored extensively is the development of better image compression schemas based on entropy encoding a limited number of spectral coefficients. Optical and radio frequency imaging systems often suffer from missing or degraded Fourier samples beyond and/or within the focal plane, and spectral estimation often seeks to mitigate the detrimental effects that are manifested in the image domain.

In the following work, we seek to address the above problems. Specifically, for a fast MRI acquisitions, we present an a solution that utilizes compressive sensing theory to find the optimal Fourier sampling geometries that are associated with fixed CS model parameter ranges that guarantee levels of image reconstruction quality. The same methodology can be extended to other image acquisition problems, provided that the data are collected in the Frequency

domain. To address spectral image compression and restoration approaches, new statistical models are explored for modeling the discrete Fourier spectra of different types of satellite images. Our approach is to explore statistical models that lead to fast and optimal interpolation methods that can be used to reconstruct the spectra from limited numbers of samples. These novel approaches provide a general framework that is extendable beyond the applications explored here; namely partial fMRI K-space acquisition and reconstruction and satellite image reconstruction from reduced magnitude and phase spectra samples.

This dissertation presents two different methods that share the same motivation – to reconstruct digital images from limited frequency domain samples using both deterministic and statistical models of the discrete Fourier spectra. The first approach uses compressive sensing (CS) theory and numerical optimization to find the best solution to the spectral reconstruction problem for a given convex system of equations over any arbitrary sampling geometry. The second approach is based on a new framework that applies geostatistical theory to the discrete Fourier domain and uses the optimal linear estimator, referred to as Kriging, to reconstruct uniformly sampled magnitude and phase spectra.

1.2. Thesis Statement

The spectral models and techniques developed in this dissertation seek to achieve the best image reconstructions from data that is partially sampled in the Fourier domain. To accomplish this I present extensions of two relatively new

mathematical theories. In reverse chronological order, the first is based on compressive sensing, which has recently (since 2004) found much popularity in the field of digital signal processing, and especially in image processing. The second is based on statistical models for spatial data, which was formalized from geostatistics in 1993.

Since these disciplines are relatively new, I seek to both enhance and extend their application to specific problems in medical imaging and remote sensing. In the case of CS, where I propose to find the optimal partial K-space sampling geometry for fMRI reconstructions, enhancing prior work that has shown improved images are obtained by solving specifically designed CS optimization problems. The solution adds a layer of optimization on top of the CS objective function that seeks deterministic cost function weights that maximize the reconstructed image quality.

The second half of this dissertation claims to be the first extensive application of spatial statistics for the discrete Fourier space. Here, I extend concepts developed for describing spatial covariance to the Fourier domain. I found that appropriate statistical models can be developed for a dyadic partition of the Fourier spectrum. Here, unlike the CS models that model the 2D FFT complex coefficients, I investigate independent models for the magnitude and phase. This is an important distinction because it allows one to develop scalable models that can be adjusted for providing independent quality control for the magnitude and

phase. Here, as I will demonstrate in the results, optimal model fitting produces high quality reconstructions for the magnitude and lower quality for the phase. Furthermore, appropriate spatial statistical models are only possible because of the dyadic partitioning of the spectrum and after applying the logarithm to the magnitude spectrum and performing phase unwrapping. As I discuss in the results, there are significant statistical variations over different parts of the Fourier spectrum. The proposed approach provides localized spectral covariance modeling and optimal estimation using Kriging for a variety of types of images. Here, I consider various satellite imagery specifically selected to represent one of three commonly encountered scene types: rural, urban, and natural.

Both of the methods presented in this dissertation result in image reconstructions with significant image quality improvement over comparable methods that do not utilize the proposed methods.

1.3. Innovations and Contributions

A summary of innovations and contributions in this dissertation are listed below:

- Development of an optimization framework that can provide, prior to MRI scanning, appropriate CS model parameter weights for guaranteeing the quality of the reconstructed images.
- Design of a collection of functional MRI (fMRI) partial K-space sampling geometries that can be described as either (i) sampling in such a way that sampling time is reduced as much as possible and (ii) sampling in such a

way to adhere to the requirement of sample to transform basis incoherence laid forth in CS theory.

- Using the previously mentioned optimized CS framework, the development of a catalog of sampling geometries that are optimized for fast data acquisition and from which the resulting partial K-space samples can be reconstructed from a range of determined reconstruction weights that for the majority ($> 75\%$) of the fMRI scans are guaranteed to produce a certain level of reconstruction quality.
- Development of a Matlab framework for importing spectral image components into the R statistical software suite. This allows for the utilization of extensive geostatistical packages to perform variogram estimation and Kriging steps in a compiled, run-time environment.
- Development of statistical models describing the spectral covariance that are used in Kriging interpolation of discrete magnitude and phase samples obtained by the 2D FFT applied to satellite imagery of various scene types (rural, urban, and natural).
- Development of various spectral covariance models for unwrapped 2D phase spectra, as wrapped phase values, which are constrained between $(-\pi, \pi]$, do not exhibit spectral covariance.
- Development of a scalable partitioning of the discrete Fourier spectrum that is dyadic, which allows for the following statistical applications to be explored:

1. The excellent approximation of the Fourier magnitude spectrum over a localized, intrinsically stationary random field over a bounded domain from non-stationary data samples, by the application of the logarithm operator.
2. The verification of the appropriateness of an isotropic covariance model of the Fourier magnitude spectrum over medium spectral regions. Here, we recognize that the medium spectral blocks contain more energy and it is very encouraging to confirm that we can provide accurate fits using isotropic statistical models that also provide for very fast and optimized (Kriging) reconstructions.
3. Explore a scalable approach by assigning different sample rates to high frequency, medium frequency, and low frequency regions of the Fourier domain.
 - Development of spectral sampling geometries based on the above partitioning that allow for fast interpolation of any spectral component at any spectral frequency.
 - Development of an adaptive model selection procedure that ensures each spectral block generated by spectral partitioning and the associated removed samples are interpolated in a way that high quality spatial image reconstructions are achieved for a variety of image types and sizes.

1.4. Overview of the dissertation

The dissertation is organized into the following chapters:

- **Chapter 2** presents a brief background on partial K-space sampling and reconstructions, focusing primarily on fast partial K-space sampling geometries and the use of CS for partial K-space reconstruction. This is followed by a theoretical description of the CS objective function we optimized and presents the steps required for calculating the optimal weight parameters using the Nelder-Mead simplex search algorithm. We present four specifically engineered sampling geometries of which two are designed to quickly sample the partial K-space domain by restricting samples in the phase encoded dimension in a deterministic fashion. The other two sampling geometries incorporate a degree of randomness to ensure meet the theoretical requirements stated in CS theory. The results of the parameter search process are then used to determine the optimal range of parameters that can be used to achieve desired reconstruction PSNR values of individual fMRI image slices for each sampling geometry class. These results are compared to zero-filling the partial K-space defined by the sampling geometries.
- **Chapter 3** presents the development of statistical interpolation models of magnitude and phase for the Fourier spectra reconstruction of satellite imagery. Again, a brief literature review is presented that describes the use of geostatistics in remote sensing applications. Particular attention is paid to studies that have used Kriging for spatial image (pixel domain) interpolation. This review is followed by a description of the data set that was obtained from various public sources. The development of a spectral

statistical approach is described, in which the need for partitioning the Fourier spectrum is presented, as well as magnitude and phase spectra transformations using the logarithm and phase unwrapping algorithms, respectively. Optimal interpolation using ordinary Kriging is then presented, followed with a description of the spectral sampling methods, considerations for estimating and fitting the proper variogram model to individual spectral blocks, and the optimization of selecting the proper number of known samples for Kriging. The description of the above methods is followed by a series of related results and a comparison the Kriging interpolated magnitude spectra to other commonly used 2D interpolation algorithms. The phase spectra reconstructions using the various phase unwrapping methods are compared to determine which method is best suited for simple Kriging.

- **Chapter 4** presents a comparison of spatial image reconstructions using Kriging and the optimal CS procedure from Chapter 2. First, a brief description of the structural similarity index is presented, which is used to quantify the quality of the reconstructed image, along with the PSNR. This is followed by a comparison of image reconstructions using the magnitude and phase spectra sample rates first presented in Chapter 3. This is followed by the comparison of both spectral data estimation methods. A sub image data set is selected to allow for the comparison of CS and Kriging to be made without additional preprocessing required by transform constraints in the CS procedure. Care is taken to ensure the

- **Chapter 5** summarizes the work described in this dissertation and discusses the conclusions inferred from this dissertation. A list of extensions of what is presented in this dissertation is formalized and presented as future work.

Chapter 2

Optimal Compressed Sensing

Reconstructions of fMRI using

Deterministic and Stochastic

Sampling Geometries

2.1. Introduction

Using compressed sensing (CS), we can recover certain signals and images exactly from limited numbers of Frequency domain samples. In theory, to reconstruct images from a limited number of samples, we require that the signal exhibits *sparsity* and the sensing modality exhibits *incoherence*. For one-dimensional signals, when these conditions are met, the sampling rate can be reduced to $\log(N)$ where N denotes the Nyquist rate [1].

When the required conditions are met, perfect reconstruction is possible from a limited number of samples. For example, for piecewise constant signals, very impressive results have been obtained from a very limited number of Fourier samples. Figure 2.1 contains the popular example where the Shepp-Logan

phantom is exactly reconstructed from the Fourier coefficients along 22 radial sampling lines, which equates to a sampling rate almost 50 times smaller than the Nyquist rate [1].

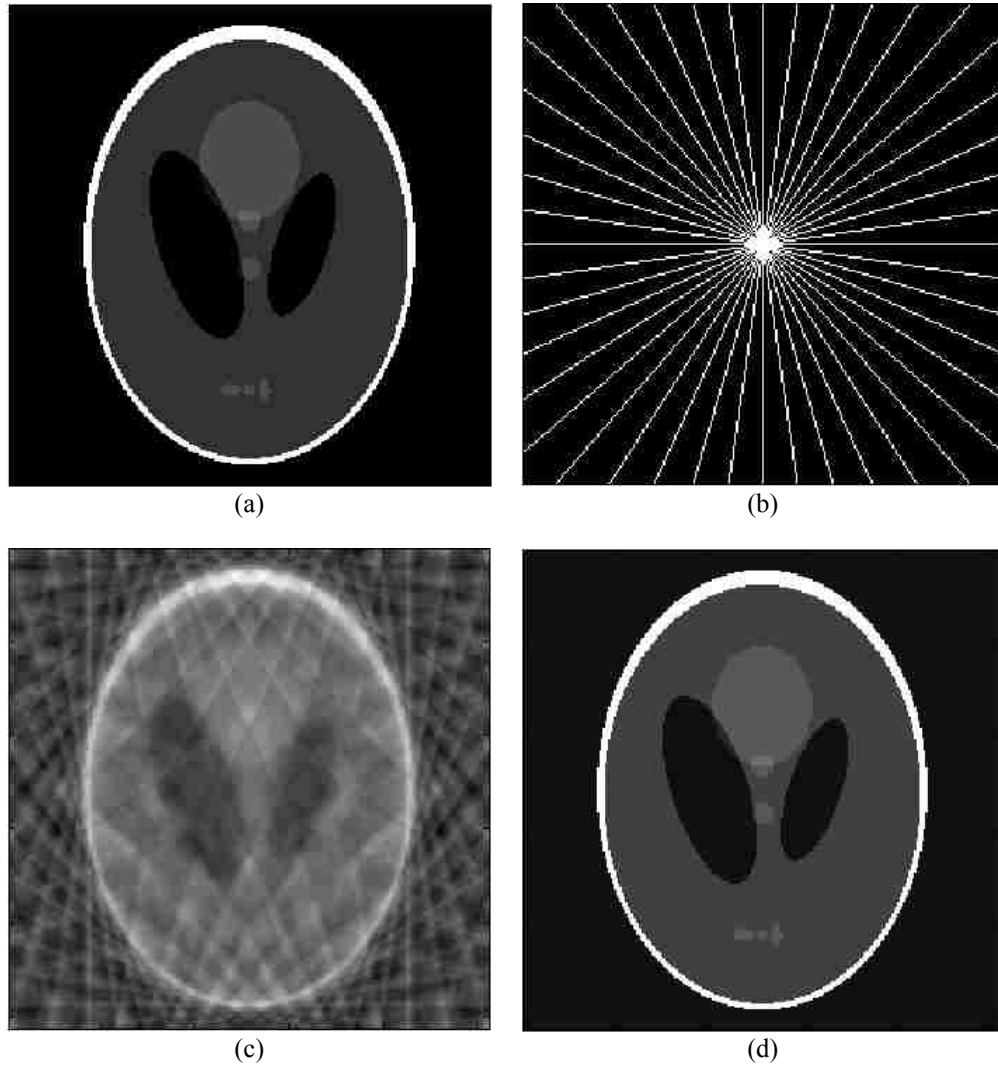


Figure 2.1: Example of a simple CS reconstruction problem. (a) The Logan-Shepp phantom test image. (b) The sampling geometry from which Fourier coefficients are sampled along 22 approximately radial lines. (c) The zero-filling result, where non-sampled coefficients are set to zero and an inverse Fourier transformation is applied. (d) Reconstruction obtained using CS methods. The reconstruction is an exact replica of the image in (a).

Unfortunately, such idealized models may not necessarily fit more complex, non-piecewise smooth images, such as standard MRI images [2]. To help appreciate the problem, we present a typical fMRI slice image in Figure 2.2. Figure 2.2 depicts an fMRI data set, containing a brain slice of a patient “at rest” and the same patient while performing a prescribed task or activity. The K-space data is also depicted, revealing the energy in K-space being concentrated around the center of K-space.

In what follows, we will extend the reconstruction paradigm first developed in [3] by exploring more general sampling geometries that take into consideration MRI scanner acquisition time instead of complying with the conventional compressive sensing requirements that require the use of random, radial, or other more complicated sampling geometries (such as those presented in [4]) that incur a longer acquisition time. Because our focus is on low acquisition times, we explore an optimization process that solves for the compressive sensing objective function parameters that maximize the PSNR obtained by fast, yet somewhat, non-traditional CS sampling geometries.

Acquisition time is a function of both the number of Frequency-domain samples as well as the required scanner motion from sample to sample. In other words, the Frequency-domain scanning order is very important in determining the actual image acquisition times. In particular, the fastest reconstructions can be obtained by scanning using a spiral sampling geometry [5].

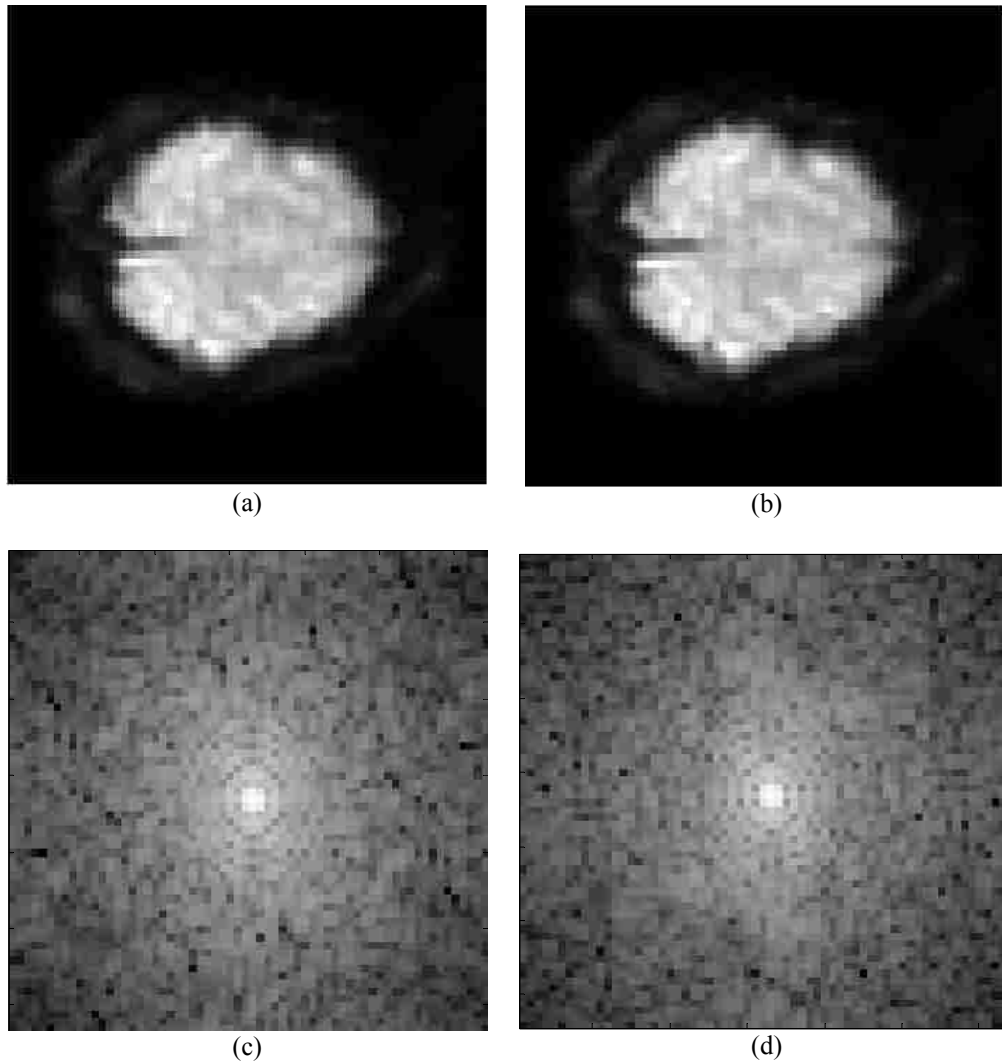


Figure 2.2: MRI image slices with the corresponding Fourier magnitude Spectra. Here, we approximate the Fourier magnitude spectra using a 2D FFT. (a) At rest (OFF) brain slice. (b) Active (ON) brain slice. (c) Log-magnitude 2D FFT of (a). (d) Log-magnitude 2D FFT plot of (d).

On the other hand, to satisfy theoretical Compressive Sensing requirements, we are led to consider random sampling geometries. In addition to these two, we also consider a sampling geometry that restricts the number of phase encoded samples, as they require greater acquisition time than the frequency encoded samples. Our solution for such a sampling geometry was to

down-sample along the phase encoded dimension at dyadic intervals in the outer parts of K-space.

To compare different sampling geometries, we also want to optimize for the best reconstructed image quality. As we shall describe in this chapter, parameter optimization for the Compressive Sensing formulation can have a dramatic impact on the reconstruction. We investigate the estimation of optimal parameter regions that can provide high quality reconstructions over 75% of the MRI images. We also investigate the relative impact of each parameter and the regularity of the optimal region. Therefore, we provide an optimization framework to help determine scanning parameters and scanning geometries that should work for the majority of the cases.

Here, we note the conflicting goals. Clearly, the best reconstructions will require the largest number of Frequency domain samples. Thus, we are interested in determining the minimum acceptable quality that also yields acceptable reconstruction with the minimum number of required Frequency-domain samples. To this end, we determine effective PSNR ranges and associate them with different image reconstruction qualities.

We limit our study to optimizing for the best MRI image reconstructions without solving for activity detection. We thus avoid issues of activity artifact removal and activity detection optimization. We refer to the body of work

described in [6-13], which utilize a wide variety of signal detection, correlation analysis, and statistical tests to infer brain activity in fMRI difference images.

In this chapter, we present literature review of partial K-space reconstruction using CS and traditional methods, noting the restrictions imparted upon K-space by the described methods. We will then provide a theoretical description and motivation of the algorithms used in this study. A detailed description of our method of identifying the optimal range of CS reconstruction parameters is provided in Chapter 2.4, followed by a summary of our results. We close this chapter with a discussion of the results, and a conclusion that briefly reviews the key concepts and notable results developed and presented here.

2.2. Literature Review

As mentioned earlier, one key component of the CS framework for MRI is the exploitation of the *transform sparsity* of MRI images. Transform sparsity refers to objects that are being recovered that have a sparse representation in a known and fixed mathematical transform domain. Medical images of complex physiological structures may not be sparse in the spatial (pixel) domain, but they do exhibit transform sparsity in certain domains (Fourier and Wavelet being two examples). The second requirement imposed by CS theory states that the reduced K-space samples must result in incoherent artifacts in the chosen transform domain. This incoherence requirement is dependent upon on how K-space is sampled. Intuitively, completely random sampling within K-space would produce high incoherence of artifacts in the transform domain.

CS methods have been developed that resulted in improved spatial resolution from reduced K-space sampling, and encompass the fourth class of partial K-space reconstruction techniques. The work presented here falls into this category of partial K-space reconstruction methods, and is closely related to that of Lustig, Donoho, and Pauley [14]. Lustig et al. also provide a general framework for K-space sampling and reconstruction using CS theory [4]. While the sampling geometries presented here are designed to maximize the CS criteria, random and pseudo-random sampling of K-space would result in slower acquisition due to scanner programming constraints. We intend to support the use of deterministic sampling geometries that result in faster acquisitions, at the expense of incoherence. The studies listed below all incorporate a type of random sampling in an attempt to satisfy the incoherence requirement set forth in the CS theory.

Most of the subsequent literature on CS applications to MRI imaging explores the merging of CS theory and other fast MRI acquisition techniques, unique K-space sampling methods, and novel reconstruction algorithms. Gamper, Boesiger, and Kozerke meet the sparsity condition of CS theory by applying the Fourier transformation along the temporal dimension while assuming that the only parts of the field-of-view change at a high temporal rate while other parts remain stationary or change slowly. Their methods show the effectiveness of CS reconstruction for accelerated dynamic (continuous sampling) MRI reconstruction by comparing them to k-t BLAST reconstructions over the same data sets [15].

Their sampling scheme can be described as randomly skipping phase-encoding lines in each dynamic frame. Jung et al. developed k-t FOCUSS to provide a general framework beyond k-t SENSE and k-t BLAST for model-based dynamic MRI by applying CS theory to randomly sampled reconstruction of the prediction and residual encoding that are significantly sparse [16].

Recent studies have focused on extending the work in [14] to non-Fourier bases. Haldar, Hernando, and Liang use selective RF pulses to better satisfy the incoherence requirement of CS theory [17]. Liu, Zou, and Ling apply CS theory to parallel reconstruction using sensitivity encoding. Their extension of SENSE to CS is based upon a reconstruction method using Berman iteration [18]. Trzakso, Manduca, and Borisch present a CS method that minimizes the L-0 semi-norm using re-descending M-estimator functions instead of L-1 norms typically found in CS literature [19]. The extension of the sparsity measure to multi-scale form allows for rapid reconstructions compared to the non-trivial solutions described in [14-19]. Jeromin, Calhoun, and Pattichis have shown that additional constraints in the non-linear reconstruction step of CS methods can be optimized so that reconstructions using deterministic sampling trajectories perform better reconstruction (in terms of PSNR) than random sampling on fMRI data collections [3].

Many non-CS methods have been developed to help preserve image quality when the number of K-space samples violates the Nyquist criterion. One

class of such methods can be described as attempting to seek incoherence in the artifact responses, which would make them less noticeable in the spatial (image) domain. Typically, such approaches come at the expense of a lower signal to noise ratio (SNR). One such method, presented by Marseille et al., utilizes non-uniform down sampling in the phase-encoding dimension of K-space and performs Bayesian reconstruction and edge preserving filters to reduce ringing artifacts in the interpolated image [20]. Wajer et al present an iterative Bayesian image reconstruction technique on sparsely, non-uniformly sampled K-space data. For the 2-D case, a spiral sampling geometry is used, resulting in significant acceleration to the maximum a-posteriori reconstructed image by weighting the likelihood term with the inverse of the sampling density [21]. Circular field-of-view imaging techniques were shown to reduce reconstruction artifacts when polar K-space sampling is under sampled to increase temporal and spatial resolution [22]. Tsai and Nishimura propose a variable-density K-space sampling method to reduce aliasing artifacts. The premise of their work is that downsampling the outer regions of K-space, where little energy is contained compared to the center of K-space, will result in less low-frequency aliasing artifacts [23]. Most methods purposefully retain the central region of K-space intact, as image reconstruction is improved with its inclusion over high-frequency K-space spectra.

Methods that exploit the spatial and/or temporal redundancy of K-space data provide a way of describing another class of partial K-space reconstructions.

A recent study by Lindquist et al. describes methods for obtaining a 3-D echovolumar fMRI imaging sequence by sampling the small central portion of K-space at a high temporal rate [5]. The sampling trajectory is sampled successively across temporal samples instead of successively over each temporal slice, and is constrained to a spiral pattern. Other temporal MRI processing techniques can be found in [24, 25, 26, 27, 28].

2.3. Theoretical Background

2.3.1. Compressed Sensing Image Reconstruction Framework

Most applications of CS theory are based upon the seminal works of Candès and Donoho [29, 30]. This subsection will describe the CS techniques used to reconstruct fMRI images containing n pixels from m samples of K-space, where $m \ll n$. The need for sparsity and incoherence will be first discussed, followed by the motive for the reconstruction techniques employed herein. A signal can be thought of as sparse if the number of samples that contain information are much less than the samples that contain little information. In some unique cases, an image is “naturally” sparse, meaning that the number of non-zero pixels in the image is small compared to the image size. Since this is not the typical case, CS image reconstruction utilizes transform sparsity.

To provide a summary of the basic ideas, we begin with the input image expanded in terms of Wavelet basis functions as given by

$$f(t_1, t_2) = \sum_{i=1}^n x_i \psi_i(t_1, t_2) \quad (1)$$

where the input image f is expanded in terms of a finite number of wavelet basis functions given by $\Psi = [\psi_1 \psi_2 \dots \psi_n]$ and x is the vector of transform coefficients. Here, the transformation matrix is given by Ψ . Using this matrix notation f can be expressed as $x\Psi$. Next, we let f_s denote the reconstructed image using signal samples that have been transformed by a subset of coefficients x_s containing S “large” coefficients. Such a basis is referred to as being S -sparse. The orthonormality of Ψ allows implies that:

$$\|f - f_s\|_{\ell_2} = \|x - x_s\|_{\ell_2}. \quad (2)$$

If the sorted magnitudes of x decay quickly then x can be approximated well by x_s , resulting in the error $\|f - f_s\|_{\ell_2}$ being small. One can infer that the remaining $S-n$ coefficients can be discarded and an acceptable reconstruction via the basis transformation is possible.

Incoherence, in the light of CS theory, can be defined as the least amount of correlation between the sensing basis (in this case, the K-space/Fourier samples) Φ , and the transform basis functions Ψ . The incoherence between bases can be measured using

$$\mu(\Phi, \Psi) = \sqrt{n} \cdot \max_{1 \leq k; j \leq n} |\langle \varphi_k, \psi_j \rangle|. \quad (3)$$

It is clear that from (3) if Φ and Ψ are highly correlated, the sensing coherence is large. The metric in (3) is used in the determination of the m , the number of

sparse measurements required for optimal reconstruction within the context of CS. The review of CS theory in [31] provides a concise description of various signal/basis pairs that have high incoherence.

The work in [1], which includes a discussion on the lower theoretical bounds of m in light of incoherence and sparsity, concludes that if the transform coefficients x of f in the basis Ψ is S -sparse, then the number of measurements samples in Φ must be such that

$$m \geq C \cdot \mu^2(\Phi, \Psi) \cdot S \cdot \log n \quad (4)$$

for some constant $C > 0$.

The publications which first presented CS signal recovery move on from establishing and proving the sparsity and incoherence requirements for exact signal recovery to the use of ℓ_1 minimization. The reconstruction method typically employed in CS image reconstruction uses $\hat{f} = \Psi \hat{x}$ where \hat{x} is the solution to the convex optimization problem

$$\min_x \|x\|_{\ell_1} \quad (5)$$

such that

$$\|\mathfrak{F}(\Psi x) - y\|_{\ell_2} \leq \varepsilon.$$

where \mathfrak{F} denotes the Fourier transform sampling operator, y contains the measured Fourier samples, ε is a nominal (low) value to ensure the transformed data using the x coefficients are consistent with the observed image samples.

Many solutions to (5) have been developed over the past few years, and those specific to MRI image reconstruction from sparse K-space sampling have already been summarized in Section 2.2.

The addition of a *total variation* term to the objective function of ℓ_1 norm minimization problem (4) has been shown to improve MRI image reconstruction [14]. Here, the total variation of a signal can be thought of as a finite-difference approximation to the gradient and is well suited for data recovery when the primary tenets of CS theory (incoherence between sparsely sampled data) are met [1]. The total variation norm (TV Norm) is defined as

$$TV(X) = \sum_{x,y} \sqrt{|D_1 m(x,y)|^2 + |D_2 m(x,y)|^2} \quad (6)$$

where $D_1 m = m(x,y) - m(x-1,y)$, $D_2 m = m(x,y) - m(x,y-1)$ denote finite differences along each dimension. TV Norm minimization is the key component to the problem of recovering data from a sparse basis. The TV Norm is an excellent candidate for reconstructing piece-wise constant signals, but tends to over-smooth the resulting pixel data. It is well documented in [1] as the objective function being minimized to provide a solution for the reconstruction of an under-sampled Fourier spectrum of the Shepp-Logan phantom image (refer back to Figure 2.1).

When considering sparse image reconstruction of data that is not piece-wise constant, the TV-Norm tends to lack the ability to pick up regions of smooth gradients. We follow [14, 32] and include a TV penalty on the objective function

in (5) to counter the effects of the ℓ_2 term. Thus, our objective function becomes

$$\min_x \beta \|x\|_{\ell_1} + \alpha \text{TV}(\Psi x) \quad (7)$$

such that

$$\|\mathfrak{F}_k(\Psi x) - y\|_{\ell_2} \leq \varepsilon.$$

where we have added the TV penalty parameter α , as well as a transform penalty parameter β to allow for a compromise between the opposing effects of ℓ_1 and ℓ_2 norms in the objective function and the constraint.

To account for different spectral sampling geometries, we use \mathfrak{F}_k where k is used to denote the k^{th} sampling geometry from the general geometry class denoted by κ .

2.3.2. Optimal TV Norm and Wavelet Transform Penalty

For each spectral sampling geometry we optimize the cost parameters α and β for optimal reconstruction. An optimal solution is sought so that the peak signal to noise ratio (PSNR) of the reconstructed fMRI image using (7) is maximized. For all candidate values of the penalty parameters, we solve (7) via the non-linear conjugate gradient and backtracking algorithm described in [14], (for which reliable Matlab implementation is available).

To define the new optimization framework, let z denote the original input image. As discussed earlier, we let \mathfrak{T}_k denote the Fourier sampling geometry that is being considered. For each sampling geometry, we seek the optimal CS model parameters α, β such that the PSNR is maximized. Here, let P_k denote the optimal PSNR level that can be achieved. It is given by

$$P_k(x, z) = 20 \cdot \log_{10} \left(\frac{\text{Max}(z)}{\sqrt{\frac{\sum_{i=1}^n (\Psi x - z)^2}{n}}} \right).$$

The nested optimization problem can thus be expressed as:

$$\max_{\alpha, \beta} P_k(x, z) \quad (8)$$

where the transform coefficients x are obtained using

$$\min_x \beta \|x\|_{\ell_1} + \alpha \text{TV}(\Psi x)$$

such that

$$\|\mathfrak{T}_k(\Psi x) - y\|_{\ell_2} \leq \varepsilon.$$

For the CS model parameter optimization, we choose the Nelder-Mead or simplex search algorithm [33] since it does not require the derivative calculations typically found in steepest descent optimization algorithms. Such a requirement would be difficult to achieve since the parameter search objective function (8) relies on the solution to a separate objective function (7). Instead, the simplex search algorithm only requires function values at given points in the R^2 search space, putting it in the class of solvers known as direct search methods [34].

Our basic problem here is that the original images are not available to us if they are to be collected using a reduced K-space geometry. Thus, our basic assumption is that the same range of optimal parameters can be made to work for most of the images of the same class. As we demonstrate in the results section, this basic assumption is valid and can be verified. Thus, we can select appropriate parameter ranges for α, β and use them to provide image reconstructions that will provide a PSNR level that is above a certain desired level.

To estimate appropriate parameter ranges, we consider a class of fMRI images collected from the same scanner. Using the objective function values at each simplex step, which is the PSNR of the on or off image reconstruction using the current α and β values, we can interpolate to a range of values for both parameters that we claim will produce a specific PSNR value for that image. We then overlap the estimated ranges of values for all images so that we can provide a recommended range of operating parameters.

For comparing among different sampling geometries we looked at the PSNR level that can be achieved as a function of the number of spectral samples that are used. Thus, when both geometries use the same number of spectral samples, the one with the highest PSNR values will be considered to be better. Here, we note that we do not consider the acquisition time directly. Thus, in the results section, we will also comment on the expected acquisition time associated

with each sampling geometry. Fortunately, as we shall discuss later, the best geometries will turn out to be the fastest in terms of acquisition time.

2.4. Methods

2.4.1. Data Set and fMRI Activity Detection

In blood oxygenation-level dependent (BOLD) fMRI, neural activity is detected by changes in the $T2^*$ relaxation time due to changes in blood oxygenation levels in response to local activation. All images were acquired on a 3T Siemens TIM TRIO system with a 12-channel radio frequency (RF) coil. The fMRI experiment used a standard Siemens gradient-echo EPI sequence modified so that it stored real and imaginary data separately. We used a Field-of-View (FOV) = 240 mm, Slice Thickness = 3.5 mm, Slice Gap = 1 mm, Number of slices = 32, Matrix size = 64×64 , TE = 29ms, and TR = 2s. The fMRI experiment used a block design with periods of 30 s OFF and 30 s ON. The subjects who participated in this study tapped the fingers of their right hand during the ON period. There were five and a half cycles, starting with OFF and ending with the OFF period.

The BOLD fMRI data was then preprocessed to account for motion artifacts and spatially normalized into the standard Montreal Neurological Institute space. This spatial normalization was then sub-sampled to $3 \times 3 \times 4$ mm, resulting in $53 \times 63 \times 46$ voxels. An individual slice was then selected that ensured measureable regions of activity based on the task being performed by the test subjects.

Temporal smoothing also tends to better localize detected activity across all temporal slices within a single run. Instead of utilizing the temporal information, our reconstructions are of two individual ON and OFF BOLD images. The less dense collection of temporal samples provides a worst-case scenario for detecting neural activity. We detected neural activity in fMRI by calculating the difference image of the reconstructed ON and OFF images. Individual slices were reconstructed by resolving (7) using the parameters obtained by solving (8) for different sampling geometries. At this juncture, the neural activity detection problem becomes a segmentation problem. Localized regions in the difference image with high relative values denote the region of the brain where activity occurred.

Activity segmentation can be performed by many alternate methods than the rudimentary process that was described above. Here, we will not consider optimization over a variety of different activity detection algorithms. We do note however that the activity detection algorithms that employ low-pass filtering will tend to favor zero-filling over interpolation by Compressive Sensing or any other method. The reason for this is that low-pass filtering attenuates high-frequency components that are estimated by the interpolation/reconstruction method. Ultimately, any segmentation for BOLD fMRI images will be governed by the accuracy of the reconstructed images themselves. Thus, for considering activity detection, we present the reconstructed difference images for visual quality comparisons.

2.4.2. Partial K-Space Sampling Geometries

The sampling geometries we pursued in this work are similar to those presented in [3], but we took more care to design our sampling geometries based on the literature (e.g. spiral sampling around DC as in [5]) and fast acquisition times. Two sampling geometry classes, a spiral low-pass and dyadic downsampling along phase encodes, are deterministic, while two geometry classes are based on random sampling.

First, we consider geometries that restrict down sampling in the phase-encoded dimension only. Our chief motivation of including a constraint on how samples are obtained is that reducing the number of phase encodes provides a greater reduction in scan time when considering only down sampling the frequency encoded samples instead. In addition, we wish to compare partial K-space sampling in just the phase-encoded dimension to partial K-space sampling in both dimensions around the center of K-space.

As noted in the literature review, the central region of K-space is essential in obtaining reconstruction performance that is acceptable. Almost all non-CS reconstruction of partial K-space included the center of K-space in the data that was sampled. A dyadic sampling geometry class was developed that considers sparse sampling along the phase-encoded dimension of K-space. All geometries of this class are shown in the first row of Table 2.1. This geometry includes samples from a collection of contiguous frequency encoded vectors centered over

the center of K-space. The width of the central region can be varied to generate a number of unique geometries that are members of this class. Nine unique geometries are generated based on a central region that sample $1/2$, $1/3$, $1/4$, $1/6$, $1/8$, $1/10$, $1/12$, $1/16$, and $1/32$ of the phase encoded samples. Beyond the bounds of the central region of the geometry, additional frequency encoded vectors are sampled every 2^{nd} , 4^{th} , 8^{th} , etc. phase encoded sample until the entire support of the scanned K-space has been included. The dyadic characteristic of the gap size between subsequent high-frequency samples was intentionally designed to sample more densely near the center of K-space, and in hopes that such sampling in K-space might coincide with the Wavelet transform our reconstruction method utilized.

An interesting characteristic of this class is that the size of the central region is inversely proportional to the number of frequency-encoded vectors at higher frequencies. This class will be referred to as the Dyadic Phase Encoded (DPE) geometry class in the remainder of this paper. We note that the DPE class does not attempt to utilize randomness in sampling to decrease coherence in terms of CS reconstruction. We are relying on the system incoherence between samples of K-space (Fourier) data, wavelet coefficients, and the spatial image space.

We also consider two additional geometry classes which attempt to increase the incoherence between the sensing (Φ) and transform bases (Ψ) by introducing an element of randomness in how the samples were selected. The

first class, which is referred to as the Random Phase Encoded (RPE) geometry class, samples frequency-encoded vectors along random phase encoded samples. This sampling method was selected as a comparison to the dynamic CS MRI in [16]. In a two image, single fMRI study, such sampling would not expect to provide acceptable reconstruction due to the possibility of excluding a portion of the central region of K-space. This deficiency is less apt to be problematic in dynamic applications as successive temporal samples likely include central K-space data that can be utilized in the final analysis. Each of the Random Phase Encoded geometries contains the same number of samples as one of the Dyadic Phase Encoded geometries. Due to the one-to-one geometry correspondence across classes, there are nine total geometries in the RPE class. All of the Random Phase Encoded geometries are shown in the second row of Table 2.1.

The second geometry class that incorporates randomness into the sampling scheme can be described as random sampling along a 1-D probability distribution function across the phase encoded samples at each frequency-encoded sample. This geometry class will be referred to the Random Sampling PDF (RSP) class.

The motivation of this geometry is from [14], but we alter the distribution to be replicated at each frequency-encoded sample instead being defined over both K-space dimensions. We use a fifth-order polynomial of the form

$$f(u, v) \propto \left(1 - \sqrt{u^2 + v^2}\right)^5, \quad -\frac{U}{2} < u \leq \frac{U}{2}, \frac{V}{2} < v \leq \frac{V}{2}, \quad (9)$$

where U and V are the number of K-space samples in the frequency and phase encoded dimension. Our motivation for this geometry was to attempt a compromise between the inclusion of the center of K-space and also imparting incoherence into the CS problem through a pseudo-random sampling geometry. All of the representative geometries of the RSP class are depicted in the third row in Table 2.1. It is important to note that while the RSP geometry would ensure high incoherence, regardless of the basis relationships of our CS framework, but would require more scanning time during acquisitions.

Finally, we include a geometry class that restricts K-space sampling in both the phase encoded and frequency-encoded dimensions. This geometry is very similar to the Centered Low Pass geometry in [3], but we generate the nine geometries by sampling along a Cartesian spiral emanating from the center of K-space. Such sampling geometries are more typical of the classical partial K-space reconstruction techniques found in literature [21-25]. This class is referred to as the Spiral Low Pass (SLP) geometry class all geometries that comprise this class are shown in the fourth row of Table 2.1.

2.4.3. Optimization of CS Penalty Parameters

We want to compute optimal α and β values in (7) that maximize the PSNR of the image reconstructed from one of the partial K-space geometries presented above. The primary motivation of the following methods was to provide a range

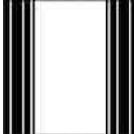
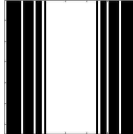
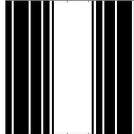
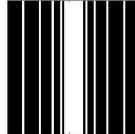
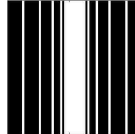
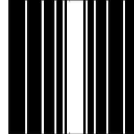
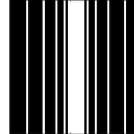
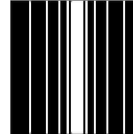

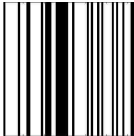
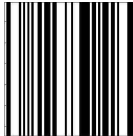
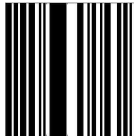
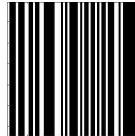
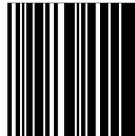
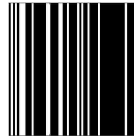
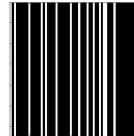
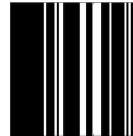
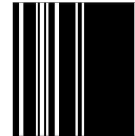






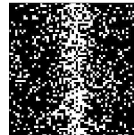



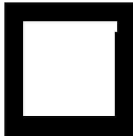
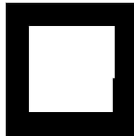
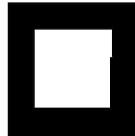
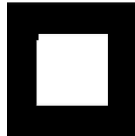
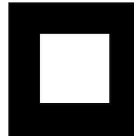


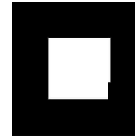
of α and β values for each geometry that would achieve a minimum acceptable PSNR level.

To accomplish this, we first reconstructed the twenty-four fMRI images from the twelve runs that were obtained for this study. While differences between these two images are not readily apparent to the human eye, the method of data encoding provides meaningful information when properly processed for neural activity detection. First, we zero pad the images from size 53×63 to 64×64 . We use the 2D FFT to generate K-space data for our experiments.

The thirty-six geometries shown in Table 2.1 were applied to the K-space samples. A baseline reconstruction is obtained by applying the inverse-Fourier transform to the partial K-space data. This reconstruction will exhibit the aliasing artifacts that the approaches presented in the introduction seek to suppress. The partial K-space data is then operated upon by the two-level optimization scheme described above.

We initialize the α and β values with zeros. At each new simplex in the parameter space (7) is re-solved for the values of α and β at each vertex of the simplex. The PSNR of the solutions to (7) for each simplex are treated as the functional evaluation upon which the simplex will adjust. One of the drawbacks of the simplex search algorithm is that it can take a long time to converge to the optimal solution; continually re-adjusting without gaining much improvement on

TABLE 2.1
K-SPACE SAMPLING GEOMETRY CLASS EXAMPLES

Geometry Class \ % Retained Samples	62.5%	48.5%	40.6%	32.8%	28.1%	26.6%	25.0%	21.9%	20.3%
Dyadic Phase Encoded (DPE)									
Random Phase Encoded (RPE)									
Random Samples on a PDF (RSP)									
Spiral Low Pass (SLP)									

This table contains all of the geometric sample masks explored in this study. The columns of the table are sorted by the percentage number of samples. The rows of the table indicate a geometry class. We are interested in comparing the results of geometries across columns, as they can provide insight into the minimum number of samples that can be used that still allow us to obtain an acceptable level of PSNR.

the functional being explored. We applied three stopping criteria to the search algorithm that solved (8). The first is that if the change in α and β fell below a tolerance of $1e-5$, the algorithm would terminate. This tolerance was selected after trial runs revealed the scale of the α and β space. The second stopping criterion is a threshold on the change of the functional. If the difference between the current functional(s) and the functional(s) of the previous simplex exceeded the functional tolerance of 0.05 the algorithm would terminate. The final stopping criterion was a limit on functional evaluations, which was selected at 200.

All of the above reconstruction steps are depicted in the flowchart in Figure 2.3. We then analyzed the search surfaces for each partial K-space sample on each image with the intention of finding consistency in the optimal solutions across patients. The simplex steps for each image processed by our method were interpolated to provide a smooth, 2-D parameter search surface. Inspection of these contours revealed flat regions around the minimum, which lend themselves to a threshold operation based on the functional value (PSNR) within these regions. These can then be intersected across patients for each mask, taking care to note the number of intersections within the parameter space.

Analysis of the intersecting parameter surfaces would then provide a range of values for both α and β that achieve a certain level of reconstruction

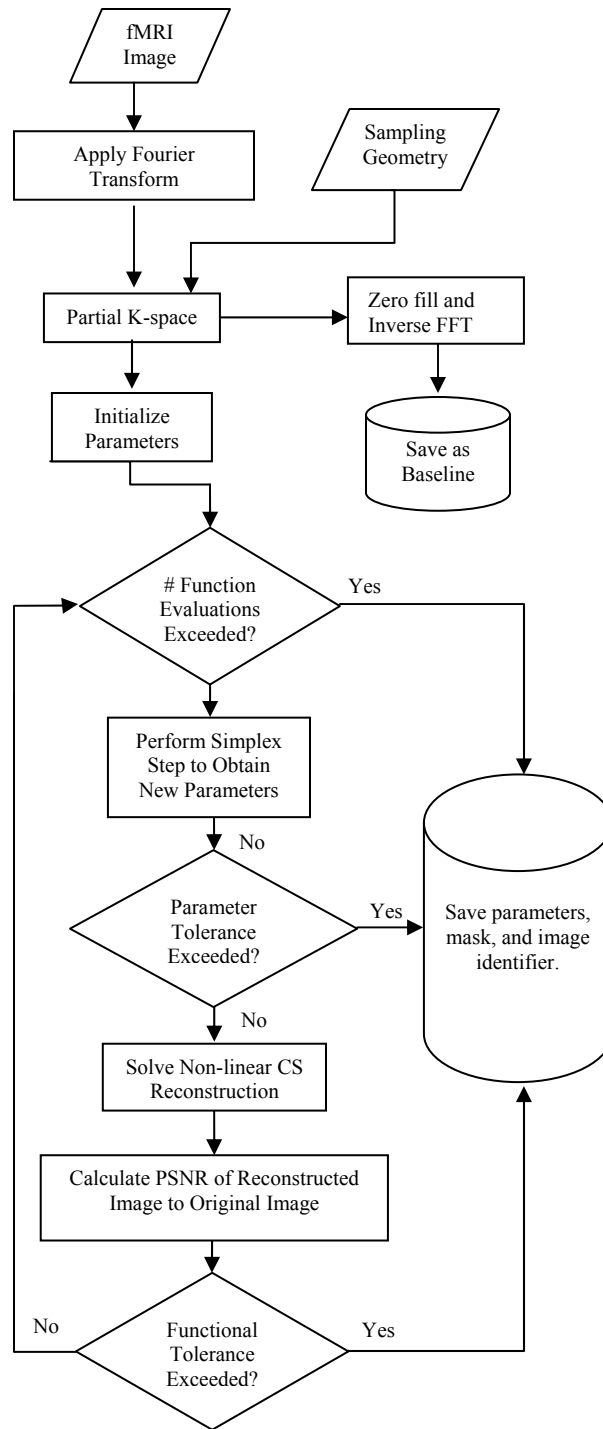


Figure 2.3: Parameter optimization flow chart. The above chart depicts the sequential process that is implemented in this work for determining the optimal reconstruction parameters for each image. This process is repeated on the same image for all thirty-six partial K-space data generated by the sampling geometries depicted in Table 2.1.

performance for any partial K-space data set sampled by any of the geometries outlined by the four classes in this study.

To provide a quantitative method for region consistency, we estimate outer and inner bounding boxes of the optimal regions (see Figure 2.8). Here, we use the ratio of the outer to inner bounding boxes as an indication of the complexity of the optimal operating region. Empirically, a value between 1 and 2 indicates the inner bounding box closely follows the contours of the outer bounding box. Higher values indicate a more complex region, where the range of α might be much larger than the corresponding range for β . Our approach seeks to identify partial K-space geometries that provide acceptable image quality from a well defined range for the objective function parameters used in the CS reconstruction in (7).

2.5. Results

We considered the TV penalty coefficients, α and β , as being “sufficiently optimal” if they lead to partial K-space reconstructions that achieve a suitable level of PSNR quality. For each image ON and OFF image, the optimal PSNR values for each reconstruction using the solution to (8) are shown for the four geometry classes in Figure 2.4. The PSNR values obtained by simply zero-filling the missing partial K-space samples are displayed as a comparison. Figure 2.4(a) and Figure 2.4(d) are the two non-random classes (DPE and SLP), and a brief inspection reveals the PSNR values for the DPE and SLP geometry classes are

higher than the RPE and RSP geometry classes. The Dyadic Phase Encoded geometry class exhibited the most consistency between PSNR values across images for the same geometry, but had a lower average PSNR value across images than the Spiral Low Pass geometry class. The random classes exhibited a greater improvement over zero-filling, but did not achieve reconstructed images as accurately as the deterministic classes (for the same number of samples). It was concluded that the spiral low pass sampling technique continued to demonstrate the best results in terms of PSNR, in which each mask resulted in average PSNR values that could be described as producing excellent reconstructed (PSNR > 40 dB) images. The average PSNR values for each class are listed in Table 2.2 for all four classes.

The linearly interpolated function evaluations during the Nelder-Mead simplex search algorithm of the reconstruction of the fMRI images in Figure 2.2(a) and Figure 2.2(b) are shown as contour plots in Figure 2.5. Figure 2.5(a) is the contour plot of the α and β search surface when solving for the optimal parameters for reconstructing the OFF image, Figure 2.5(b) is a contour plot of the parameter space when solving for the optimal parameters for reconstructing the ON image. The PSNR values are included for each simplex vertex calculated during the search. In the examples depicted in Figure 2.5, the Nelder-Mead simplex method demonstrated rapid “descent” toward the optimal solution, but then slowed down, while performing many smaller iterations until the tolerances were achieved. We observed near-exact search surfaces between the ON and

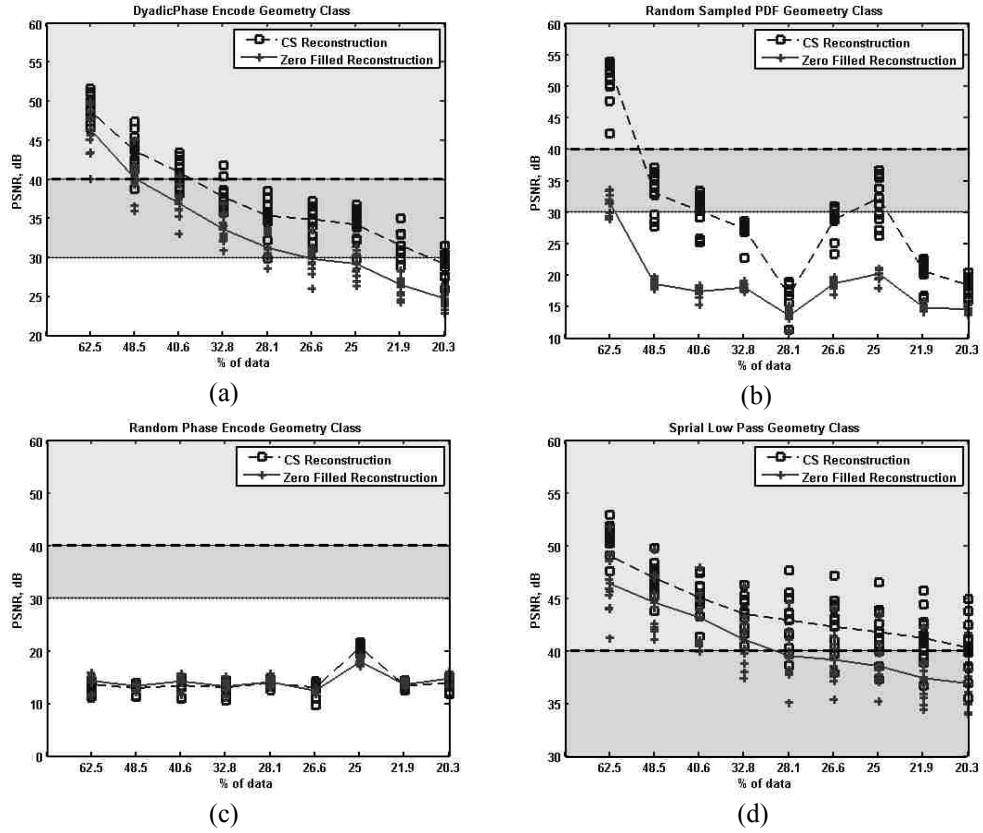
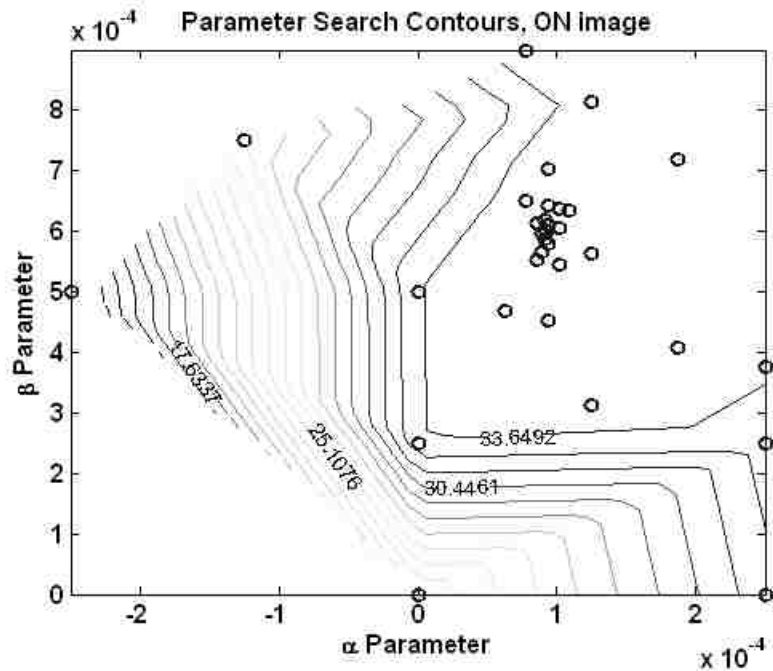


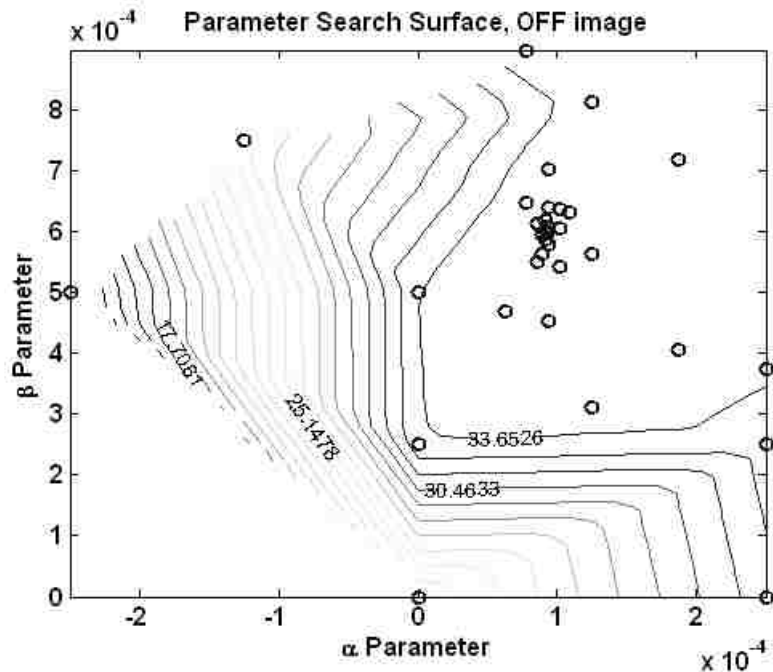
Figure 2.4: Optimal PSNR values for CS reconstructions for each sampling geometry for both ON and OFF images. (a) The results of sampling K-space with the DPE geometry class. (b) The results of the RPE geometry class. (c) The results of the RSP geometry class. (d) The results of the SLP geometry class.

TABLE 2.2
AVERAGE MAXIMUM PSNR PER GEOMETRY CLASS

% K-space Samples	DPE Class	RPE Class	RSP Class	SLP Class
62.5	48.67 dB	13.65 dB	53.03 dB	49.01 dB
48.5	43.59 dB	12.93 dB	33.03 dB	46.90 dB
40.6	40.87 dB	13.44 dB	30.27 dB	45.05 dB
32.8	37.71 dB	13.91 dB	27.39 dB	43.49 dB
28.1	35.31 dB	13.08 dB	16.84 dB	42.99 dB
26.6	34.88 dB	13.05 dB	28.78 dB	42.27 dB
25.0	34.18 dB	20.61 dB	32.27 dB	41.28 dB
21.9	31.54 dB	13.41 dB	20.64 dB	41.19 dB
20.3	29.11 dB	13.95 dB	18.43 dB	40.29 dB



(a)



(b)

Figure 2.5: Parameter optimization surface of an fMRI image pair. (a) The α and β parameters for the ON image. (b) The α and β parameters for the OFF image. Of note is the consistency of the contour plots in (a) and (b).

OFF resulting optimal parameter search method for all of the twelve runs. This result would allow for additional fMRI studies to be processed with the above methods in less time, since either the ON or OFF image would provide a surface that alone represents the patient. The plots in Figure 2.6 show the α and β values at the Nelder-Mead simplex iterations for both the ON and OFF images of a single fMRI sample, depicting how the final parameter values for both images are equal.

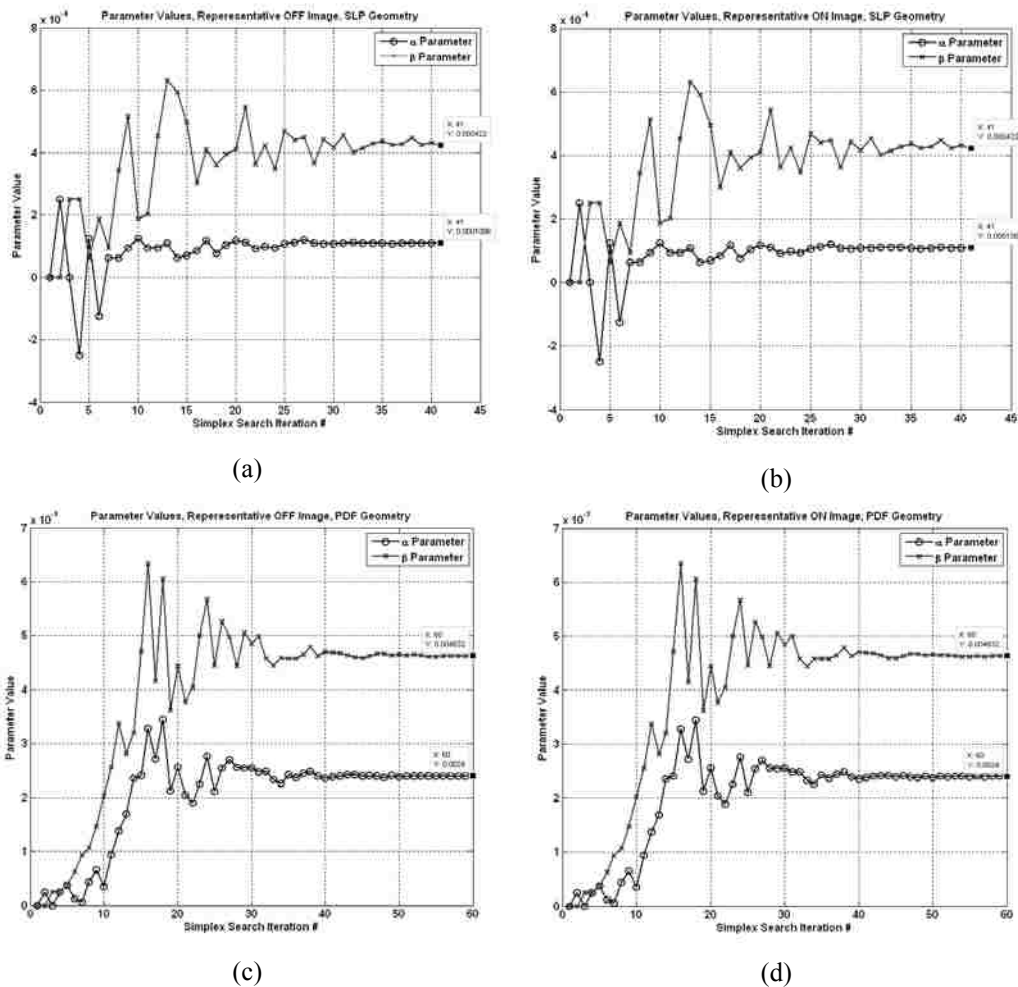


Figure 2.6: Individual parameter values at each simplex iteration for an fMRI image pair. (a) and (c) are the OFF image parameter values. (b) and (d) are the ON image parameters. The parameters are identical for each simplex iteration.

The flat attribute of the search surface in the parameter space was consistently observed for the DPE and SLP geometry classes. It was this observation that motivated the use of parameter search surface intersections across images to provide a range of reconstruction parameters for all geometries. Binning the PSNR results at the optimal operating parameters allowed us to establish a comparison of the effectiveness of the sampling geometries. This also allowed for the quantification of generalized solutions for the geometries based on an area metric from the intersected parameters spaces.

Based on visual evaluation of the results, we consider an *excellent* reconstruction resulting from PSNR values greater or equal to 40 dB. An *acceptable* reconstruction can be described as having a PSNR value between 30 and 40 dB, while an *marginal* reconstruction can be described as having a PSNR value less than or equal to 30 dB. Figure 2.7 contains the resulting reconstruction of an ON image using two of our sampling geometries using reconstruction parameters to that result in PSNR values of each of these quality levels.

To determine the minimum acceptable reconstruction quality, we consider PSNR values from 20 dB to 45 dB (see Figure 2.7). For a given sampling geometry and a required image quality, all parameter regions were intersected together to determine the maximum number of images for which the same parameter regions will work. Thus, for each quality level, we can have a

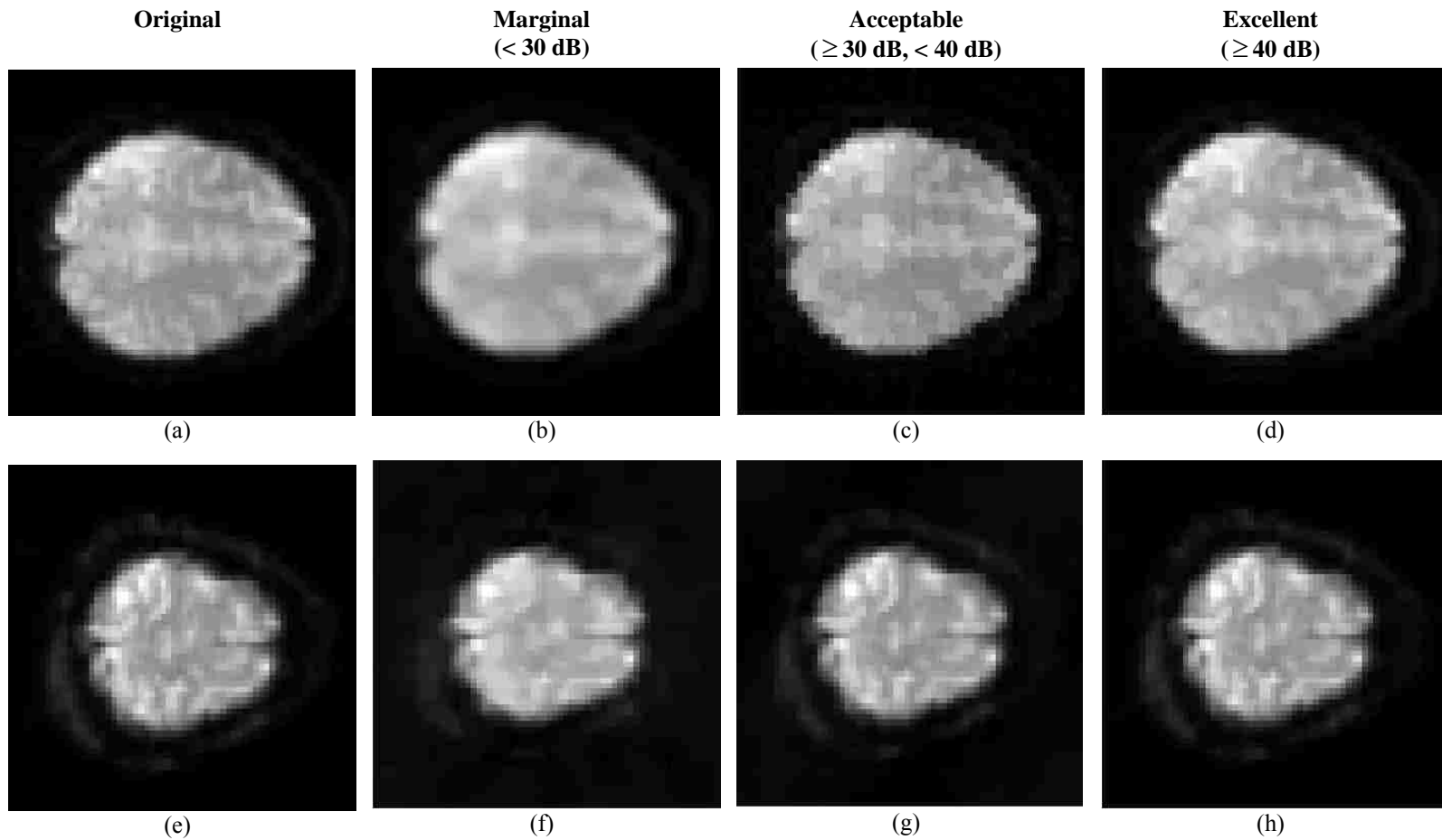


Figure 2.7: Example of reconstruction quality for two sample images. The top row contains reconstructions from various SLP sampling geometries, not necessarily using the optimal reconstruction parameters. The bottom row contains reconstruction from the RSP sampling geometry class. (a) and (e) are the original ON images. (b) and (f) are marginal reconstructions of 28.35 and 24.22 dB, respectively. (c) and (g) are acceptable reconstruction of 34.97 and 39.64 dB. (d) and (h) are excellent reconstructions of 48.35 and 56.69 dB, respectively.

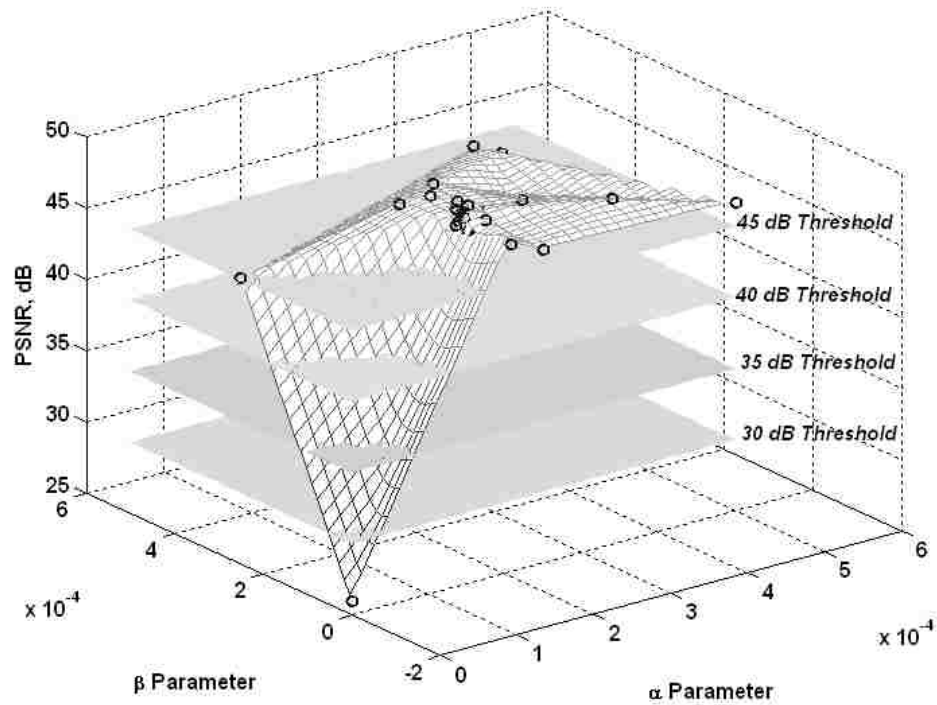


Figure 2.8: Reconstruction image quality as a function of parameter optimization. The surface shown here is generated from the functional evaluations of the simplex search parameter search method using the DPE geometry retaining 62.5% of K-space samples on a single image.

maximum of 24 images, indicating that the same optimal region provided this minimum quality for all reconstructions. To avoid outliers, we consider an optimization region to be successful in meeting the image quality criterion if 75% or more of the images maintain a level above what is required.

The resulting parameter regions ranged from -0.0007 to 0.007 for α and from -0.0002 to 0.006 for β . A bounding box area technique was employed to quantify the extent of each parameter space. The ratio of the smallest outer bounding box to the largest inner bounding box was calculated as an indicator of

the complexity of the optimal region. Larger outer and inner areas, combined with lower ratios indicate a more desirable solution. Here, our interest in stable solutions reflects our desire to use the same parameter setting for a variety of different images.

Table 2.3 contains all of the bounding box ratios for each geometry and PSNR reconstruction quality level. The data in Table III reveals that the DPE and SLP geometry class outperform the RPE and RSP classes. Neither of the random classes provided a suggested set of optimal parameter values to achieve excellent reconstruction. It was expected that the RPE class exhibit poor reconstruction, since the geometries do not contain sufficient samples from the center of K-space. And only a single geometry, the Random Sampled on a PDF geometry including 62.5% of samples resulted in a suggested operating parameter space for achieving acceptable reconstruction.

On the other hand, the DPE class achieved excellent reconstruction from two geometries (62.5% and 48.5%) and the SLP class achieved excellent reconstruction from the three geometries that retained the most number of K-space samples (60.5%, 48.5%, and 40.6%). As the reconstruction requirement becomes more lenient, fewer samples are required for acceptable reconstruction.

Twelve additional DPE geometries were found to satisfy the parameter space threshold and intersection procedure. All eighteen SLP geometries that

TABLE 2.3
 BOUNDING BOX RATIOS FOR PARTIAL K-SPACE GEOMETRIES;
 LARGER VALUES INDICATE MORE COMPLEX OPTIMIZATION REGIONS.

Class	T	62.5 % Sampling Rate	48.5 % Sampling Rate	40.6% Sampling Rate	32.8 % Sampling Rate	28.1% Sampling Rate	26.6 % Sampling Rate	25.0 % Sampling Rate	21.9 % Sampling Rate	20.3 % Sampling Rate
<i>DPE</i>	20 dB	2.85	3.32	3.33	2.88	3.80	3.62	4.07	2.94	2.77
<i>DPE</i>	25 dB	2.85	3.32	3.33	2.88	3.80	3.95	4.45	3.33	4.88
<i>DPE</i>	30 dB	2.85	4.15	3.41	4.18	8.75	8.21	6.00	12.83	N/A
<i>DPE</i>	35 dB	3.32	5.30	5.90	11.92	N/A	N/A	N/A	N/A	N/A
<i>DPE</i>	40 dB	3.97	5.71	N/A	N/A	N/A	N/A	N/A	N/A	N/A
<i>DPE</i>	45 dB	3.79	N/A	N/A	N/A	N/A	N/A	N/A	N/A	N/A
<i>RPE</i>	20 dB	N/A	N/A	N/A	N/A	N/A	N/A	N/A	N/A	N/A
<i>RPE</i>	25 dB	N/A	N/A	N/A	N/A	N/A	N/A	N/A	N/A	N/A
<i>RPE</i>	30 dB	N/A	N/A	N/A	N/A	N/A	N/A	N/A	N/A	N/A
<i>RPE</i>	35 dB	N/A	N/A	N/A	N/A	N/A	N/A	N/A	N/A	N/A
<i>RPE</i>	40 dB	N/A	N/A	N/A	N/A	N/A	N/A	N/A	N/A	N/A
<i>RPE</i>	45 dB	N/A	N/A	N/A	N/A	N/A	N/A	N/A	N/A	N/A
<i>RSP</i>	20 dB	3.07	31.59	33.71	18.00	N/A	N/A	N/A	N/A	N/A
<i>RSP</i>	25 dB	3.07	29.79	52.07	13.3	N/A	N/A	N/A	N/A	N/A
<i>RSP</i>	30 dB	3.07	N/A	N/A	N/A	N/A	N/A	N/A	N/A	N/A
<i>RSP</i>	35 dB	3.54	N/A	N/A	N/A	N/A	N/A	N/A	N/A	N/A
<i>RSP</i>	40 dB	4.38	N/A	N/A	N/A	N/A	N/A	N/A	N/A	N/A
<i>RSP</i>	45 dB	6.00	N/A	N/A	N/A	N/A	N/A	N/A	N/A	N/A
<i>SLP</i>	20 dB	3.00	2.18	2.84	4.00	9.38	10.31	9.17	10.31	6.88
<i>SLP</i>	25 dB	3.00	2.18	2.84	3.73	7.88	9.63	8.56	8.75	7.00
<i>SLP</i>	30 dB	3.00	2.18	2.84	3.47	13.00	10.00	10.00	9.00	9.00
<i>SLP</i>	35 dB	3.00	2.18	2.84	3.84	18.00	16.00	16.00	14.77	18.00
<i>SLP</i>	40 dB	3.27	3.86	5.96	N/A	N/A	N/A	N/A	N/A	N/A
<i>SLP</i>	45 dB	5.77	N/A	N/A	N/A	N/A	N/A	N/A	N/A	N/A

were included in this experiment satisfied our requirement for acceptable reconstruction. Based on the results in Figure 2.4 and Table 2.3, we limited the reconstruction and brain activity analysis to only the DPE and SLP classes.

These classes outperformed the RPE and RSP classes in peak PSNR and in the attributes for all geometries that sampled less than 50% of K-space. The best geometry designed with randomness was the RSP geometry sampling at 62.5%. While reconstructions performed with this geometry could be considered excellent, only two other geometries from the RSP class would be considered acceptable in performance.

We also compared the difference images of the original ON and OFF samples, the CS reconstructed ON and OFF samples, and also the reconstruction values of zero-filling the missing partial K-space samples. We selected the lowest SLP geometry (sampling only 20.3% of K-space) as our comparison.

We also provide a qualitative assessment of the difference images. As shown in some selected examples in Figures 2.9, 2.10, and 2.11, the difference images from CS reconstructions appear sharper than the smoother, zero-filled reconstructions. The ON and OFF slices were reconstructed using the 20.3% sampled SLP geometry. The geometry is shown in the last entry of Table 2.1. We divide this entire image set into three separate figures to allow for larger representation (four patients per figure) to support visual assessment claims. We

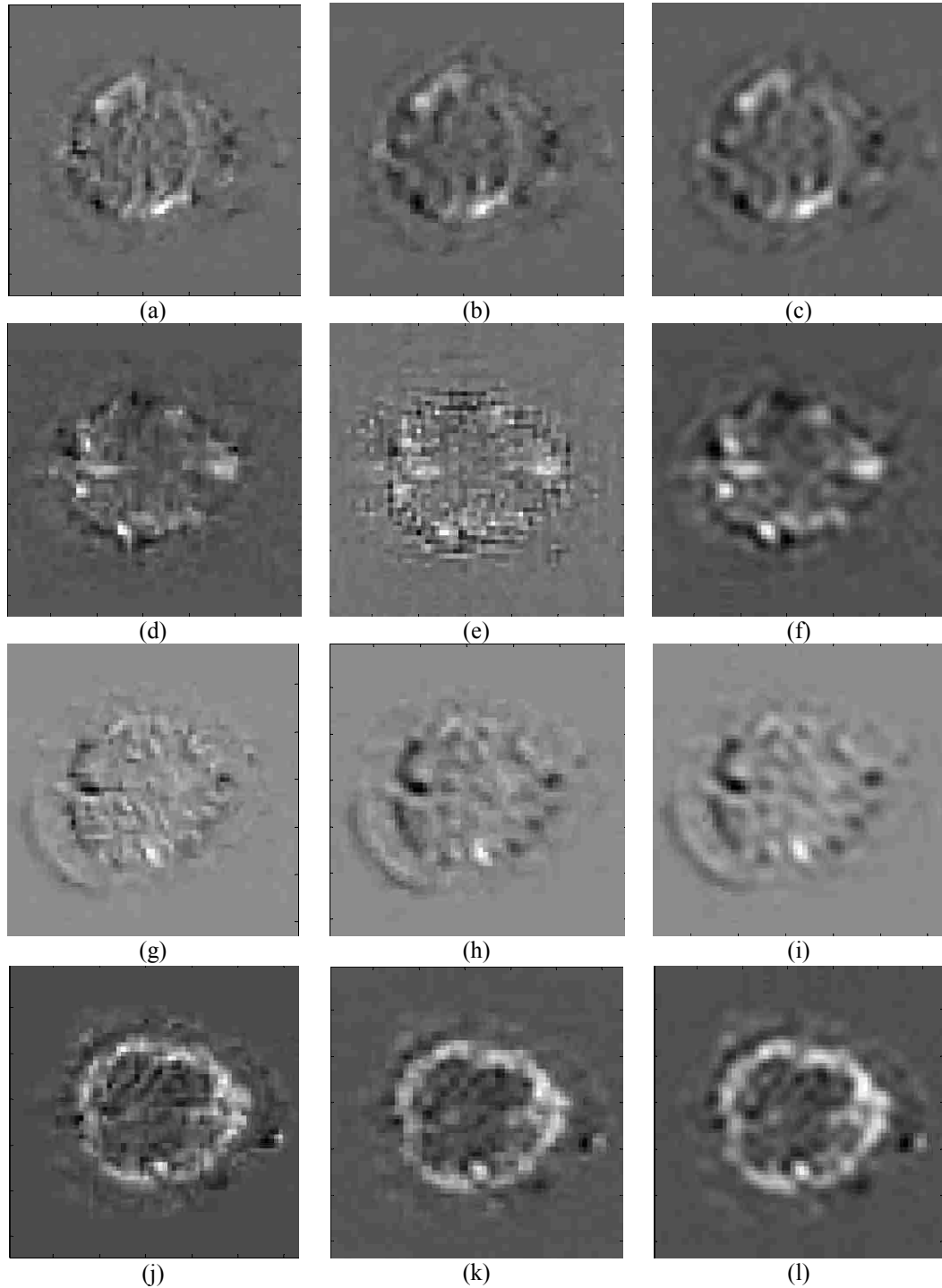


Figure 2.9: Difference images obtained from four individual fMRI sample sets I. (a), (d), (g), and (j) are the difference images obtained from full K-space sampling. (b), (e), (h), and (k) are the difference images obtained by reconstructing the partial K-space our proposed CS methods. The final column, containing images (c), (f), (i), and (l), are obtained by zero-filling the missing K-space samples. Visual assessment of the second and third columns reveals a greater amount of detail.

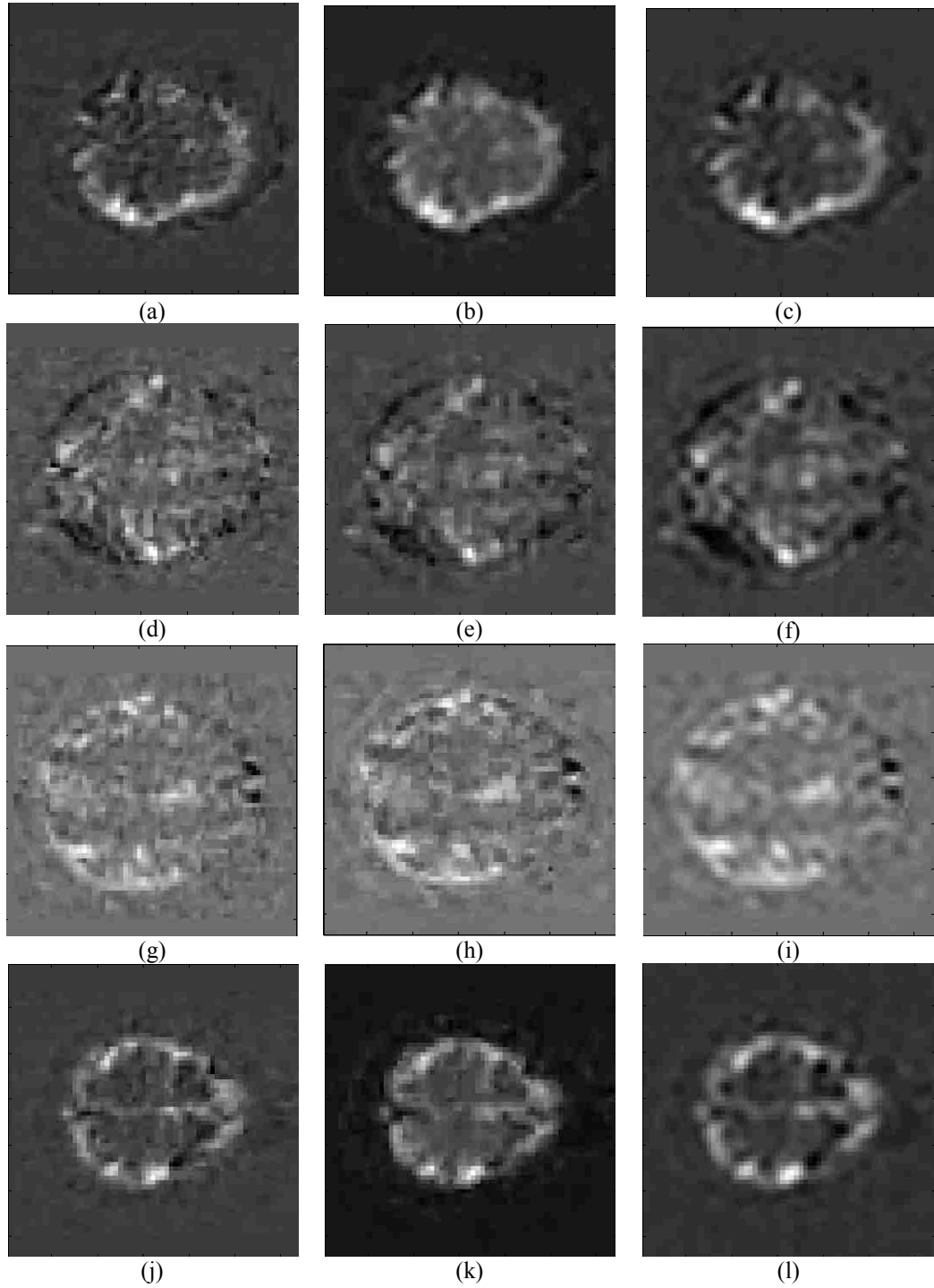


Figure 2.10: Difference images obtained from four individual fMRI sample sets II. (a), (d), (g), and (j) are the difference images obtained from full K-space sampling. (b), (e), (h), and (k) are the difference images obtained by reconstructing the partial K-space our proposed CS methods. The final column, containing images (c), (f), (i), and (l), are obtained by zero-filling the missing K-space samples. Visual assessment of the second and third columns reveals a greater amount of detail.

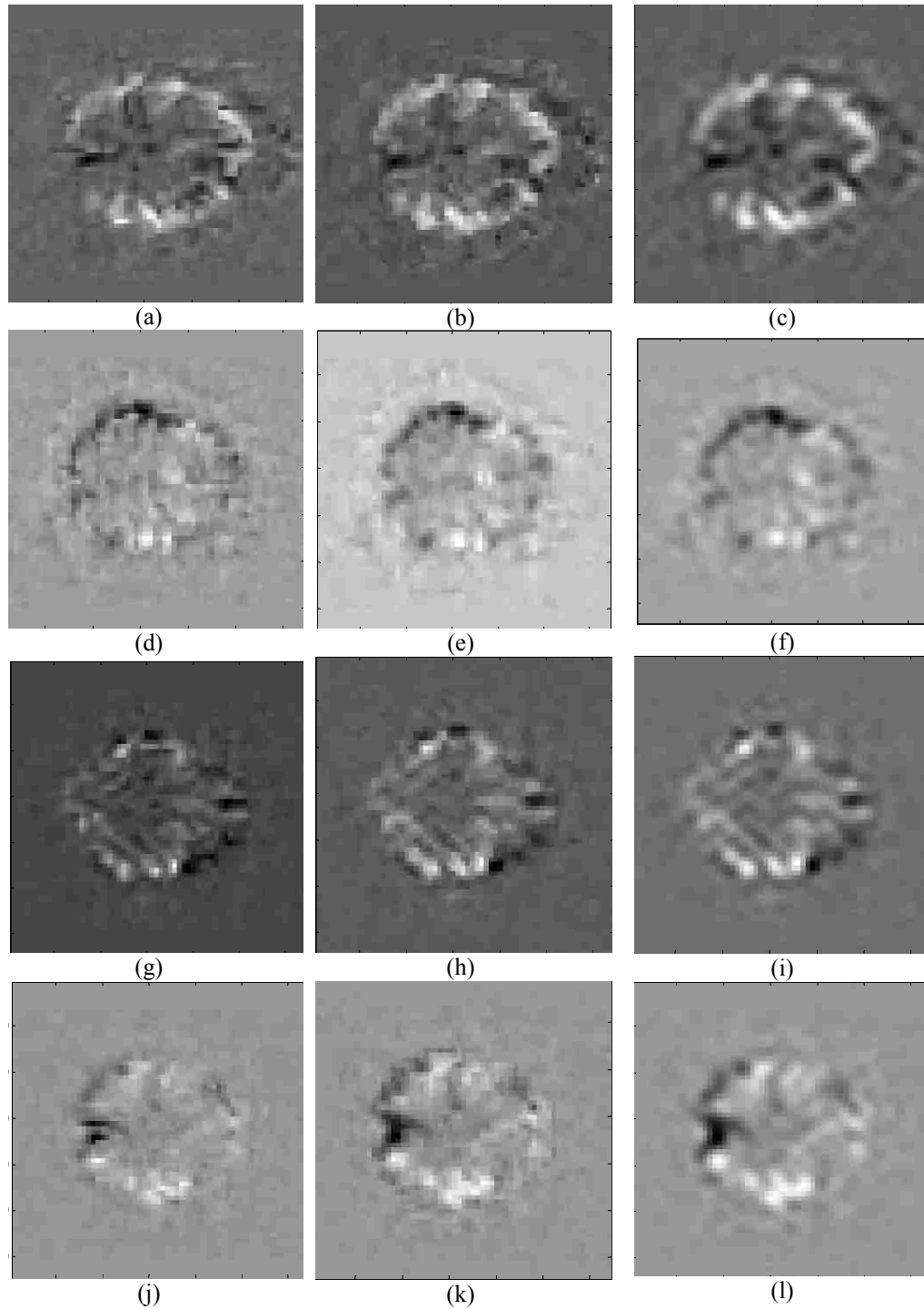


Figure 2.11: Difference images obtained from four individual fMRI sample sets III. (a), (d), (g), and (j) are the difference images obtained from full K-space sampling. (b), (e), (h), and (k) are the difference images obtained by reconstructing the partial K-space our proposed CS methods. The final column, containing images (c), (f), (i), and (l), are obtained by zero-filling the missing K-space samples. Visual assessment of the second and third columns reveals a greater amount of detail.

feel that the reconstructed high-frequency content resulting from the CS method enhances the individual ON and OFF sample reconstructions, resulting in a more detailed difference image than what was obtained with zero-filling. This result implies that more accurate activity segmentation would be possible with a CS reconstructed difference image than a zero-filled reconstructed difference image.

The majority of the CS reconstructed images depicted in Figures 2.9, 2.10, and 2.11 resulted in acceptable reconstructions when using visual assessment techniques. A single sample, shown in Figure 7(e) does not appear to have been reconstructed as well as all of the other remaining samples. Examination of the individual ON and OFF slice reconstructions revealed ringing artifacts due to non-convergence of the CS solution in (7).

2.6. Discussion

We have found that parameter optimization achieved significant image quality improvements using a relatively small number of iterations. Typically, five iterations were required to improve PSNR by over 10 dB from the initial values of $\alpha = 0$, $\beta = 0$ and achieve reconstructions that were within 5% of the optimal quality value.

Smaller parameter regions result from higher performance criteria. The sampling geometry governs the size of the optimal performance area. Sampling

geometries with lower sampling densities result in lower PSNR values, as shown in Figure 2.4.

The combined parameter plots over all images indicate the number of images that meet the quality criteria. We present an example in Figure 2.12. Figure 2.12(c) depicts the inner and outer bounding regions, where 75% of the

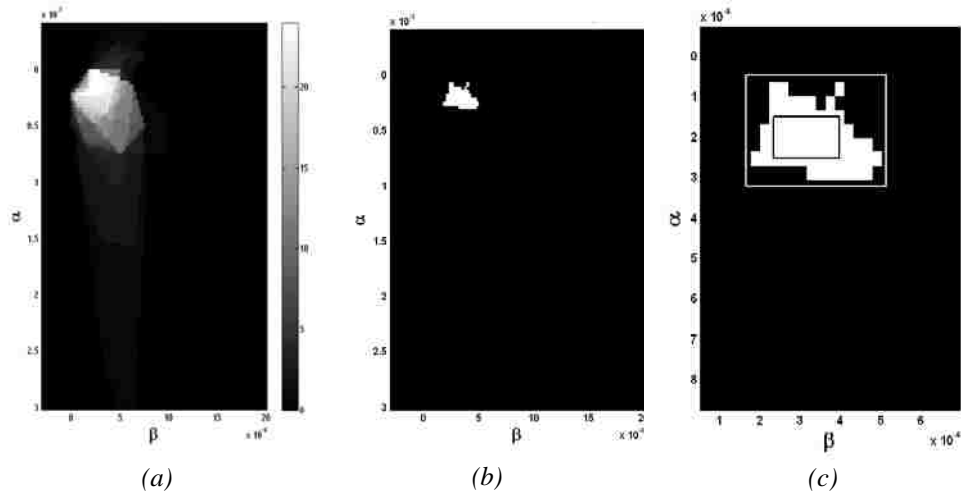


Figure 2.12: Optimal parameter regions over an entire fMRI image data. (a) Parameter region plot indicating the number of images that were reconstructed with >40 dB image quality level (max=24). (b) Parameter region where 75% of the images exhibited image quality >40 dB (c) Inside and outside bounding boxes meant to characterize the complexity of the optimization region.

images meet the quality requirements. The complexity of this optimal region is reflected in an area ratio of 5.71, indicating that the area of the outer box is 5.71 times larger than the inner bounding box.

The relative shape of the bounding boxes indicate that the α parameter is more sensitive (has a smaller dimension) than the β parameter. Our experiments

did not reveal that the ratio of α to β ranges was consistent across geometries or geometry classes. We want to take a closer look at the α and β ranges for select geometries from the DPE and SLP classes. We selected both the DPE and SLP geometries with the *least* number of samples that still provided reasonable performance regions in the optimal quality regions for 30 dB, 35 dB, 40 dB, and 45 dB.

TABLE 2.4
ESTIMATED PARAMETER RANGES FOR SELECT BOUNDING BOX REGIONS

Geometry Class	Threshold	Inner Bounding Box			
		Min α	Max α	Min β	Max β
<i>DPE 62.5 %</i>	45 dB	8.0808e-05	2.8687e-04	2.5758e-04	3.9697e-04
<i>DPE 48.5 %</i>	40 dB	1.4949e-04	2.5253e-04	2.3434e-04	3.9697e-04
<i>DPE 32.8 %</i>	35 dB	2.1111e-04	3.0404e-04	3.8990e-04	4.9293e-04
<i>DPE 21.9 %</i>	30 dB	4.2424e-04	6.3030e-04	2.8081e-04	3.2727e-04
<i>SLP 62.5 %</i>	45 dB	2.5253e-04	4.2424e-04	1.4141e-04	1.8788e-04
<i>SLP 40.6 %</i>	40 dB	1.4949e-04	2.8687e-04	7.1717e-05	2.1111e-04
<i>SLP 20.3 %</i>	35 dB	8.0808e-05	1.4949e-04	4.8485e-05	9.4949e-05
<i>SLP 20.3 %</i>	30 dB	1.2121e-05	1.4949e-04	2.5253e-05	9.4949e-05
Geometry Class	Threshold	Outer Bounding Box			
		Min α	Max α	Min β	Max β
<i>DPE 62.5 %</i>	45 dB	-2.2222e-05	3.8990e-04	1.8788e-04	4.6667e-04
<i>DPE 48.5 %</i>	40 dB	4.6465e-05	3.2121e-04	1.6465e-04	5.1313e-04
<i>DPE 32.8 %</i>	35 dB	1.1818e-04	3.7374e-04	1.4949e-04	5.9596e-04
<i>DPE 21.9 %</i>	30 dB	1.4141e-04	3.9697e-04	2.5253e-04	7.3333e-04
<i>SLP 62.5 %</i>	45 dB	4.6465e-05	4.5859e-04	7.1717e-05	3.0404e-04
<i>SLP 40.6 %</i>	40 dB	2.8687e-04	4.2424e-04	2.0202e-06	3.0404e-04
<i>SLP 20.3 %</i>	35 dB	-2.2222e-05	2.5253e-04	-2.1212e-05	1.8788e-04
<i>SLP 20.3 %</i>	30 dB	-5.6566e-05	2.5253e-04	-2.1212e-05	2.5758e-04

Examining the range of the parameters provides a more detailed description of the parameter space, and which constraint in (7) is essential for acceptable reconstructions. The minimum and maximum parameter values that define the vertices of the inner and outer bounding boxes are listed in Table 3.4.

Three instances in the above table stand out because the minimum alpha and/or beta parameters are negative. These values are a by-product of the interpolation and intersection method used to calculate the parameter ranges. When negative parameter values were inserted into the optimization algorithm, the reconstruction algorithm breaks down. In these cases, we replace the negative value with zero, which still results in an acceptable result.

It is imperative that our discussion turn to the effect of a zero parameter value for either constraint in the reconstruction problem. Typically, the effect of $\alpha = 0$ is a more prominent presence of high-frequency errors in the spatial domain, as well as a higher amount of artifacts from the sampling geometry. Conversely, the effect of $\beta = 0$ is a loss of high-frequency spatial components in the spatial domain reconstruction. In this case, the TV-norm tends to drive the solution to a result whose finite differences in each dimension is minimized. Thus, we observed the equalization of pixel intensities in contiguous regions of the reconstructed image. Examples of reconstructions using the 20.3% SLP sampling geometry where $\alpha = 0$ and β is chosen from within the inner bounding box as well as the converse; where $\beta = 0$ are shown in Figure 2.13. When $\alpha = 0$ and $\beta = 6e-5$ (the inner bounding box in this case was [2.5253e-5, 9.494e-5]) the reconstructed PSNR for a randomly selected image was 37.04 dB. The reconstructed image is shown in Figure 2.13(c). When $\beta = 0$ and $\alpha = 1.2e-4$ (the inner bounding box is [1.2121e-5, 1.4949e-4]) the reconstructed PSNR for a

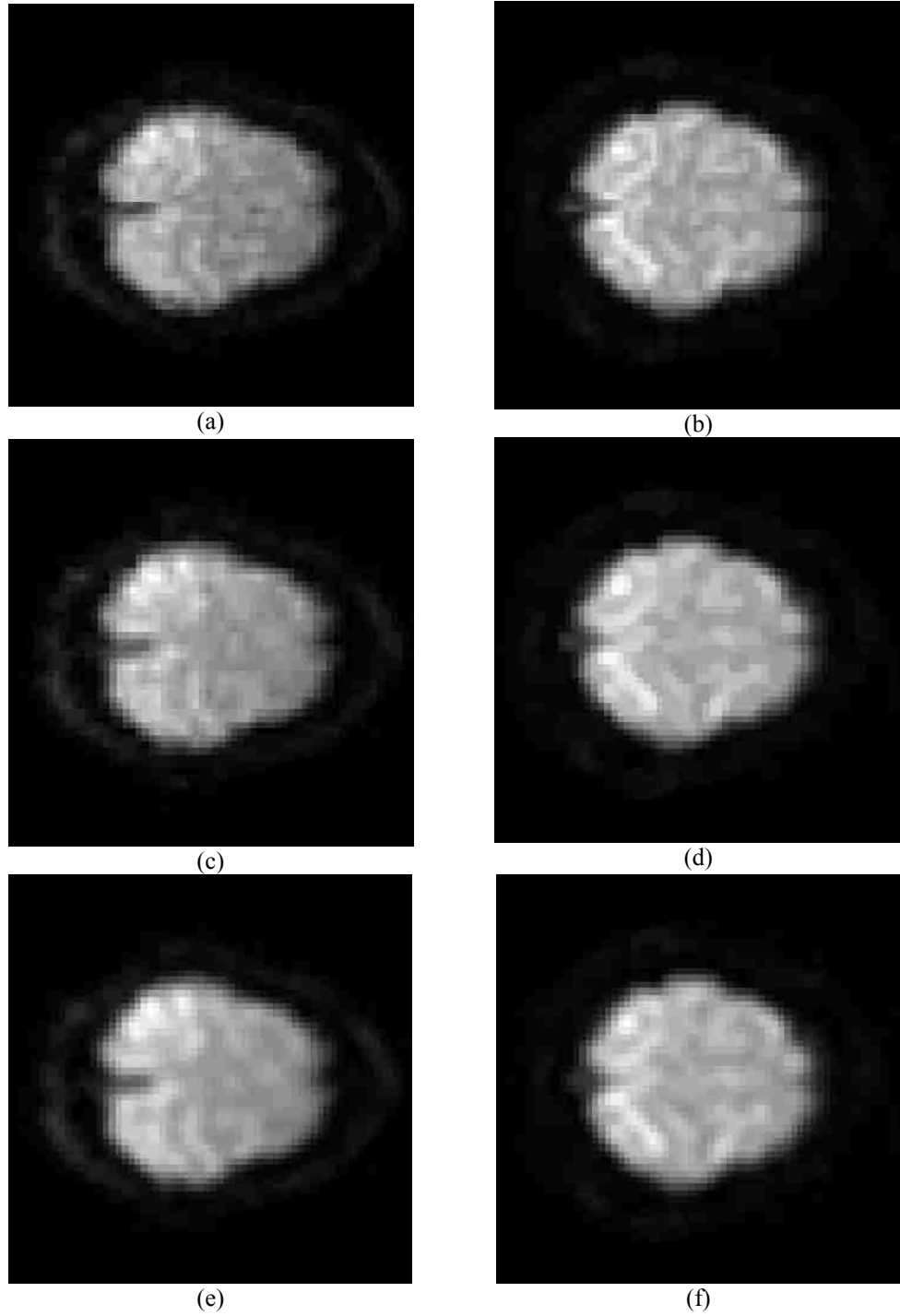


Figure 2.13: A comparison of results when either of the reconstruction parameters is zero. (a) and (b) are the original images. (c) is reconstructed with $\alpha = 0$ and β chosen from within the inner bounding box for the 20.3% SLP sampling geometry. (d) is reconstructed with $\beta = 0$ and α chosen from within the same inner bounding box. (e) and (f) are reconstructions with both parameters equal to zero.

randomly selected image was 40.47 dB. We show the special case of $\alpha = 0$ and $\beta = 0$ for each image in Figure 2.13(e) and Figure 2.13(f) resulting in PSNR values of 26.28 dB and 24.53 dB. In both cases, when non-zero values were used for either parameter, the PSNR increased. This indicates that removing one of the penalty terms in the CS objective function may result in a usable reconstruction, but it is not the optimal solution.

For most cases, the results in Table 3.4 coincide with the theoretical support for the inclusion of the two penalty parameters in (7). The transform penalty parameter (β) helps maintain the details in the reconstruction, while the TV-norm penalty increases the effectiveness of the reconstruction by utilizing CS theory. If both parameters are zero, then the reconstruction simply becomes a solution based on wavelet coefficients which minimize the difference in K-space samples. This special parameter case served as our initial value for the parameter search method, which resulted in reconstruction accuracy nearly 10dB lower on average than the optimal values. But we have shown that for some sampling geometries, it is possible to achieve acceptable image quality when one of the two parameters is zero, but not both. While completely removing one of the penalty terms in (7) may result in acceptable reconstructions in terms of PSNR, increased PSNR can be achieved by using non-zero, optimal values.

2.7. Conclusion

While compressive sensing has shown that exact signal recovery can be achieved under certain conditions (see Figure 2.1), images exhibiting more finer texture and objects of interest that are spatially represented by a small number of pixels require a more robust objective function beyond the total variation norm. A modified objective function, first shown to be useful in reconstructing MRI data by [14], was improved upon by constructing an optimization framework around the objective function that solved for the cost parameters that result in reconstructed images with maximized PSNR. We have found that CS parameter optimization can dramatically improve fMRI image reconstruction quality. Furthermore, fast MRI scanning geometries based on [5] consistently provided for the best image reconstruction results.

The implication of this result is that less complex sampling geometries will suffice to achieve better reconstructions than random sampling, provided the TV-Norm and Transform penalty parameters are selected from the range of values we have calculated in our proposed methodology. We have found that parameters from stable parameter-space regions can be used to achieve specific levels of image reconstruction quality when combined with specific K-space sampling geometries. Our results allow for reconstruction performance of certain quality to be obtained with a 75% probability of achieving the desired quality.

This work not only introduces significant implications for the use of compressive sensing reconstruction of partial K-space data in MRI, but it also reveals that the commonly accepted tenets of CS (data *sparsity* and *incoherence*) are not required if exact signal reconstruction is not required. The solution to the convex reconstruction algorithm used in this work resulted in excellent image reconstructions using well thought out deterministic sampling geometries. Our geometries did not require MRI scanning to conform to compressive sensing theory. Rather, our approach fit a compressive sensing solution into the constraints of MRI data scanning with impressive results.

References

- [1] E. Candès, J. Romberg, and T. Tao, “Robust uncertainty principles: Exact signal recovery from incomplete frequency information”, *IEEE Trans. Information Theory*, vol. 52, pp. 489-509, February 2006.
- [2] T. Chan, S. Esedoglu, F. Park, and A. Yip, “Recent developments in total variation image restoration,” in *Mathematical Models of Computer Vision*, Springer Verlag, 2005.
- [3] O.M. Jeromin, V.D. Calhoun, and M.S. Pattichis, “Optimal sampling geometries for TV-Norm reconstruction of fMRI data,” to be published in the proceedings of Asilomar Conference on Signal Processing. October, 2008.
- [4] M. Lustig, D.L. Donoho, J.M. Santos, and J.M. Pauly, “Compressive Sensing MRI,” *IEEE Signal Processing Magazine*, 25(2), pp. 72-82, March 2008.
- [5] M. A. Lindquist, C. Zhang, G. Glover, and L. Schepp, “Rapid three-dimensional functional magnetic resonance imaging of the initial negative BOLD response,” to appear in *Journal of Magnetic Resonance*, 2008.

- [6] O. Friman, J. Cedefamn, P. Lundberg, M. Borga, and H. Knutsson, "Detection of neural activity in functional MRI using canonical correlation analysis," in *Magnetic Resonance in Medicine*, vol.45, pp. 323-330, 2001.
- [7] F. Nan and R. Nowak, "Generalized likelihood ratio detection for fMRI using complex data," in *IEEE Trans. Medical Imaging*, Vol. 18, pp. 320-329, 1999.
- [8] M. A. Berstein, D. M. Thomasson, and W. H. Perman, "Improved detectability in low signal-to-noise ratio magnetic resonance images by means of a phase-corrected real reconstruction," in *Med. Phys.*, vol. 16, pp. 813-817, 1989.
- [9] L. R. Frank, R. B. Buxton, and E. C. Wong, "Probabilistic analysis and functional magnetic resonance imaging data," in *Med. Phys.*, vol. 39, pp. 132-148, 1998.
- [10] S. Lai and G. H. Glover, "Detection of BOLD fMRI signals using complex data," in *Proc. Int. Society Magnetic Resonance Medicine Meeting 1997*, p.1671.
- [11] K. Sekihara and H. Koizumi, "Detecting cortical activities from fMRI time-course data using MUSIC algorithm with forward and backward covariance averaging," in *Magnetic Resonance in Medicine*, vol. 35, pp. 907-813, 1996.
- [12] B. Siewert, B. M. Bly, G. Schlaug, D. G. Darby, V. Thangaraj, S. Warach, and R. Edelman, "Comparison of the bold- and epistar- technique for functional brain imaging using signal detection theory," in *Magnetic Resonance in Medicine*, vol. 36, pp 249-255, 1996.
- [13] S. C. Strother, I. Kanno, and D. A. Rottenberg, "Principle component analysis, variance partitioning, and functional connectivity," in *J. Cerebral Blood Flow Metabol.*, vol. 15, pp. 353-360, 1995.
- [14] M. Lusting, D. Donoho, and J.M. Pauly, "Sparse MRI: The application of compressed sensing for rapid MR Imaging," in *Magnetic Resonance in Medicine*, vol. 58, pp. 1182-1195, December 2007.
- [15] U. Gamper, P. Boesiger, and S. Kozerke, "Compressed sensing in dynamic MRI," in *Magnetic Resonance in Medicine*, vol. 59, pp. 365-373, 2008.

- [16] H. Jung, J.C. Ye, and E.Y. Kim, "Improved k-t BLAST and k-t SENSE using FOCUSS," *Physics in Medicine and Biology*, vol. 52, pp. 3201-3226, 2007.
- [17] J.P. Haldar, D. Hernando, and Z. Liang, "Compressed sensing in MRI with non-Fourier encoding," submitted to *Magnetic Resonance in Medicine*.
- [18] B. Liu, Y.M. Zou, L. Ying, "Sparsesense: An application of compressed sensing in parallel MRI," in proceedings of the 2008 International Conference on Technology and Information in Biomedicine, pp. 127-130, May 2008.
- [19] J. Trzasko, A. Mancuda, and E. Borisch, "Sparse MRI reconstruction via multiscale L0-continuation," in proceedings of the IEEE/SP 14th Workshop on Statistical Signal Processing, pp. 176-180, August, 2007.
- [20] G.J. Marseille, R. de Beer, M. Fuderer, A.F. Mehlkopf, and D. van Ormondt, "Non-uniform phase-encoded distributions for MRI scan time reduction", *Journal of Magnetic Resonance*, vol. 111, pp. 70-75, 1996.
- [21] F. Wajer, "Non-Cartesian MRI scan time reduction through sparse sampling," Ph.D Thesis, Delft University of Technology, NL, 2001.
- [22] K. Scheffler and J. Henning, "Reduced circular field-of-view imaging," in *Magnetic Resonance in Medicine*, vol. 40, pp.474-480, 1998.
- [23] C.M. Tsai and D. Nishimura, "Reduced aliasing artifacts using variable-density K-space sampling trajectories", in *Magnetic Resonance in Medicine*, vol. 43, pp, 452-458, 2000.
- [24] A. Greiser and M. von Kienlin, "Efficient K-space sampling by density-weighted phase-encoding", in *Magnetic Resonance in Medicine*, vol. 50, pp. 1266-1275, 2003.
- [25] D.C. Peters, F.R. Korosec, T.M. Grist, W.M. Block, J.E. Holden, K.K. Vigen, and C.A. Mistretta, "Under sampled projection reconstruction applied to MR angiography," in *Magnetic Resonance in Medicine*, vol. 43, pp.91-101, 2000.

- [26] G. McGibeny, M.R. Smith, S.T. Nichols, and A. Crawley, “A Quantitative evaluation of several partial Fourier reconstruction algorithms used in MRI,” *Magnetic Resonance in Medicine*, vol.30, pp. 51-59, 1993.
- [27] K.P. Pruessman, M. Weiger, M.B. Scheidegger, and P. Boesiger, “SENSE: Sensitivity encoding for fast MRI,” in *Magnetic Resonance in Medicine*, vol. 42, pp. 952-962, 1999.
- [28] D.K. Sodickson and W.J. Manning, “Simultaneous acquisition of spatial harmonics (SMASH): Fast imaging with radiofrequency coil arrays,” in *Magnetic Resonance in Medicine*, vol. 38, pp. 591-603, 1997.
- [29] E. Candès and T. Tao, “Near optimal signal recovery from random projections: Universal encoding strategies?,” *IEEE Trans. Inform. Theory*, vol. 52, no. 12, pp. 5406-5425, Dec. 2006.
- [30] D. Donoho, “Compressed sensing,” *IEEE Trans. Inform. Theory*, vol. 52, no. 4, pp 1289-1306, Apr. 2006.
- [31] E. Candès and M.B. Wakin, “An introduction to compressive sampling,” *IEEE Signal Processing Magazine*, vol. 25, pp. 21-30, March 2008.
- [32] Y. Tsaig and D.L. Donoho, “Extensions of compressed sensing,” in *Signal Processing*, vol. 86, pp. 533-548, 2006
- [33] J.A. Nelder and R. Mead, “A simplex method for function minimization”, in *Comput. J.*, vol. 7, pp. 308–313, 1965.
- [34] M.J.D. Powell, “Direct search algorithms for optimization calculations”, in *Acta Numerica*, A. Iserles (Ed.), Cambridge University Press, Cambridge, UK, pp. 287–336, 1998.

Chapter 3

Fourier Spectra Reconstructions of Satellite Imagery Part I: Statistical Interpolation Models of the Magnitude and Phase

3.1. Introduction

We propose a new spectral-domain model based on statistical (variogram) models and Ordinary Kriging [1]. In this chapter, we consider a fast, spectral domain extension for interpolating the magnitude and phase spectra over different sub regions. Reconstruction is performed using the Inverse Fast Fourier Transform.

Not only does Kriging produce reconstructions of the magnitude and phase spectra with significantly higher peak signal to noise ratios than other two dimensional interpolation techniques, the predictor also provides an error bound for the predicted values that fall within a 95% confidence interval.

3.2. Literature Review

We present a review of work related to employing Kriging applications in image processing. In remote sensing, Kriging has been used to estimate the values of obscured pixels from cloud cover and shadows, denoising, and image enhancement using super-resolution techniques. These applications are described below.

Past uses of Kriging in remote sensing applications vary considerably. Cheng, Yeh, and Tsai used Kriging to interpolate terrain elevation information to rectify SPOT satellite images [2]. An example of utilizing Kriging to interpolate missing data in remotely sensed images is the interpolation of pollution maps. This work, performed by Kanaroglou *et al.* uses Differential Texture Analysis to measure the Aerosol Optical Thickness in the Visible spectrum (AOTV). Universal Kriging was used to estimate the missing pollution map levels when ground cover and clouds obstruct measurement. In this case, a second-degree surface model was used to de-trend the data [3].

Rossi, Dungan, and Beck [4] use the Indicator Kriging to interpolate unknown image regions of Landsat Thematic Mapper images. Ferretti, Prati, and Rocca, utilize Kriging to filter and resample the atmospheric permanent scatterers that influence the accuracy of SAR interferometry [5]. Blaschke utilized Kriging for object classification in remotely sensed images to assist in appending a geographic information system (GIS) database to the image data [6].

Djamdji and Bijaoui utilize Kriging to map the disparities over a couple of stereo images. The disparity map is then used to register the two images that constitute the pair [7]. Image restoration can also be performed via Kriging methods, as shown by Pham and Wagner [8], and their results are compared to the Weiner Filter. Oh and Lindquist develop the Indicator Kriging to assign a probability of whether a boundary pixel between two class objects falls into either class. After assigning pixels based on two global thresholds, the ambiguous pixels that fall between the thresholds are assigned a class based on a Kriging estimate from a finite pixel neighborhood [9]. Chandra et al. attempt to reconstruct complex textures using Kriging from samples of the original image [10]. Carr demonstrates that Kriging can be modeled in a way to achieve less smoothing in Kriging by performing a two-step Kriging process, where the outputs are combined in a way that is analogous to summing high and low-pass filtered images [11].

Kriging has been applied to image sequence coding and data compression. A study by Decenciere *et al.* resulted in a smoothing function termed *Inverse Kriging* which can be used to smooth textures and interpolation of motion vector fields [12]. Here, Kriging was applied to a small set of control points in the moving region of a subsequent video frame to interpolate the motion vector field for the entire image. The Kriging result was used for effective motion compensation in sample image sequences. In addition to the exploration of point

Kriging/Inverse Kriging methods on motion vector fields, the authors explored the various point Kriging techniques on digital images. The authors downsampled uniformly by 8 pixels when reconstructing the actual grayscale pixel values and used the empirical covariance instead of variogram models in their estimators. They also explored Kriging using samples non-uniformly selected from the image based on texture measurements, such as the Laplacian.

Grinstead, Koschan, and Abidi use a simple Kriging method to preserve the sharp features of 3-D images in the form of digital elevation maps obtained by laser scanning [13]. In this study, the authors compared Kriging to other commonly used spatial interpolation techniques for non-uniformly sampled data (linear, bi-cubic estimators and Inverse-Distance Weighting). To compensate for the over-smoothing that results from applying Kriging to the entire image, regions of interest were automatically detected using region growing and merging techniques. To address the need for localized variogram estimation over the detected ROIs, a variogram model was selected and fitted using a least squares optimization technique on lag shorter lag values.

Kriging interpolation was used by Panagiotopoulou and Anastassopoulos to create high-resolution image reconstructions from sub-pixel shifted, aliased low-resolution frames [14]. In their approach, they use Kriging as a super-resolution technique which combines twenty low-resolution into a single high-resolution image. Their technique is only applicable after motion estimation

results are used to calculate any displacement between frames, which places the low-resolution frame pixel locations into the super-resolution data space. Experiments were performed on a single set of data, using a fitted Gaussian variogram as the covariance model when performing Kriging.

As one can see from the above literature review, the applications of Kriging have been broad in the field of remote sensing. Although the use of Kriging in remote sensing image processing has expanded over the past decade, the application of Kriging to magnitude and phase spectra reconstruction is new and we have not seen any prior research in this area.

3.2.1. Data Set Description

The images analyzed in this study were obtained from various multispectral and satellite image databases. Since satellite imagery varies widely based on the content in the scene being imaged, we intended to obtain a collection of images that could be described as depicting representative examples of rural, urban, and natural scenes. The rural scene type can be best described as containing few manmade structures, but do exhibit the effects of human activity. Examples of human activity include the presence of roads and agriculture. Urban scenes can be described as having significant manmade structures, including infrastructure (roads, utilities) and buildings. Natural scenes can be described as having little to no evidence of human activity in the scene. Such data is typically collected for environmental studies. In our data samples, urban and natural scenes tend to

exhibit a greater amount of high-frequency content in the Fourier domain, while rural scenes have less high-frequency content and subsequently contain smooth regions in the image domain.

Two rural scenes we explored in this study were obtained from the Laboratory for Applications of Remote Sensing at Purdue University. Both of the images we have selected from this data set were obtained using the ITD Spectral Visions multispectral sensor and contain aerial views of the Agronomy Research Center [15] and the Farm Progress Show Site [16]. A view of the Purdue Agronomy Research Center is shown in Figure 3.1(a) and a view of the Farm Progress Show site is shown in Figure 3.1(b). An additional rural scene was obtained by selecting an outlying region of a large (2635x3685 pixels) satellite image of London, England. The source image was obtained by ASTER (Advanced Spaceborne Thermal Emission and Reflection Radiometer) sensor onboard the NASA Earth Observing System (EOS) [17]. The third rural sample image is shown in Figure 3.1(c).

The full-sized image of London, from which we selected five sub-regions to comprise our urban satellite data set, is shown in Figure 3.2. The locations of the sub-regions are indicated by the boxes overlaid on the image. Each of the sub-regions are shown in Figure 3.3, along with their representative Fourier spectrum.

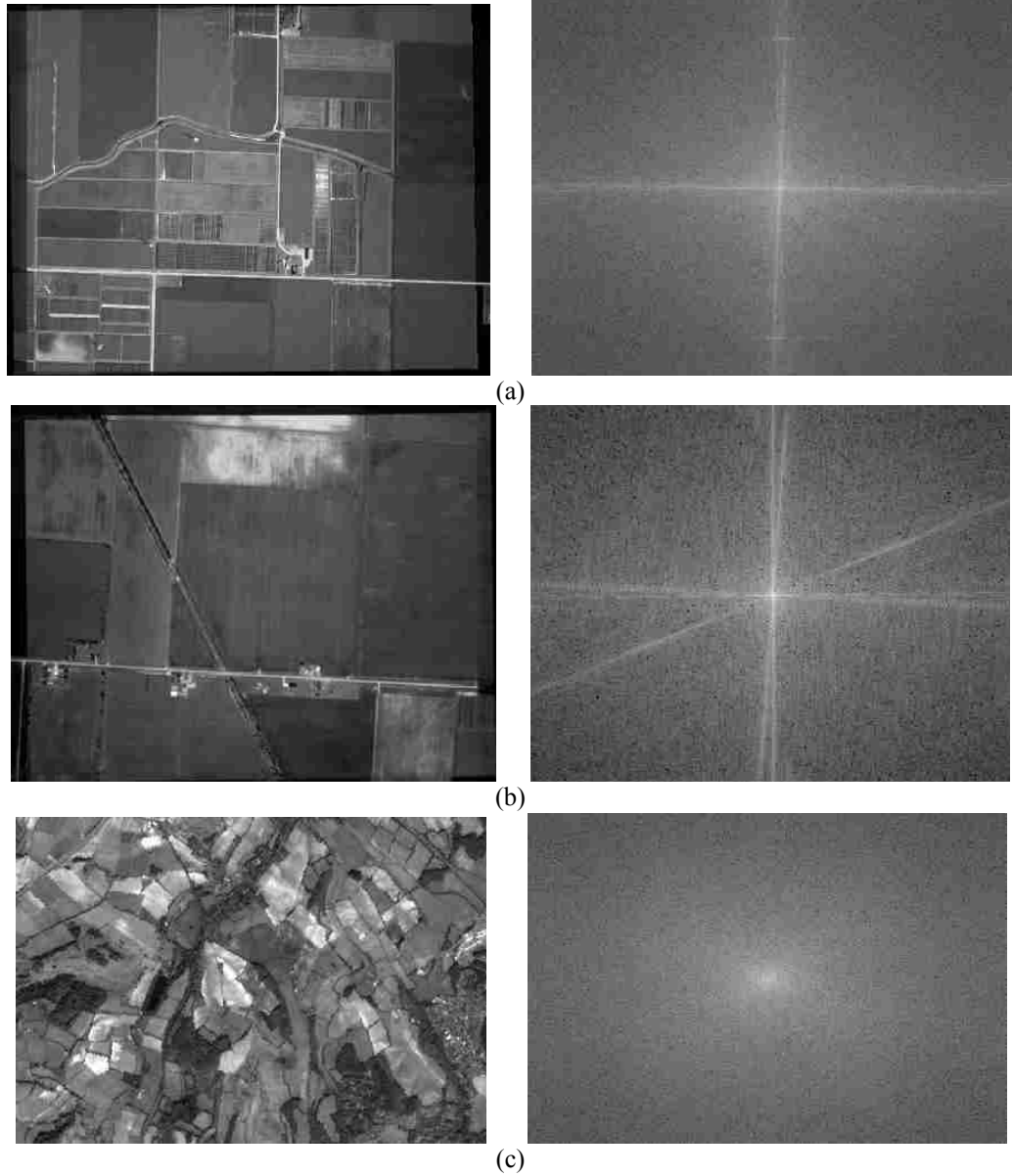


Figure 3.1: Rural scene satellite image data set and log-transformed magnitude Fourier spectrum. (a) Purdue University Agronomy Research Center¹, size 1069x1374. (b) Farm Progress Show Site², size 267x343. (c) Rural sub scene outside of London, England³, size 311x451.

1. http://www.lars.purdue.edu/home/image_data/spectral_vision_data.html, Name: sv010813_ARC_F106_1m

2 http://www.lars.purdue.edu/home/image_data/spectral_vision_data.html, Name: sv010706_FPS_south_1m

3 <http://asterweb.jpl.nasa.gov/gallery/images/london-final.jpg>

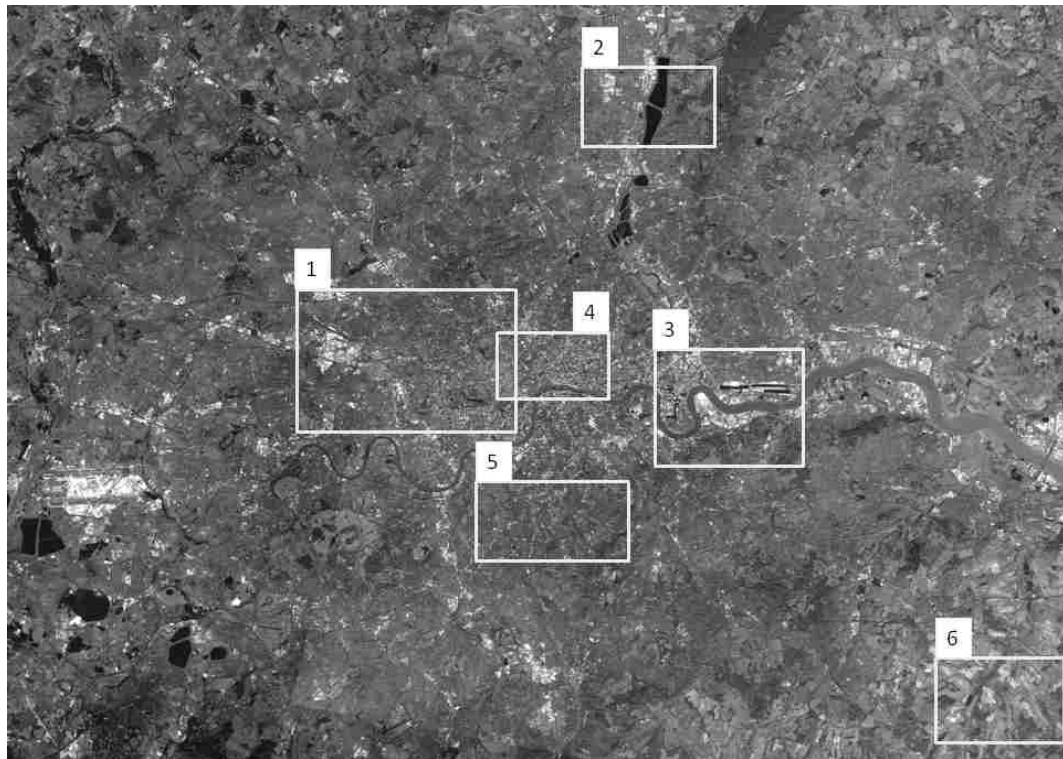
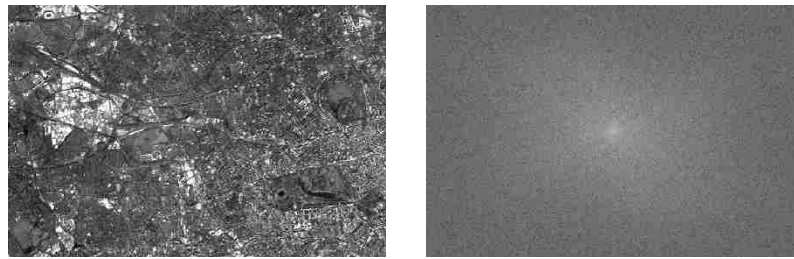


Figure 3.2: Full resolution satellite image of London, England¹ depicting five urban sub regions. The third rural sub region is also indicated.

1. <http://asterweb.jpl.nasa.gov/gallery/images/london-final.jpg>

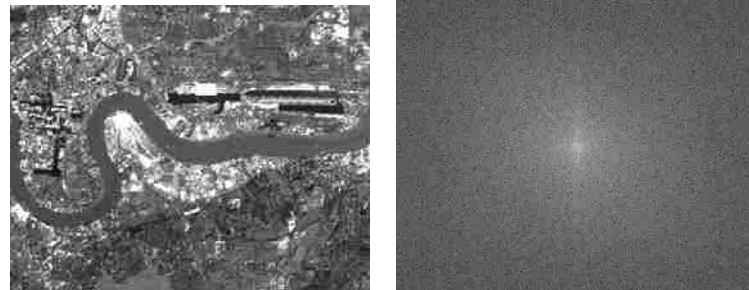
The two natural images we obtained bring the total number of multispectral images explored in this study to ten. The first natural image depicts the Grand Canyon and other natural features in Northern Arizona, and is shown in Figure 3.4(a). This image was generated using the NASA Multi-angle Imaging SpectroRadiometer sensor [19]. Another ASTER-generated image contains a view of the Erebus Ice Tongue protruding from the Erebus glacier in Antarctica into McMurdo Sound.



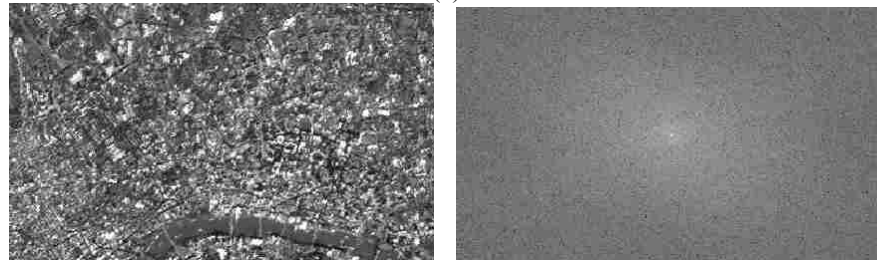
(a)



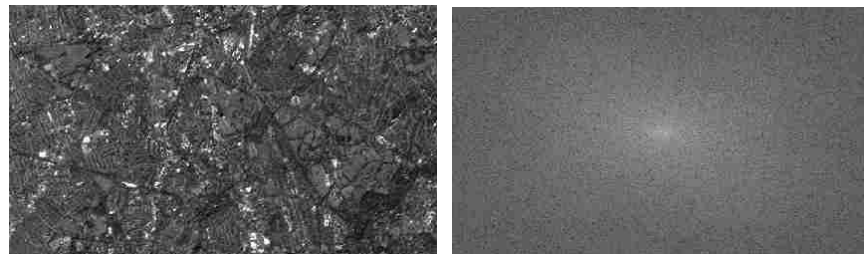
(b)



(c)



(d)



(e)

Figure 3.3: Urban scene satellite image data set and log-transformed magnitude Fourier spectrum. These were selected from the full sized satellite image of London, England in Figure 3.2 (a) 1 in Figure 3.2, size 501x751. (b) 2 in Figure 3.2, size 301x451. (c) 3 in Figure 3.2, size 401x501. (d) 4 in Figure 3.2, size 236x401. (e) 5 in Figure 3.2, size 296x501.

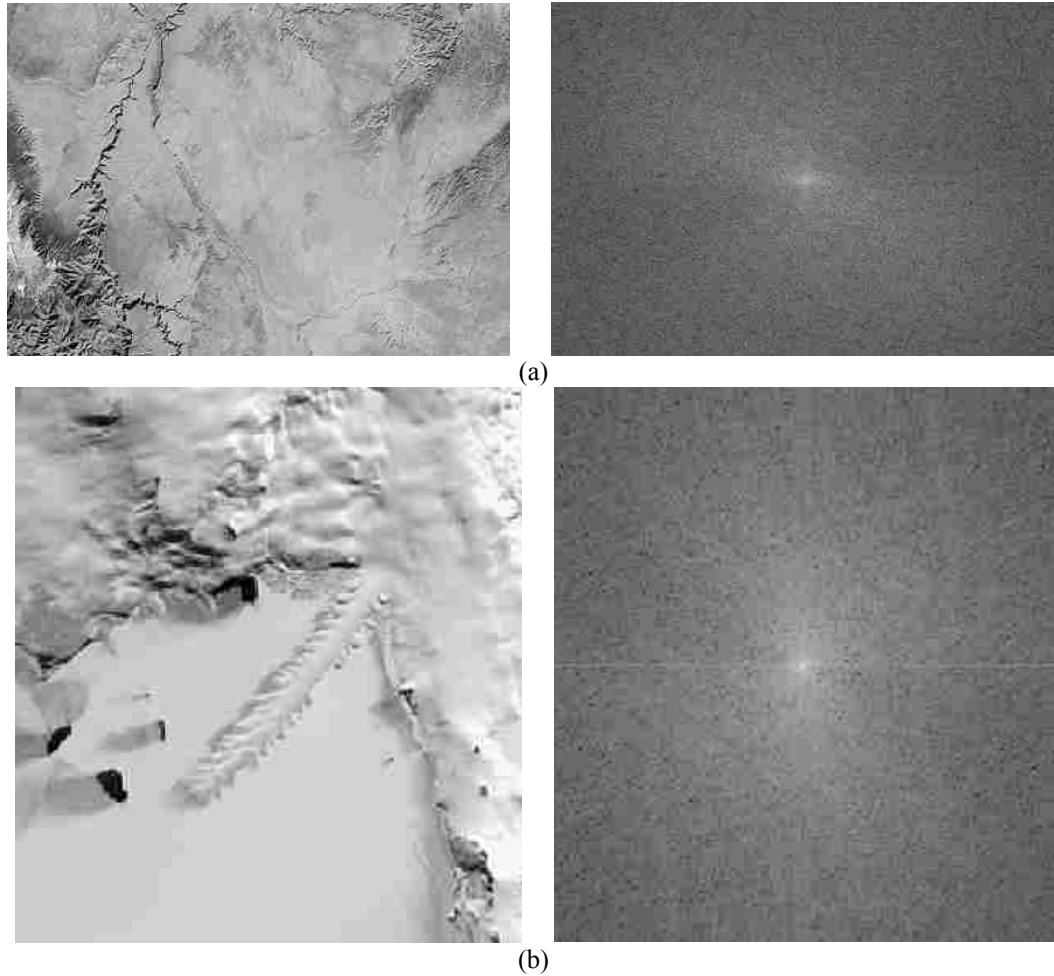


Figure 3.4: Natural scene satellite image data set and log-transformed magnitude Fourier spectrum. (a) The Grand Canyon and surrounding country¹, size 351x501. (b) Erebus Ice Tongue², size 254x231.

1. <http://photojournal.jpl.nasa.gov/catalog/PIA03402>

2 <http://asterweb.jpl.nasa.gov/gallery/images/glacier-tongue.jpg>

To recapitulate the content of our data set, three images were classified as containing rural scenes. Five images, each of which were sub images of single ASTER image of London, England, were classified as containing urban scenes. Finally, two satellite images were classified as containing natural scenes. These classifications will be used in categorizing the assessment of our reconstruction method.

3.3. Theoretical Background

3.3.1. Spectral Statistical Approach

Digital images are characterized by a discrete spectrum that is periodic, with a fundamental 2D Frequency support from $-\pi$ to π . The 2D Fast Fourier Transform (FFT) of an image produces a discrete lattice of regularly-spaced frequency samples from the continuous-interval of $[-\pi, \pi]^2$. Here, we would like to investigate the use of methods from Spatial Statistics that allow us to interpolate the 2D FFT frequencies from a limited subset.

The implication of discrete spectral interpolation goes beyond standard frequency domain image processing techniques such as image restoration. Various applications, such as magnetic resonance imaging (MRI), computed tomography (CAT scans), and synthetic aperture radar (SAR) sample data in the Fourier domain. Under certain conditions, such applications may be band-limited and the ability to interpolate Fourier data would provide improvement to the final data product (typically an image).

Here, we are interested in the discrete frequency spectrum lattice as indexed by (u_i, v_i) . We shall denote the horizontal frequency coordinate with u_i and the vertical frequency coordinate with v_i .

For any increment, $\mathbf{s}_1 - \mathbf{s}_2$, defined by the spectral locations $\mathbf{s}_1, \mathbf{s}_2 \in F$, and the measured values at these locations, $Z(\mathbf{s}_1)$ and $Z(\mathbf{s}_2)$, the second-order stationary *variogram* is defined as:

$$2\gamma(\mathbf{s}_1 - \mathbf{s}_2) = \text{var}(Z(\mathbf{s}_1) - Z(\mathbf{s}_2)). \quad (1)$$

Here, the variogram is a function of the increment, normally called the *lag*, and commonly denoted as \mathbf{h} .

For an intrinsically stationary random field, the method of moments estimator, commonly referred to as the *classical* variogram estimator, is given by:

$$2\hat{\gamma}(\mathbf{h}) \equiv \frac{1}{|N(\mathbf{h})|} \sum_{(i,j) \in N(\mathbf{h})} (Z(\mathbf{s}_i) - Z(\mathbf{s}_j))^2 \quad (2)$$

where $N(\mathbf{h})$ is defined by $N(\mathbf{h}) \equiv \{(i, j) : \mathbf{s}_i - \mathbf{s}_j = \mathbf{h}\}$ and $|N(\mathbf{h})|$ is the number of elements in the set $N(\mathbf{h})$. The classical estimator is **unbiased** but *not robust*. When estimating the variogram, intrinsic stationarity is often assumed.

Due to the periodic nature of the 2D FFT domain, intrinsic stationarity cannot be assumed over the entire spectrum. In order to have confidence in our variogram estimates, we sought a partitioned spectral domain that allowed independent spectral statistical modeling within the regions defined by the partition. Figure 3.5 depicts the fourteen partitions generated by dividing the entire 2-D FFT domain into dyadic blocks. We assume intrinsic stationarity of the semivariance model over each of the sub regions. Mathematically, we are assuming

$$E(Z(\mathbf{s}_i) - Z(\mathbf{s}_j))^2 = 2\gamma(\mathbf{s}_i - \mathbf{s}_j) \quad (3)$$

holds for the spectral components contained within each of the sub regions, where $2\gamma(\mathbf{s}_i - \mathbf{s}_j)$ is unique for each region.

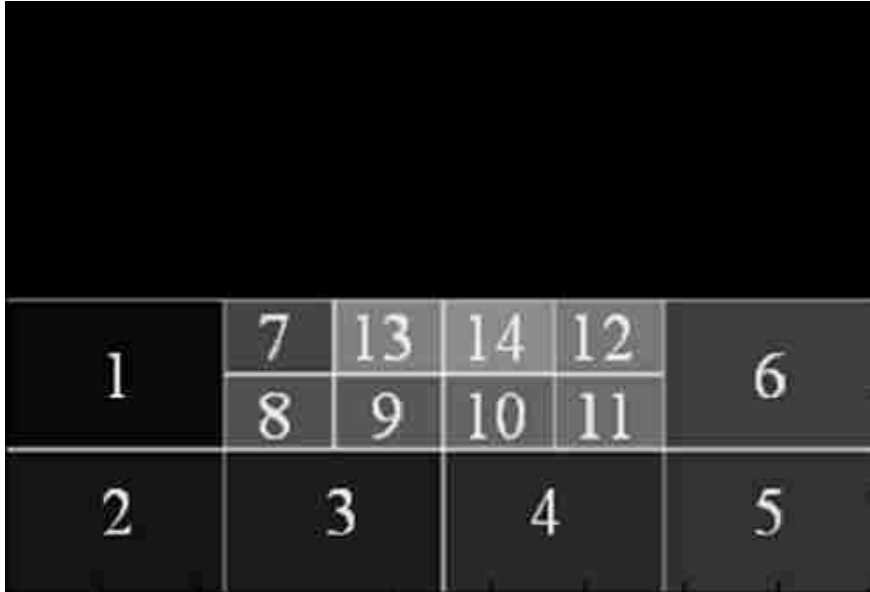


Figure 3.5: Spectral partition map. The partitions shown above define the regions of the spectral data which we model individually for analysis. The original size of the image used to generate this map was 301x401 pixels. The spectral data contained in regions 13 and 14 was not included in any of the down sampling rates used in this study. The sizes of the outer regions for this mask are 75x112 pixels, while the sizes of the inner regions are 37x56 pixels.

We selected a dyadic partitioning scheme because it is well supported in Wavelet theory, and we want to ensure a scalable down sampling model that emphasizes the importance of retaining low frequency components. In other words, the dyadic approach allows us to refer to two distinct portions of the spectrum based on whether it encompasses the high frequency or medium frequency regions of the centered Fourier spectrum. In addition, we desire the freedom to explore our spectral models using a scalable framework. The dyadic partitioning results in outer regions that are four times as large as the next smaller

regions. These high frequency regions contain less spectral energy and we would like to perform more interpolation here. Conversely, the inner-most contain the low frequency information of the image and we want to preserve this. So in all of our experiments regions 13 and 14, assuming DC is at the center of the spectrum, remain intact. Logically, the intermediate frequencies, indentified by regions 7-12, are not interpolated as much as the high frequency regions. We are restricting the spectral modeling over half of the 2-D FFT domain because we can utilize the symmetry of the spectrum to extrapolate the upper half.

3.3.2. A Magnitude Spectrum Model using the Logarithm

In what follows, we want to argue for the use of the logarithmic function over each spectral domain region. Suppose that a given spectral-domain region violates the stationarity assumptions.

In this case, it may be reasonable to expect that we can provide good, stationary, approximations over a disjoint partition of sub-regions of the original region. Furthermore, instead of requiring stationarity over the entire region, it is reasonable to assume that the **relative variogram**, defined by

$$2\gamma_Z^{(j)}(\mathbf{h}) / \mu_j^2, \quad (4)$$

will remain approximately constant over all sub regions, independent of j . It can be shown that the application of the logarithmic transformation will produce an approximately intrinsically stationary random field over the entire region [1]. The importance of this result is that here, the logarithmic transformation allows us to

apply our methods over the entire region, without requiring any knowledge of the specific boundaries of the constituent sub regions.

Within the framework of the logarithmic approximation to the relative variogram, we are able to estimate the variogram using the method of moments estimator shown in (2) on the log-transformed magnitude spectrum within each sub-region. For each spectral region, we sought to fit each empirical variogram with one of the following three theoretical semivariance models:

- The Spherical Model:

$$\gamma(\mathbf{h}) = \begin{cases} 0, & \mathbf{h} = 0, \\ \sigma + \alpha \left\{ \frac{3}{2} (\|\mathbf{h}\| / \beta) - \frac{1}{2} (\|\mathbf{h}\| / \beta)^3 \right\}, & 0 < \|\mathbf{h}\| \leq \beta, \\ \alpha + \sigma, & \|\mathbf{h}\| > \beta, \end{cases} \quad (5)$$

$\sigma \geq 0, \alpha \geq 0, \text{ and } \beta \geq 0.$

- The Exponential Model:

$$\gamma(\mathbf{h}) = \begin{cases} 0, & \mathbf{h} = 0, \\ \sigma + \alpha \{1 - \exp(-\|\mathbf{h}\| / \beta)\}, & \mathbf{h} \neq 0, \end{cases} \quad (6)$$

$\sigma \geq 0, \alpha \geq 0, \text{ and } \beta \geq 0.$

- The Gaussian Model:

$$\gamma(\mathbf{h}) = \begin{cases} 0, & \mathbf{h} = 0, \\ \sigma + \alpha \{1 - \exp(-\|\mathbf{h}\|^2 / \beta^2)\}, & \|\mathbf{h}\| \neq 0, \end{cases} \quad (7)$$

$\sigma \geq 0, \alpha \geq 0, \text{ and } \beta \geq 0.$

In the above models, σ is the nugget effect, which was termed by Matheron as a representation of small scale variations (in our case, sub spectral sample

variations) that manifest themselves as a discontinuity at the minimum measurable range value. α is referred to as the variogram sill, and it is defined as the limit of the variogram as the distance between samples approaches infinity. Typically, a good estimate for the variogram sill is the sample variance. Finally, β is referred to as the variogram range, and can be thought of as the lag at which $Z(\mathbf{s})$ and $Z(\mathbf{s} + \mathbf{h})$ are no longer correlated. It can be used as a guide to determining the lag distances required to include in spatial prediction.

We selected the spherical and Gaussian model because they are bounded by the total variance of the individual spectral region. The exponential model is commonly used as well, and it asymptotically approaches the total variance between all points in the spectral sub region.

3.3.3. Two-Dimensional Phase Unwrapping

Since we are reconstructing the Fourier domain samples of the satellite images in our dataset, special attention had to be shown in processing the phase of the Fourier spectra. The phase data generated by a Fourier transformation of an image is constrained to the interval $(-\pi, \pi]$. Since phase is related to the temporal and/or spatial wavelength, its influence on the signal is only through phase values that lie within the above interval. Mathematically, the absolute phase, φ , is wrapped into the interval $(-\pi, \pi]$ by the following operation within the Fourier transform

$$\psi(u, v) = \varphi(u, v) + 2\pi k(u, v), \quad (8)$$

where $k(u, v)$ is an integer function that constrains the wrapped phase to $-\pi < \psi \leq \pi$ and the spectral coordinate pair (u, v) define a spectral location (\mathbf{s}) .

While many coherent signal applications seek $\varphi(\mathbf{s})$ because it represents a physical measurement such as surface topography in interferometry [20-27], we seek the absolute phase because the wrapped phase typically does not provide a spatial variance field that can be well modeled using the variogram.

We explored the use of five different two-dimensional phase unwrapping techniques that are described and implemented software [28]. Three of the algorithms we applied to the phase spectra are path following techniques: Goldstein's Branch Cut method, quality guided path following, and Flynn's minimum discontinuity method. The other two methods can be described as minimum norm methods, which approach phase unwrapping in a mathematically formal manner. These are the preconditioned conjugate gradient (PCG) algorithm and the weighted multigrid algorithm.

While we are referring to each of these algorithms as being unique, all but the Goldstein algorithm represent a class of phase unwrapping algorithms that support a wide variety of approaches. For the sake of brevity, we limited our exploration of the effects of the various phase unwrapping algorithms to a single algorithm of each type. We will now briefly describe each of the algorithms.

3.3.3.1 Path Following Algorithms

Path following algorithms try to find the best integration path to one pixel of unwrapped phase starting from another pixel. The first path following algorithm we applied to the phase spectra was Goldstein's Branch Cut algorithm [21], which uses a nearest neighbor method to find a configuration of branch cuts with lengths that have a minimized sum. Branch cuts are boundaries connecting positive and negative phase residues (points within a contour integral whose phase derivative are $\pm 2\pi$) through which a phase integration path cannot cross. This method produces an unwrapped phase surface where the wrapped phase discontinuities are confined to the branch cuts, approximately minimizing the discontinuities.

The quality guided path following algorithm does not depend on residues and branch cuts, but instead uses an iterative technique that uses region growing of regions of unwrapped pixels [29]. The paths that the region growing procedure follows are dependent on the quality map, which can be defined by a number of metrics to follow. We limited our exploration of this algorithm to following the paths that minimize phase gradients contained along a path.

The third path following algorithm applied to the phase spectra was Flynn's minimum discontinuity algorithm which we used without a quality map. Flynn's algorithm finds the surface that is congruent to the wrapped phase data whose solution minimizes the amount of integer multiples of 2π required to remove phase discontinuities (pairs of pixels whose difference exceeds π in

magnitude) [30]. It has been shown that this process is equivalent to minimizing the ℓ_1 norm of the congruent solution. We prefer this method over other path following methods because it provides a globally minimized solution, although it does require more computational resources than Goldstein's or the quality guided algorithms.

3.3.3.2 Minimum-Norm Algorithms

Minimum norm techniques deviate significantly from path following techniques in the sense that they seek a global solution that minimizes some measure of the difference between the gradients of the wrapped and unwrapped phase. This approach tends to remove the undesirable characteristic of path following techniques: path following techniques tend to generate lines of discontinuity in the unwrapped phase spectra. We selected two weighted least-squares algorithms as they have been shown to compensate for residues, while unweighted algorithms unwrap through residues rather than around them.

The preconditioned conjugate gradient (PCG) algorithm introduces weights that are defined by a user-supplied quality map. This process intends to zero-weight regions where residues are likely to lie. The search algorithm is preconditioned using the unweighted solution to speed convergence. The conjugate gradient solution is described in detail in [31].

Similarly, the weighted multi-grid algorithm utilizes weights on the residual to correct the phase derivatives at the boundaries of discontinuity regions.

It is a desirable example of a weighted least-squares phase unwrapping solution because it tends to converge more quickly than the PCG algorithm. It also does not require the use of discrete cosine transforms or fast Fourier transforms since it does not use conjugate gradient techniques. A comparison of the different representation of each of these algorithms applied to the actual phase spectra of one of our images is shown in Figure 3.6.

Figure 3.6(a) contains the original unwrapped phase. Figure 3.6(b) contains the result of Goldstein's branch cut algorithm. The discontinuities at the branch cuts are evident. Figure 3.6(c) contains a result of the quality guided algorithm using the minimum variance as a quality mask. It clearly depicts the distinct regions that were grown in the unwrapping process. Figure 3.6(d) shows the result of Flynn's minimum discontinuity algorithm. This is the best global result, which is supported by having the smallest range of unwrapped phase values compared to the other results. Finally, Figure 3.6(e) and Figure 3.6(f) contain the result of the weighted multi-grid algorithm and the precondition conjugate gradient methods, respectively. The minimum norm methods produce the smoothest surfaces, but result in a very large range of unwrapped values. Severe unwrapping is undesirable because the quality of the reconstructed phase is bounded within the range of $(-\pi, \pi]$, regardless of the unwrapping method. Larger unwrapped phase values will, in turn, result in larger absolute error values of the interpolated phase values. Thus, we focus on unwrapped surfaces with the

smallest range of unwrapped values (e.g. Flynn's minimum discontinuity method).

Due to the localized discontinuities of wrapped phase data, it is ill suited for our spectral statistical approach and does not adhere to our regionalized spectral modeling paradigm. Figure 3.7 shows the variogram estimates for the wrapped phase of two spectral sampling regions (4 and 7) from a representative urban image from our data set. Figure 3.8 shows the variogram estimates for the same regions, but from the unwrapped phase using Flynn's minimum discontinuity method. The same variogram models in (5), (6), and (7) were revealed as acceptable, bounded spectral statistical models for the phase data we typically encountered in this work.

It is clear from Figures 3.7 and 3.8 that the unwrapped phase does not support any spectral covariance model, as the empirical variogram values are all located near the global variance within the selected block. In addition, the sample covariance within individual blocks is equal to the global sample variance. This is expected based on the fundamental property of phase spectra exhibiting a probability density function that is uniform spanning the interval $(-\pi, \pi]$.

The unwrapped phase, on the other hand, produces excellent spatial covariance model estimates, which are well fitted by all three of the theoretical

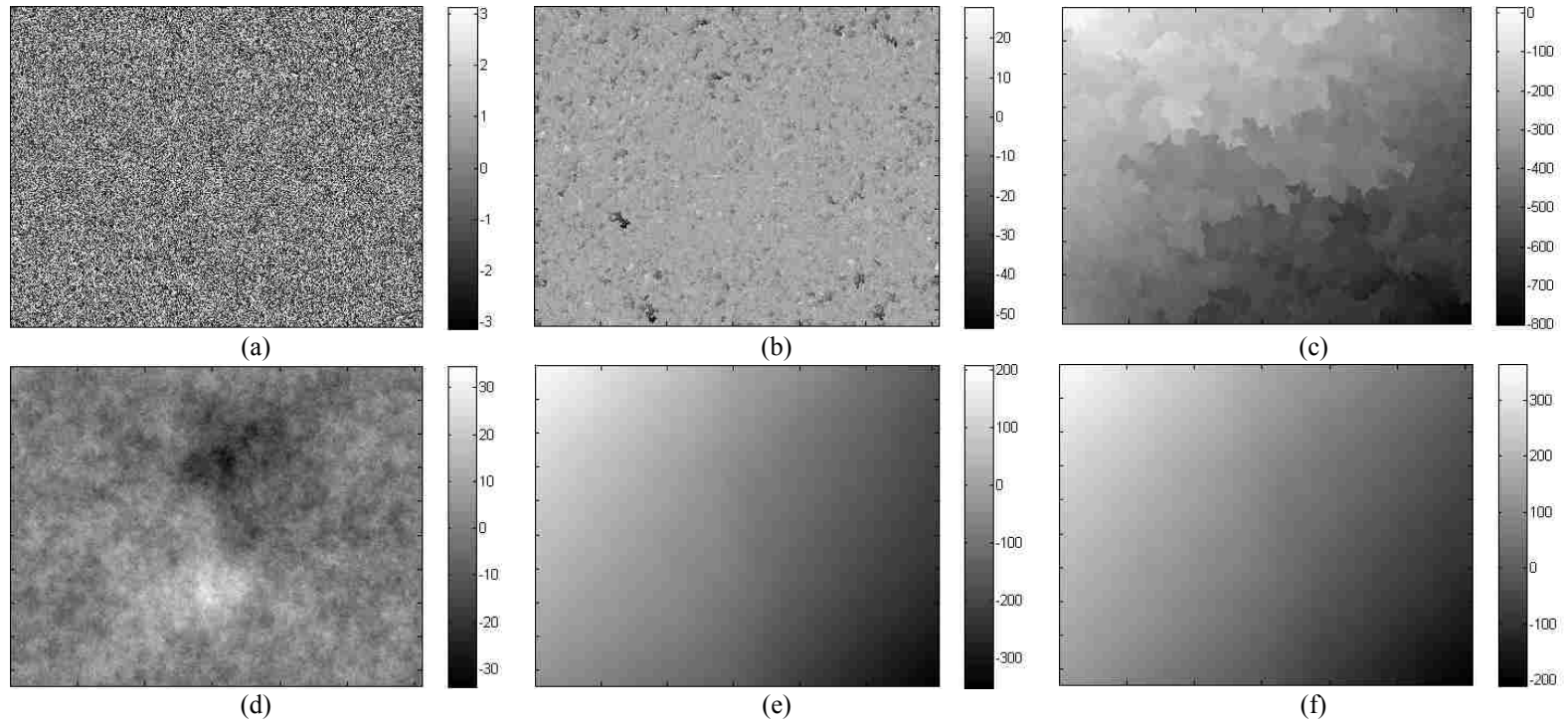
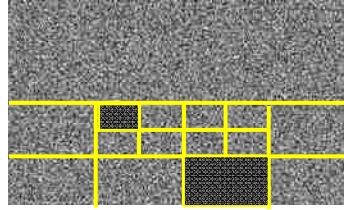
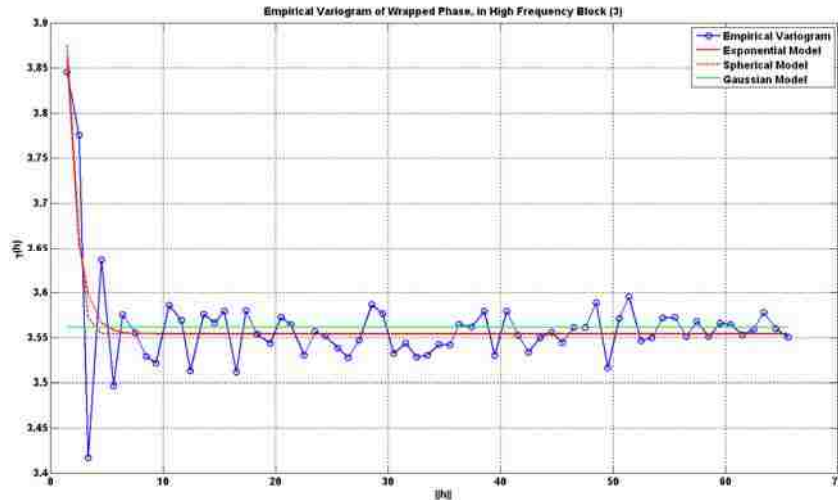


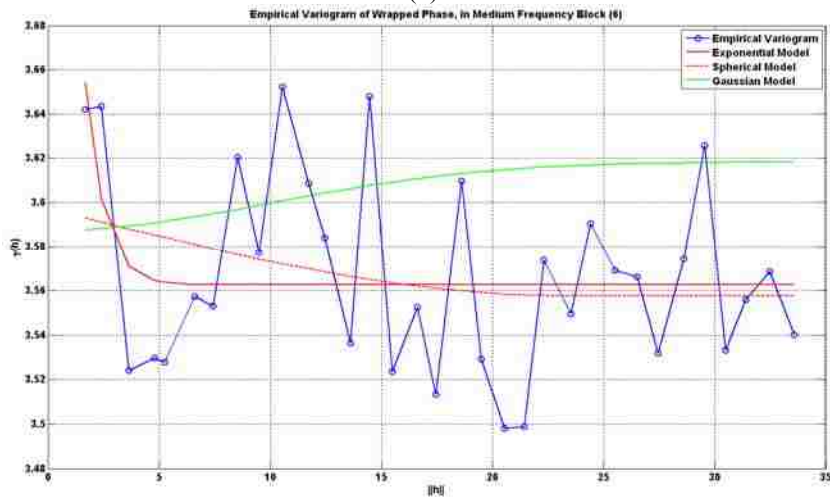
Figure 3.6: Comparison of phase unwrapping methods. This figure contains the original, wrapped phase spectra of an image from our data set that contains a natural scene and the five results of the two-dimensional phase unwrapping techniques we explored in this work. (a) The original phase. (b) The result of Goldstein's branch cut algorithm. (c) The result of the quality-guided algorithm using the minimum variance as a quality mask. (d) The result of Flynn's minimum discontinuity algorithm. (e) The result of weighted multi-grid algorithm and (f) shows the result of the preconditioned conjugate gradient (PCG) methods.



(a)



(b)

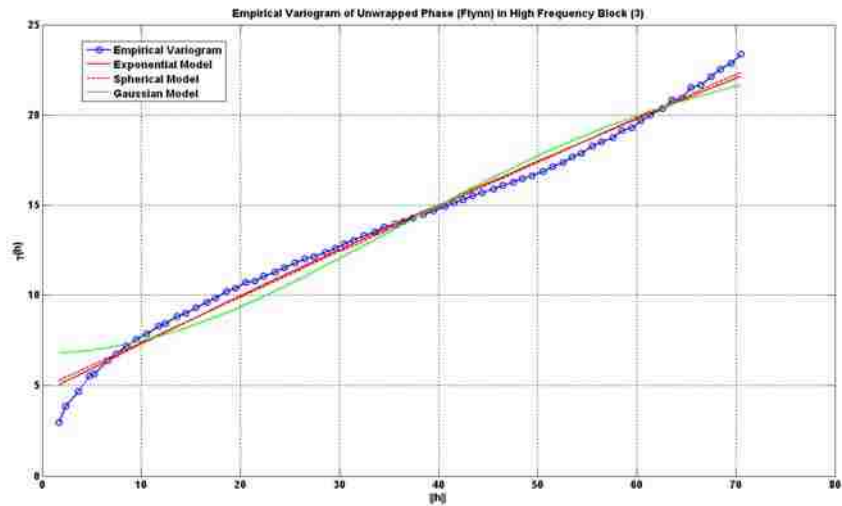


(c)

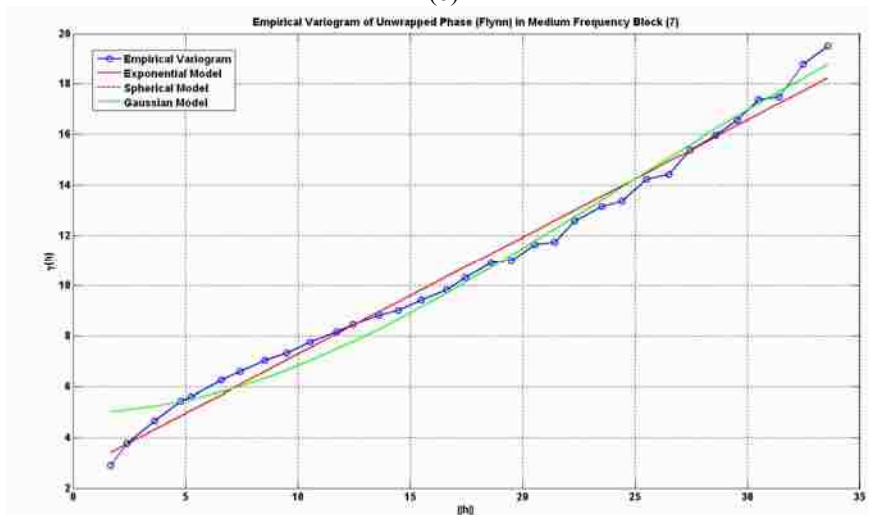
Figure 3.7: The wrapped phase image of a sample urban scene. (a) and the empirical variograms from a medium frequency and high frequency block. (b) The empirical variogram of the high frequency block shaded in (a). (c) The empirical variogram of the medium frequency block shaded in (a).



(a)



(b)



(c)

Figure 3.8: The unwrapped phase image of a sample urban scene obtained by Flynn's minimum discontinuity method. (a) and the empirical variograms from a medium frequency and high frequency block. (b) The empirical variogram of the high frequency block shaded in (a). (c) The empirical variogram of the medium frequency block shaded in (a).

models listed above. We also note that the maximum lag, \mathbf{h} , in Figure 3.7(b) and Figure 3.8(b) is greater than the maximum in Figure 3.7(c) and Figure 3.8(c). The reason for this is that we adaptively calculate the variogram out to a lag that is dependent on the bounds imposed by our partitioning of the spectrum into distinct blocks. This is discussed in greater detail later.

3.3.4. Optimal Interpolation using Kriging

Over each spectral sub-region we assume that the random field can be modeled using

$$Z(\mathbf{s}) = \mu + n(\mathbf{s}), \quad \mathbf{s} \in F, \quad \mu \in \mathfrak{R} . \quad (9)$$

where μ is a constant mean term, $n(\mathbf{s})$ is a spatially varying covariance function defined by locations within the Fourier spectrum. We simplify this model by assuming isotropy, which we verified experimentally. An isotropic covariance model, when intrinsic stationarity is met, allows $n(\mathbf{s})$ to be defined radially, instead of along specific directions. The implication of this assumption is two-fold. First, it allows for more data samples in both the covariance model estimate and the interpolation step. Second, it removes the need analytical assessment of directional variogram estimates to discern which directional model (typically, the directional variogram with that provides the best fit in the least-squares sense is selected) best fit the model in (9).

In ordinary Kriging, we estimate the optimal linear predictor based on the random model of (9) using a weighted sum of the known data points within a region, \mathbf{B} :

$$p(\mathbf{Z}; \mathbf{B}) = \sum_{i=1}^n \lambda_i Z(\mathbf{s}_i). \quad (10)$$

Since we assume that the random field model is zero-mean, we also require that the optimal data points should satisfy:

$$\sum_{i=1}^n \lambda_i = 1, \quad (11)$$

which guarantees uniform unbiasedness. The optimal filter provided by (10) must minimize the mean-squared prediction error:

$$\sigma_e^2 \equiv E\{(Z(\mathbf{B}) - p(\mathbf{Z}; \mathbf{B}))^2\} \quad (12)$$

while upholding the constraint in (11).

The minimization of (12) carried out over $\lambda_1, \dots, \lambda_n$, subject to the weight constraint (11), for the data model in (10) is assumed to hold with the variogram defined in (1). For single point prediction, say $B = \{\mathbf{s}_0\}$, the problem can be reformulated to one of minimizing

$$E\left\{\left(Z(\mathbf{s}_0) - \sum_{i=1}^n \lambda_i Z(\mathbf{s}_i)\right)^2\right\} - 2m\left(\sum_{i=1}^n \lambda_i - 1\right) \quad (13)$$

with respect to $\lambda_1, \lambda_2, \dots, \lambda_n$, and m , where m is the Lagrange multiplier that ensures the constraint holds. Using the constraint that the lambdas must add up to

1, and after taking partial derivatives with respect to m and the lambdas, we get the following $n+1$ equations and $n+1$ unknowns:

$$\begin{aligned}
 -\sum_{j=1}^n \lambda_j \gamma(\mathbf{s}_i - \mathbf{s}_j) + \gamma(\mathbf{s}_0 - \mathbf{s}_i) - m &= 0 \\
 \sum_{i=1}^n \lambda_i &= 1
 \end{aligned} \tag{14}$$

The system of equations in (14) can be represented as the following system of linear equations

$$\Gamma_0 \lambda_0 = \gamma_0 \tag{15}$$

where:

$$\lambda_0 \equiv [\lambda_1, \dots, \lambda_n, m]^T \tag{16}$$

$$\gamma_0 \equiv [\gamma(\mathbf{s}_0 - \mathbf{s}_1), \dots, \gamma(\mathbf{s}_0 - \mathbf{s}_n), 1]^T \tag{17}$$

$$\Gamma_0 \equiv \begin{cases} \gamma(\mathbf{s}_i - \mathbf{s}_j), & i, j = 1, \dots, n, \\ 1, & i = n+1, j = 1, \dots, n \\ 0, & i = n+1, j = n+1 \\ 1, & j = n+1, i = 1, \dots, n \end{cases} \tag{18}$$

which results in a real-symmetric matrix Γ_0 of size $(n+1) \times (n+1)$, which solve the system of $(n+1)$ equations. Next, consider the following substitutions:

$$\Gamma_0 \text{ by } \Gamma \equiv \gamma(\mathbf{s}_i - \mathbf{s}_j), \tag{19}$$

where the $(i,j)^{\text{th}}$ element is $\gamma(\mathbf{s}_i - \mathbf{s}_j)$,

$$\gamma_0 \text{ by } \gamma = [\gamma(\mathbf{s}_0 - \mathbf{s}_1), \dots, \gamma(\mathbf{s}_0 - \mathbf{s}_n)]^T, \tag{20}$$

$$\lambda_0 \text{ by } \boldsymbol{\lambda} = [\lambda_1, \dots, \lambda_n]^T \quad (21)$$

These substitutions, provided from the information from the fitted variogram model over the region of data used for estimation, result in the following simplified equations:

$$\boldsymbol{\lambda}^T = \left(\boldsymbol{\gamma} + \mathbf{1} \frac{(\mathbf{1} - \mathbf{1}^T \Gamma^{-1} \boldsymbol{\gamma})}{\mathbf{1}^T \Gamma^{-1} \mathbf{1}} \right)^T \Gamma^{-1} \quad (22)$$

$$m = -(\mathbf{1} - \mathbf{1}^T \Gamma^{-1} \boldsymbol{\gamma}) / (\mathbf{1}^T \Gamma^{-1} \mathbf{1}) \quad (23)$$

where $\mathbf{1} = [1, 1, \dots, 1]^T$ which is length n .

Using the equations for the optimal predictor, we can estimate the minimized variance, often referred to the *Kriging (or prediction) variance*, which is given by

$$\sigma_k^2(\mathbf{s}_0) = 2 \sum_{i=1}^n \lambda_i \gamma(\mathbf{s}_0 - \mathbf{s}_i) - \sum_{i=1}^n \sum_{j=1}^n \lambda_i \lambda_j \gamma(\mathbf{s}_0 - \mathbf{s}_i) \quad (24)$$

which is equal to $\boldsymbol{\lambda}^T \boldsymbol{\gamma} + m$ from (23) and (24).

If $Z(\cdot)$ is Gaussian, then over the joint distribution of $Z(\mathbf{s}_0), Z(\mathbf{s}_1), \dots, Z(\mathbf{s}_n)$, we have from (10), (15), and (24) that the predicted value \hat{Z} has

$$\mathbf{A} = (\hat{Z}(\mathbf{s}_0) - 1.96\sigma_k(\mathbf{s}_0), \hat{Z}(\mathbf{s}_0) + 1.96\sigma_k(\mathbf{s}_0)) \quad (25)$$

as a 95% confidence interval for $Z(\mathbf{s}_0)$ in the sense that $\Pr(\hat{Z}(\mathbf{s}_0) \in \mathbf{A}) = 95\%$. It is important to note that the variance defining the prediction interval is underestimated since it is based on variogram estimates [1].

The computational complexity of the Kriging interpolation step is dependent on the size of Γ , which has dimensions size $N \times N$, where N is the number of interpolated samples being sought.

3.4. Methods

3.4.1. Spectral Sampling Rates

At this point, we present two diagrams that concisely represent the procedures we follow in the Kriging approach to spectral data estimation. The first diagram, shown in Figure 3.9, summarizes the procedure of frequency domain sampling and modeling, which we based on the theoretical background provided above. The second diagram, shown in Figure 3.10, summarizes the procedure we follow to reconstruct an image from the statistical models produced by the procedure depicted in the first diagram.

Our reconstruction technique utilizes a region-based spatial statistical model. Taking this into consideration, we developed a scalable, adaptive spectral lattice sampling scheme that can be effectively implemented using the 2D FFT.

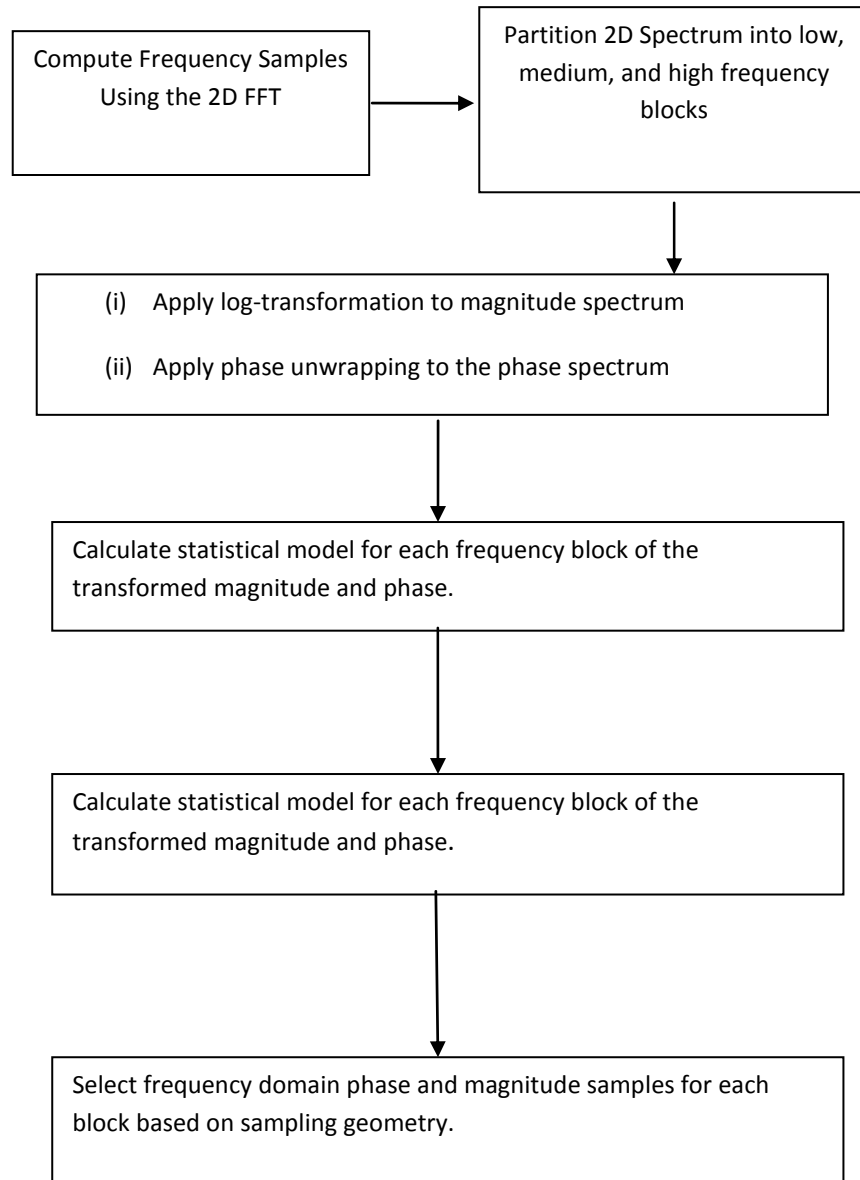


Figure 3.9: Spectral modeling procedure flow chart. The above procedure diagram that shows the logical flow of operations we perform to statistically model and sample the magnitude and phase spectra of the Fourier domain.

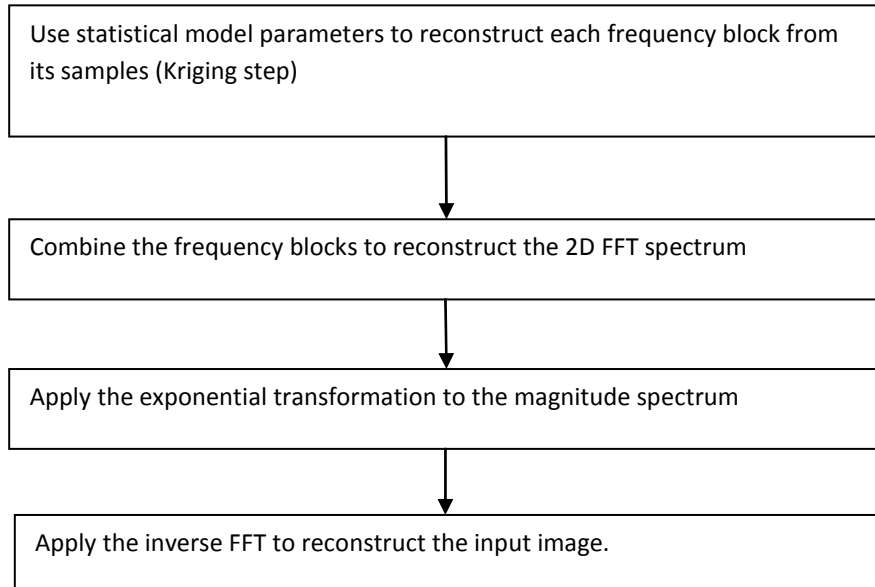


Figure 3.10: Fourier and spatial image reconstruction flow chart. This diagram summarizes the procedure we use for Fourier spectrum reconstruction from the spectral statistical models obtained by the procedure in Figure 3.9 to reconstruct the input image from reduced spectral samples.

Here, we consider different Frequency-domain sampling rates for the magnitude and phase components of the spectrum.

First, we utilize the symmetry that is inherent to the Fourier domain. Since we are working with real-valued images, we note that the Fourier transform satisfies:

$$F(u, v) = F^*(-u, -v), \quad (26)$$

where F^* is the complex conjugation operation. When expressing the Fourier domain as magnitude and phase samples, then the Magnitude symmetry gives $|F(u, v)| = |F(-u, -v)|$ and the phase symmetry gives $\angle F(u, v) = -\angle F(-u, -v)$.

Thus, we can represent an $N \times N$ image completely with $(\frac{N}{2} + 1) * N$ spectral samples. Before continuing, we want to define terms that denote which spectral region is being considered – both for consistency sake here and in the descriptions of our reconstructions which are presented later. We will refer to the three classifications of spectral regions; the region denoted by the *high frequency blocks*, the region denoted by the *medium frequency blocks* and *low frequency blocks*. Referring back to Figure 3.5, we connect the labeled regions with our new terminology. The high frequency blocks are represented by the outer blocks (labeled as 1-6 in Figure 3.5). The medium frequency blocks are represented by the next layer of blocks (labeled as 7-12 in Figure 3.5). The innermost blocks represent the low frequency blocks.

Next, we want to consider different sampling rates for the three types of blocks. For providing a standard comparison of the proposed sampling rates, we use the uniformly-spaced sampling produced by the 2D FFT as a reference. Here, we are interested in reducing the number of frequency samples as a function of the relative frequency magnitude.

First, we note that the majority of the image energy is concentrated around the low frequency components. It is thus of little benefit to expect any significant reduction in sampling rates for the low frequencies. Instead, we expect most of the reductions to come from reducing sampling rates of the higher and medium frequency components. We will thus consider the use of the uniform 2D FFT

sampling rates over the lower frequencies. Here, we are treating the lower frequency component as a “base layer” that will help us provide a minimum level of reconstruction quality.

Our goal is thus one of considering sampling rate reductions for the medium and high frequency blocks that can still provide us with acceptable image reconstructions. Given the fact that the medium frequency components are expected to contain significantly more energy than the higher frequency components, we want to consider denser sampling rates for the medium frequency components. Given the dyadic configuration of the blocks, we are led to consider sampling rates that are twice as dense (in each dimension) for the medium frequencies compared to the high frequency components.

For example, we consider a minimum sampling rate reduction of 2 along each dimension. This will result in a four-fold reduction in the sampling rate as compared to the standard 2D FFT over the same frequencies. Furthermore, for a four-fold reduction of the medium frequencies, we will have a sixteen-fold reduction for the high frequency blocks.

Ultimately, we are interested in the overall reduction in the number of samples, as summarized in Table 3.1.

TABLE 3.1
SPECTRAL STATISTICAL DATA SAMPLE RATES

MAGNITUDE SAMPLING PHASE SAMPLING REDUCTION RATE	4x/16x	16x/64x	64x/256x
NONE: 1x/1x	18.75%	11.97%	10.17%
1x/4x	17.26%	15.57%	15.12%
4x/16x	9.38%	7.68%	7.23%
16x/64x	7.68%	5.99%	5.54%

This table contains all of the sampling rates that were explored in this study. We report two values for each sampling geometry. The first value (e.g. $N \times$ from $N \times / M \times$) refers to the sampling rate reduction rate for the medium frequency blocks. The second number refers to the reduction rate for the high frequency blocks. Here the reduction rate refers to the number of samples kept divided to the samples kept by the standard uniform sampling rate produced by the 2D FFT. The percentage values refer to the overall reduction.

3.4.2. Statistical Models for Magnitude and Phase Spectra

To compute an appropriate statistical model, we begin with the collection of variogram models described in Section 2.3.1. Here, we present our approach at discovering the optimal model and parameters that best describe the medium and high frequency blocks in terms of interpolation accuracy. There are three main items that must be taken into consideration when developing a model that best describes the spectral correlation of the data being modeled. The first is whether or not isotropy can be assumed and the implications of such an assumption. The second is selecting the proper range parameter when calculating the empirical variogram. Finally, we must consider the effects of various variables under our

control in the process of fitting the empirical variogram to a theoretical model. We explore each of these items in the following sub sections.

3.4.2.1 Isotropy Model Considerations

The variogram models we defined above are isotropic, which implies that they are defined by the relationship of all points that are radially separated across a desired range of lag values. Anisotropy, in our case, would imply that spatial correlation between points is dependent on direction *and* distance. The primary implication of a non-isotropic model would be additional computational complexity arising from the need to calculate as many separate variograms as directions being considered.

At this point, it is important to remind the reader that our models are defined in a bounded, discrete representation of the continuous Fourier spectrum. Therefore, lag that is expressed in terms of distances in the discrete (FFT) frequency domain does not depend on the size of the input image. This is a considerable deviation from the traditional understanding of classical geostatistics. Our samples are defined in a normalized domain that is represented by multiplying the traditional spatial distance index, which is unity in the image domain, by $2\pi/N$ where the input image size is $N \times N$.

Because the portions of the spectrum represented by the frequency blocks in which we sample are continuous, we can define our models with fewer samples in the discrete frequency plane. It is important to realize that the number of samples is not indicative of distance. Even though the 2D FFT generates uniform FFT samples, other discrete signal processing methods can generate an arbitrary number of samples in any of the continuous, bounded spectral blocks. One way to accomplish this would be by using the Chirp-Z transform, which generates any number of samples in any continuous bounded region within the Fourier domain [32].

Isotropic variograms more accurately estimate the variogram because we do not have to consider a large number of discrete directions in order to fit the model. Each direction constrains the number of sample pairs along the considered vector. For example, an anisotropic model that considers N discrete directions to fit the continuum of possible directions will utilize only $\sim 1/N$ of the total samples that would be available to the isotropic model. In addition to providing a more accurate empirical variogram estimate, the isotropic model will be computationally faster as we will not need to consider a large class of variogram models. The isotropic models are also easier to computationally fit, as fewer parameters are optimized.

3.4.2.2 Variogram Range Selection

Due to the scalability of our design, we want to ensure that the variogram is estimated across the extent of all the samples within the frequency block under consideration. Therefore, we calculate the maximum radial distance that can exist from a known sample to an unknown sample and calculate over the lag values ranging from spectral data points separated by one sample out to the number of samples between the approximate center sample of the frequency block to the any of the samples located at the corners of the frequency block.

While acceptable reconstruction may be achieved for lower sampling rates when the size of the maximum lag considered in the variogram calculation is scaled to better reflect the sampling rate of the data, we accept the additional computational cost of variogram calculation over the entire frequency block. Again, we support this design decision to ensure that our method is scalable; allowing multiple sampling rates to be explored from a single variogram estimate. In other words, we ensure that the estimated model provides a semivariance for the largest possible sampling rate. We now consider methods that provide the optimal spectral model that fits our scalable design constraint.

3.4.2.3 Variogram Model Selection and Fitting

Since we take care to calculate the variogram from the full extent of samples in each frequency block, we can dictate how far out the spectral covariance model is defined. From the empirical variogram of each frequency block, we can fit a

theoretical variogram model by solving for the model parameters. Here, we calculate the model parameters so that they minimize the error between the model and the empirical data using the interior trust-region algorithm provided in the *lsqcurvefit* Matlab function.

The sampling rate in applied to each block will govern the size of the maximum lag we select to which we fit the models. Since Kriging utilizes the theoretical covariance model to adaptively weight known samples based on the distance of the samples to the unknown data point, we see that there is an optimal range in which distant samples beyond it are shown to have little effect on the interpolated result. In addition to this, we note that variogram estimates at larger lag values tend to be less accurate than estimates at shorter distances. This is due to the variability in the number of samples available for producing the covariance estimates. Since our estimation is from gridded data over bounded domains, it is clear that fewer samples are used to estimate the variogram at large distances.

Furthermore, the more accurately the model fits the estimated variogram at shorter lag values, the better the Kriging interpolator will perform. This is because there is much more correlation over shorter distance than larger distances. An example, we note the success of the nearest neighbor interpolator, where the unknown value is assigned the single sample that is nearest. Over large distances, the correlation between samples tends to zero, and fitting variogram models at

large discrete frequency distances amounts to fitting semivariance values that do not accurately model the covariance field

Therefore, we limit the parameter optimization to a range of lag values that are between two and five times the radial distance defined by the sampling rate, but not exceeding 25. Exploration of our data set revealed that three times the radial distance of the sampling rate resulted in the best interpolated magnitude and phase spectra on a block by block basis. If this value exceeds 25 for a given sampling rate, the model fit will be truncated.

Next, we optimize the parameters for each of the three models in (5)-(7) and ultimately select the model that produced the lowest error when comparing the estimated semivariance values to the model evaluated at the selected maximum value of \mathbf{h} . In other words, we select the model that best fits the estimated variogram.

3.4.3. Kriging Interpolation of Magnitude and Phase Spectra

3.4.3.1 Magnitude Spectra Estimation

The second step for reconstruction is to perform simple Kriging, which provides the optimal linear estimator of the missing FFT samples. The basic idea is that we can provide near-perfect reconstruction by interpolating the missing FFT samples and performing an inverse 2D FFT.

There are two parameters that we need to consider for optimal interpolation performance: the *max-distance* and the *max-samples* as shown in Figure 3.11. Here, the *max-distance* parameter refers to the circular radius of the maximum discrete-frequency space distance that needs to be considered for estimating the missing sample. For Kriging, all known FFT sample values that fall within the circle with radius *max-distance* are used to form the estimate. The *max-samples* parameter refers to the exact maximum number of known FFT samples that are considered when solving for the Kriging sample estimate. The idea is that the number of available samples is a function of the location of the unknown missing value, as demonstrated in Figure 3.11.

Two examples of the number and location of the known points used for estimation that are limited by a specified radial distance are shown in Figure 3.11. The solid circle in Figure 3.11 has the same radius as the dashed circle (seven samples), but depending on the location of the unknown point being estimated (represented by the 'x' marker), the number of known samples used in the estimator differs. The solid circle contains eight known samples (represented by the '•' marker), while the dashed circle contains ten known samples. If a maximum number of points is explicitly specified, the location of the points will depend on the sampling rate that was applied to the spectral block being reconstructed.

Significant edge artifacts will occur when specifying the number of known samples for Kriging is based on the max-distance parameter. At the corners of the frequency blocks, the circle of radius max-distance that includes known samples is constrained to a quarter-circle. This effectively reduces the number of samples that could be included in the sampling region by 75%. Not as dramatic, but also influential would be the known samples selected by a radius of max-

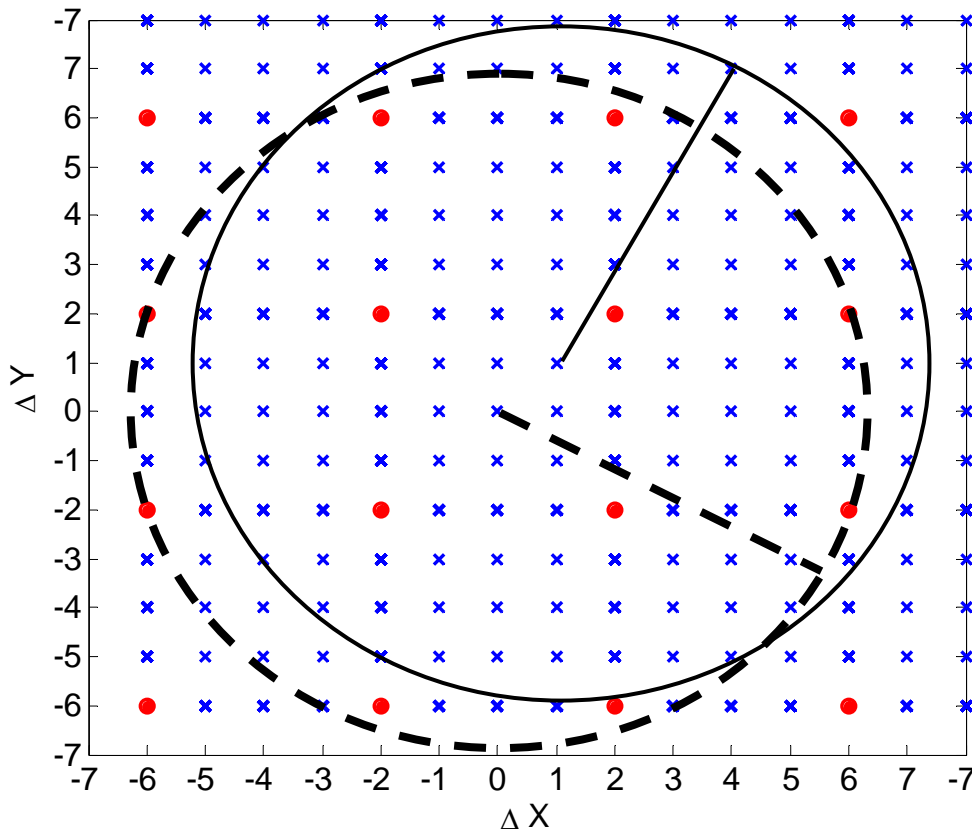


Figure 3.11: A grid of FFT discrete frequency samples, where we only consider one of every four samples in each dimension. The circles represent the region, centered at two unknown samples (unknown samples are represented using the 'x' marker) with a radius of seven samples. The number of neighboring available samples (known samples are represented using the '•' marker) differs based on the location of the unknown sample being estimated. The solid circle encompasses eight known samples, while the dashed circle encompasses ten known samples.

distance for unknown points along the edge of the frequency block. In this case, the most samples that can be included will fall within a half-circle, effectively

reducing the number of known points by 50%. While these special cases are extreme examples of the inconsistency of the reconstruction model provided by using max-distance, they support our selection of using the max-samples parameter.

For sufficiently large values of the max-distance and max-samples parameters, we have found that optimization for either parameter performed equally well. Ultimately, we chose to use max-samples in further experiments because the number of known samples used in the estimate does not change based on the location of the unknown sample being estimated. We provide more details on the number of samples in the results section.

Using the best Kriging parameter resulting from the above process, we reconstructed the magnitude spectra using a fixed number of semivariance values to fit the theoretical variogram models. The empirical variograms were calculated from the full spectra. The individual magnitude spectra estimates for each spectral block were compared to other two-dimensional interpolation algorithms: the nearest-neighbor, bilinear, and spline interpolation algorithms [33]. A quantitative comparison was made using the PSNR of the reconstructions compared to the log-transformation of the original magnitude data.

3.4.3.2 Phase Spectra Estimation

We conducted two studies on the five two-dimensional phase unwrapping methods described above. The first was a quantitative study on the variogram estimates obtained from each inner and outer spectral block. Our intention was to learn if any of the unwrapped phase surfaces produced empirical variograms that were not well fit by any of the models defined by (2-4) using the residual least-squared error from the optimal model fitting approach described in the magnitude spectral estimation section.

For the sake of consistency, we constrained the variogram length to be twenty-five samples and we fit all twenty-five semivariance values for all of the spectral blocks under test. The second study consisted of comparison of reconstruction quality between the five two-dimensional phase unwrapping algorithms used in this study. Each method was applied to the wrapped phase resulting from the Fourier transformation operation on the original satellite image and the phase spectra contained in the medium and high frequency spectral blocks were sampled and then reconstructed in accordance to the sample rates shown in Table I. Using the estimated variogram model of the fully sampled, unwrapped phase spectra and the samples resulting from each sampling rate, we reconstructed the phase data using Kriging and compared PSNR values of the reconstructed phase to competing interpolation algorithms used to compare the magnitude spectra reconstructions. These methods were the nearest-neighbor, bilinear, and cubic spline interpolation methods.

3.5. Results

We present the results of our spectral modeling methods based on image type and frequency blocks. In the following, representative images from the three class types are used to support the assumptions we have made regarding the use of isotropy, the size of the empirical variograms calculated for the blocks, and our approach to finding the optimal theoretical model.

The variogram model results are followed by tabulated results comparing the reconstruction results for various sampling rates of both the magnitude and phase based on the statistical models we concluded worked best.

3.5.1. Variogram Isotropy

Typically, isotropy is validated by visual assessment of variograms estimated from samples along discrete directions. We selected directions are defined as 0, 45, 90 and 135 degrees, where 0 is defined as the vertical direction upwards from the center of the spectrum. Figure 3.12 contains the directional variograms of four blocks (one medium frequency unwrapped phase block, one medium frequency magnitude block, one high frequency unwrapped phase block and one high frequency magnitude block) from a single rural image. We selected Block 6 for the high frequency block and Block 11 for the medium frequency blocks. The magnitude and Flynn's Minimum Discontinuity unwrapped phase for

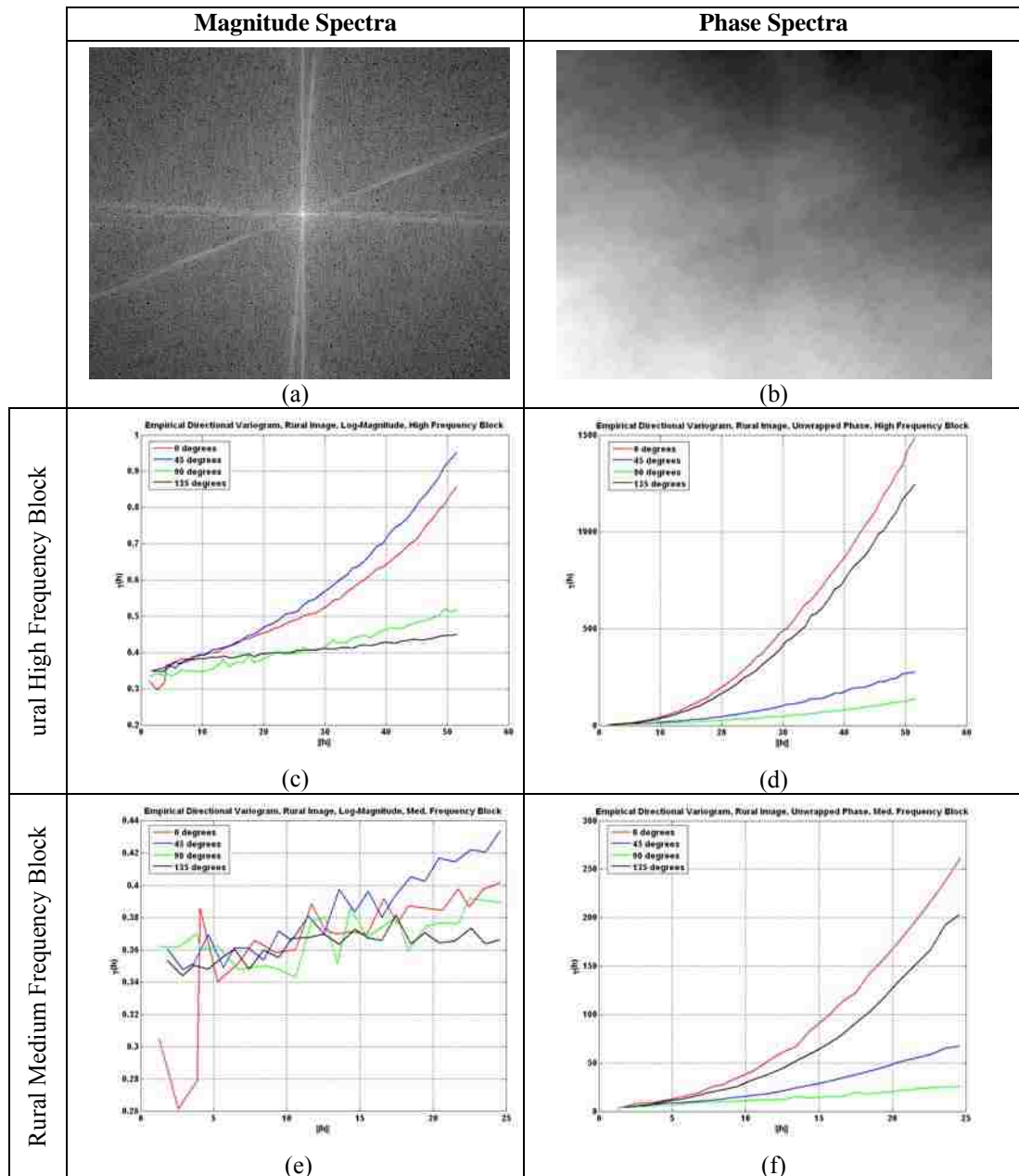


Figure 3.12: Anisotropic variograms of a high and medium frequency block from a rural image. (a) The magnitude spectra. (b) The unwrapped phase spectra. (c) High frequency block magnitude variograms. (d) High frequency block phase variograms. (e) Medium frequency block magnitude variograms. (f) Medium frequency block phase variograms.

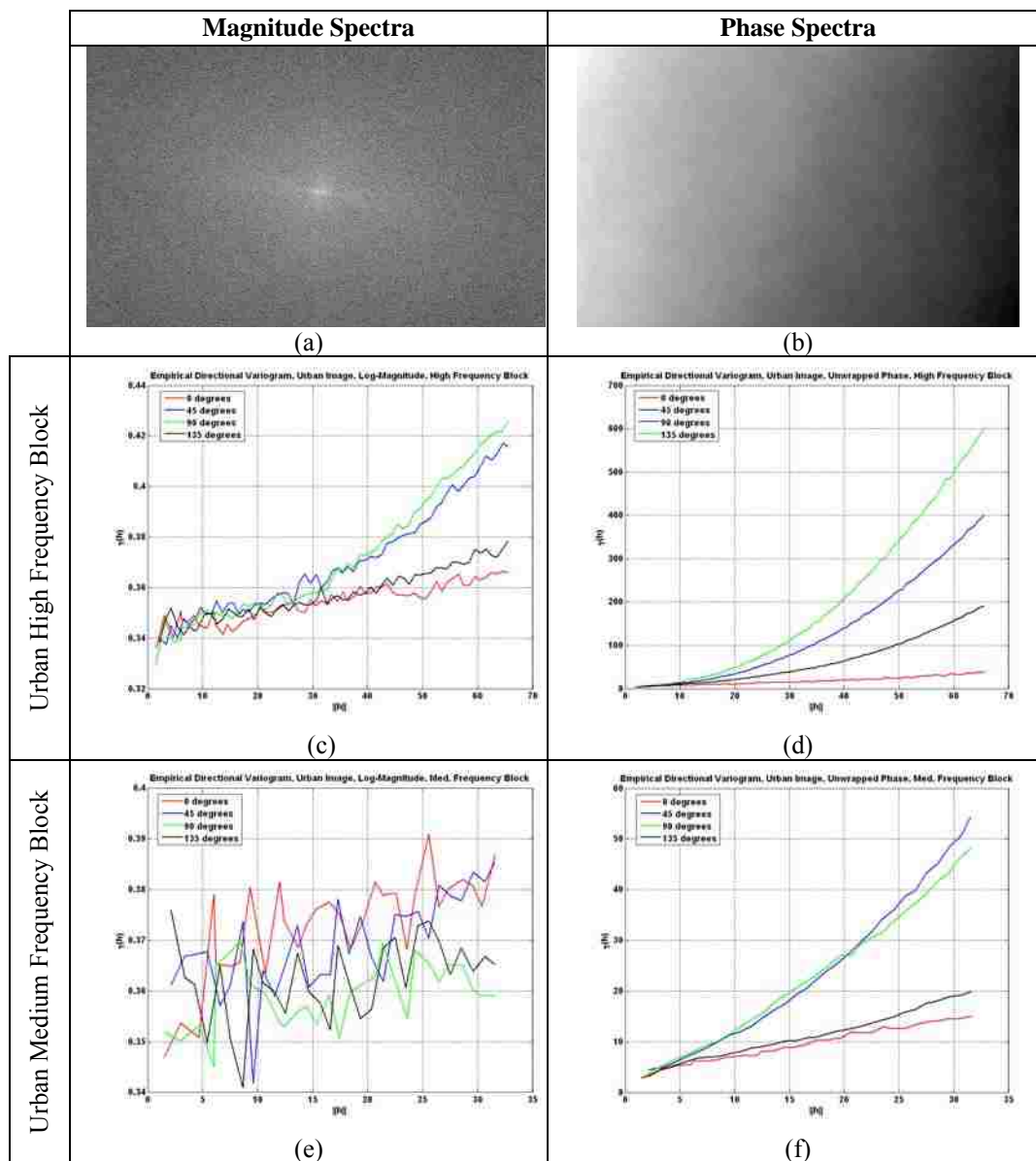


Figure 3.13: Anisotropic variograms of a high and medium frequency block from an urban image. (a) The magnitude spectra. (b) The unwrapped phase spectra. (c) High frequency block magnitude variograms. (d) High frequency block phase variograms. (e) Medium frequency block magnitude variograms. (f) Medium frequency block phase variograms.

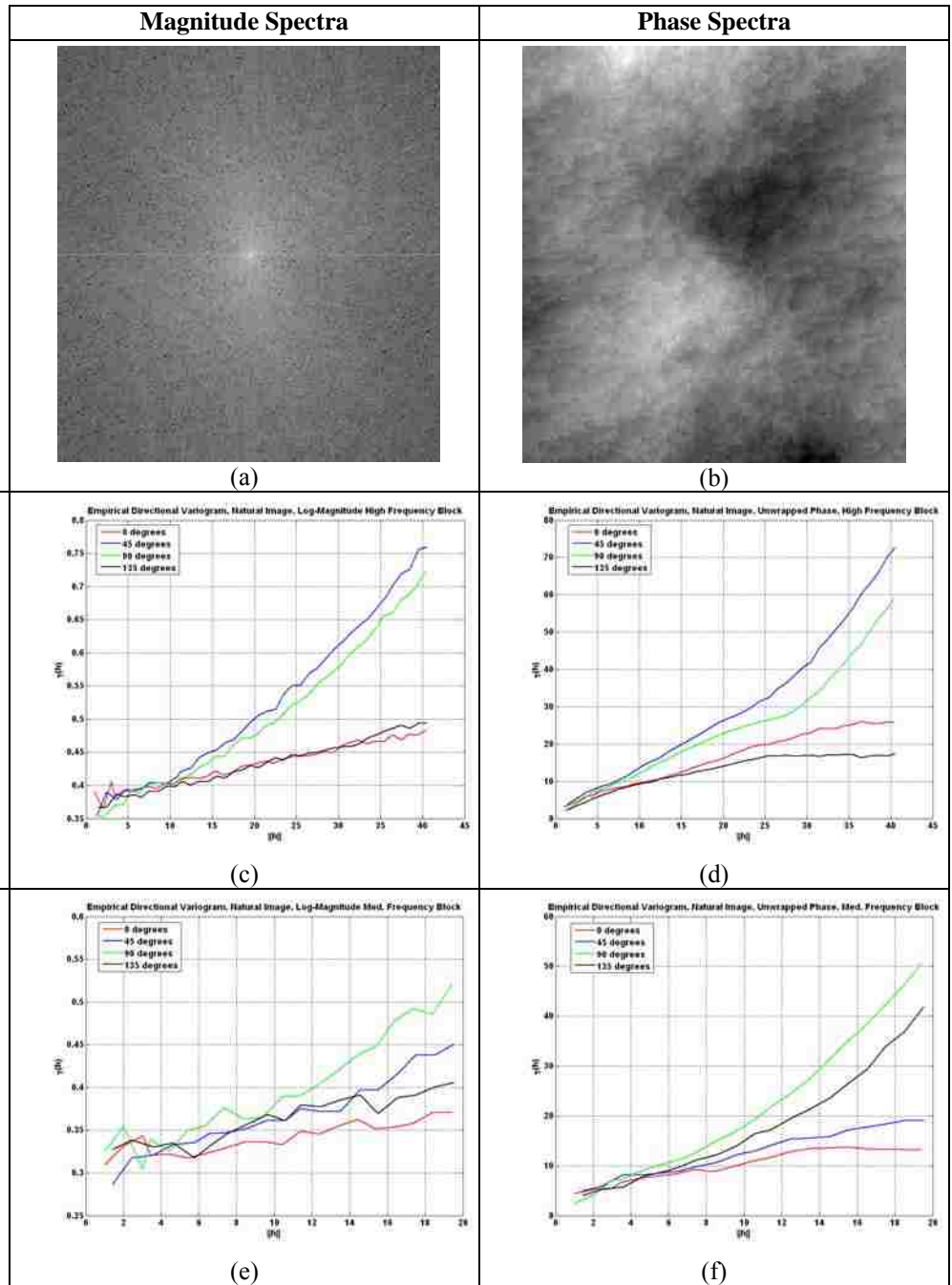


Figure 3.14: Anisotropic variograms of a high and medium frequency block from a natural image. (a) The magnitude spectra. (b) The unwrapped phase spectra. (c) High frequency block magnitude variograms. (d) High frequency block phase variograms. (e) Medium frequency block magnitude variograms. (f) Medium frequency block phase variograms.

the rural sample image are shown in Figure 3.12(a) and Figure 3.12(b), respectively. Figure 3.13 and Figure 3.14 are the directional variograms over the same blocks as in Figure 3.12, but the spectra are representative of an urban image (Figure 3.13) and a natural image (Figure 3.14).

From these results, it is clear that the phase spectra exhibit anisotropy for all image types, regardless of the spectral block description. There are clear directional trends evident in the unwrapped phase images above. Exploration of the phase spectra from bounded by the blocks we selected do clearly show greater variation among samples in the direction associated with the larger semivariance values. The magnitude spectrum, on the other hand does exhibit isotropy for the medium frequency blocks, but not as much for the high frequency blocks. The magnitude spectra in the above images are an indication of whether or not isotropy is the correct model assumption. For example, the urban sample in Figure 3.13 does not reveal significant directional correlation in the magnitude plot (Figure 3.13(a)), and accordingly, the directional variograms exhibit the least amount of variation compared to the directional variograms of the magnitude of the rural scene in figure 3.12(a), which exhibits strong directional correlation.

Also, the medium frequency blocks tend to exhibit less variation than the high frequency blocks for magnitude data samples. This result is considerable, as the number of samples available for variogram estimation is bounded by the spectral partitioning, and samples could be limited to the point where the

directional variogram estimates are not stable. In addition, we have confidence that our isotropic model assumptions hold for the more critical medium frequency regions of the magnitude spectrum, as more energy is contained within the spectra encompassed by the medium frequency blocks. Accurately predicting values within these regions will have a larger effect on overall image quality.

We now present a plot of an example of directional variograms from a spectral block with the isotropic variogram over the same spectral block included

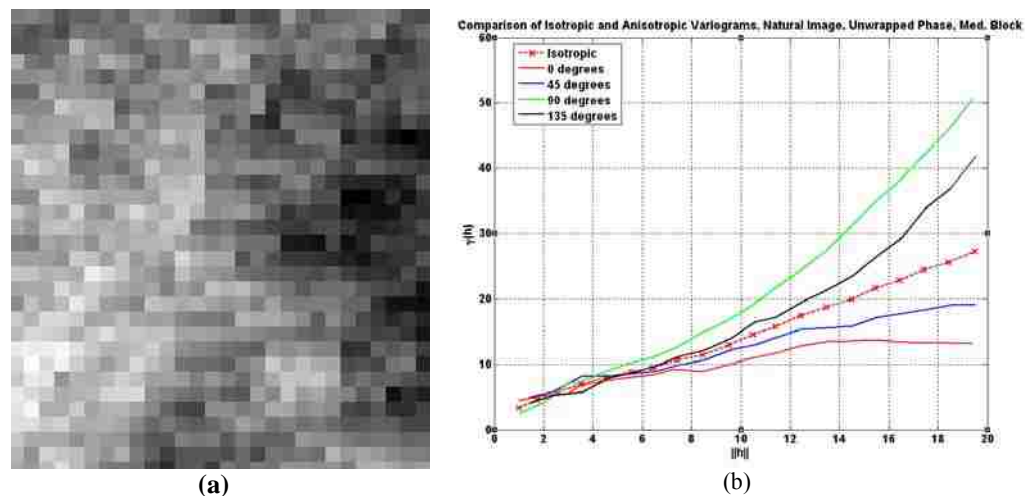


Figure 3.15: Isotropic and anisotropic variogram estimates. (a) The medium frequency block (index 11) unwrapped phase of the Erebus Ice Tongue natural image. (b) Isotropic variogram is depicted by the dashed plot, while the directional variograms are the solid plots.

as well. Figure 3.15 depicts both the variogram when isotropy is assumed (the dashed line in the plot) and the directional variogram when anisotropy is assumed. The isotropic variogram is an approximate bisection of the directional variograms, since we have examined directions that were uniformly divided between 0 and 180 degrees. This model behavior was shown to be consistent for all of our images.

3.5.2. Variogram Range Selection, Estimation, and Model Fitting

Here, we present the estimated variograms based on spectral block classification (high or medium), spectra type (magnitude and phase), and image type (rural, urban, or natural). The most concise way to present all of this information is by displaying the variograms of all frequency blocks from one image for each scene type. We also fit each variogram using the distance associated with a reduction of the FFT sampling rate by 8 in each dimension for the high frequency blocks and by 4 in each dimension for the middle frequency blocks. Thus, we keep one out of every 64 samples in the high frequency blocks and one out of every 16 samples in the medium frequency blocks. The calculated parameters from the fit are tabulated for each image.

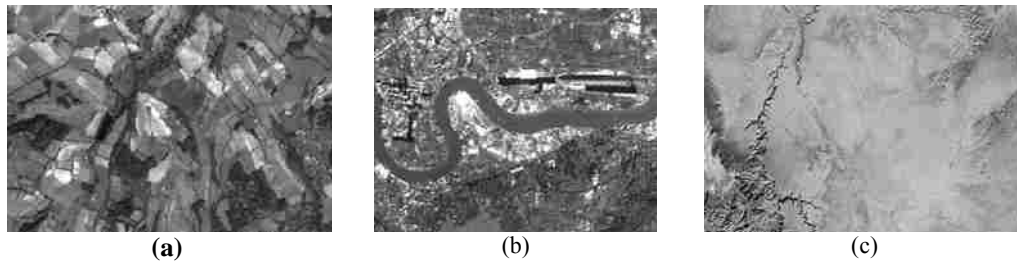
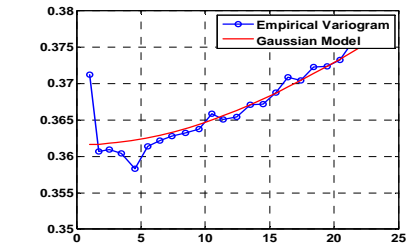
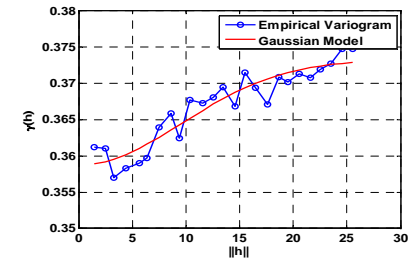
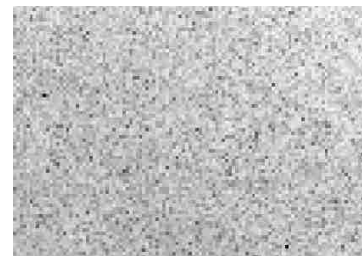


Figure 3.16: Selected image for which we calculate all of the variogram estimates for each spectral block. (a) Sample rural image. (b) Sample urban image. (c) Sample natural image.

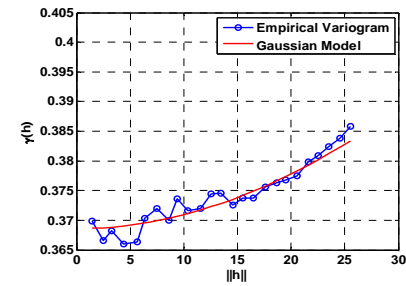
Figure 3.17 depicts the high frequency blocks and magnitude spectrum isotropic variogram estimates and fitted models for the rural image shown in Figure 3.16(a). Figure 3.18 is similar to Figure 3.17, but instead of showing the high frequency log transformed magnitude data and associated variograms, it



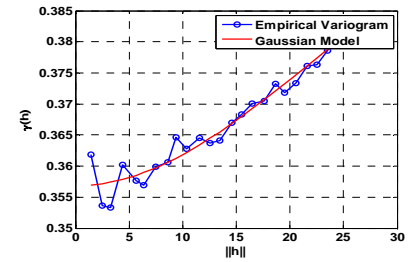
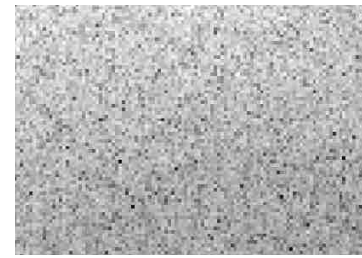
(a?)



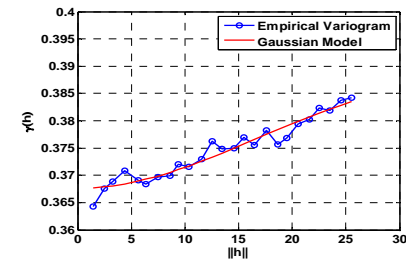
(b)



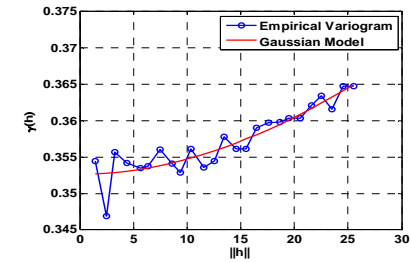
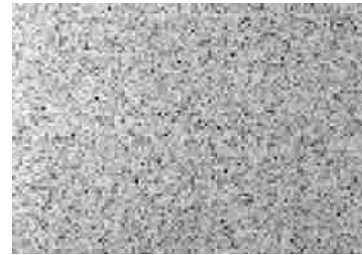
(c)



(d)



(e)



(f)

Figure 3.17: The high frequency block variogram estimates and adaptively fitted models for the log-transformed magnitude spectra of the rural image depicted in Figure 3.16(a). (a) Block 1, MSE = 3.4519e-004 (b) Block 2, MSE = 8.0585e-005 (c) Block 3, MSE = 6.1308e-005. (d) Block 4, MSE = 8.7423e-005. (e) Block 5, MSE = 4.6925e-005. (f) Block 6, MSE = 7.3069e-005.

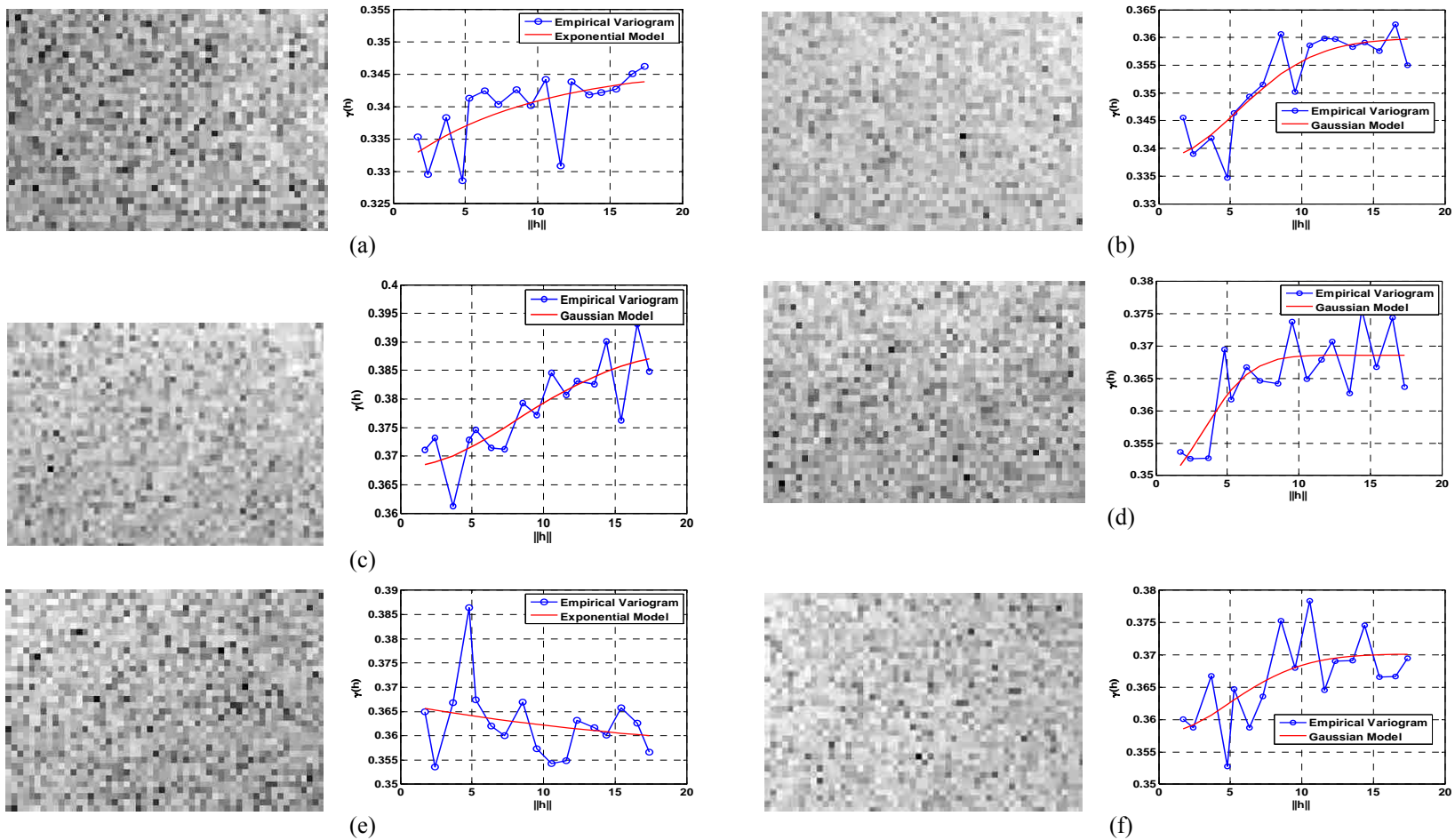
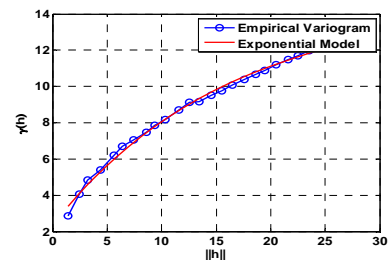
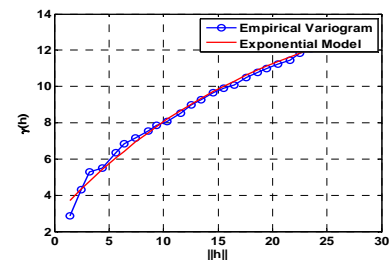


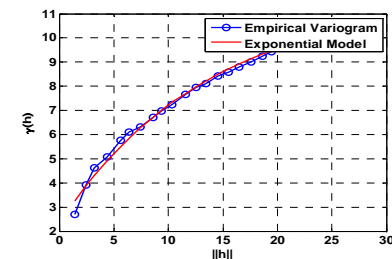
Figure 3.18: The medium frequency block variogram estimates and adaptively fitted models for the log-transformed magnitude spectra of the rural image depicted in Figure 3.16(a). (a) Block 7, MSE = $1.7851e-004$ (b) Block 8, MSE = $2.9468e-004$ (c) Block 9, MSE = $3.7012e-004$. (d) Block 10, MSE = $1.6075e-004$. (e) Block 11, MSE = $2.6847e-004$. (f) Block 12, MSE = $3.3123e-004$.



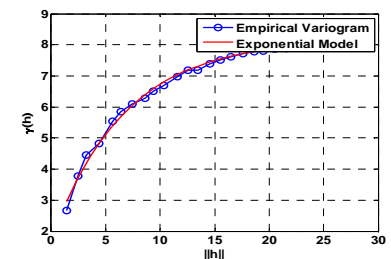
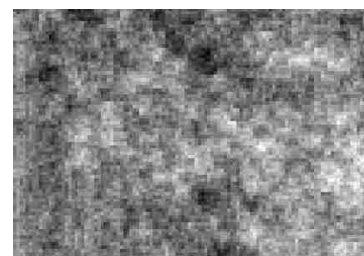
(a)



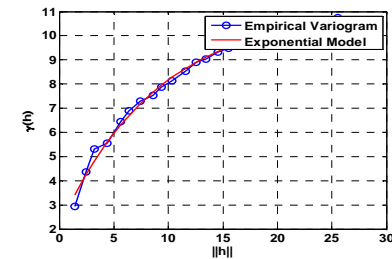
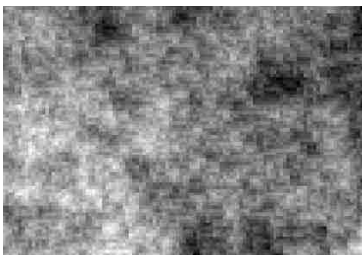
(b)



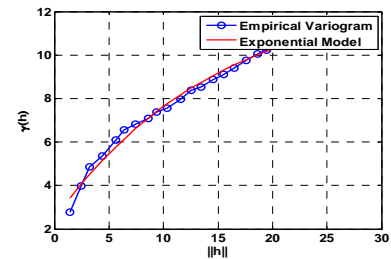
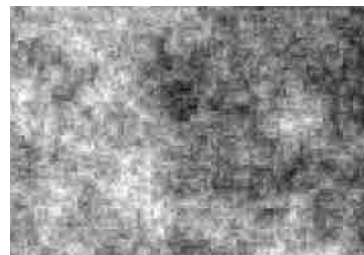
(c)



(d)

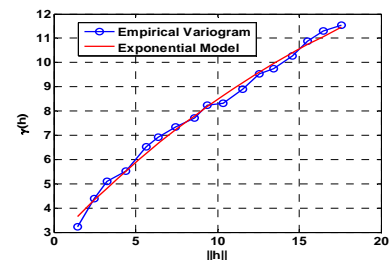
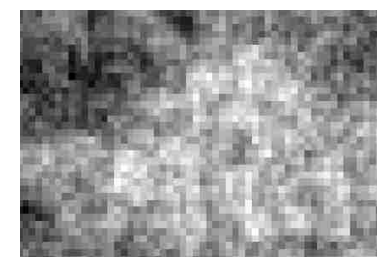


(e)

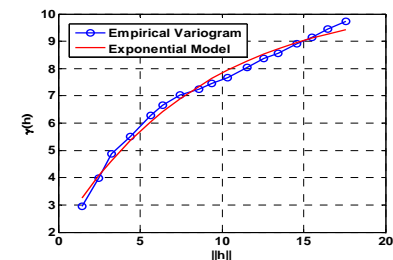
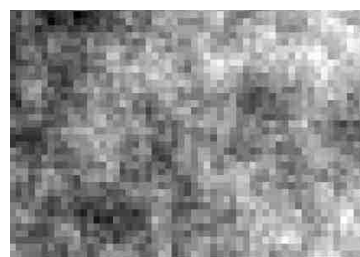


(f)

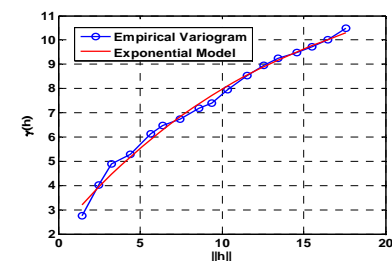
Figure 3.19: The high frequency block variogram estimates and adaptively fitted models for the unwrapped phase spectra using Flynn's Minimum Discontinuity method of the rural image depicted in Figure 3.16(a). (a) Block 1, MSE = 0.8544 (b) Block 2, MSE = 3.7851 (c) Block 3, MSE = 0.7454 (d) Block 4, MSE = 0.4016 (e) Block 5, MSE 0.9805 (f) Block 6, MSE 0.9265



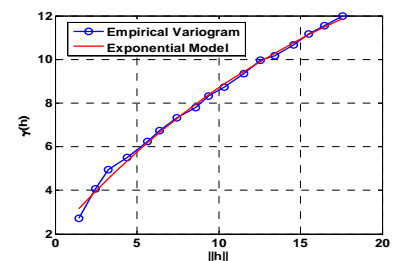
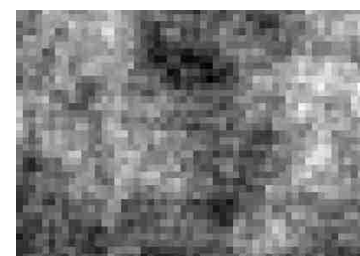
(a)



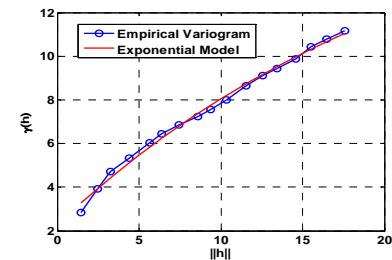
(b)



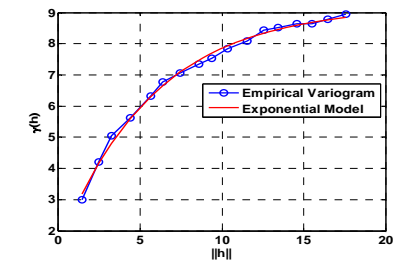
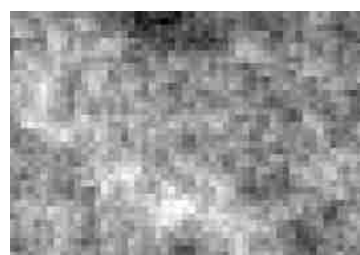
(c)



(d)



(e)



(f)

Figure 3.20: The medium frequency block variogram estimates and adaptively fitted models for the unwrapped phase spectra using Flynn's Minimum Discontinuity method of the rural image depicted in Figure 3.16(a). (a) Block 7, MSE = 0.5604 (b) Block 8, MSE = 0.6049 (c) Block 9, MSE = 0.4175 (d) Block 10, MSE = 0.3800 (e) Block 11, MSE = 0.5496 (f) Block 12, MSE = 3.3123e-004.

TABLE 3.2
RURAL IMAGE VARIOGRAM MODEL PARAMETERS

RURAL IMAGE	LOG-TRANSFORMED MAGNITUDE SPECTRA				FLYNN'S MINIMUM DISCONTINUITY UNWRAPPED PHASE SPECTRA			
	MODEL	NUGGET σ	PARTIAL SILL α	RANGE β	MODEL	NUGGET σ	PARTIAL SILL α	RANGE β
HIGH FREQUENCY BLOCKS								
BLOCK #1	Gau	0.3616	0.0547	41.4781	Exp	2.3030	12.3223	15.8918
BLOCK #2	Exp	0.3590	1.3359	38.4214	Exp	2.7546	13.3833	19.8413
BLOCK #3	Gau	0.3694	0.9123	130.0659	Exp	2.3093	9.4190	13.6046
BLOCK #4	Gau	0.3579	7.6244	304.3171	Exp	1.6964	6.4891	6.6871
BLOCK #5	Gau	0.3684	0.0800	36.8298	Exp	2.0602	9.0636	8.9176
BLOCK #6	Gau	0.3527	0.0659	39.3733	Exp	2.4397	10.6408	14.9786
MEDIUM FREQUENCY BLOCKS								
BLOCK #7	Gau	0.3630	0.1911	75.8179	Exp	2.7399	23.0698	36.7073
BLOCK #8	Exp	0.3451	0.1286	61.3807	Exp	2.0909	9.3389	11.3517
BLOCK #9	Gau	0.3678	0.1208	37.2828	Exp	2.0055	11.8192	14.7781
BLOCK #10	Gau	0.3478	0.0937	28.9546	Exp	1.9269	17.2233	20.5342
BLOCK #11	Gau	0.3520	0.9406	136.7583	Exp	2.3750	25.0061	40.7375
BLOCK #12	Sph	0.3553	0.0449	36.1683	Exp	1.8129	7.9293	7.8809

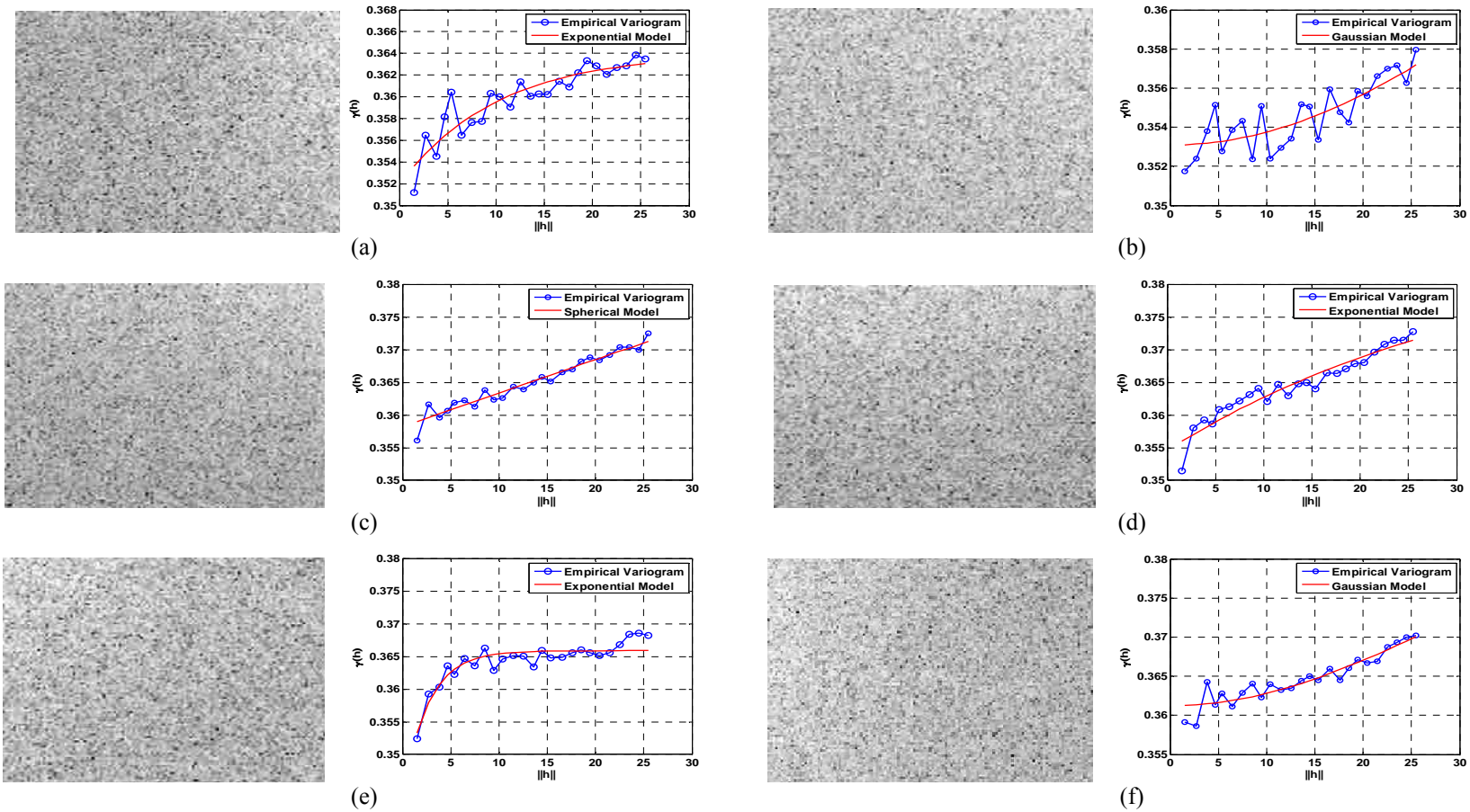


Figure 3.21: The high frequency block variogram estimates and adaptively fitted models for the log-transformed magnitude spectra of the urban image depicted in Figure 3.16(b). (a) Block 1, MSE = 2.214-005 (b) Block 2, MSE = 2.314-005 (c) Block 3, MSE = 5.049-005. (d) Block 4, MSE = 4.475-005. (e) Block 5, MSE = 2.6847e-004. (f) Block 6, MSE = 3.124-005.

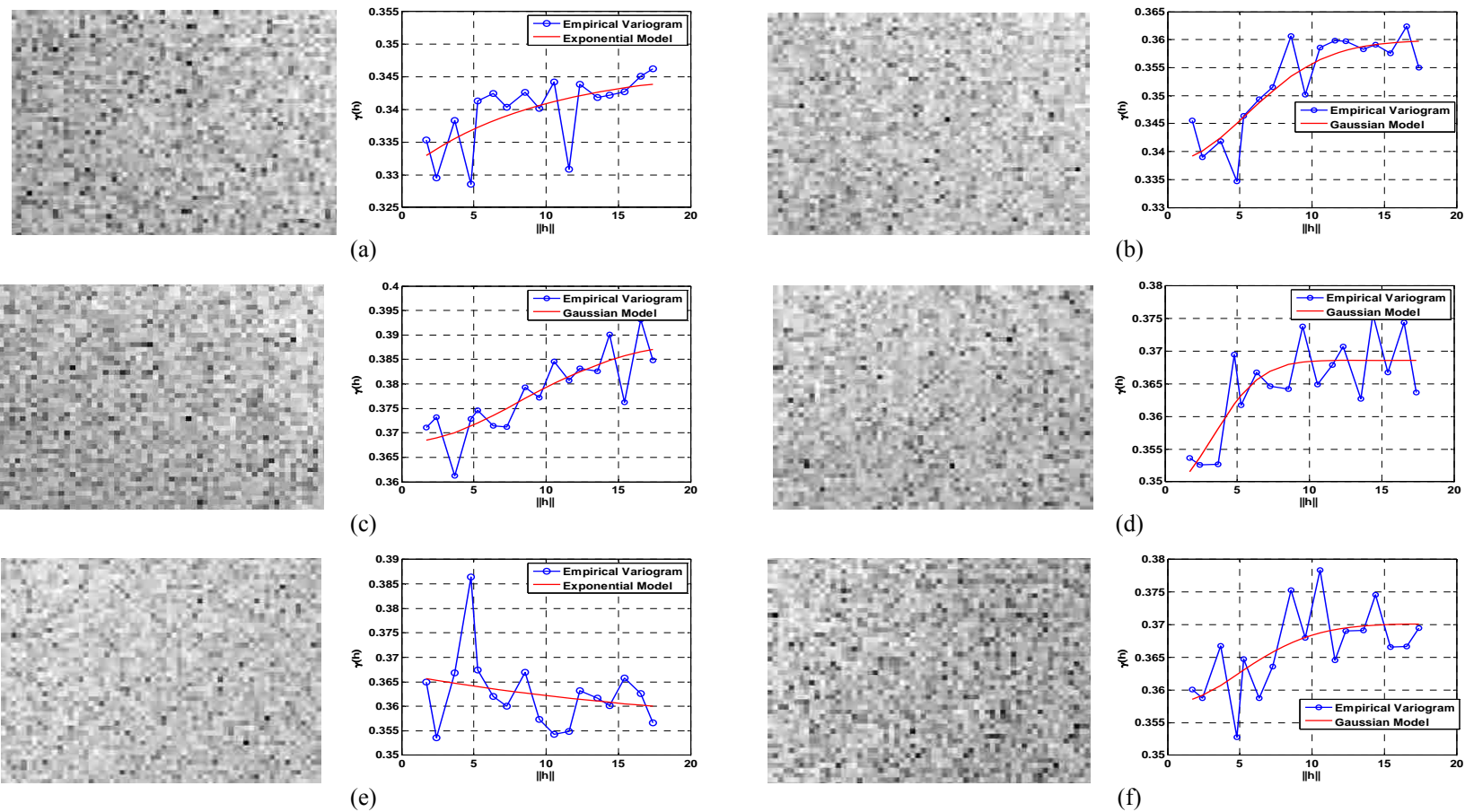
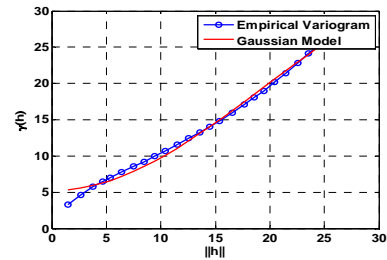
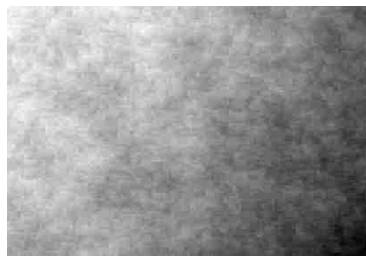
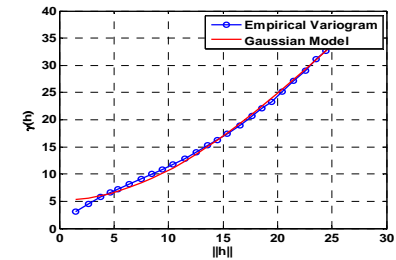


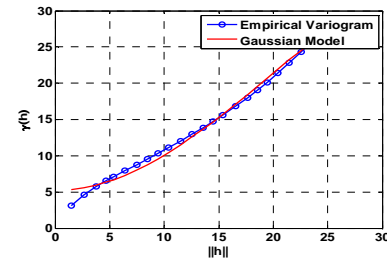
Figure 3.22: The medium frequency block variogram estimates and adaptively fitted models for the log-transformed magnitude spectra of the urban image depicted in Figure 3.16(b). (a) Block 7, MSE = 1.692-004 (b) Block 8, MSE = 1.797-004 (c) Block 9, MSE = 1.837-004 (d) Block 10, MSE = 1.146-004. (e) Block 11, MSE = 1.900-004. (f) Block 12, MSE = 6.492-005.



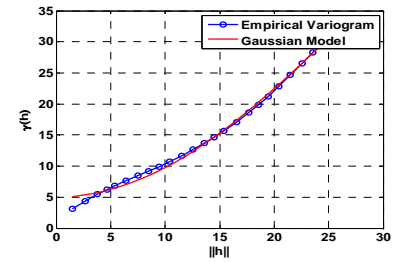
(a)



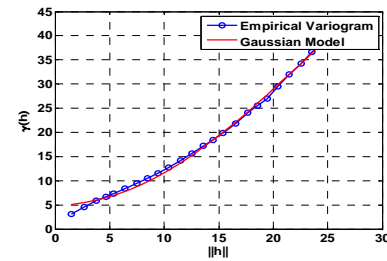
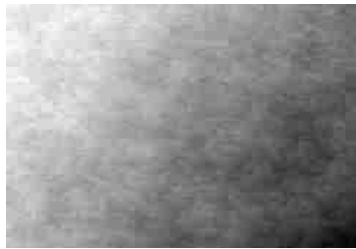
(b)



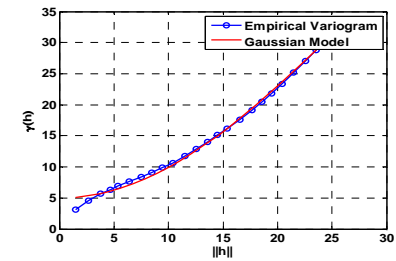
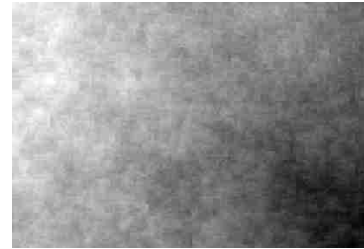
(c)



(d)

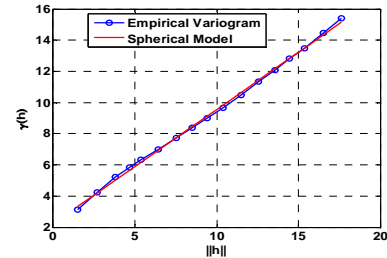
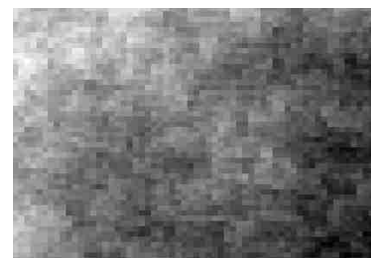


(e)

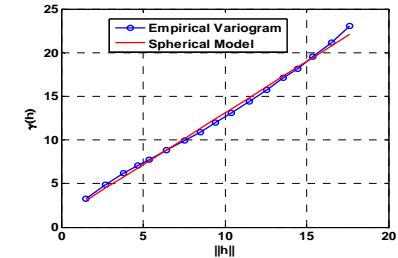


(f)

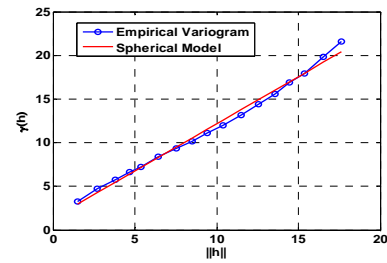
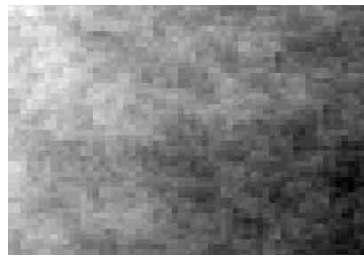
Figure 3.23: The high frequency block variogram estimates and adaptively fitted models for the unwrapped phase spectra of the urban image depicted in Figure 3.16(b). (a) Block 1, MSE = 9.6371 (b) Block 2, MSE = 10.9645 (c) Block 3, MSE = 11.7188. (d) Block 4, MSE = 8.6363. (e) Block 5, MSE = 9.5283. (f) Block 6, MSE = 6.8242.



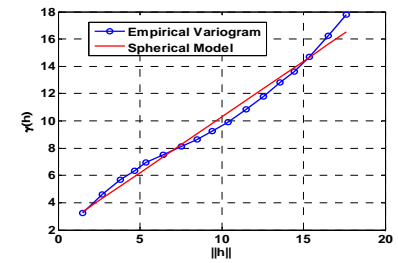
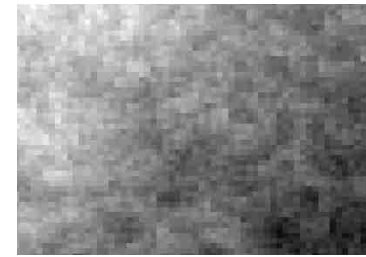
(a)



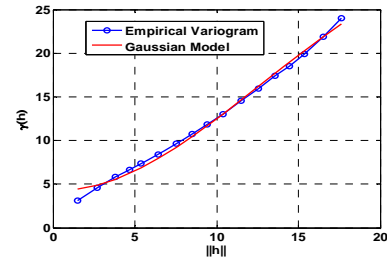
(b)



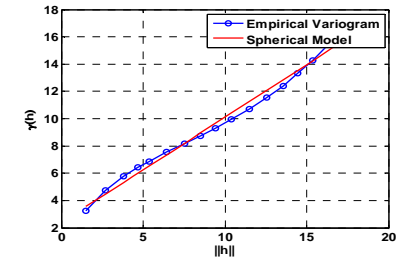
(c)



(d)



(e)

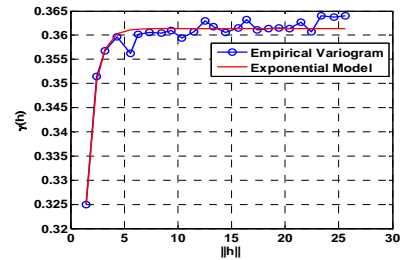
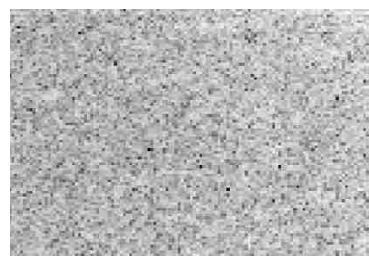


(f)

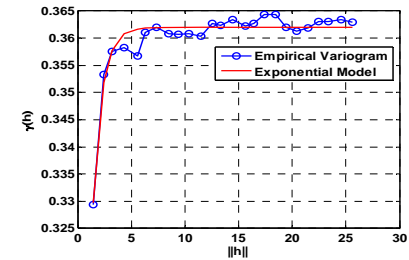
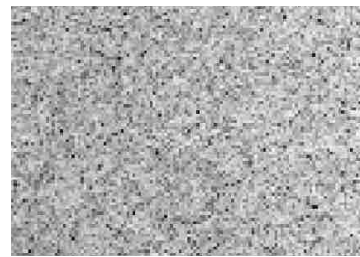
Figure 3.24: The medium frequency block variogram estimates and adaptively fitted models for the unwrapped phase spectra of the urban image depicted in Figure 3.16(b). (a) Block 7, MSE = 4.5509 (b) Block 8, MSE = 11.1402 (c) Block 9, MSE = 12.6231 (d) Block 10, MSE = 6.0065. (e) Block 11, MSE = 13.7835 (f) Block 12, MSE = 8.0128.

TABLE 3.3
URBAN IMAGE VARIOGRAM MODEL PARAMETERS

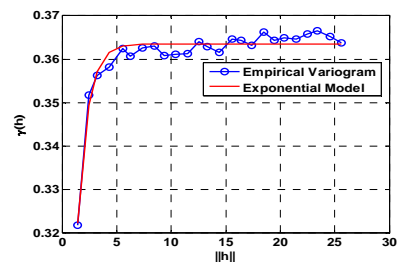
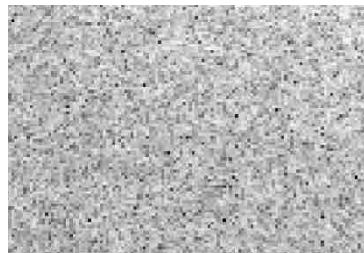
URBAN IMAGE	LOG-TRANSFORMED MAGNITUDE SPECTRA				PRECONDITIONED CONJUGATE GRADIENT UNWRAPPED PHASE SPECTRA			
	MODEL	NUGGET σ	PARTIAL SILL α	RANGE β	MODEL	NUGGET σ	PARTIAL SILL α	RANGE β
HIGH FREQUENCY BLOCKS								
BLOCK #1	Exp	0.3519	0.0121	10.0644	Gau	5.2124	35.5886	27.1156
BLOCK #2	Gau	0.3531	0.0381	75.4755	Gau	5.1938	75.1953	36.2740
BLOCK #3	Sph	0.3583	0.0679	197.7969	Gau	5.2389	40.9733	28.2459
BLOCK #4	Exp	0.3546	0.0326	34.8910	Gau	5.0000	82.1963	40.8793
BLOCK #5	Exp	0.3434	0.0225	2.6090	Gau	4.9716	93.4360	36.7180
BLOCK #6	Gau	0.3612	0.0286	42.0272	Gau	4.9786	80.7191	39.7428
MEDIUM FREQUENCY BLOCKS								
BLOCK #7	Gau	0.3606	0.1274	87.9702	Sph	1.6614	4.310e3	36.7073
BLOCK #8	Exp	0.3650	0.0271	22.6977	Gau	5.2857	4.960e2	11.3517
BLOCK #9	Exp	0.3449	0.3302	189.8808	Gau	5.4041	3.606e3	14.7781
BLOCK #10	Gau	0.3517	0.2952	88.2899	Gau	4.9790	6.210e2	20.5342
BLOCK #11	Sph	0.3737	-0.0091	7.9741	Gau	5.2371	1.956e3	40.7375
BLOCK #12	Gau	0.3550	0.0353	34.3829	Gau	5.2610	1.450e3	7.8809



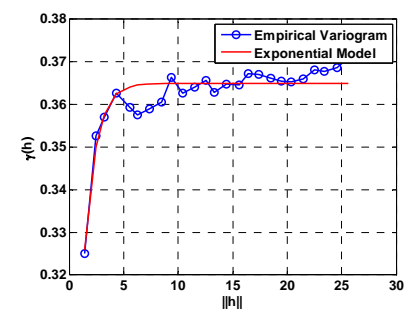
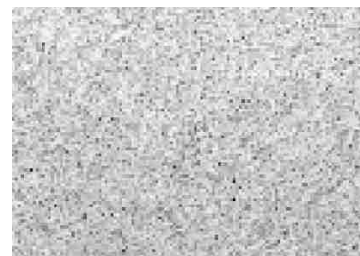
(a)



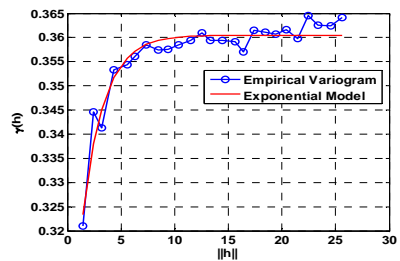
(b)



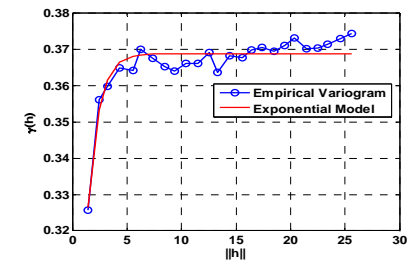
(c)



(d)

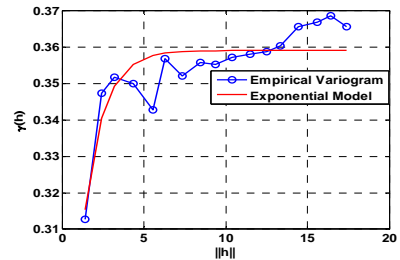
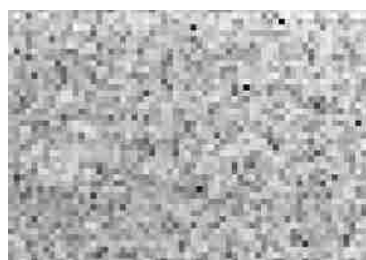


(e)

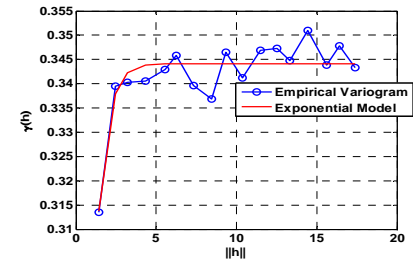


(f)

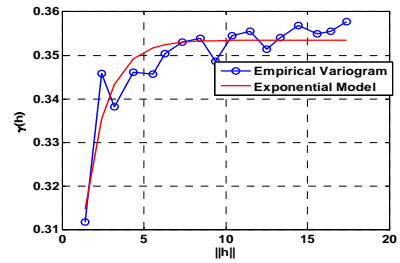
Figure 3.25: The high frequency block variogram estimates and adaptively fitted models for the log-transformed magnitude spectra of the natural image depicted in Figure 3.16(c). (a) Block 1, MSE = 6.0171e-005 (b) Block 2, MSE = 6.2416e-005 (c) Block 3, MSE = 7.9567e-005. (d) Block 4, MSE = 2.2777e-004. (e) Block 5, MSE = 1.3775e-004. (f) Block 6, MSE = 2.0030e-004.



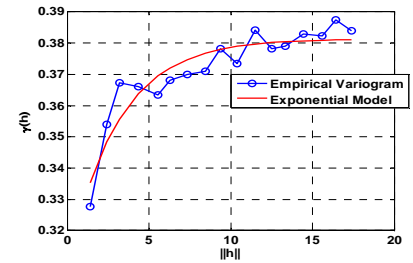
(a)



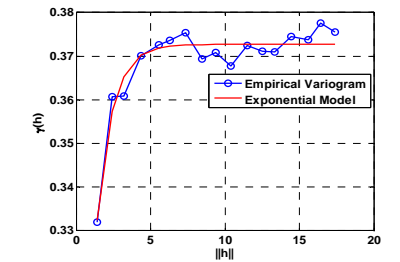
(b)



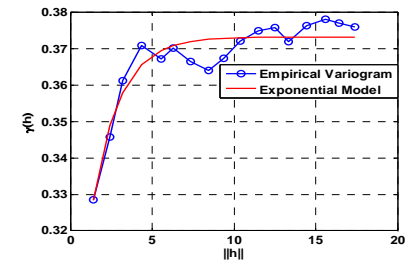
(c)



(d)



(e)



(f)

Figure 3.26: The medium frequency block variogram estimates and adaptively fitted models for the log-transformed magnitude spectra of the natural image depicted in Figure 3.16(c). (a) Block 7, MSE = 7.8661e-004 (b) Block 8, MSE = 4.5098e-004 (c) Block 9, MSE 5.6939e-004 (d) Block 10, MSE = 4.9588e-004. (e) Block 11, MSE = 2.6569e-004. (f) Block 12, MSE = 4.4269e-004.

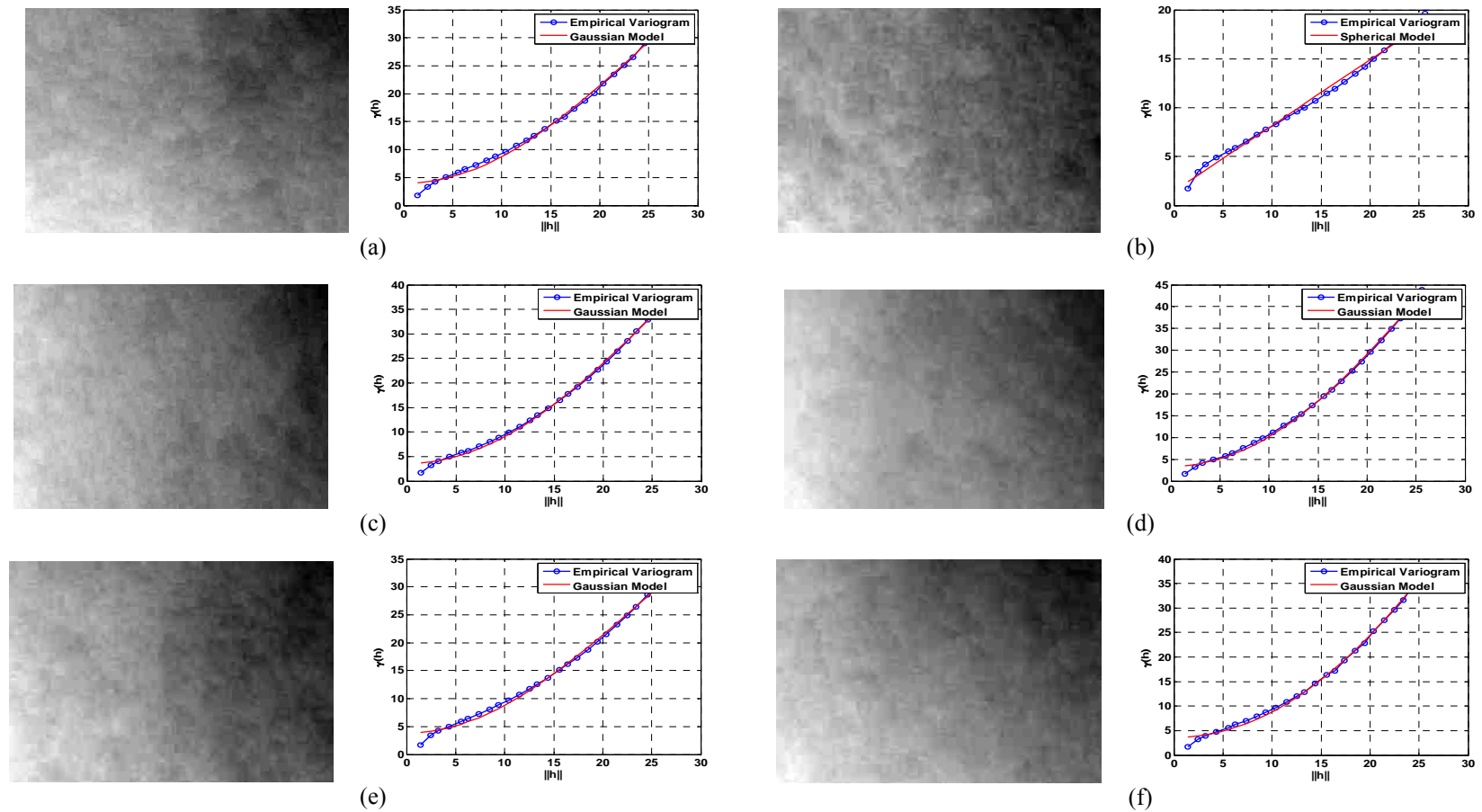


Figure 3.27: The high frequency block variogram estimates and adaptively fitted models for the unwrapped phase spectra of the natural image depicted in Figure 3.16(c). (a) Block 1, MSE = 9.7911 (b) Block 2, MSE = 4.5381 (c) Block 3, MSE = 7.0495. (d) Block 4, MSE = 5.9942. (e) Block 5, MSE = 9.2806. (f) Block 6, MSE = 7.3173.

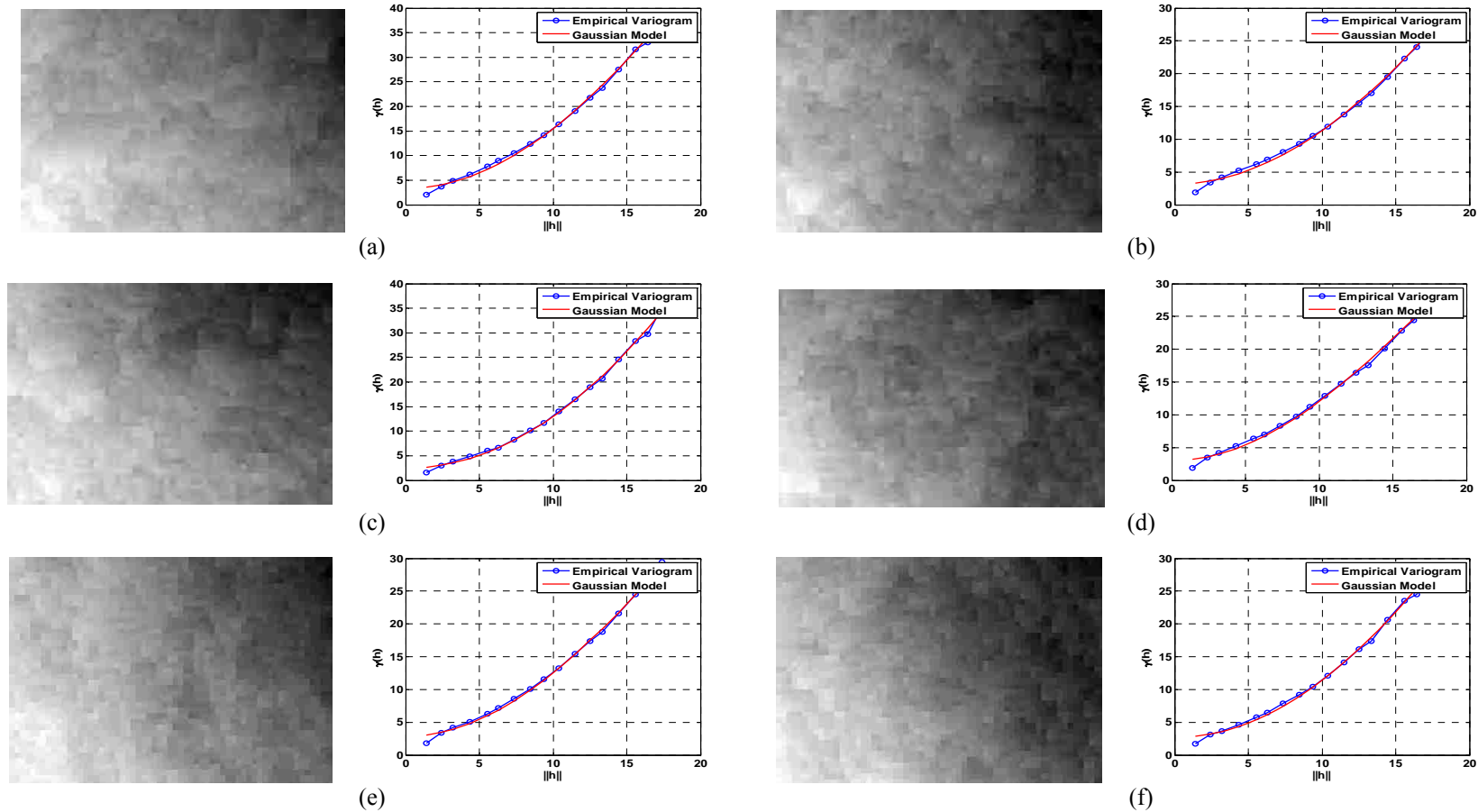


Figure 3.28: The medium frequency block variogram estimates and adaptively fitted models for the unwrapped phase spectra of the natural image depicted in Figure 3.16(c). (a) Block 7, MSE = 9.1889 (b) Block 8, MSE = 3.6291 (c) Block 9, MSE = 8.4823 (d) Block 10, MSE = 5.8084. (e) Block 11, MSE = 6.0859 (f) Block 12, MSE = 6.8156.

TABLE 3.4
NATURAL IMAGE VARIOGRAM MODEL PARAMETERS

NATURAL IMAGE	LOG-TRANSFORMED MAGNITUDE SPECTRA				FLYNN'S MINIMUM DISCONTINUITY UNWRAPPED PHASE SPECTRA			
	MODEL	NUGGET σ	PARTIAL SILL α	RANGE β	MODEL	NUGGET σ	PARTIAL SILL α	RANGE β
HIGH FREQUENCY BLOCKS								
BLOCK #1	Exp	0.1628	0.1986	0.8389	Gau	3.9231	75.9363	39.0670
BLOCK #2	Exp	0.1976	0.1643	0.8758	Sph	1.4454	3.1683e3	7.0682e3
BLOCK #3	Exp	0.1752	0.1883	0.9391	Gau	3.5527	103.9497	42.7032
BLOCK #4	Exp	0.2134	0.1515	1.0536	Gau	3.4094	178.5269	50.8369
BLOCK #5	Exp	0.2850	0.0755	2.0114	Gau	3.8578	62.4113	34.8267
BLOCK #6	Exp	0.1921	0.1767	1.0022	Gau	3.5847	1.1276e3	146.4274
MEDIUM FREQUENCY BLOCKS								
BLOCK #7	Exp	0.3185	0.0501	5.7614	Gau	3.3833	9.9424e3	290.9899
BLOCK #8	Exp	0.1930	0.1535	0.9115	Gau	3.3199	2.9957e3	195.2382
BLOCK #9	Exp	0.3072	0.0527	3.8801	Gau	1.7931	1.2738e4	336.3380
BLOCK #10	Exp	0.3180	0.0664	4.0010	Gau	3.5976	3.6167e3	213.5812
BLOCK #11	Exp	0.2427	0.1320	1.2398	Gau	3.2356	7.8627e3	298.6366
BLOCK #12	Exp	0.2914	0.0845	2.2580	Gau	2.2609	1.0624e3	343.9256

contains the magnitude spectra contained in the medium frequency blocks. Figure 3.19 and Figure 3.20 are the extensions of Figures 3.17 and 3.18 to the unwrapped phase spectrum. Table 3.2 summarizes these figures by providing model and parameters that were selected for the magnitude and phase spectra blocks.

We present the related results of the urban and natural images in the subsequent figures and tables after Table 3.2. Figures 3.21-3.24 and Table 3.3 contain the spectral model fitting results of the urban sample image in Figure 3.16(b). Figure 3.25-3.28 and Table 3.4 contain the spectral model fitting results of the natural sample image depicted in Figure 3.16(c).

In the above figures, we note that the number of variogram coefficients that were fit for the high frequency blocks was truncated to be 25, since the high frequency sample rate was one out of every eight samples. The radial lag spanning three samples in each dimension is 33.94, which is beyond the limit we have found to produce the best fits. The medium frequency blocks are fit out to a lag of 17, since the sample rate in these blocks is one out of every four samples in each dimension. These plots are a good representation of the adaptive and scalable solution our method provides. We also deviated from the use of Flynn's minimum discontinuity method in the urban image unwrapped phase. Here we used the PCG method, which demonstrated the highest median unwrapped phase reconstruction PSNR.

3.5.3. Magnitude and Phase Kriging

The results of Kriging methods are best summarized by a comparison of the individual reconstruction quality of the magnitude spectra, the individual reconstruction quality of the phase spectra. The overall comparison of the reconstructed spatial image using Fourier synthesis of the reconstructed magnitude and phase spectra is deferred to the following chapter, in which the Kriging result is compared to other spectral estimators.

Since the magnitude spectra do not require the additional processing steps introduced by phase unwrapping, we limited the comparison of the extent of the \mathbf{h} to constrain the number of semivariance values used in the model-fitting step to the magnitude spectra Kriging results. In addition, we combined this experiment with the grid search described above to compare the affect of n , the number of neighboring known samples used in the predictor. The value for n was selected for both the max-distance and max-samples parameter. For the basic Kriging parameters, we summarize our consistent observations into three points:

1. The number of data semivariance values used in the variogram model-fitting step does not have a significant impact on reconstruction performance.
2. As the number of known samples used in the Kriging estimator increases, the reconstruction quality approaches an asymptotic maximum.
3. The max-distance and max-samples Kriging parameters that govern the number of known samples used by the estimator provide differing results

at lower values for n , with the max-distance parameter outperforming the max-samples parameter. As n approaches the asymptotic PSNR limit, the performance of the two parameters is virtually equal.

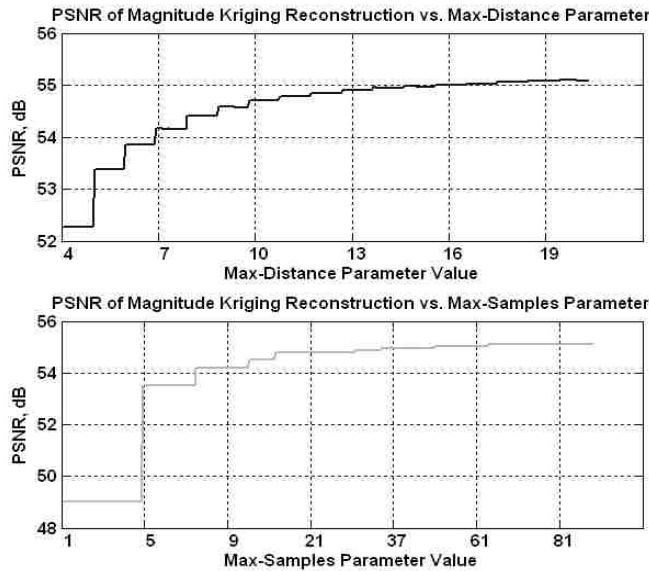
3.5.3.1 Parameter Optimization Results

Figure 3.29 provides a high frequency block example of our observations. In the example in Figure 3.29, we reduce the FFT sampling rate by 4 in each dimension. Thus in two-dimensions, we keep one out of every 16 samples.

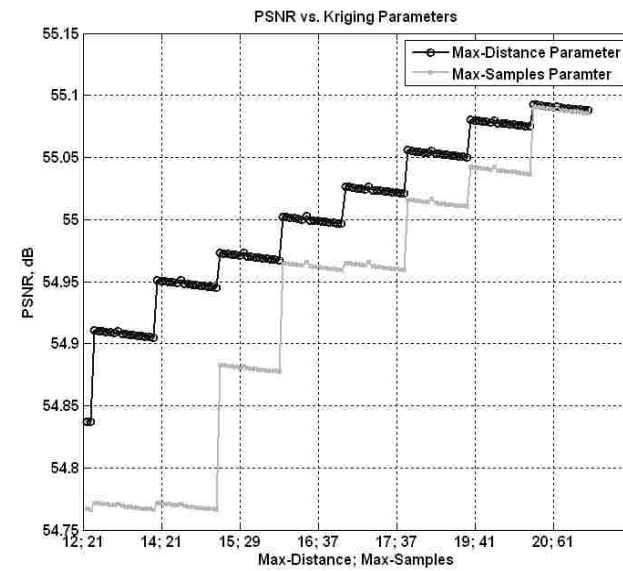
For the adaptive variogram estimation problem, we considered the following parameters: (i) the max-distance, (ii) the max-sample and (iii) the number of samples that were fitted. From our experiments, it became clear that the max-distance parameter provided better interpolation results and that these results were asymptotically, closely approximated by the max-samples parameter. We demonstrate this observation in the example of Figure 3.29.

Based on the sampling rates that were considered and the range of the empirical variogram models, we considered fitting the variogram from five to twenty samples.

The combination of these parameters led us to perform a search for the optimal estimation parameters for Kriging reconstruction on both the magnitude and unwrapped phase data, respectively. The inclusion of the \mathbf{h} parameter in this experiment results in the flat regions of the PSNR plots in Figure 3.29. The top



(a)



(b)

Fig. 3.29: Kriging parameter optimization example for the max-distance and max-samples parameters. The plots shown above compare the PSNR values of the Kriging reconstructed magnitude spectra of the spectral block labeled “8” in Figure 2. The steps present in the plots are from a result of fitting the variogram model (Gaussian, in this case) using the first five through twenty empirical semivariance values. The max-distance parameter provides a better result when a smaller number of known samples are included in the estimator. Figure 5(b) is a detailed region of Figure 5(a) and reveals that the reconstruction performance converges as the max-distance and max-samples increase. In addition, the plot shows that fitting less semivariance values results in a slightly higher reconstruction quality, although the difference is negligible ($<0.01\%$).

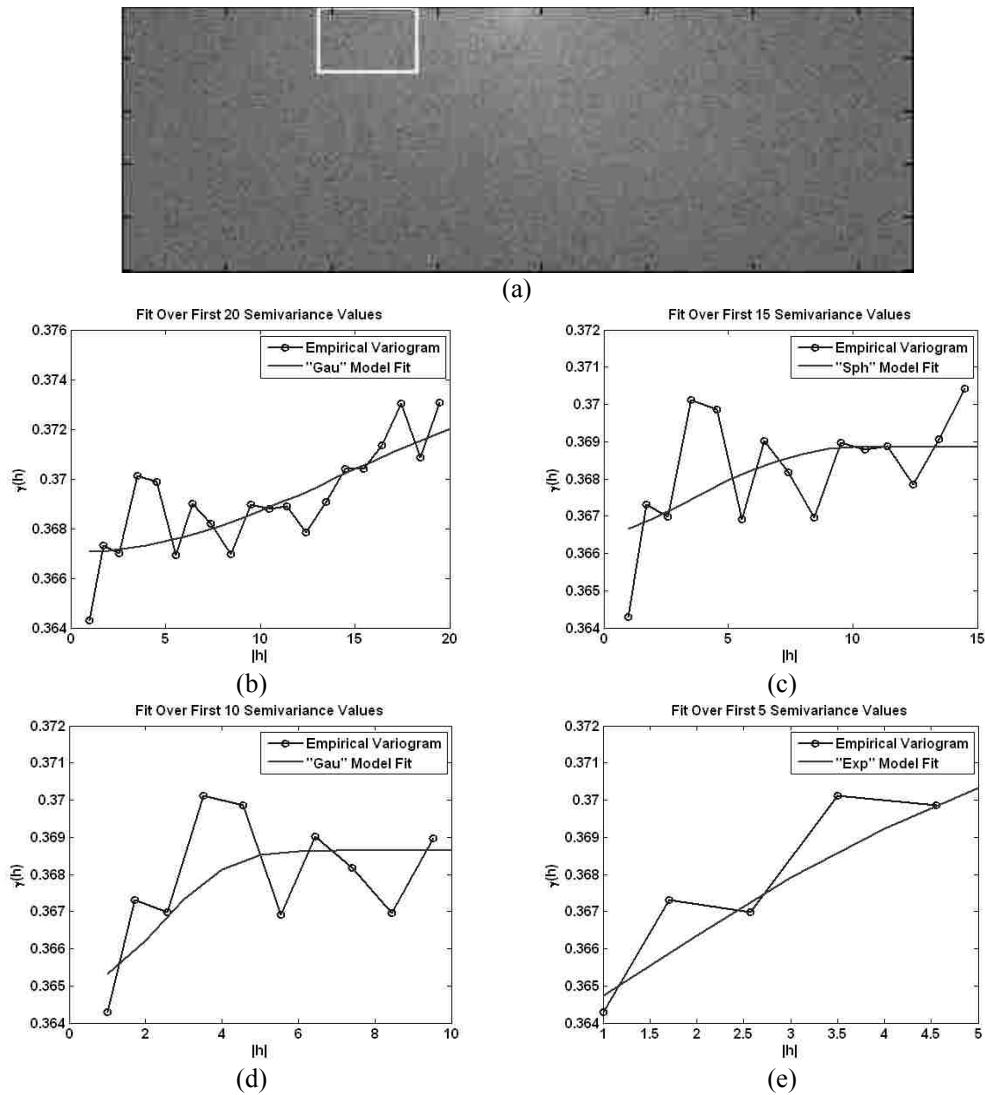


Figure 3.30: Variogram model fitting for a medium-frequency block of an urban scene. (a) lower-half of log magnitude FFT spectrum with block boundary. (b) Gaussian model fit for first 20 samples, least squares error = $3.4727e-5$. (c) Spherical model fit for first 15 samples, least squares error = $2.4805e-5$. (d) Gaussian model for the first 10 samples, least squares error = $1.4023e-5$. (e) Exponential model fit for the first 5 samples, least squares error = $2.985e-6$.

plot in Figure 3.29(a) depicts the PSNR value when max-distance is adjusted, while the bottom plot in Figure 3.29(a) depicts the PSNR value for when the max-samples parameter is adjusted. Figure 3.29(b) shows the region in which the plots asymptotically approach the limit of achievable reconstruction quality. This

search was intended to provide a comparison of the interaction between the number of semivariance values used in the model fitting step and the number of known samples, n in (11), used in the predictor. Figure 3.30 contains plots of the empirical variogram of an inner region of the magnitude spectra of an urban scene and the fitted theoretical variogram models when the number of empirical semivariance values used in the fitting procedure is altered. Figure 3.30(a) depicts the portion of the magnitude spectra that is being modeled by the variogram. Figure 3.30 (b) – 3.30 (e) show the empirical variograms and the optimal model based on fitting the first 20, 15, 10, and 5 semivariance values, respectively.

3.5.3.2 Magnitude Reconstruction Results

Table 3.5 contains non-parametric summary statistics of the high frequency block magnitude reconstruction PSNR values over all ten images. The statistics we have chosen are the minimum, first quartile, median, third quartile, and maximum PSNR values of all reconstructions at the three high frequency sample reduction rates and the three medium frequency sample reduction rates. We include the same statistics for the cubic spline, nearest neighbor and linear interpolation algorithms as a comparison. The mean PSNR values of the magnitude reconstructions for the high frequency blocks are shown in Figure 3.31(a). Table 3.6 and Figure 3.31(b) show the analogous statistics for the medium frequency blocks. These results were obtained by fitting the minimum number of semivariance values up to either a radius of 25 for sample rates greater than 8; or

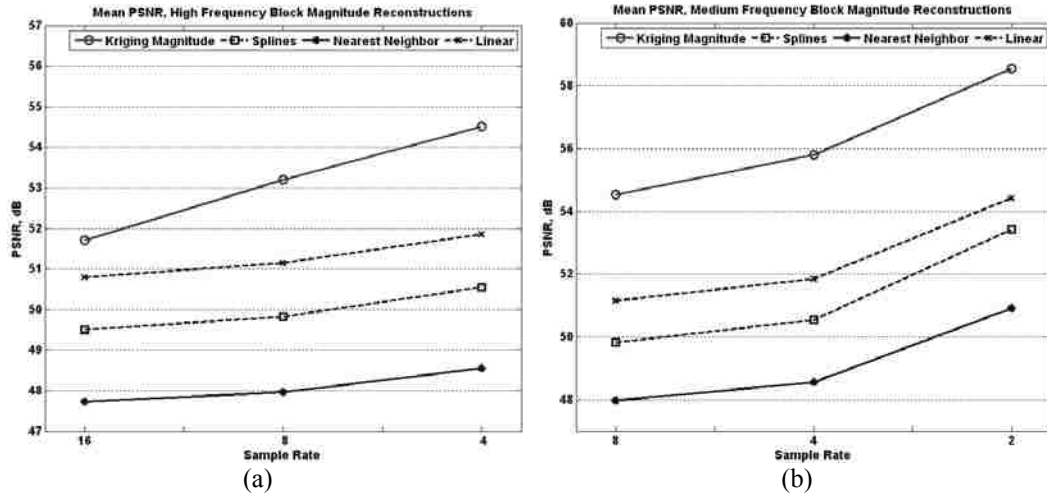


Figure 3.31: High frequency and low frequency block magnitude reconstruction comparison of Kriging, splines, Nearest Neighbor and linear interpolators. (a) The mean PSNR of the high frequency block reconstructions. (b) The mean PSNR of the medium frequency block reconstructions.

TABLE 3.5 – HIGH FREQUENCY BLOCK RECONSTRUCTION PSNR, MAGNITUDE

Statistic	Sample Reduction Rate	Min	1 st Quartile	Median	3 rd Quartile	Max
Kriging	16x	44.9250	50.2470	52.1638	53.3509	55.0397
	8x	46.7038	51.6753	53.7825	54.7097	56.7870
	4x	46.7038	53.4854	55.1832	55.7543	57.7496
Spline	16x	43.5644	47.8149	50.0642	51.1259	53.3444
	8x	45.8346	48.8110	50.8671	51.2437	52.9376
	4x	45.8207	50.0140	50.3334	51.6328	53.4519
Nearest	16x	41.7850	45.9392	48.2797	49.5575	51.3172
	8x	43.7956	46.6477	48.2320	49.4008	51.0215
	4x	43.8480	47.8078	48.8800	49.5472	51.3849
Linear	16x	45.7441	49.1677	51.5058	52.3860	53.7980
	8x	46.7093	50.2485	51.4099	52.5443	54.2441
	4x	47.2029	51.2519	52.2092	52.9615	54.7953

TABLE 3.6 – MEDIUM FREQUENCY BLOCK RECONSTRUCTION PSNR, MAGNITUDE

	Statistic Sample Reduction Rate	Min	1 st Quartile	Median	3 rd Quartile	Max
Kriging	8x	50.2653	53.6246	54.7165	55.6315	57.4620
	4x	51.0898	54.8056	56.0640	56.8262	58.4081
	2x	54.8583	57.6402	58.6109	59.6397	61.1700
Spline	8x	45.8346	48.8110	50.0642	51.2437	52.9376
	4x	45.8207	50.0140	50.8671	51.6328	53.4519
	2x	48.8627	52.7184	53.7884	54.5474	56.4266
Nearest	8x	43.7956	46.6477	48.2320	49.4008	51.0215
	4x	43.8480	47.8078	48.8800	49.5472	53.8498
	2x	46.3429	50.0563	51.2612	52.0159	51.3849
Linear	8x	46.7093	50.2485	51.4099	52.5443	54.2441
	4x	47.2029	51.2519	52.2092	52.9615	54.7953
	2x	49.8943	53.7752	54.7845	55.5544	57.4253

the radial distance equal to three times the sampling rate for sample rates less than 8. The Kriging steps were performed using the derived max-samples from a max-distance parameter value of 25 for the high frequency blocks and 20 for the medium frequency blocks. Experiments on both the high and medium frequency blocks revealed that these are the optimal parameter values. Going beyond 25 neighbors does not gain significant improvement in reconstructions. The additional computational cost is not worth an unperceivable gain in reconstruction quality.

Focusing on the unwrapped phase spectra interpolation, we compared the summary statistics of the Kriging interpolated frequency blocks using each phase unwrapping method. While we have noted that the phase unwrapping methods

TABLE 3.7 – HIGH FREQUENCY BLOCK RECONSTRUCTION PSNR, UNWRAPPED PHASE

Statistic Sample Reduction Rate	Min	1 st Quartile	Median	3 rd Quartile	Max	
	Flynn	8x	13.42	41.62	52.94	62.50
	4x	18.23	47.99	62.14	70.20	93.44
	2x	21.96	55.14	67.54	76.04	112.14
Goldstein	8x	8.90	27.25	38.25	43.45	56.94
	4x	24.21	40.27	46.18	50.36	64.89
	2x	21.06	46.79	51.96	54.80	63.99
Quality	8x	11.36	41.70	46.94	55.22	77.20
	4x	11.36	44.63	54.30	60.61	86.05
	2x	16.50	45.12	56.49	62.32	80.48
WMG	8x	11.36	46.30	57.50	65.38	86.12
	4x	16.28	52.27	60.71	71.65	94.32
	2x	20.82	58.12	65.94	76.82	101.02
PCG	8x	8.41	49.33	65.96	71.84	85.21
	4x	11.70	52.27	68.50	75.03	89.14
	2x	11.71	51.61	69.61	77.87	94.48

TABLE 3.8 – MEDIUM FREQUENCY BLOCK RECONSTRUCTION PSNR, UNWRAPPED PHASE

Statistic Sample Reduction Rate	Min	1 st Quartile	Median	3 rd Quartile	Max	
	Flynn	4x	14.93	42.88	50.10	57.93
	2x	29.63	50.60	59.22	64.67	103.66
Gold	4x	12.24	32.51	38.87	44.10	52.68
	2x	27.57	44.28	46.68	50.91	61.29
Qualit	4x	14.01	40.19	52.29	57.34	72.91
	2x	29.90	44.33	53.04	61.69	76.67
WMG	4x	4.99	52.27	49.97	71.65	77.52
	2x	11.60	58.12	55.57	76.82	89.93
PCG	4x	14.97	44.40	55.97	63.29	79.14
	2x	26.12	49.07	61.30	70.10	84.33

differ in computational complexity, we intend to explore the difference between the methods in terms of effectiveness in adaptive model selection and, subsequent spectral estimation via Kriging. Table 3.7 and Table 3.8 contain the summary statistics for each unwrapping method for the high and medium frequency blocks, respectively.

The first noticeable characteristic of these results is the large amount of variability between these results. We want to consider the median values as an indicator of which unwrapping method is better suited for Kriging based on the PSNR of the unwrapped frequency block reconstructions. According to the tables, the Preconditioned Conjugate Gradient method shows the highest median PSNR values. The overall best reconstructions (based on the maximum achieved PSNR) were achieved using Flynn's Minimum Discontinuity method. Both of these results are indicated by the bold font in Table 3.7 and Table 3.8. Both methods show similar statistical values and our choice again is motivated by the amount of unwrapping performed by each method.

As noted previously, Flynn's Minimum Discontinuity method produces the globally minimal phase unwrapping solution. Errors within an unwrapped surface that is represented by a smaller range of phase values will produce a smaller absolute error when the phase is re-wrapped by the inverse FFT operation than an unwrapped surface with greater range in the unwrapped phase values. The PCG and Flynn method are both iterative as they solve optimization

problems. From our tables, it is clear that the other path following algorithms, although very fast, do not achieve acceptable results. Our assumption is that computational cost is not as much a factor as overall reconstruction performance. To provide a summary of the above results, we present the mean PSNR values of each of all phase unwrapping methods in Figure 3.32.

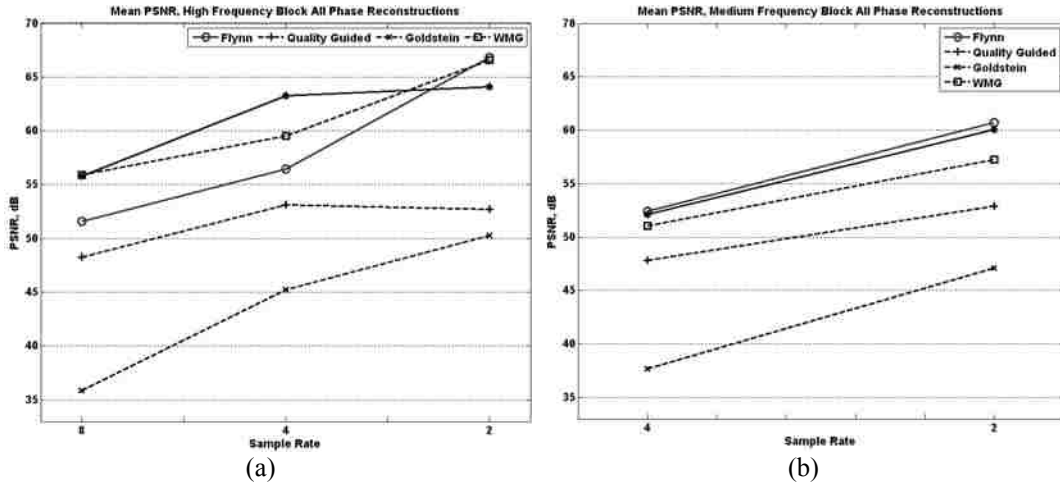


Figure 3.32: High frequency and low frequency block unwrapped phase reconstruction using Kriging to compare unwrapping methods. (a) The mean PSNR of the high frequency block reconstructions. (b) The mean PSNR of the medium frequency block reconstructions.

In Figure 3.32(b), we see that the mean PSNR values for the medium frequency reconstructions were the best when modeling the phase that has been unwrapped with Flynn’s Minimum Discontinuity method. This result further supports our assumption, as the medium frequency components of the discrete FFT require more accurate reconstruction. As mentioned previously, reconstruction errors over the medium frequency blocks will be more noticeable in the spatial domain image.

3.6. Discussion

In this section, we briefly review some of the key concepts that were developed in this chapter and provide further analysis on the results that were obtained. Because this chapter focused on the development of statistical spectral models and the interpolation of the magnitude and phase of the images in our data set, the results and subsequent analysis of the spatial image reconstruction summarized in the reconstruction procedure diagram in Figure 3.10 are deferred to the next chapter.

Here, we want to return to the three main concepts of spectral model selection and the application of the optimal models used in Kriging reconstruction. Recall that three points must be considered when defining the statistical model for each spectral block. These are whether or not isotropy is assumed, the size of the variogram that is to be estimated in each block, and how much of the empirical variogram is to be used in calculating the best model.

3.6.1 Remarks on Spectral Statistical Models

We conclude that the isotropic model assumption is valid for the medium frequency blocks on the log-transformed magnitude spectra. This is a key result, as the isotropic model will result in a larger number of spectral samples from which to calculate the method of moments estimate in (2). Following the law of large numbers, the greater the number of samples used in the estimate, the more accurately the variogram estimate becomes. If we were required to work under

an anisotropic model, the number of points for each directional variogram would be reduced by a factor equal to the number of individual directions considered.

In spectral blocks where the isotropic model assumption violates the actual data, as was the case for both the high and medium frequency blocks of the unwrapped phase, we still argue for the use of isotropic variogram estimation and models. We showed that the isotropic model is a general model that is approximately equal to the mean of the directional variograms (refer to Figure 3.15). The use of an isotropic model also reduces the complexity of the model in each spectral block. Thus, we accept a generalized model over the high frequency blocks in magnitude, when the data exhibits some anisotropy, to reduce the complexity of the solution. Again, we note that when our assumptions violate the spectral covariance in this way, the generalization is isolated to a bounded region of the spectrum due to the scalability built into the design of our spectral sampling procedure.

Our results revealed that it is not necessary, and even advantageous, to fit a reduced number of lag values when calculating the variogram model. Further exploration into the effects of reducing the size of the variogram estimates on reconstruction is something that we have considered to be outside of the scope of this work. We did find that all variogram coefficients should not be fitted, because the models that are calculated from the full empirical variogram tend to over-fit the coefficients at large lag values. It is more beneficial for the model to

fit the variogram estimate at the smaller lag values, as the samples that are the closest neighbors to the sample being estimated have are more influential than known samples further away.

Our experiments revealed that a single empirical variogram can be represented by a number of unique model parameters based on the extent of the lag that is being fit. Each model shown in Figure 3.30 is the best fit for the number of lag values being considered. This supports our claim that an adaptive model, based on the spectral sampling rate, is feasible and results in a more accurate predictor.

3.6.2 Magnitude and Phase Kriging Remarks

A key contribution we have presented is the fact that we have found the limit of the number of samples that produce the optimal reconstructed spectral blocks. Going beyond the number of samples contained in a radius of 25 in the high frequency and 20 in the medium frequency blocks does not result in a noticeable improvement in the Kriging process. Based on the range parameters presented in Tables 3.2, 3.3, and 3.4, we realize that the theoretical range that best fits the empirical variogram does not provide a reasonable value for the number of samples to include in the estimator. Since our process is adaptive and seeks the optimal model for each frequency block being tested, we expected and observed large variation in the range parameter of the model. Since these values are used to

mathematically define the model applied in Kriging, we rely on the consistencies revealed by our search for the optimal number of prediction points for each block.

Clearly, the magnitude reconstruction using Kriging outperforms the competing interpolation methods we tested. When comparing the behavior of the magnitude and phase reconstructions, we notice a considerable difference between the Kriging reconstructions of the magnitude spectra and the unwrapped phase spectra. We also see the potential for magnitude spectra extrapolation of samples that are restricted to the low frequency regions based on the overall performance of the magnitude spectra reconstructions here. We defer this experiment to Chapter 4, as its effects will be best noted by examining the spatial image from the extrapolated magnitude and full phase spectra. The phase spectra exhibit much more variability in reconstruction performance. We note the large range between the minimum and maximum values for all phase unwrapping methods in Tables 3.7 and 3.8 compared to the tight bounds of the Kriging results in Tables 3.5 and 3.6.

Inaccurate phase reconstructions will result in spatial domain reconstruction artifacts and a poor overall reconstruction. We take this into consideration when selecting the amount of phase sampling to be included. A discussion on our decision making process for sample rate selection is deferred to Chapter 4, which examines the input image reconstruction for various magnitude and phase rates.

We show two spectral reconstructions in Figure 3.33. The phase reconstruction for the first image was selected because it resulted in the best phase reconstruction using the 4x/2x sample rate of all images in our data set. The

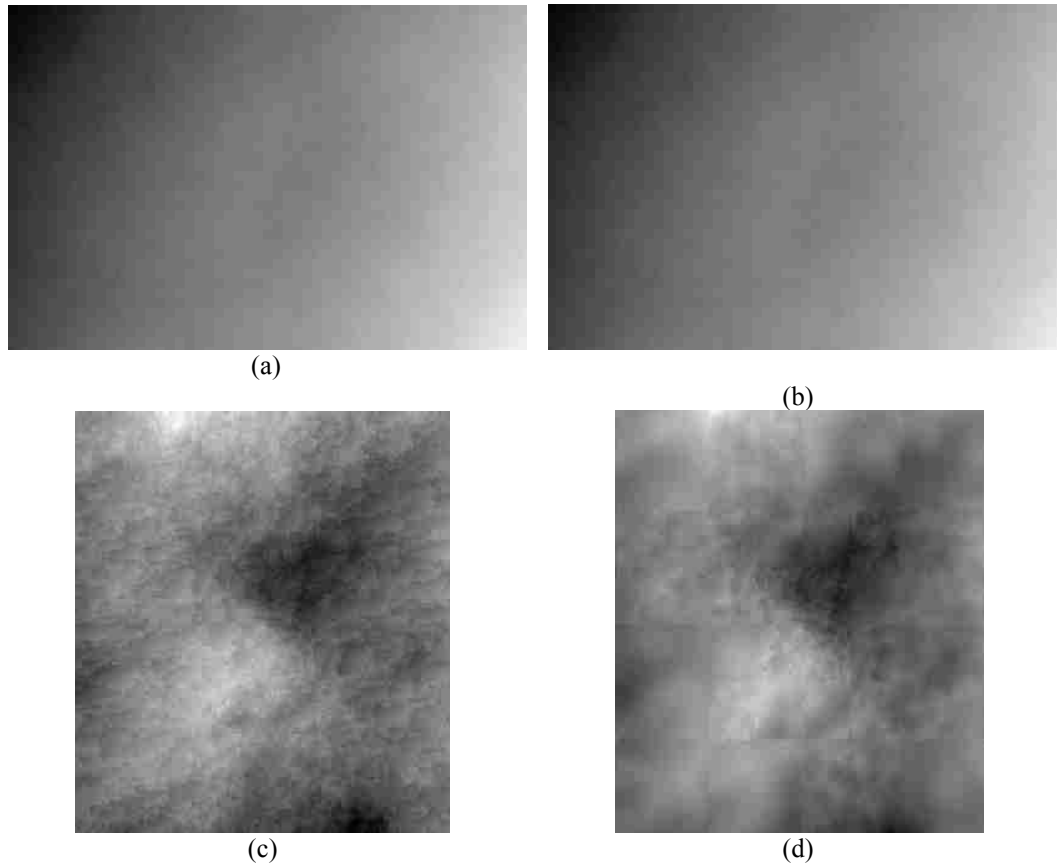


Figure 3.33: Example of best and worst phase reconstructions. (a) Original unwrapped phase spectra for rural image in Figure 3.1(c). (b) Kriging reconstruction of (a). (c) Original unwrapped phase spectra for natural image in Figure 3.4(b). (d) Kriging reconstruction of (c).

average phase PSNR for the high frequency blocks in Figure 3.33(b) is 88.40 dB and the medium frequency blocks is 87.42 dB.

The phase reconstruction for the second image was selected because it resulted in the worst phase reconstruction using the 4x/2x sample rate. The

average phase PSNR for the high frequency blocks in Figure 3.33(d) is 42.31 dB and the medium frequency blocks is 44.52 dB. This example shows the wide variability in unwrapped phase reconstruction performance, and leads us to focus on reconstructions of Fourier spectra where the magnitude spectra is sampled and reconstructed and the phase spectra is left undisturbed. These experiments are developed and presented in Chapter 4.

3.7. Conclusion

In this chapter, we have developed a spectral covariance modeling technique and Fourier spectra reconstruction method by extending geostatistical theory to the discrete Fourier domain. We found that the problem of spectral modeling is well suited for scalability, in which magnitude and phase sampling is performed in a manner that the frequency content with more energy (which, for naturally occurring images, is located at the center of the spectrum) is given greater importance in governing the spatial image quality. Therefore, we proposed combinations of sampling rates that are applied separately to the high and medium frequency blocks generated by the dyadic partitioning of the spectral data.

By bounding the discrete Fourier domain into blocks, we were able to localize the problem of determining the spectral covariance model over small, intrinsically stationary regions. Theoretical variogram models were then adaptively calculated for each block variogram estimate, ensuring the best model for each high and medium frequency block sampling rate. Using the optimal

models, we were able to interpolate the removed magnitude and phase spectrum. Using the large number of individual reconstructions from ten images and twelve frequency blocks per image, we were able to explore the effect of the number of samples (which is proportional to the block sample rate) used in the Kriging estimate, and discovered that a relationship exists between the number of samples used in Kriging and the reconstruction accuracy. We discovered that an asymptotic limit exists for both the high and medium frequency blocks. This discovery revealed that including samples beyond the limit will only increase the computational cost of model fitting and estimation.

The large number of Kriged phase blocks allowed for a quantitative comparison between phase unwrapping methods. The path following phase unwrapping algorithms resulted in unique phase surfaces. We have shown that some unwrapping methods resulted in phase data that is better suited for our spectral statistical modeling approach. It was shown that both the Flynn's Minimal Discontinuity and both minimum norm methods (Weighted Multi-Grid and Preconditioned Conjugate Gradient) resulted in much better block reconstructions. Our decision to implement Flynn's method was due to the fact that it generally results in a smaller range in the unwrapped values, from which localized interpolation values will result in a smaller absolute error when the inverse 2D FFT is applied to the reconstructed magnitude and phase spectra.

Overall, our adaptive approach yielded spectral reconstructions that were between 2 and 4 dB higher than a 2D linear interpolator, 3 to 6 dB higher than cubic spline interpolation, and 4 to 9 dB higher than nearest-neighbor interpolation. The ordinary Kriging model we present is well suited for the difficult task of discrete Fourier spectrum estimation. While more complicated Kriging algorithms do exist, the computational complexity they require increases the attractiveness of our simple, general models.

References

- [1] N. A. Cressie. *Statistics for Spatial Data*. John Wiley and Sons, New York, revised edition, 1993.
- [2] K. Cheng, H. Yeh, and C. Tsai, "An anisotropic modeling approach for remote sensing image rectification," *Remote sensing and the environment*, vol. 73, pp. 46-54, 2000.
- [3] P. S. Kanaroglou, N. A. Soulakellis, and N. I. Sifakis, "Improvement of satellite derived pollution maps with the use of a geostatistical interpolation method," *Journal of Geographic Systems*, vol. 4, pp. 193:208, 2002.
- [4] R. E. Rossi, J. L. Dungan, and L. R. Beck, "Kriging in the shadows: geostatistical interpolation for remote sensing," *Remote sensing and the environment*, vol. 49, pp. 32-40, 1994.
- [5] A. Ferretti, C. Prati, and F. Rocca, "Permanent scatterers in SAR interferometry," *IEEE Trans. On Geoscience and Remote Sensing*, vol. 39, pp. 8-20, 2001.
- [6] T. Blaschke, "Object-based contextual image classification build on image segmentation," In *IEEE workshop on advances in techniques for analysis of remotely sensed data*, pp. 113-119, October, 2004.
- [7] J. Djamdji and A. Bijaoui., "Disparity analysis: a wavelet transform approach," *IEEE Trans. On Geoscience and Remote Sensing*, vol. 33, pp. 67-76.

- [8] T. Pham and M. Wagner, "Image restoration by fuzzy convex ordinary Kriging," In *Proceedings of the international conference on image processing*, vol. 1, pp. 113-116, September 2000.
- [9] W. Oh and B. Lindquist, "Image thresholding by indicator Kriging," *IEEE Trans. on Pattern Analysis and Machine Intelligence*, vol. 21, pp. 590-602, 1999.
- [10] S. Chandra, M. Petron, and R. Piroddi, "Texture interpolation by ordinary Kriging," In *Pattern recognition and image analysis*, vol. 3523, pp. 183-190, 2005.
- [11] J. R. Carr, "Spectral and textural classification of single and multiple band digital images," *Computer and Geosciences*, vol. 22, pp. 1063-1079, 1990.
- [12] E. Decenciere, C. Fouquet, and F. Meyer, "Applications of Kriging to image sequence coding," *Signal processing: image communication*, vol. 13, pp 227-249, 1998.
- [13] B. Grinstead, A. Koschan, and M. A. Abidi, "Geometry refinement of 3D surfaces using Kriging," In *Proceedings of the Third International Symposium on 3D Data Processing, Visualization, and Transmission (3DPVT'06)*, pp. 719-726, 2006.
- [14] A. Panagiotopoulou and V. Anastassopoulos, "Super-resolution image reconstruction employing Kriging interpolation technique," *14th International Workshop on Systems, Signals, and Image Processing*, pp. 144-147, June 2007.
- [15] Purdue University Laboratory for Applications of Remote Sensing. (2006). Image sv010813_ARC_F106_1m. Retrieved, April 27, 2009 from ITD Spectral Visions Multispectral Image Database. Web site: http://www.lars.purdue.edu/home/image_data/spectral_vision_data.html.
- [16] Purdue University Laboratory for Applications of Remote Sensing. (2006). Image sv010706_FPS_south_1m. Retrieved January 16, 2009 from ITD Spectral Visions Multispectral Image Database. Web site: http://www.lars.purdue.edu/home/image_data/spectral_vision_data.html.

- [17] NASA/GSFC/METI/ERSDAC/JAROS, and U.S/Japan ASTER Team. (2001). London, England. Retrieved January 16, 2009 from ASTER Project Image Database. Website: <http://asterweb.jpl.nasa.gov/gallery/images/london-final.jpg>.
- [18] NASA/GSFC/LaRC/JPL, MISR Team. (2000). The Grand Canyon. Retrieved March 3, 2009 from MISR Image Gallery. Website: <http://photojournal.jpl.nasa.gov/catalog/PIA03402>.
- [19] NASA/GSFC/METI/ERSDAC/JAROS, and U.S/Japan ASTER Team. (2001). Erebus Ice Tongue. Retrieved March 7, 2009 from ASTER Project Image Database. Website: <http://asterweb.jpl.nasa.gov/gallery-detail.asp?name=Erebus>
- [20] L. C. Graham, "Synthetic interferometer radar for topographic mapping," *Proceedings of the IEEE*, vol. 62, pp.763-768, 1974.
- [21] R. M. Goldstein, H. A. Zebker, and C. L. Werner, "Satellite radar interferometry: Two-dimensional phase unwrapping," *Radio Science*, vol. 23, pp. 713-720, 1988.
- [22] H. A. Zebker and R. M. Goldstein, "Topographic mapping from interferometric synthetic aperture radar observations," *Journal of Geophysical Research*, vol. 91, pp 4993-4999, 1986.
- [23] F. K. Li and R. M. Goldstein, "Studies of multibaseline spaceborne interferometric synthetic aperture radars," *IEEE Transactions of Geoscience and Remote Sensing*, vol. 28, pp. 88-97, 1990.
- [24] A. L. Gray and P. J. Farris-Manning, "Repeat-pass interferometry with airborne synthetic aperture radar," *IEEE Transactions of Geoscience and Remote Sensing*, vol. 31, pp. 180-191, 1993.
- [25] P. H. Eichel, D. C. Ghiglia, C. V. Jackowatz, Jr., P. A. Thompson, and D. E. Wahl, "Spotlight SAR interferometry for terrain elevation mapping and interferometric change detection," Sandia National Laboratories Report, SAND93-2072, 1993.

- [26] D. Massonnet, M. Rossi, C. Carmona, F. Adragna, G. Peltzer, K. Feigl, and T. Rabaute, "The displacement field of Landers earthquake mapped by radar interferometry," *Nature*, vol. 364, pp. 138-142, 1993.
- [27] D. C. Ghiglia and P. H. Eichel, "High-resolution synthetic aperture radar interferometry: Technology for precise terrain elevation mapping," *DSP and Multimedia Technology*, vol. 3, 1994.
- [28] D. C. Ghiglia and M. D. Pritt, *Two-Dimensional Phase Unwrapping: Theory, Algorithms, and Software*, John Wiley and Sons, New York, 1998.
- [29] M. W. Roth, "Phase unwrapping for interferometric SAR by the least-error path". Johns Hopkins University Applied Physics Lab Technical Report, Laurel, MD, 1995.
- [30] T. J. Flynn, "Two-dimensional phase unwrapping with minimum weighted discontinuity," *Journal of the Optical Society of America A*, vol. 14, pp. 2692-2701, 1997.
- [31] G. H. Golub and C. F. Van Loan, "Iterative method for linear systems," *Matrix Computations*, 2nd Ed. Johns Hopkins University Press, Baltimore, MD, 1990.
- [32] L. Rabiner, "The chirp z-transform algorithm – A lesson in serendipity," *IEEE Signal Processing Magazine*, March 2004, pp. 118-119.
- [33] C. de Boor, *A practical guide to splines*, revised edition, Springer-Verlag, New York, 2001.

Chapter 4

Fourier Spectra Reconstructions of Satellite Imagery Part II: Reconstructions from Statistical Models and Compressive Sensing.

4.1 Introduction

Two different approaches to spectral reconstruction have been presented thus far, and while the end goal of each method is similar, the means to the end used by each approach differ considerably. Image reconstruction from under sampled data in a sparse (e.g. Fourier) basis is the primary motivation of compressive sensing theory. Spatial data estimation using Kriging, on the other hand, is based on spatial statistical modeling known spatial data points and using semivariance models to provide the best weighted linear predictor for unknown values.

Clearly, Kriging relies on statistical models of the known data to provide an interpolated result, while the compressed sensing approach can be viewed as a black-box (from the perspective of the Fourier domain samples), brute-force optimization approach to finding the interpolated result. Using the following

comparisons, we want to explore whether there is any significant image reconstruction benefit from the statistical modeling method required by Kriging. In other words, we want to understand which Fourier spectra reconstruction method gives the best reconstruction perceptually by using the structural similarity and in the mean-squared error sense by calculating the peak signal to noise ratio. The answer will become clear as we approach the same data set with the spectral estimation techniques we developed using CS and Kriging and compare the results based on these image quality metrics.

The quality of image reconstruction is typically quantified by the peak signal to noise ratio (PSNR) and provides a measure of the amount of noise introduced to the image from the reconstruction method used. The PSNR is defined as:

$$PSNR = 20 * \log_{10} \left(\frac{\max(I)}{\sqrt{MSE}} \right) \quad (1)$$

MSE is the mean square error result between the reconstruction result K_c and the original image:

$$MSE = \frac{1}{mn} \sum_{i=0}^{m-1} \sum_{j=0}^{n-1} \|I(i, j) - K(i, j)\|^2 . \quad (2)$$

While the PSNR metric provides objective measure of reconstructed image quality, the subjective assessment of an observer is tends to play a large part in determining the performance of an image compression result. The human vision system (HSV) can be assumed to be highly adapted in extracting structural information from a scene and can judge the effectiveness of compression or

“correctness” of the reconstructed image. It is this characteristic of the HSV that the Structural Similarity Index (SSIM) attempts to quantify [1].

SSIM attempts to provide an image quality metric based on the fact that natural images are highly structured. In other words, there is high dependence between pixels that are in close proximity to one another because they are likely to be part of the same object, or structure, in the image. A key difference between SSIM and other metrics of structural degradation is that SSIM assumes that the structural information in an image is independent of scene illumination. The SSIM index can be defined as a function of three comparison operators on the original and distorted (reconstructed) image: a luminance comparison $l(I, K)$, a contrast comparison $c(I, K)$, and a structural comparison component $s(I, K)$:

$$SSIM(I, K) = f(l(I, K), c(I, K), s(I, K)) \quad (3)$$

In what follows, we will provide mathematical definitions of each component. First, we note that to ensure that the component definitions need to allow for (i) SSIM index adheres to the conditions of symmetry, (ii) boundedness (the SSIM index is less than or equal to 1), and (iii) produces a unique maximum. The luminance comparison is defined as:

$$l(I, K) = \frac{2\mu_I\mu_K + C_1}{\mu_I^2 + \mu_K^2 + C_1} \quad (4)$$

where C_1 is a constant that is included to ensure stability if $\mu_I^2 + \mu_K^2$ is very close to zero. Typically, C_1 is selected based on a small percentage of the dynamic range of the image being reconstructed. Also, μ_I is the mean value of the original

image and μ_K is the mean value of the distorted image. The contrast comparison is similar to (4), but instead of being based on the mean intensity value of the image, it is based on σ_I and σ_K , the unbiased discrete estimate of the standard deviation of the original and distorted images, respectively:

$$c(I, K) = \frac{2\sigma_I\sigma_K + C_2}{\sigma_I^2 + \sigma_K^2 + C_2}. \quad (5)$$

The structure comparison is defined as:

$$s(I, K) = \frac{\sigma_{IK} + C_3}{\sigma_I\sigma_K + C_3} \quad (6)$$

and is combined with (4) and (5) to provide a formal definition for the SSIM index between the original image, I , and the compressed image, K :

$$SSIM(I, K) = [l(I, K)]^\alpha \cdot [c(I, K)]^\beta \cdot [s(I, K)]^\gamma, \quad (7)$$

where $\alpha > 0$, $\beta > 0$, and $\gamma > 0$ are parameters that allow for emphasis on specific comparison measurements. We applied the mean SSIM index with $\alpha = 1$, $\beta = 1$, and $\gamma = 1$, along with the default values for the constants in each term as defined by mean-opinion scores from large data sets described in [1].

We selected a new sub image data set, taking care to provide significant variation of image scenes in the satellite data set, to provide us with an indication of general performance of both spectral estimation approaches. Since the sampling method utilized in each approach differ, care was taken to ensure that the number of samples retained for both methods was equal when reconstructions were compared. In other words, the number of samples from the high, medium,

and low frequency blocks used in the Kriging reconstruction will define the number of samples used in the compressive sensing sampling geometries.

A secondary image quality comparison will be presented in which select images from the original satellite data set are used instead of sub images of a fixed size. Since the original satellite image data set contains arbitrarily shaped samples, additional pre and post processing steps are required to reshape the Fourier spectrum so both dimensions are an equal power of two in length for the CS algorithm.

Finally, this chapter will conclude with a comparison of the computational cost of the two methods by examining processing time between the two reconstruction approaches and an approximation of the total number of multiplications and additions for a given image required by each technique. While newer CS reconstruction algorithms have been developed to increase the efficiency in solving problems minimizing the ℓ_1 norm, such as [2], we can still expect that the latest compressive sensing solutions would still require significantly more computational resources than Kriging. A summary of the computational complexity in terms of function evaluations and matrix inversions of each method will also be presented.

4.2 Sub Image Data Set Selection

The image subset we chose to use in this experiment is made up of nine satellite sub images and a single brain slice. This comparison data set selected from the satellite data set was chosen in a way that each scene type (rural, urban, and natural) was represented by three sub images. Therefore, the comparison image set totals ten images. These images, along with the magnitude of the Fourier spectrum (after a logarithmic transformation to compress the dynamic range for better visual representation) are depicted in Figure 4.1. Three sub images of the rural scene class are shown in Figure 4.1(a)-(c). Figure 4.1(d)-(f) are the three sub images of the urban scene class. Figure 4.1(g)-(i) depict the three sub images that represent the natural scene class. Figure 4.1(j) is the brain slice that was included in the comparison study.

The nine sub images selected from the satellite data set are 128×128 pixels. The height and width of the images used in the fMRI study were constrained to of size 2^N using zero padding to allow the use of the WaveLab software package [3]. The brain scan in Figure 4.1(j) was zero-padded to be 64×64 pixels.

The compression rates explored on each of the sub images are consistent with the experiments performed in Chapter 3. Compressive sensing sampling

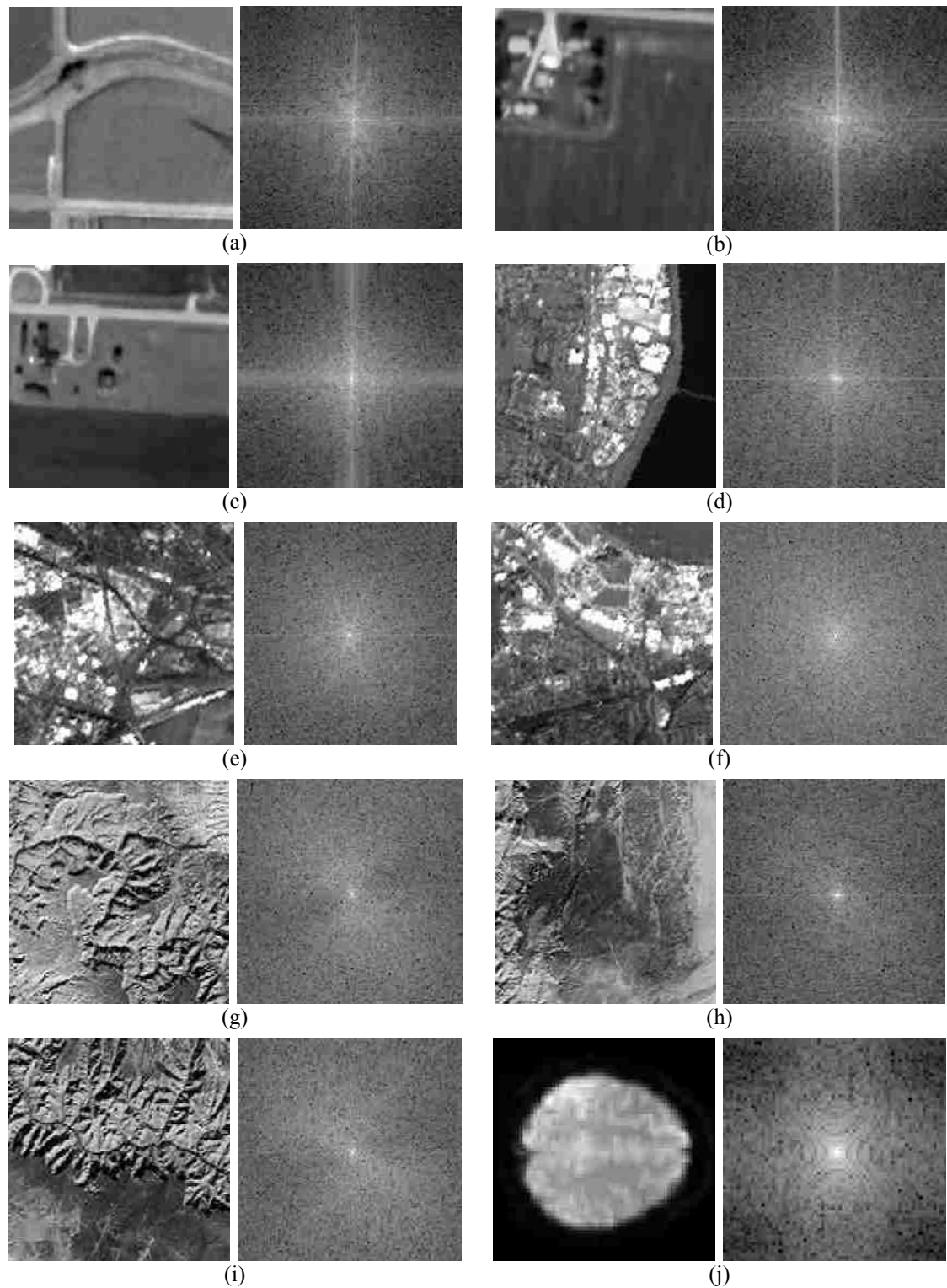


Figure 4.1: Images that comprise our sub image data set. The subsequent magnitude spectrum of the Fourier domain for each image is also shown. (a)-(c) Rural sub images. (d)-(f) Urban sub images (g)-(i) Natural sub images. Figure (j) Single brain slice image.

geometries were generated of the Spiral Low Pass (SLP) class in Chapter 2, as well as a modified version of the Random Sampling on a PDF (RSP) class. In this case, we defined the sampling probability distribution function along both image dimensions instead of just along the phase-encoded (image width) dimension. This new class was motivated by the success of the SLP class in the fMRI reconstruction experiments, and this referred to as the RSP2 class. The

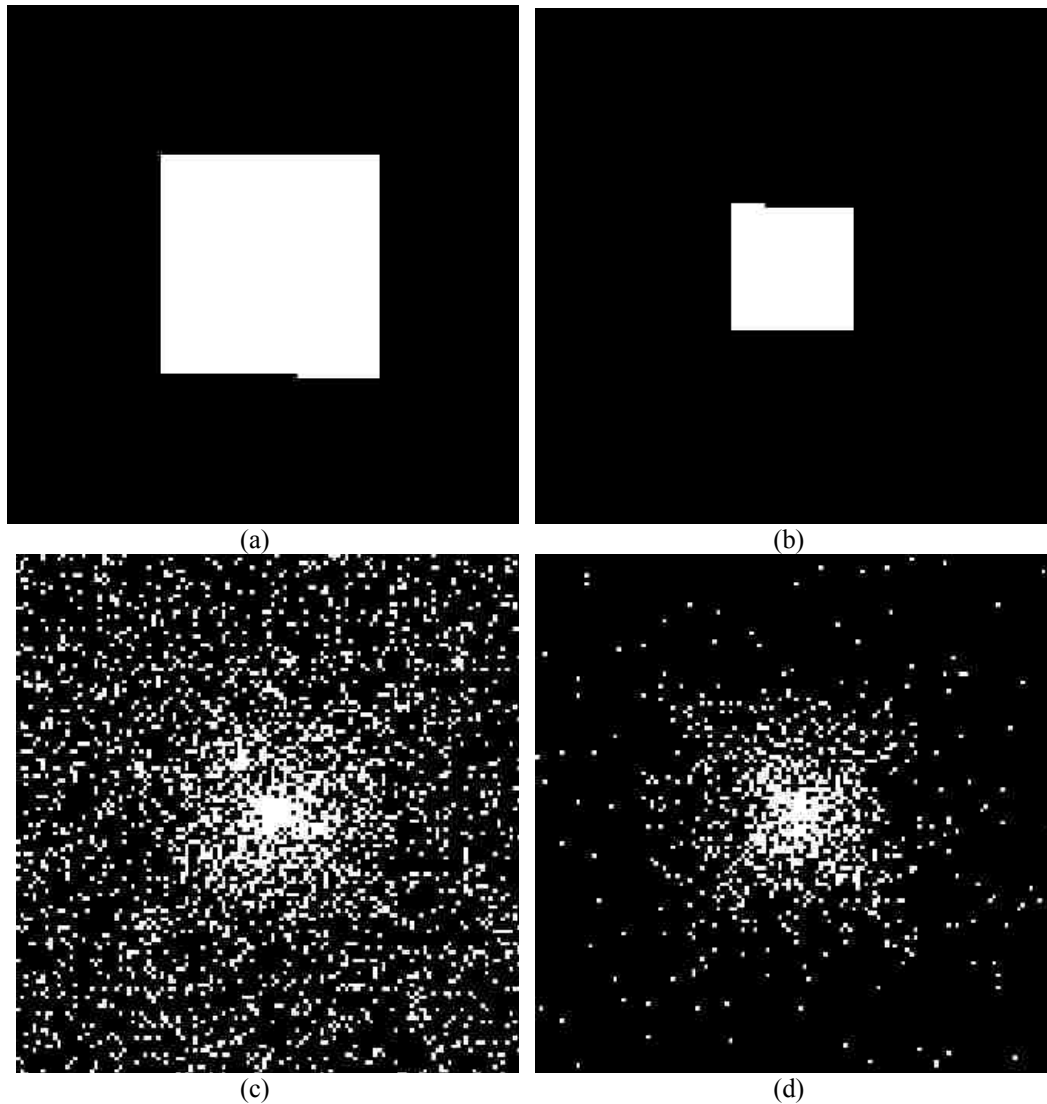


Figure 4.2: (a) SLP using 18.75% of the data samples. (b) SLP using 9.91% of the data samples. (c) RSP2 using 18.75% of the data samples. (d) RSP2 using 9.91% of the data samples.

random nature of the RSP2 sampling geometry class is supported by the compressive sensing theory of maximizing incoherence between the transformation basis and the reconstructed sample space. Two sampling geometries of different rates for the SLP class and the new RSP2 class are shown in Figure 4.2. We differentiated the Kriging reconstructions into two approaches: interpolation of the magnitude spectra only and interpolation of both the magnitude and the phase spectra. Due to the small size of the images in the comparison data set, the sampling reduction rates was limited to 4, 8, 16, and 24 samples in the high frequency spectral blocks and 2, 4, 8, and 12 for the medium frequency spectral blocks as shown in Figure 3.5 in Section 3.3.1. These rates were used for the magnitude spectra interpolation. Combining the first three magnitude rates with high frequency sampling reduction rates of 8, 4, and 2 and medium frequency reduction rates of 4, 2, and 0 for the phase spectra, we were able to compare nine (eight unique) data reduction rates when Kriging both magnitude and phase. In terms of sample reduction, we compared sampling rates of 18.75%, 11.97%, 10.17%, and 9.91% when estimating magnitude spectra only, and reconstructing using all of the phase spectral samples. When performing Kriging on both magnitude and phase, we compared sampling rates of 17.26%, 15.57%, 15.12%, 9.38%, 7.68%, 7.23%, 5.99%, and 5.54%.

For comparing full size images, we selected one image of each of the three satellite image types. The images we selected are significantly larger than those in the sub image data set above: the largest is 351×501 pixels, while the smallest

we have chosen in 236×401 pixels. The larger image sizes in the full comparisons allowed us to explore several sampling reduction rates for both the medium and the high frequency spectral blocks. We increased the high frequency spectral block reduction rate from 24 to 32 and 64 times and the medium frequency spectral block reduction rate from 12 to 16 and 32 times.

4.3 Comparison of Reconstructed Image Quality

4.3.1 Kriged Magnitude Spectra and CS Reconstruction Comparison

Our intention in this comparison study was three-fold. First, we desired to know whether or not the optimized compressive sensing objective function provides a general solution that can be applied to other image types, such as aerial images. Second, we used this opportunity to quickly analyze the positive or detrimental effects of phase spectra interpolation using Kriging. This is an important point to consider, as estimating the phase spectra comes at an additional computational cost in the form of phase unwrapping, which may be considerable when one considers the straight-forward approach of applying Ordinary Kriging to the magnitude data. This must be taken into consideration, especially when phase interpolation does not achieve a substantial reduction in samples beyond magnitude interpolation by itself. And, of course, the third motivation of this comparison was already mentioned in the introduction and holds considerable significance. If our Kriging model outperforms compressive sensing then a new

approach to spectral and, in turn, image reconstruction paradigm has been developed using elegant statistical models that result in a simple solution from a linear system of equations.

Beginning with the more conservative and simple Kriging implementation, we compared the image reconstruction metrics when interpolation the magnitude spectra at Fourier sampling rates 18.75%, 11.97%, 10.17%, and 9.91%. Comparable SLP and RSP2 compressive sensing sampling geometries were generated at these rates. Summary statistics for the PSNR and the mean SSIM index values for this comparison shown in Table 4.1 through Table 4.4. The statistical measurements we chose were the non-parametric minimum, 1st quartile, median, 3rd quartile, and maximum.

From Tables 4.1, 4.2, 4.3, and 4.4, it is clear that Kriging interpolation of the limited samples of the magnitude spectra significantly outperforms the CS reconstructions. Figure 4.3 depicts the mean PSNR and mean SSIM index for each method. We also included the mean zero-filling reconstructions using the CS sampling geometries. Here, the zero-filled PSNR and SSIM values were slightly (1-2 dB) higher for the zero filled result than the CS result when using the SLP sampling geometry for the urban image class. This indicates that the optimization of the CS Wavelet coefficients did not produce the appropriate results, since our search for the optimal CS model parameters starts with the zero-

TABLE 4.1
SUMMARY STATISTICS OF PSNR AND SSIM FOR 18.75% EFFECTIVE SAMPLING RATE
(MAGNITUDE SAMPLING RATE IS 9.375%)

Reconstruction Method	PSNR					SSIM				
	Min	25%	Median	75%	Max	Min	25%	Median	75%	Max
Kriging (Mag)	52.71 dB	58.80 dB	64.45 dB	81.31 dB	88.98 dB	0.8181	0.8285	0.8835	0.9086	0.9632
Opt CS, SLP Class	41.62 dB	46.20 dB	52.27 dB	72.98 dB	86.41 dB	0.6316	0.6612	0.7887	0.8661	0.9756
Opt CS, RSP2 Class	38.04 dB	42.67 dB	50.20 dB	61.68 dB	74.97 dB	0.4169	0.4859	0.5959	0.7230	0.8807

TABLE 4.2
SUMMARY STATISTICS OF PSNR AND SSIM FOR 11.97% EFFECTIVE SAMPLING RATE
(MAGNITUDE SAMPLING RATE IS 5.985%)

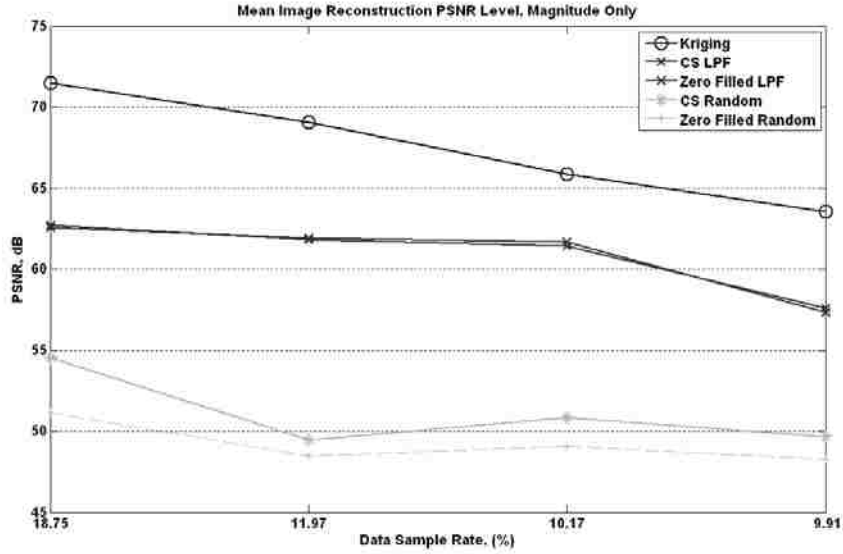
Reconstruction Method	PSNR					SSIM				
	Min	25%	Median	75%	Max	Min	25%	Median	75%	Max
Kriging (Mag)	52.71 dB	56.94 dB	63.13 dB	78.30 dB	86.48 dB	0.8060	0.8138	0.8569	0.8961	0.9509
Opt CS, SLP Class	39.12 dB	45.00 dB	50.83 dB	69.83 dB	80.43 dB	0.5065	0.5779	0.7107	0.8194	0.9586
Opt CS, RSP2 Class	36.06 dB	41.92 dB	46.85 dB	51.94 dB	62.26 dB	0.3983	0.4265	0.5636	0.6389	0.8806

TABLE 4.3
SUMMARY STATISTICS OF PSNR AND SSIM FOR 10.17% MAGNITUDE SAMPLING RATE
(MAGNITUDE SAMPLING RATE IS 5.085%)

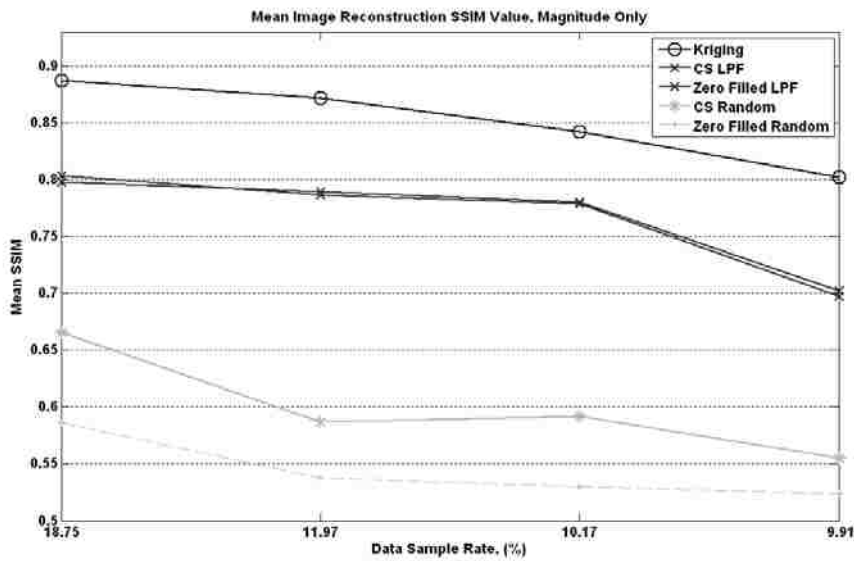
Reconstruction Method	PSNR					SSIM				
	Min	25%	Median	75%	Max	Min	25%	Median	75%	Max
Kriging (Mag)	47.47 dB	49.07 dB	59.38 dB	68.25 dB	83.39 dB	0.7263	0.7490	0.8302	0.8689	0.9388
Opt CS, SLP Class	38.48 dB	43.85 dB	49.79 dB	67.99 dB	77.82 dB	0.4675	0.5328	0.6777	0.8016	0.9487
Opt CS, RSP2 Class	36.14 dB	39.79 dB	49.63 dB	57.57 dB	64.63 dB	0.3502	0.4714	0.5950	0.6250	0.8915

TABLE 4.4
SUMMARY STATISTICS OF PSNR AND SSIM FOR 9.91% MAGNITUDE SAMPLING RATES
(MAGNITUDE SAMPLING RATE IS 4.955%)

Reconstruction Method	PSNR					SSIM				
	Min	25%	Median	75%	Max	Min	25%	Median	75%	Max
Kriging (Mag)	44.33 dB	44.81 dB	57.00 dB	64.53 dB	79.00 dB	0.6795	0.7109	0.7890	0.8425	0.9198
Opt CS, SLP Class	38.37 dB	43.54 dB	49.68 dB	68.10 dB	77.70 dB	0.4642	0.5299	0.6720	0.7908	0.9497
Opt CS, RSP2 Class	35.96 dB	40.24 dB	45.97 dB	56.70 dB	60.83 dB	0.0224	0.3170	0.4822	0.5681	0.8364



(a)



(b)

Figure 4.3: The mean PSNR and mean SSIM values for magnitude sample rates. (a) Mean PSNR for all sub images. (b) Mean SSIM index for all sub images. We used magnitude Kriging and the associated sample rates for the SLP and RPS2 CS sampling geometries. The mean values from zero-filling the CS sampling geometries reconstructions are also included in these

filling and attempts to improve it. However, in the defense of the original code from Stanford, it is important to note this starting point worked in nearly all cases, despite that fact that it is clearly an extreme case. The CS result when using the

RSP2 sampling geometries was consistently better than the zero filled result for the RSP2 sampling geometries.

Figures 4.4 – 4.8 contain a comparison of the reconstructed sub images from each class that resulted in the greatest combined SSIM and PSNR improvement using Kriging over the CS SLP method at a given sampling rate. Figure 4.4 shows the original and reconstructions of the second rural sub image from 11.97% of the Fourier samples. In this example, the PSNR values were 85.32dB for the Kriging reconstruction, 79.07 dB for the CS SLP reconstruction, and 48.62 dB for the CS RSP2 reconstruction. Visual assessment of this result supports the result that the Kriging reconstruction is better, even though the mean SSIM index value for magnitude interpolation for Kriging was 0.9373 compared to 0.9527 for the CS SLP reconstruction. The smooth regions of the image, representing uniform vegetation (grass, wheat, etc.) and roads, were more accurately reconstructed using the SLP compressive sensing sampling method. Referring to Figure 4.1(c), one can quickly see that the spectral energy is concentrated near the center of the Fourier spectrum. Since these samples are retained by the SLP mask, the analogous spatial domain pixels are better reconstructed (note the ringing effects of interpolating portions of the low frequency content in the spectral domain with Kriging). Conversely, the magnitude Kriging interpolation results depict much better reconstruction of the finer details of the image, such as the structures in the upper left portion of the image. Figure 4.9(a) and (b) contains the SSIM maps of the reconstructions

shown in Figure 4.4(b) and (c). From these maps, it is clear that the low pass

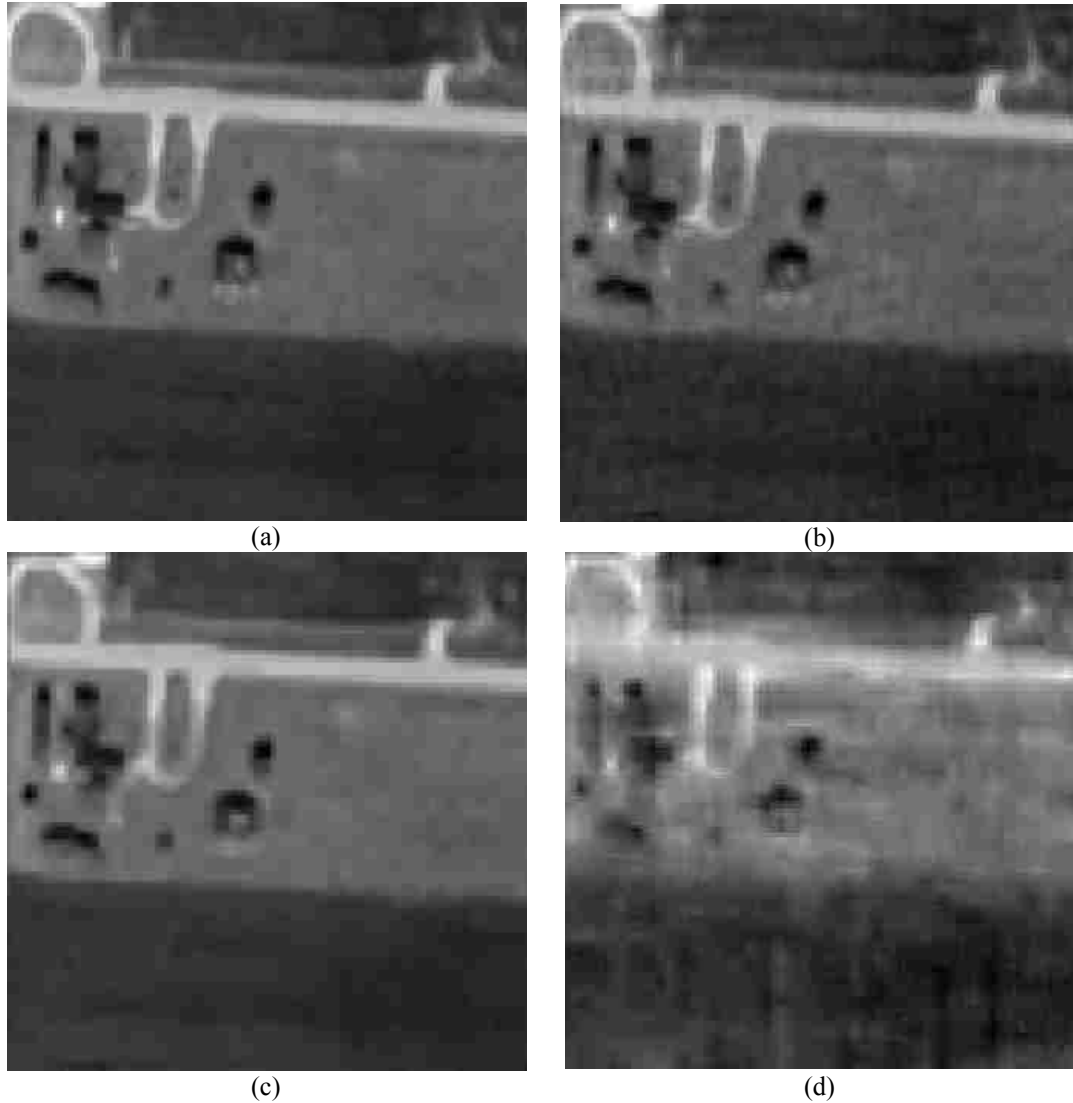


Figure 4.4: Comparative example for a rural sub scene reconstruction using 11.97% of the original samples. (a) Original image, (b) Kriging magnitude reconstruction (85.32 dB/SSIM=0.9373), (c) Optimal CS reconstruction using SLP reconstruction (79.07 dB/SSIM=0.9527), (d) Optimal CS reconstruction using RSP2 sampling geometry (48.65 dB/SSIM=0.6923).

sampling geometry boosted the reconstruction in terms of structural similarity on an image with many piecewise constant regions.

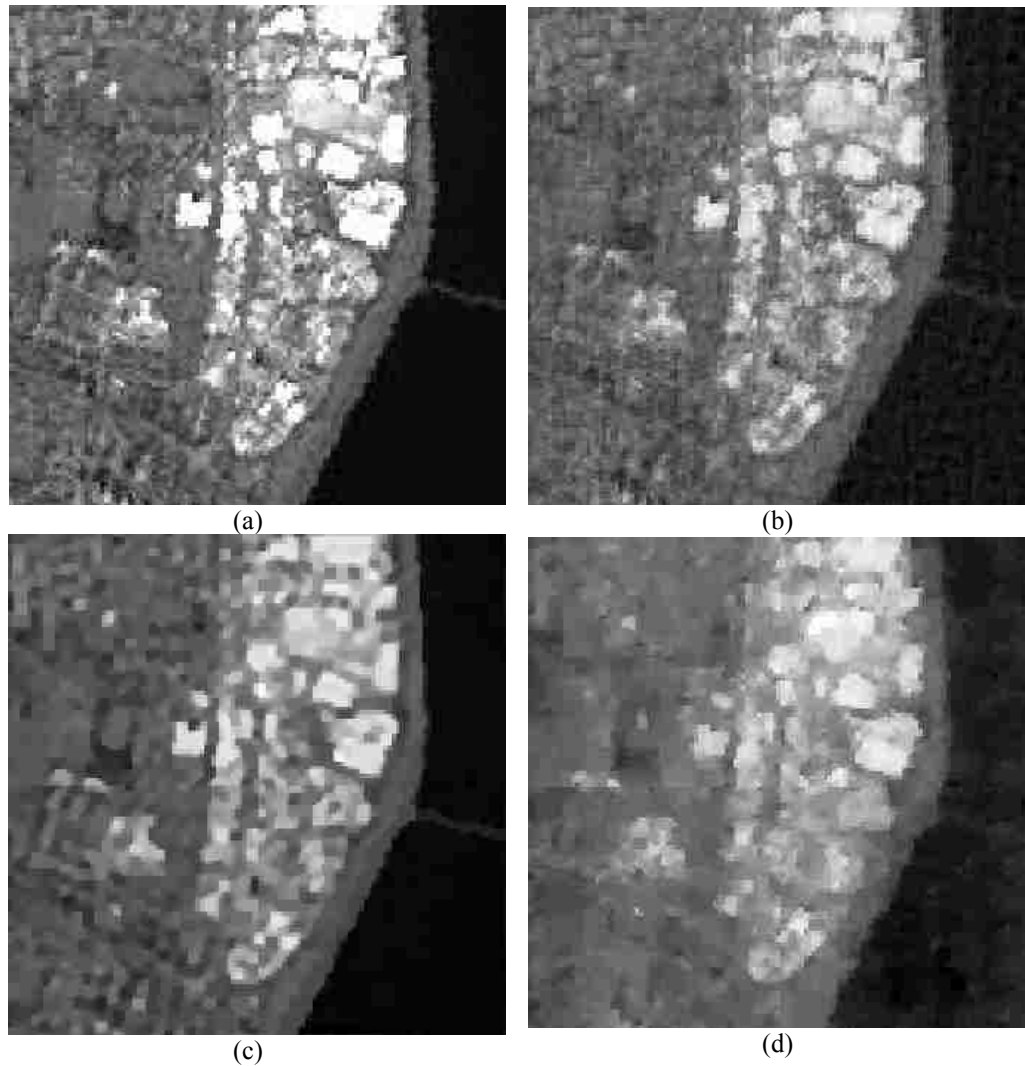


Figure 4.5: Comparative example for an urban sub scene reconstruction using 18.75% of the original samples. (a) Original image, (b) Kriging magnitude reconstruction (65.26 dB/SSIM=0.7263), (c) Optimal CS reconstruction using SLP reconstruction (50.06 dB/SSIM=0.7877), (d) Optimal CS reconstruction using RSP2 sampling geometry (50.21 dB/SSIM= 0.6398).

While the rural figures contained many smooth (piecewise constant) regions, the urban images represent the other extreme where many spatial characteristics of the image are governed by high frequencies in the Fourier domain. Figure 4.5 contains the results of the first urban image reconstructed from 18.75% of the spectral samples. The PSNR values calculated from these

reconstructions were 65.26 dB, 50.06 dB, and 50.28 dB for the Kriging, CS SLP and CS RSP2 reconstruction methods. The urban images, due to their characteristic of having more high frequency content, exhibited better reconstructions from interpolation of high frequency spectral points. This is also supported by the fact that random CS sampling geometry, which does sample from high frequency regions, outperformed the SLP CS sampling geometry. The

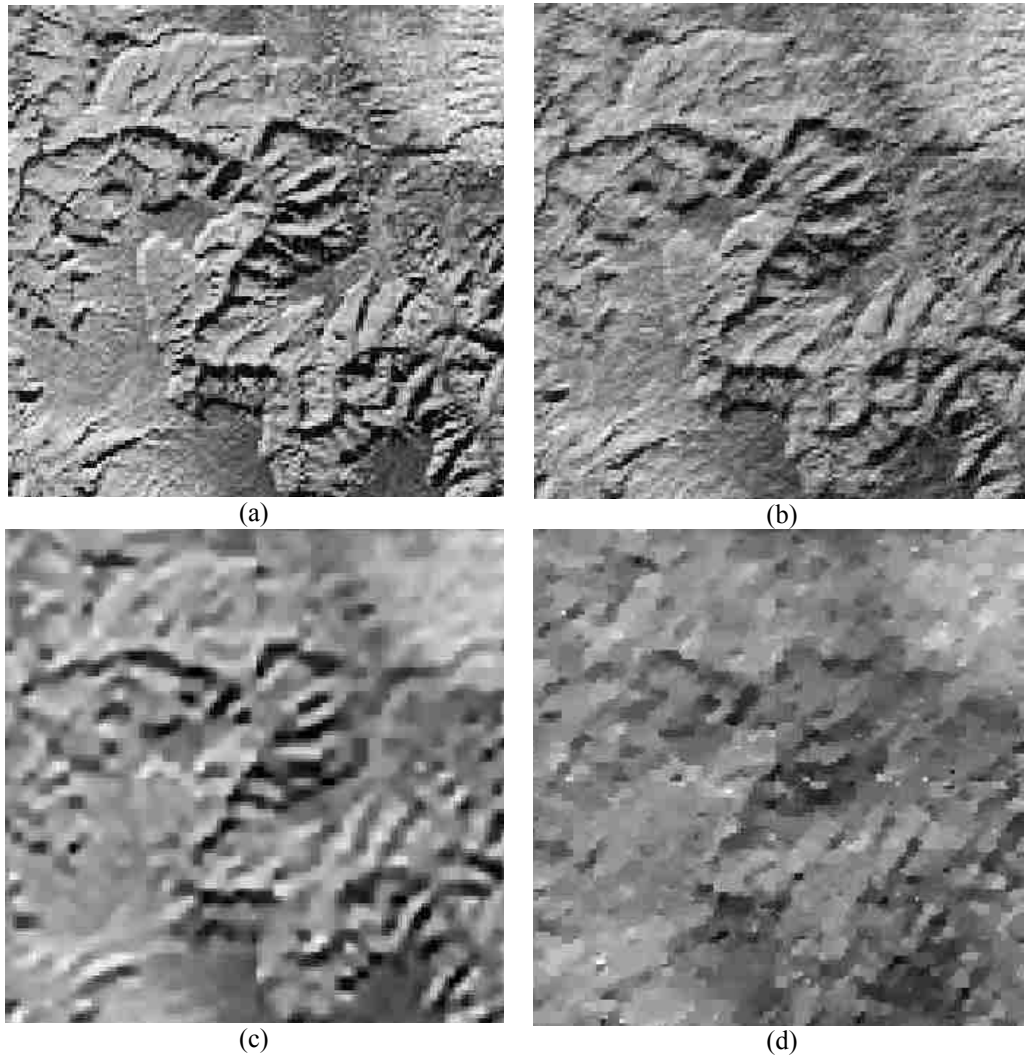


Figure 4.6: Comparative example for a natural sub scene reconstruction using 11.97% of the original samples. (a) Original image, (b) Kriging magnitude reconstruction (50.90 dB/SSIM=0.8540), (c) Optimal CS reconstruction using SLP reconstruction (39.13dB/SSIM=0.5065), (d) Optimal CS reconstruction using RSP2 sampling geometry (36.06 dB/SSIM=0.3513).

CS reconstructions, from a visual grading perspective, tend to be highly quantized, and small details in the image are completely lost, even though the SLP CS reconstruction resulted in a mean SSIM value of 0.7877. Included in Figure 4.9(c) and (d) are the SSIM index maps for the Kriging and CS SLP reconstruction for the urban sub image sample.

The natural sub images are unique in that they contain characteristics of both the rural (piecewise constant regions) and urban (small structures, highly textured regions) image scenes. Interestingly, the results in Figure 4.6 reveal that the CS reconstructions were of very low quality compared to the Kriging result. Figure 4.6 contains the comparison of reconstructed images using 11.97% of the spectral samples. These reconstructions resulted in PSNR values of 62.31 dB, 49.23 dB, and 46.86 dB using the Kriging, SLP CS, and RSP2 CS methods, respectively. The compressive sensing reconstructions are good examples as to why the SSIM index is a good additional indicator for reconstruction quality, as visual assessment reveals that neither of the reconstructions is of acceptable quality. Not only are the images overly smoothed, but considerable reconstruction artifacts are also present. The SLP geometry results in vertical and horizontal artifacts along the major axes of the reconstructed image, while the RSP2 geometry results in erroneous pixels that are not consistent with neighboring pixels. The SSIM results for these images do indicate that these images are significantly worse than the examples shown in Figures 4.4 and 4.5, as the difference in SSIM index for the SLP CS reconstruction of the urban sub

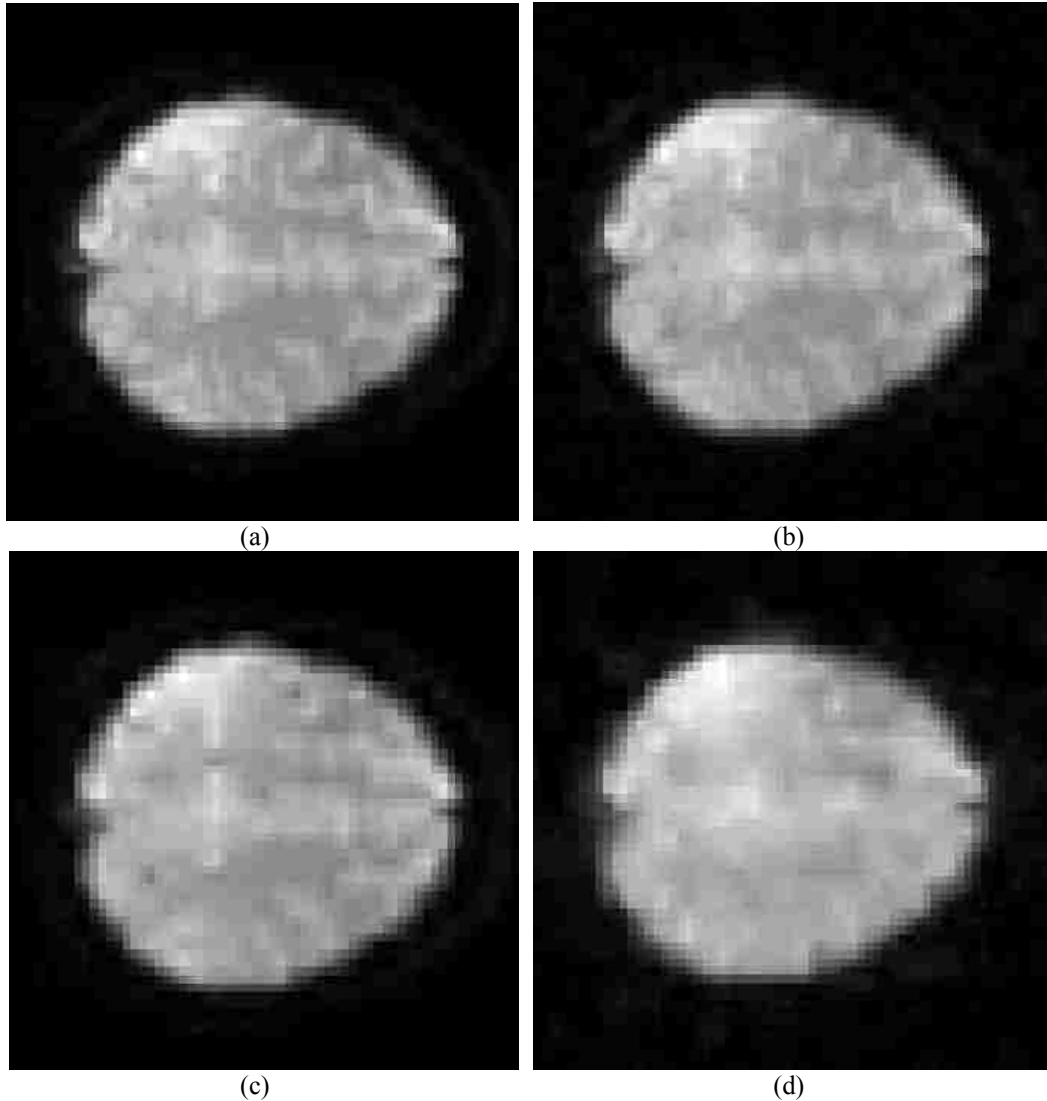


Figure 4.7: Comparative example for a brain image reconstruction using 18.75% of the original samples. (a) original image, (b) Kriging magnitude reconstruction (82.60 dB/SSIM=0.8209), (c) Optimal CS reconstruction using SLP reconstruction (74.18 dB/SSIM= 0. 8571), (d) Optimal CS reconstruction using RSP2 sampling geometry (60.52 dB/SSIM= 0. 6406).

image is 0.2065, or roughly 20% of total range of SSIM values, while the difference in PSNR is 0.72 dB, or roughly 1.2% of the total range of PSNR values for the natural image type.

The brain image reconstructions are shown in Figure 4.7 using 18.75% of the spectral samples. Again, the Kriging reconstruction outperformed the compressive sensing reconstructions. The difference in PSNR between the Kriging and the SLP CS reconstructions was 8.42 dB at the 18.75% data sampling rate and 5.89 dB at the 11.97% data sampling rate. We were unable to down sample the inner and outer spectral blocks at rates greater than 2x/4x and 4x/8x due to the smaller size of the input image (64×64).

A consistent result across all of these reconstructions where Kriging was applied to magnitude spectra interpolation only was better reconstruction of the high-frequency portion of the Fourier domain. This resulted in higher quality reconstructions than the optimal compressive sensing method of reconstructions, even when high frequency content was retained using the random sampling geometry.

4.3.2 Kriged Magnitude and Phase Spectra and CS Reconstruction Comparison

While it may seem that the phase spectrum appears random, without an apparent connection to the spatial data, the information in the phase spectrum plays an important role in image reconstruction from Fourier samples. It defines the relative position of each two-dimensional complex exponential comprising the Fourier representation of the image and plays a much larger role in defining the

overall interpretability of the spatial image, preserving the general structure in the spatial image and placing sharp edges in a scene. While incorrect magnitude estimated values will add an overall noise-like perturbation to the reconstructed image, slight errors in the phase values could destroy the fidelity of the reconstructed image. Thus, we are interested to see the effect that phase interpolation using Kriging has on the reconstructed images. Since we used less aggressive sampling rates for the inner and outer spectral phase blocks, the increase in overall data reduction is not as significant. Statistics of the PSNR and SSIM values for the eight data reduction rates achieved with magnitude and phase Kriging are shown in Table 4.5 through Table 4.12

The results in Tables 4.3 and 4.4 reveal that inclusion of the phase spectra for better data reduction is not beneficial, as Kriging was outperformed by the SLP CS reconstructions. The mean PSNR and SSIM values for these reconstruction results are shown in Figure 4.8(a) and 4.8(b), respectively. In these plots, it is clear that the probability distribution function based random sampling did not result in optimal compressive sensing reconstructions at the levels of Kriging or the spiral low pass sampling CS methods. The magnitude-only Kriging results showed greater improvement over the compressive sensing techniques on the urban and natural image types than on the rural and brain images.

TABLE 4.5
SUMMARY STATISTICS OF PSNR AND SSIM FOR 17.26% TOTAL SPECTRAL SAMPLING RATES (KRIGING BOTH MAGNITUDE AND PHASE).

Reconstruction Method	PSNR					SSIM				
	Min	25%	Median	75%	Max	Min	25%	Median	75%	Max
Kriging Mag+Phase	42.54 dB	46.79 dB	52.22 dB	73.21 dB	83.47 dB	0.6951	0.7109	0.7698	0.8205	0.9460
Opt CS, SLP Class	40.11 dB	46.08 dB	51.78 dB	72.84 dB	85.42 dB	0.5870	0.5299	0.7821	0.8627	0.9735
Opt CS, RSP2 Class	37.38 dB	42.33 dB	50.54 dB	56.08 dB	66.65 dB	0.4169	0.4859	0.5959	0.8627	0.8807

TABLE 4.6
SUMMARY STATISTICS OF PSNR AND SSIM FOR 15.57% TOTAL SPECTRAL SAMPLING RATES (KRIGING BOTH MAGNITUDE AND PHASE).

Reconstruction Method	PSNR					SSIM				
	Min	25%	Median	75%	Max	Min	25%	Median	75%	Max
Kriging Mag+Phase	42.02 dB	46.60 dB	51.88 dB	71.56 dB	81.75 dB	0.6577	0.6818	0.7476	0.8089	0.9333
Opt CS, SLP Class	40.50 dB	45.51 dB	52.22 dB	72.21 dB	84.45 dB	0.5867	0.6271	0.6720	0.8559	0.9712
Opt CS, RSP2 Class	37.38 dB	42.47 dB	49.19 dB	49.28 dB	63.39 dB	0.3983	0.4265	0.5636	0.6389	0.8806

TABLE 4.7
SUMMARY STATISTICS OF PSNR AND SSIM FOR 15.12% TOTAL SPECTRAL SAMPLING RATES (KRIGING BOTH MAGNITUDE AND PHASE).

Reconstruction Method	PSNR					SSIM				
	Min	25%	Median	75%	Max	Min	25%	Median	75%	Max
Kriging Mag+Phase	41.20 dB	44.02 dB	51.69 dB	70.77 dB	81.75 dB	0.5911	0.6449	0.7165	0.7957	0.9231
Opt CS, SLP Class	40.14 dB	45.69 dB	50.96 dB	72.38 dB	83.64 dB	0.5642	0.6075	0.7571	0.8577	0.9694
Opt CS, RSP2 Class	33.88 dB	41.44 dB	49.10 dB	55.95 dB	69.10 dB	0.3502	0.4714	0.5950	0.6250	0.8915

TABLE 4.8
SUMMARY STATISTICS OF PSNR AND SSIM FOR 9.38% TOTAL SPECTRAL SAMPLING RATES (KRIGING BOTH MAGNITUDE AND PHASE)

Reconstruction Method	PSNR					SSIM				
	Min	25%	Median	75%	Max	Min	25%	Median	75%	Max
Kriging Mag+Phase	37.48 dB	42.06 dB	48.08 dB	64.21 dB	73.18 dB	0.4831	0.5110	0.5873	0.6907	0.8728
Opt CS, SLP Class	38.08 dB	42.65 dB	48.85 dB	67.54 dB	76.39 dB	0.4449	0.5153	0.6531	0.7816	0.9438
Opt CS. RSP2 Class	29.07 dB	35.29 dB	45.16 dB	49.21 dB	59.19 dB	0.0224	0.3170	0.4822	0.5681	0.8364

TABLE 4.9
SUMMARY STATISTICS OF PSNR AND SSIM FOR 7.68% TOTAL SPECTRAL SAMPLING RATES (KRIGING BOTH MAGNITUDE AND PHASE)

Reconstruction Method	PSNR					SSIM				
	Min	25%	Median	75%	Max	Min	25%	Median	75%	Max
Kriging Mag+Phase	37.23 dB	41.92 dB	47.91 dB	63.50 dB	72.16 dB	0.4726	0.5031	0.5778	0.6847	0.8765
Opt CS, SLP Class	37.12 dB	42.67 dB	49.31 dB	65.50 dB	72.59 dB	0.3978	0.4732	0.6147	0.7666	0.9254
Opt CS. RSP2 Class	35.22 dB	37.83 dB	44.76 dB	46.83 dB	61.02 dB	0.3028	0.3237	0.4485	0.4895	0.8430

TABLE 4.10
SUMMARY STATISTICS OF PSNR AND SSIM FOR 7.23% TOTAL SPECTRAL SAMPLING RATES (KRIGING BOTH MAGNITUDE AND PHASE)

Reconstruction Method	PSNR					SSIM				
	Min	25%	Median	75%	Max	Min	25%	Median	75%	Max
Kriging Mag+Phase	36.55 dB	41.12 dB	48.04 dB	63.01 dB	72.05 dB	0.4546	0.4735	0.5649	0.6818	0.8746
Opt CS, SLP Class	37.20 dB	42.57 dB	49.21 dB	65.72 dB	72.49 dB	0.3864	0.4549	0.6113	0.7553	0.9248
Opt CS. RSP2 Class	35.73 dB	36.19 dB	44.64 dB	48.35 dB	63.93 dB	0.3020	0.3727	0.4572	0.5322	0.8491

TABLE 4.11
SUMMARY STATISTICS OF PSNR AND SSIM FOR 5.99% TOTAL SPECTRAL SAMPLING RATES (KRIGING BOTH MAGNITUDE AND PHASE)

Reconstruction Method	PSNR					SSIM				
	Min	25%	Median	75%	Max	Min	25%	Median	75%	Max
Kriging Mag+Phase	36.36 dB	40.47 dB	46.99 dB	61.48 dB	70.80 dB	0.4138	0.4644	0.5335	0.6575	0.8645
Opt CS, SLP Class	36.13 dB	41.71 dB	47.34 dB	64.09 dB	69.16 dB	0.3224	0.4162	0.5658	0.6831	0.9026
Opt CS. RSP2 Class	32.10 dB	34.85 dB	44.15 dB	54.01 dB	66.84 dB	0.2588	0.3242	0.4622	0.5798	0.8644

TABLE 4.12
SUMMARY STATISTICS OF PSNR AND SSIM FOR 5.54% TOTAL SPECTRAL SAMPLING RATES (KRIGING BOTH MAGNITUDE AND PHASE)

Reconstruction Method	PSNR					SSIM				
	Min	25%	Median	75%	Max	Min	25%	Median	75%	Max
Kriging Mag+Phase	36.50 dB	40.74 dB	46.99 dB	61.19 dB	70.24 dB	0.4160	0.4733	0.5456	0.6599	0.8669
Opt CS, SLP Class	35.54 dB	41.71 dB	47.64 dB	64.09 dB	68.42 dB	0.2902	0.4162	0.5550	0.6831	0.8984
Opt CS. RSP2 Class	32.77 dB	35.70 dB	45.27 dB	48.31 dB	58.54 dB	0.2717	0.3122	0.4261	0.5508	0.8330

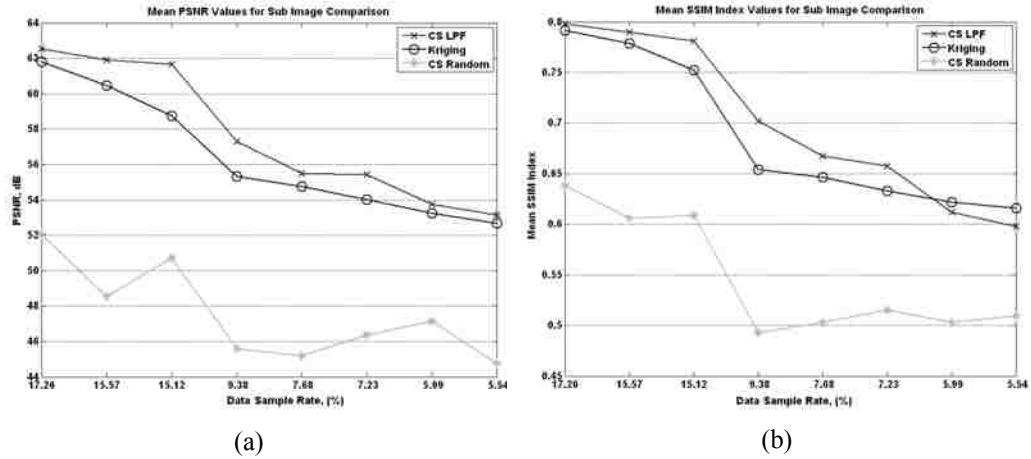


Figure 4.8: Magnitude and phase data reconstruction results. (a) The mean PSNR of all sub images are shown for magnitude and phase Kriging data rate.). (b) The mean SSIM values for all sub images.

To explore whether or not magnitude and phase Kriging is a viable solution to data reconstruction, we explored the mean PSNR and SSIM values for each of the four image types. These results, depicted in Figure 4.9 and Figure 4.10, reveal that the image type does indeed play a large role in determining which reconstruction method is the best choice for a given image. We decided to exclude the optimal CS reconstructions using RSP2 sampling geometry class average performance.

In addition to providing a suggestion of reconstruction method selection, the results reveal the difficulties with reconstructing the phase spectra and the resultant poor reconstruction of highly textured, non-smooth images when phase is processed. Figure 4.9(a), which represents the rural image class, shows an improvement in PSNR by magnitude and phase Kriging over SLP CS

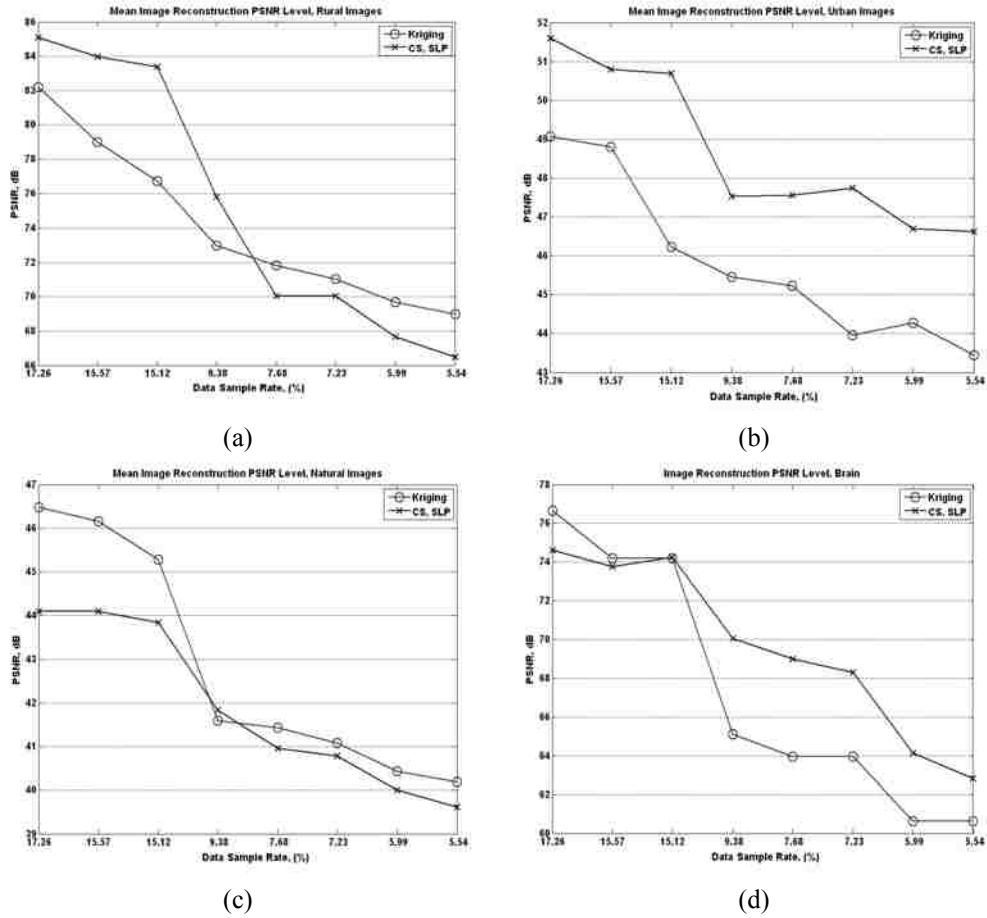


Figure 4.9: The mean PSNR values for each data sample rates based on Magnitude and Phase Kriging. (a) Mean PSNR for Rural image scenes. (b) Mean PSNR for Urban image scenes. (c) Mean PSNR of Natural image scenes. (d) Mean PSNR for Brain image.

reconstruction at the lowest data rates. The SSIM values in Figure 4.10(a), on the other hand, do not improve. Both the PSNR and SSIM values are consistently.

Although at first glance, magnitude and phase Kriging may seem like a viable solution higher from the CS SLP reconstructions for the urban image class (Figures 4.10(b) and 4.11(b)). The difficulty of phase spectra interpolation plays a significant role in reducing the performance of Kriging for this image type for

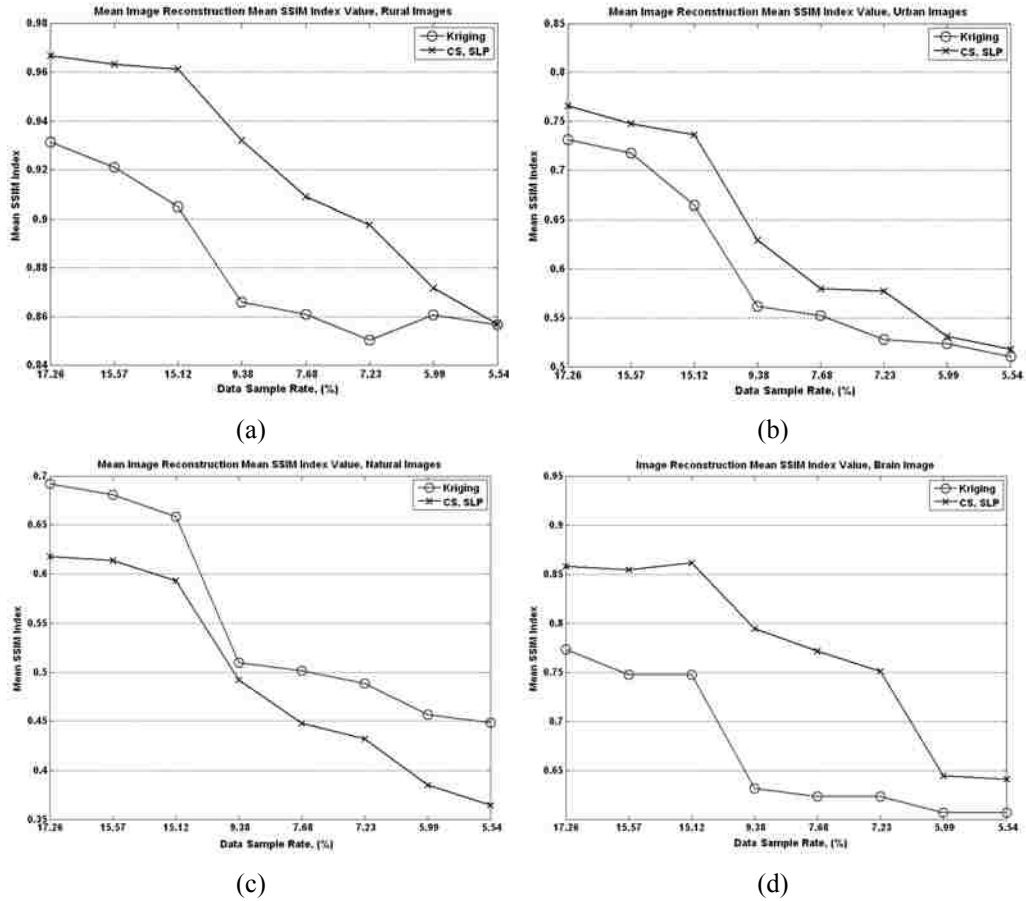


Figure 4.10: The mean SSIM Index values for each data sample rates based on Magnitude and Phase Kriging. (a) Mean SSIM Index for Rural image scenes. (b) Mean SSIM Index for Urban image scenes. (c) Mean SSIM Index of Natural image scenes. (d) Mean SSIM Index for Brain image.

the natural image class, but closer examination of the mean PSNR and SSIM values reveal that the quality level of the reconstructions was unacceptable. The overall poor performance of the CS methods on the natural images in the magnitude Kriging comparison above reveal that slight ($<3\text{dB}$) improvement in PSNR and SSIM (<0.10) over the SLP CS reconstructions at these reduction rates is unsatisfactory.

Again, we turn to visual assessment to reveal that the magnitude and phase Kriging methods do not result in suitably reconstructed images. We select two cases to examine more extensively. The first set of images, shown in Figure 4.11, is the Kriging and SLP CS results of the first rural sub image from 7.68% of the Fourier samples. The PSNR value of Kriging result was 72.16 dB, while the PSNR value of the SLP CS result was 65.31 dB. The 6.85 dB difference achieved by Kriging was the greatest difference of all the sub images, while the difference in SSIM values was a *decrease* of 0.0316 (0.8548 was achieved with Kriging and 0.8855 was achieved with SLP CS). When comparing the Kriging reconstruction in Figure 4.12(b) and the SLP CS reconstruction in Figure 4.11(c) to the original rural image in Figure 4.11(a), one can easily recognize the increase ringing throughout the image in the Kriging reconstruction from phase error artifacts. The upper and lower left-side corners contain prominent phase error artifacts. This is a classic example of PSNR incorrectly quantifying a worse reconstruction as the better quality image. The SSIM maps of the two reconstructions (Figure 4.11 (d) and Figure 4.11(e)) reveal the ringing artifacts of the Kriging reconstruction and poor structural similarity due to blurring in the CS reconstruction. If having to visually grade which reconstruction is better, the blurred errors would be more acceptable than the periodic ringing in the Kriging reconstruction.

The second case will compare the images related to the best Kriging reconstruction of the natural sub images. Our results revealed that the second

natural sub image at a data sampling rate of 18.75% resulted in a Kriging PSNR that was 2.06 dB greater than the SLP CS PSNR (52.22 dB and 50.16 dB). The SSIM index values for these results were 0.7129 and 0.6313 using Kriging and SLP CS, respectively. The original image, along with the reconstructions and SSIM maps are depicted in Figure 4.12. In this specific case, the Kriging reconstruction visually appears to be a better reconstruction, although it also exhibits significant phase error artifacts (ringing) in localized regions of the image.

All of these sub image comparisons lead to two significant conclusions. The first is that magnitude Kriging consistently produces better image reconstructions over CS methods. The second result is that the drop in image quality due to phase reconstruction errors is significant and the reduction in data samples is not great enough to justify the inclusion of phase interpolation. The Kriged magnitude and phase spectra used to reconstruct the image in Figure 4.11(b) are shown in Figure 4.13. In this example, it is clear that the phase reconstruction is inadequate to result in a reconstructed image of sufficient quality. The reconstruction errors at higher frequencies in the phase reconstruction are the cause for the significant ringing in the reconstructed image in Figure 4.11(b). In addition, the phase unwrapping process required for phase Kriging adds a significant computational burden, which has been shown to not improve image reconstruction, but rather degrade it.

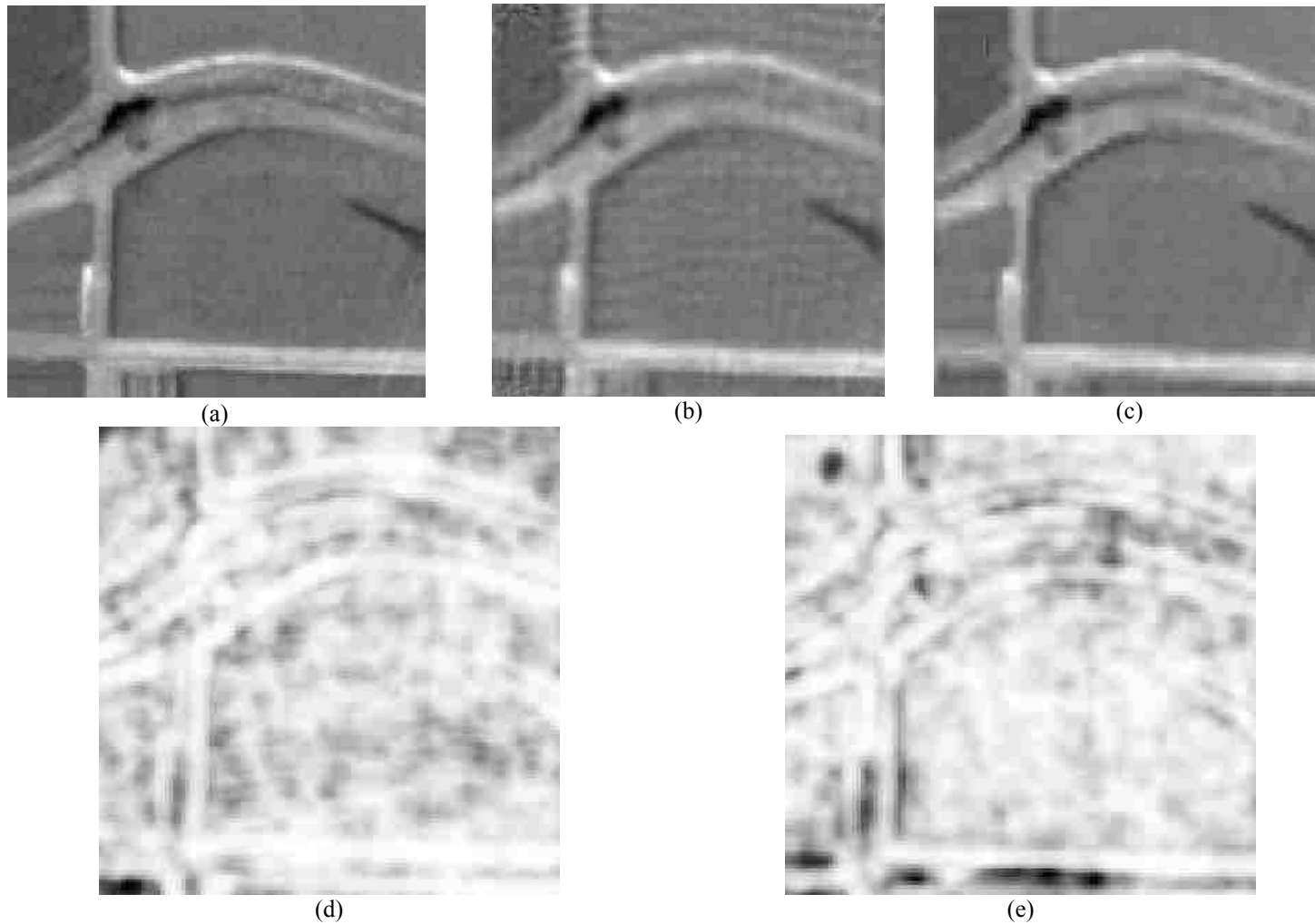


Figure 4.11: Comparison of rural sub image reconstruction and related SSIM index maps using a 7.68% data sample rate. (a) Original rural sub image. (b) Magnitude and phase spectra reconstruction with Kriging (72.16 dB). (c) The SLP CS reconstruction (65.31 dB). (d) SSIM index map of Kriging reconstruction (mean SSIM = 0.8548). (e) SSIM index map of SLP CS reconstruction (mean SSIM = 0.8855).

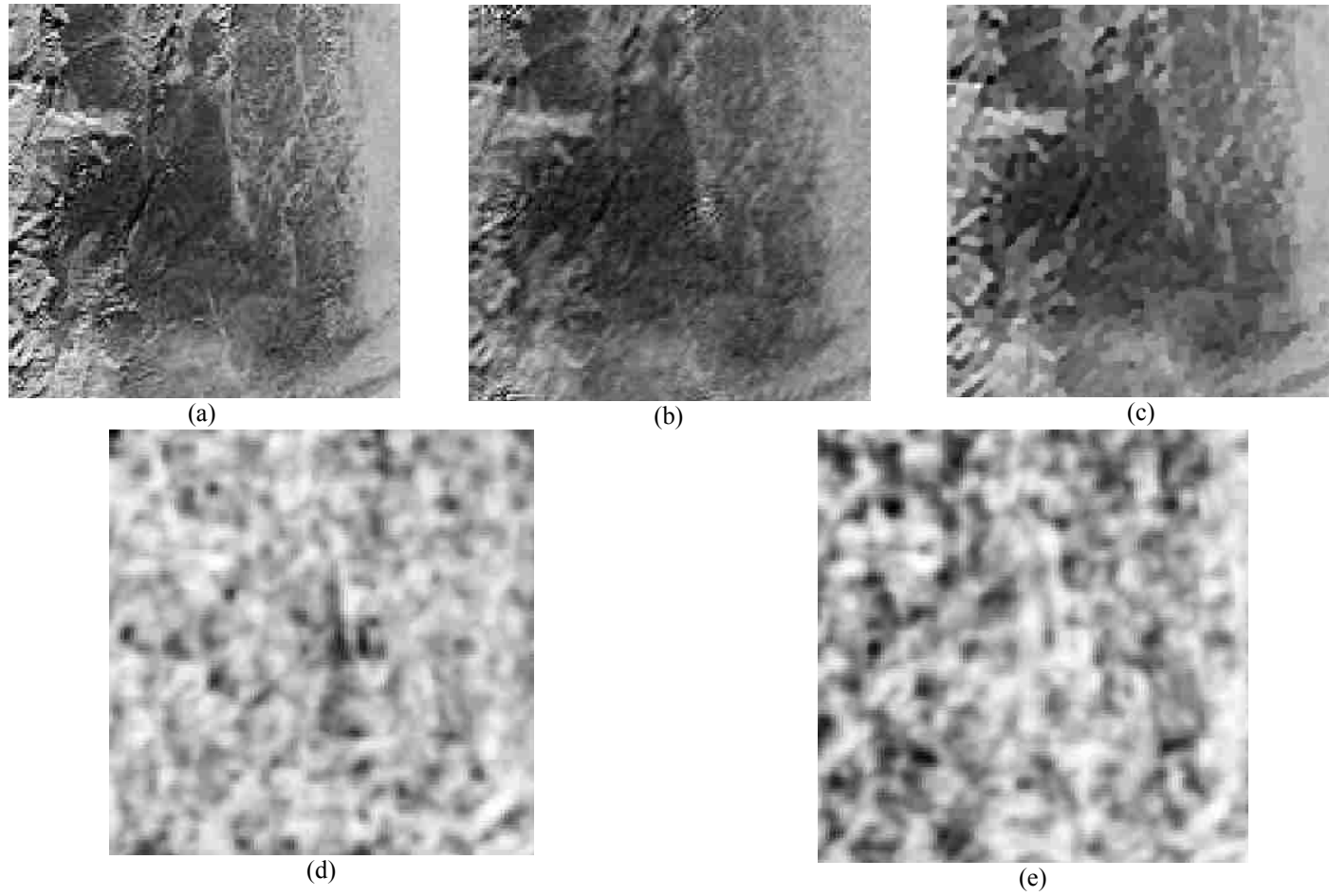


Figure 4.13: Comparison of natural sub image reconstruction and related SSIM index maps using a 17.26% data sample rate. (a) Original rural sub image. (b) Magnitude and phase spectra reconstruction with Kriging (52.22 dB). (c) The SLP CS reconstruction (50.16 dB). (d) SSIM index map of Kriging reconstruction (mean SSIM = 0.7129). (e) SSIM index map of SLP CS reconstruction (mean SSIM = 0.6313).

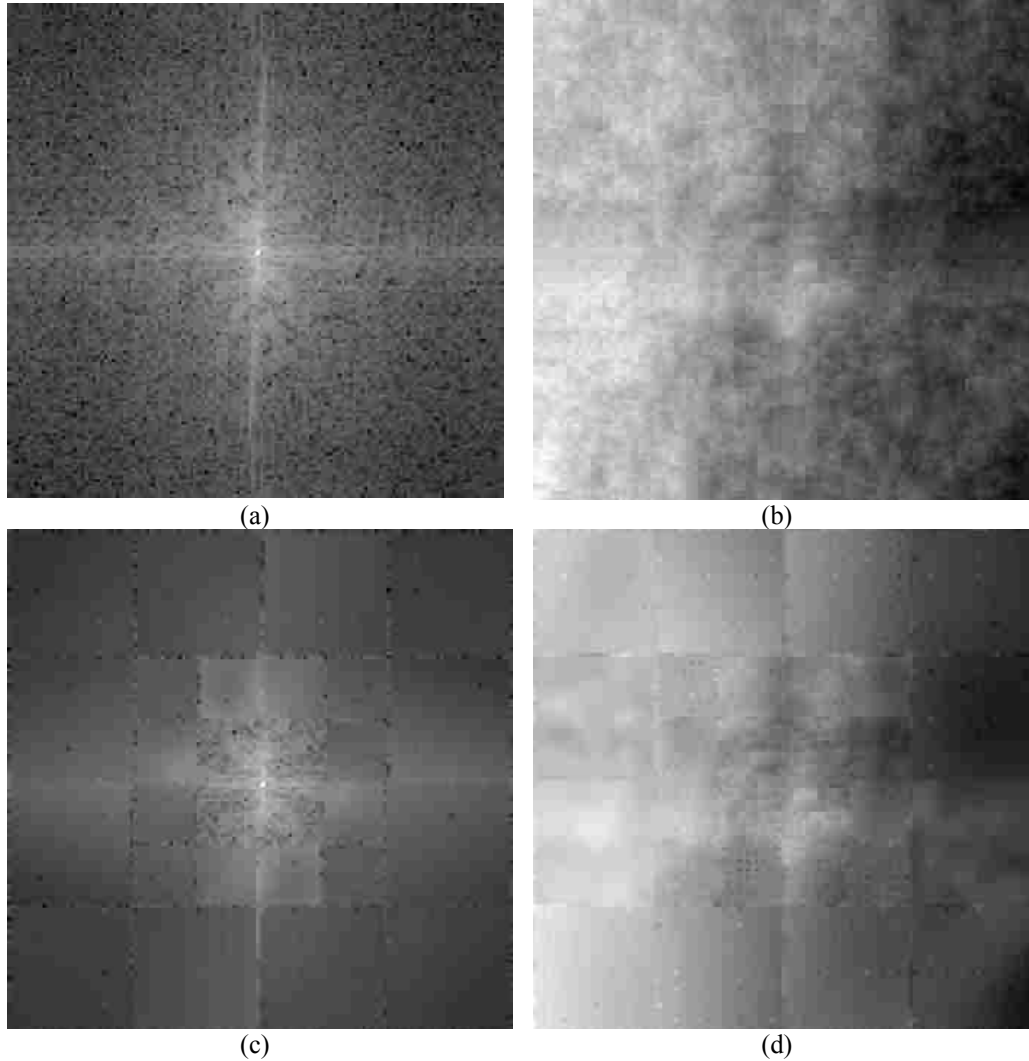


Figure 4.13: Example of Kriging reconstructed magnitude and phase spectra of rural scene in Figure 4.11(a). (a) Original log-transformed magnitude spectra. (b) Flynn's unwrapped original phase spectra. (c) Kriging interpolation magnitude using rates of 4x/8x (d) Kriging interpolation of unwrapped phase spectra using rates of 2x/4x.

4.3.3 Original Satellite Image Comparison

We wanted to explore additional, more aggressive (limited) sampling in the outer and inner spectral blocks for magnitude Kriging. To accomplish this, we used three selected full size images, one of each satellite image class. Again, we ensured that the number of spectral samples is equivalent between the Kriging and the SLP CS methods. We excluded the RSP2 CS sampling geometry from this

comparison due to its poor performance on the sub image data set. We did include the zero-filled result of the SLP sampling geometries to indicate how much of an improvement the optimal CS method obtained.

Table 4.13 contains the PSNR values of each sample image at the six sample rates defined by the outer and inner spectral block sampling rates described in Section 4.2. Table 4.14 contains the related mean SSIM index values for the full image reconstruction. Figure 4.14 depicts the rural image reconstructions and the PSNR and SSIM index plots associated with the sample rates. The reconstructed images were generated using the least number of samples (9.64% of the spectral samples). For the rural test image, PSNR values were between 5 dB and 12 dB higher using Kriging. The SSIM performance was also substantially better for Kriging.

Figure 4.15 depicts the collection of results from the sample urban satellite image. While the overall PSNR and SSIM values are lower than the rural scene, the increase in PSNR and SSIM obtained by Kriging is again substantial, ranging from 7 dB to 11 dB in PSNR. Visual assessment does reveal that such aggressive uniformly reduced sampling rates (using one every 64 FFT samples in the outer spectral blocks and one every 32 FFT samples in the inner spectral blocks) does not result in an acceptable image. But in comparison to the SLP CS result, the Kriging result is substantially better.

TABLE 4.13
 MEAN PSNR FOR MAGNITUDE SAMPLING RATES ON FULL IMAGE RECONSTRUCTION &
 VISUAL IMAGE QUALITY SCORE (LOW/MEDIUM/HIGH)

Magnitude Sample Rate \ Reconstruction Method and Statistic	18.75%	11.97%	10.17%	9.91%	9.78%	9.64%
Kriging PSNR, Rural Image	78.33 dB, High	76.84 dB, High	76.13 dB, High	75.11 dB, High	73.32 dB, High	69.78 dB, High
CS SLP PSNR, Rural Image	68.00 dB, High	65.04 dB, Medium	64.16 dB, Medium	63.79 dB, Medium	63.93 dB, Medium	63.79 dB, Medium
Zero Filling PSNR, Rural Image	69.93 dB, High	66.07 dB, Medium	64.93 dB, Medium	64.80 dB, Medium	64.67 dB, Medium	64.60 dB, Medium
Kriging PSNR, Urban Image	56.94 dB, Medium	55.56 dB, Medium	54.46 dB, Medium	53.64 dB, Medium	51.35 dB, Medium	49.58 dB, Medium
CS SLP PSNR, Urban Image	44.60 dB, Low	43.01 dB, Low	41.81 dB, Low	42.25 dB, Low	42.36 dB, Low	42.28 dB, Low
Zero Filling PSNR, Urban Image	46.74 dB, Low	44.24 dB, Low	43.45 dB, Low	43.28 dB, Low	43.23 dB, Low	43.12 dB, Low
Kriging PSNR, Natural Image	69.45 dB, High	68.23 dB, High	67.48 dB, High	67.38 dB, High	63.36 dB, High	63.08 dB, High
CS SLP PSNR, Natural Image	56.34 dB, Medium	54.61 dB, Medium	53.03 dB, Medium	52.52 dB, Medium	52.61 dB, Medium	52.53 dB, Medium
Zero Filling PSNR, Natural Image	57.69 dB, Medium	55.30 dB, Medium	54.61 dB, Medium	54.49 dB, Medium	54.44 dB, Medium	54.37 dB, Medium

TABLE 4.14
 MEAN SSIM INDEX FOR MAGNITUDE SAMPLING RATES ON FULL IMAGE RECONSTRUCTION &
 VISUAL IMAGE QUALITY SCORE (LOW/MEDIUM/HIGH)

Magnitude Sample Rate \ Reconstruction Method and Statistic	18.75%	11.97%	10.17%	9.91%	9.78%	9.64%
Kriging SSIM, Rural Image	0.9231, <i>High</i>	0.9131, <i>High</i>	0.9074, <i>High</i>	0.9017, <i>High</i>	0.8842, <i>High</i>	0.8453, <i>Medium</i>
CS SLP SSIM, Rural Image	0.8720, <i>High</i>	0.8042, <i>Medium</i>	0.7834, <i>Medium</i>	0.7750, <i>Medium</i>	0.7777 <i>Medium</i>	0.7750, <i>Medium</i>
Zero Filling SSIM, Rural Image	0.8671, <i>High</i>	0.8004, <i>Medium</i>	0.7765, <i>Medium</i>	0.7734, <i>Medium</i>	0.7703, <i>Medium</i>	0.7688, <i>Medium</i>
Kriging SSIM, Urban Image	0.8779, <i>Medium</i>	0.8622, <i>Medium</i>	0.8483, <i>Medium</i>	0.8367, <i>Medium</i>	0.8046, <i>Medium</i>	0.7921, <i>Medium</i>
CS SLP SSIM, Urban Image	0.6661, <i>Low</i>	0.5501, <i>Low</i>	0.4983, <i>Low</i>	0.4978, <i>Low</i>	0.4969, <i>Low</i>	0.4931, <i>Low</i>
Zero Filling SSIM, Urban Image	0.6878, <i>Low</i>	0.5781, <i>Low</i>	0.5368, <i>Low</i>	0.5275, <i>Low</i>	0.5240, <i>Low</i>	0.5187, <i>Low</i>
Kriging SSIM, Natural Image	0.8156, <i>High</i>	0.7992, <i>High</i>	0.7841, <i>High</i>	0.7758, <i>High</i>	0.7258, <i>High</i>	0.7170, <i>High</i>
CS SLP SSIM, Natural Image	0.7582, <i>Medium</i>	0.6828, <i>Medium</i>	0.6552, <i>Medium</i>	0.6502, <i>Medium</i>	0.6491, <i>Medium</i>	0.6468, <i>Medium</i>
Zero Filling SSIM, Natural Image	0.7499, <i>Medium</i>	0.6724, <i>Medium</i>	0.6461, <i>Medium</i>	0.6412, <i>Medium</i>	0.6397, <i>Medium</i>	0.6364, <i>Medium</i>

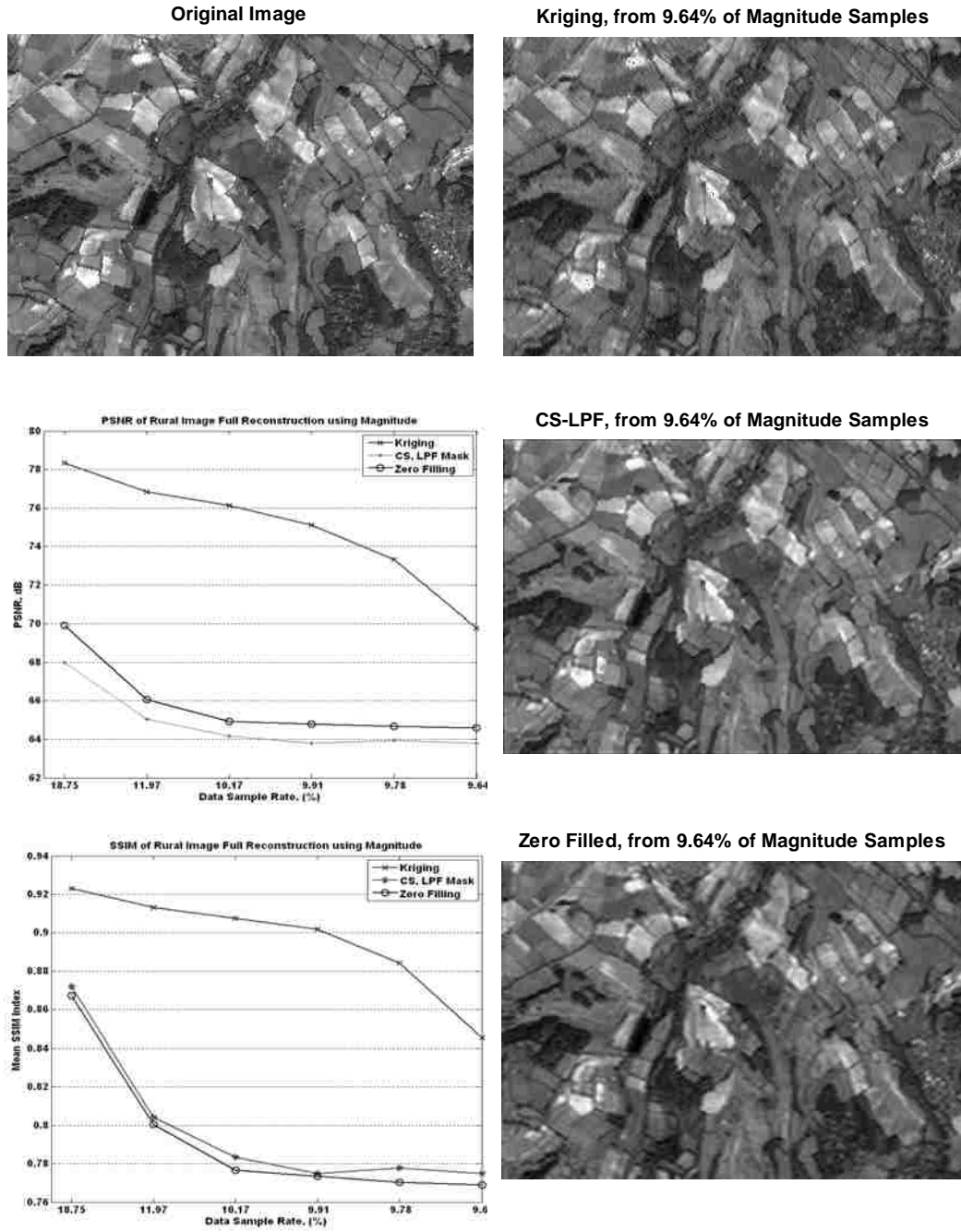


Figure 4.14: Results of magnitude spectra interpolation using Kriging, SLP CS, and Zero Filling the SLP sampling geometry on a full sized image of the rural class.

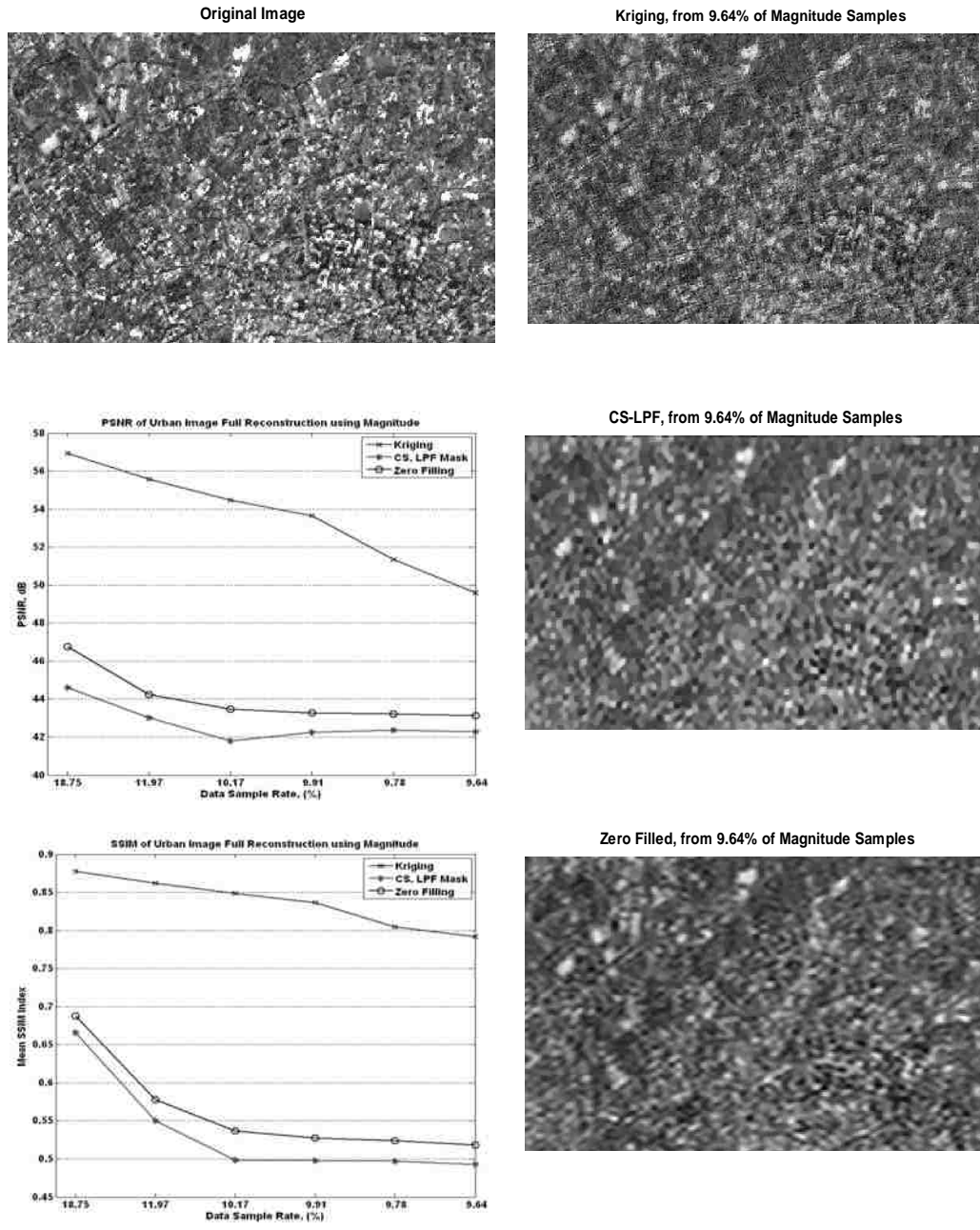


Figure 4.15: Results of magnitude spectra interpolation using Kriging, SLP CS, and Zero Filling the SLP sampling geometry on a full sized image of the urban class.

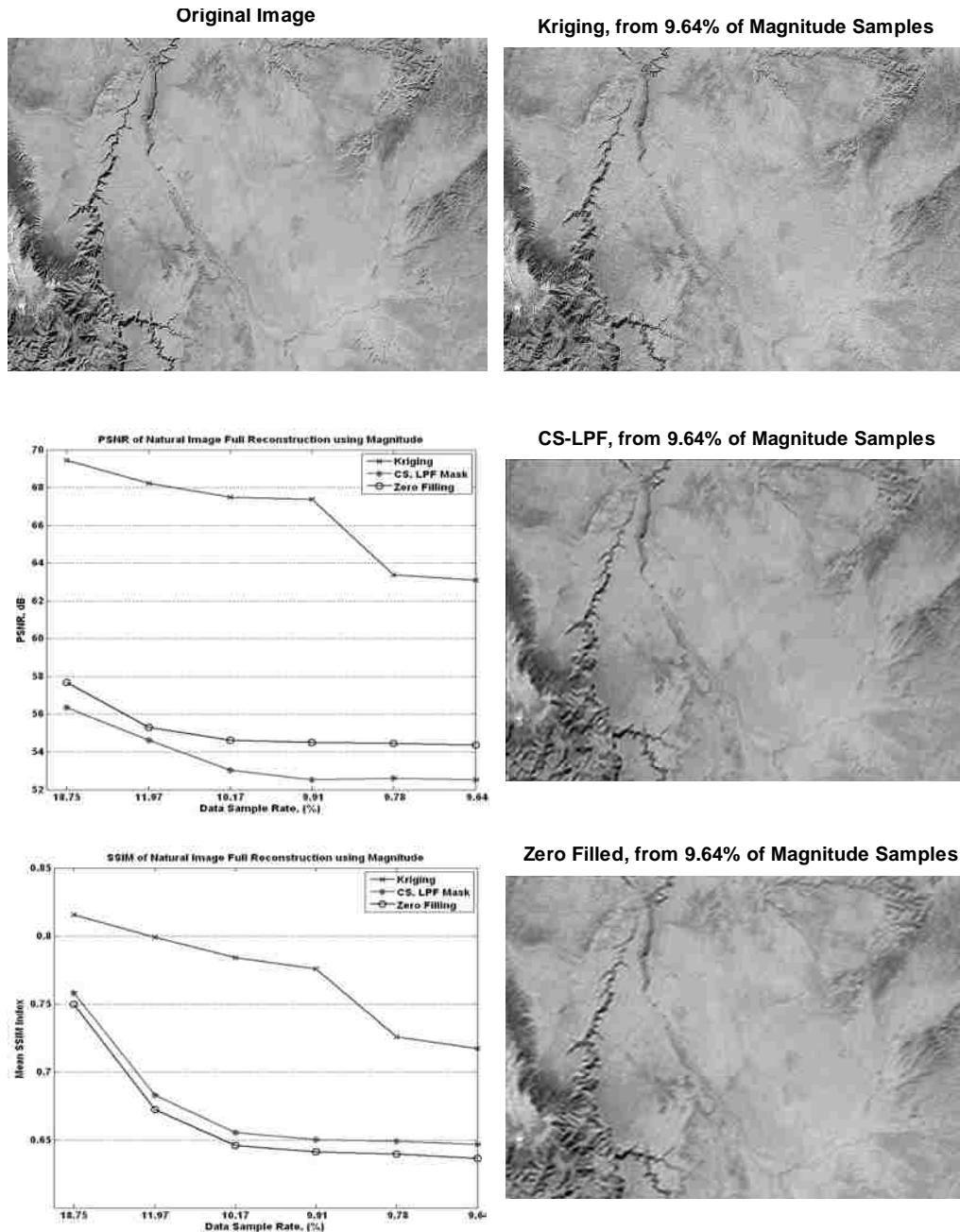


Figure 4.16: Results of magnitude spectra interpolation using Kriging, SLP CS, and Zero Filling the SLP sampling geometry on a full sized image of the rural class.

Figure 4.16 contains the results of the full natural image comparison. The Kriging result for this image showed the most improvement over the competitive

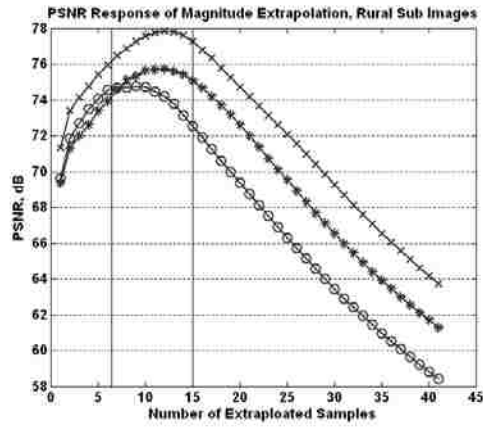
methods of any of the three full satellite image comparisons. PSNR increases ranged from 9dB to 14 dB. The unique features of the urban and rural image types are representative in this natural image sample, and the Kriging reconstruction, from a visual assessment perspective, is acceptable at even the greatest downsampling rates.

These results are encouraging; as they begin to show the effectiveness of a relatively straight forward spatial statistical model can achieve amazing image reconstruction by interpolating discrete Fourier blocks independently of each other. This work not only reveals the potential of image reconstruction from uniformly sampled magnitude spectra, but it is also based on a general framework that allows for ease of scalability for use on a wide variety of images.

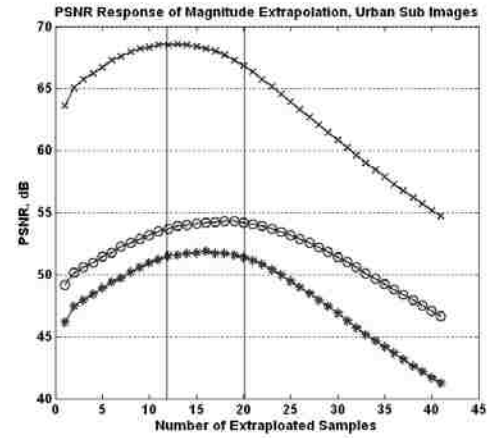
4.4 Magnitude Spectrum Extrapolation

Successful magnitude Kriging led us to explore the effectiveness of extrapolating the magnitude spectra in both dimensions. We selected an initial low pass mask size $\frac{1}{4} \times \frac{1}{4}$ in each dimension, resulting in a reduced set of the center 6.25% magnitude samples. In this experiment, we followed the following steps to identify how much, if any, improvement in image reconstruction PSNR and SSIM can be achieved through iteratively expanding the square low pass sampling mask on each of the ten sub images.

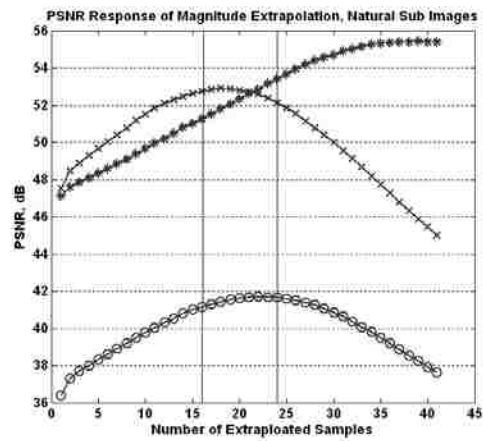
We were able to expand each to a certain extent, all the while increasing the reconstructed SSIM and PSNR values. For each image type, an effective region could be identified that provided the maximum PSNR that can be obtained by this extrapolation method. The plots in Figure 4.17 show the PSNR values of the extrapolation magnitude spectra for each image type. The vertical lines denote the region of maximum performance in terms of increased PSNR for each image class. One result, though, did not exhibit the consistent behavior exhibited by the other images, as it never reached a maximum extrapolation bound, after which additional magnitude estimation began reducing the reconstructed image PSNR and mean SSIM values. This image, shown in Figure 4.1(i), does not reveal any unique trait that would set it apart from the other natural images. Figure 4.17(e) and 4.17(f) show two of the reconstructions from this extrapolation, revealing that image quality is significantly improved at an extrapolation of 40 samples compared to just ten FFT samples. Finally, a good measure of the impact of the phase extrapolation is by calculating the ratio of the percentage of additional samples and the percentage of original samples for which an increase in PSNR is obtained. For the rural image class, the ratio of extrapolated samples is 150%. For the urban class, the ratio of extrapolated samples to original samples is 192.34%. For the natural class, the ratio of extrapolated samples to original samples is 245.83%. These results reveal that super resolution techniques may benefit greatly from Kriging extrapolation techniques of the magnitude spectra.



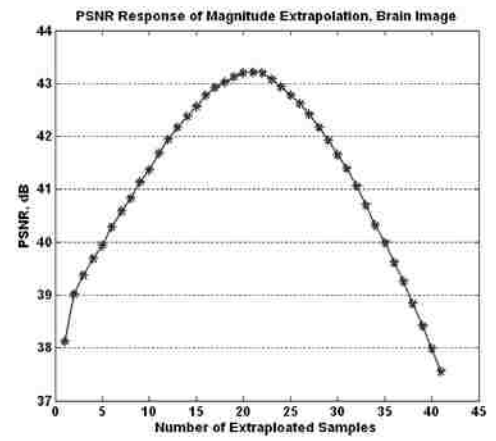
(a)



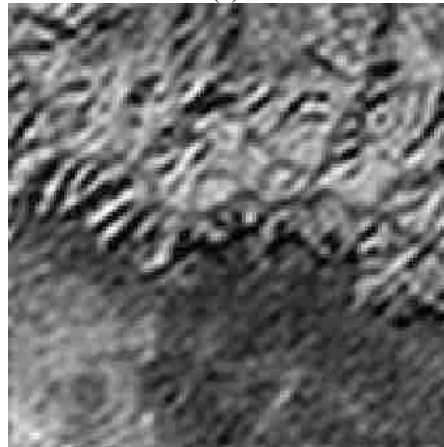
(b)



(c)



(d)



(e)



(f)

Figure 4.17: The magnitude spectra extrapolation. (a) Rural sub image extrapolation PSNR (b) Urban sub image extrapolation PSNR. (c) Natural sub image extrapolation PSNR. (d) Brain image extrapolation PSNR. (e) Example sub image with an additional 16 samples extrapolated. (f) Example sub image with an additional 41 samples extrapolated.

4.5 Comparison of Computational Complexity

The difference in computational complexity between the compressive sensing and Kriging methods we have developed is worth noting. If there was an opportunity to improve upon the compressive sensing methods (e.g. exploring additional sampling geometry classes, including a wider variety of image types, or modification to the objective function) to an extent that a new compressive sensing algorithm consistently outperforms the magnitude Kriging method, the computational complexity of compressive sensing would be something that needs to be taken into consideration. The question now becomes: What is the cost, resource wise, for a hypothetical increase in image quality? Our experience shows that within our current CS paradigm, the computational burden is too great to consider it as a viable solution in any practical application. We support this argument by comparing computational times.

Throughout the image quality comparison experiments above, we measured the collective processing time of the CS and Kriging methods to show that the Kriging solution, while producing reconstructed images of lesser quality in terms of PSNR and structural similarity, may be a more attractive solution. Table 4.15 contains the average total reconstruction times for each compression rate applied to the sub image data set of Section 4.2.1. Note that the search for optimal CS reconstruction parameters is included in the time for reconstructing an image using compressive sensing. The Kriging duration includes the variogram

estimation, variogram optimal model fitting, and Kriging steps for each compression rate. Some calculations of both methods are obtained by remote procedure calls (RPCs) to compiled C-code (either in the form of Matlab mex-functions in Matlab or in the form of an Active-X server call to the R Software Package). The experiments were performed on a 32-bit Windows XP workstation with 2.50 GHz Intel Xeon processor and 3.00 GB of RAM. The results presented in Table 4.4 reveal an average time savings on the order of 10^4 .

The difference in computing time when an entire image is being processed, as in the comparisons described in section 4.2.2, is even more pronounced. The upsampling requirement imposed by the CS reconstruction method places an even greater computational burden on the CS optimization procedures. The time required to simply reconstruct the urban and natural images given that the optimal parameters were already known was 344.08 and 283.37 seconds, respectively. Thirty-seven simplex search steps were required to find the optimal reconstruction parameters for the urban image resulted in a total search time of 189.2 minutes, or 11,532 seconds. Total search time for the natural image reconstruction was 277.81 minutes or 16,668 seconds. The total time required for the Kriging reconstruction of the urban and natural images was 15.678 seconds and 23.542 seconds, respectively.

TABLE 4.15
COMPUTATIONAL COST, IN SECONDS, OF RECONSTRUCTION METHODS IN THE
ABOVE COMPARISONS

Data Sample Rate	Mean CS Reconstruction Time (s) ¹	Mean Kriging Reconstruction Time (s)
18.75%	234.08	1.9543
17.26%	329.06	2.0048
15.57%	308.72	3.5371
15.12%	289.75	3.4866
11.97%	303.27	3.5071
10.17%	289.64	4.2488
9.91%	265.82	4.2282
7.68%	348.05	4.2787
7.23%	403.07	4.2745
5.99%	460.85	4.2540
5.54%	349.84	4.3045

The average reconstruction times of both the CS and Kriging methods on the 10 sub images employed in the comparison experiments in Section 4.2.1.

¹ Using software described in [3] and [5]

A primary cause for the extreme difference in computational times is that the spatial statistical operations (variogram estimation and Kriging) were performed in a compiled programming environment called from Matlab. Similarly, the Kriging times measured did not include the time required for the two-dimensional phase unwrapping steps. Therefore, an analysis of relative computational cost by examining the number of high-cost computational steps in each algorithm is also required.

Kriging estimates are obtained from a single system of equations that are combined using a Lagrange multiplier, resulting in a single matrix inversion per

spectral block. The variogram estimate requires $M \times N$ multiplications, where M is the number of lags being considered, and N is the number of pairs of points defined by the lag. When using P samples to estimate the variogram, we have that $N = (P/2) \times M$, due to inherent symmetry in computing the lags (positive and negative lag vectors correspond to the same lag due to stationarity). Thus, variogram estimation requires $P \times M^2 / 2$ additions and multiplications, for an input of sample of size P . Following variogram estimation, we need to fit the variogram model. This step is clearly not a function of the number of input points, and will thus not be considered in what follows.

Next, we consider the additional cost of computing the Kriging interpolation estimate. Here, we note that for all internal samples, we have the same system of linear equations to solve, at every point. Thus, we only need to invert the variogram matrix once. For boundary points, we would have to invert slightly different matrices at different samples. However, the number of boundary points grow linearly with the dimension of the spectral block, as opposed to the quadratic (area) growth associated with the number of internal points. Thus, the effective computational cost is only due to the linear vector multiplication of the spectral samples $Z(s_i)$ by the coefficients λ_i . Thus, the overall Kriging cost is of the order of $O(M \times P)$ for considering M lags at P points.

Similar comments apply when we consider all spectral blocks. After dropping the constant terms associating with sparse sampling, the overall growth of the algorithm is of the order of $O(P \times M^2)$ in terms of the number of lags and the number of points. Here, it is important to note that we only have linear growth.

In our experiments, M in the medium and high frequency blocks is equal to 20 and 25, respectively. As an approximation, we consider the medium frequency blocks to contain ~ 64 samples (based on the sub image size of 128×128). If we assumed a sample rate of keeping one out of every four samples in each dimension, the number of estimates becomes $N \approx 144$. Thus, we can approximate a requirement of 59,968 multiplications and additions per medium spectral block. Similarly, for the high frequency blocks, we can assume $N \approx 900$ sample estimates are required based on a sample rate of keeping one out of every 8 samples in each dimension. The approximate number of multiplications and additions per high frequency block becomes 562,500. We can approximate the number of required multiplications and additions for an entire image reconstruction as the combination of 6 magnitude spectra medium frequency blocks, 6 magnitude spectra high frequency blocks, 6 phase spectra medium frequency blocks, and 6 phase spectra high frequency blocks. The total computational cost can be approximated as requiring 7,469,616 multiplications and additions for an image size 128×128 .

The compressive sensing method we utilize has a significant number of additional functional evaluations, including the calculation of the Wavelet transform, the TV-Norm transform, and the Fourier transform at each conjugate gradient iteration [4,5]. Each of these are non-trivial calculations, and since we optimize two cost parameters using the simplex search method, the conjugate gradient objective function must be solved at each simplex step. In our experiments, the number of simplex iterations was typically around thirty, although stopping the simplex search after the first 10 iterations is justifiable based on the search surfaces discussed in Chapter 2. In the paper on which this software was originally applied, it is reported that approximately 80 to 200 conjugate gradient iterations are required based the data sets of ranging in size from 100×100 to 480×480 [5]. The total number of conjugate gradient iterations required for the reconstruction of a sample 128×128 sub image from our data set using arbitrary reconstruction parameters was equal to 928. This value is subjective, as we chose to run ten iterative reconstructions, using the result of the $N-1^{\text{st}}$ iteration on the N^{th} iteration.

The Big-O complexity of each conjugate gradient iteration is based on the three functionals that constitute the CS reconstruction algorithm we utilized. In terms of the number of points being considered, a 4-coefficient Wavelet transform has complexity $O(P)$ [6], while the 1-D FFT is shown to have complexity of $O(P \log_2 P)$ [7], which becomes $O(P \log_2 \sqrt{P}) = O(P \log_2 P)$ for square images. Finally, the total variation functional is represented as having complexity $O(P)$. Since the

FFT functional is the largest, the complexity of the constraint becomes $O(P \log P)$, which is the largest growth rate for the CS reconstruction algorithm. Based on the required number of iterations, we are led to require \sqrt{P} conjugate gradient steps for convergence. This gives a total complexity of $O(P^{1.5} \log P)$ without accounting for parameter optimization.

For a 128×128 sub image at the Kriging rate provided in the above example (a 4x sample rate for medium frequency blocks and an 8x sample rate for high frequency blocks), P becomes 12,528 unknown samples. The computational complexity at each conjugate gradient step is 5,746,217. When all conjugate gradient steps are taken into account, this value becomes 5,171,595,489 multiplications and additions. When comparing this value to the 7,469,616 multiplications and additions required for an image of the same size, the computational benefit of using Kriging on small, spectral blocks is clear.

4.6 Conclusion

The comparisons provided above reveal to the reader the strengths that are evident in the Spectral Statistical modeling approach to Fourier sample estimation. First, we note that on the sub image data set, when estimating magnitude samples only, the Kriging results consistently outperformed the optimal Compressive Sensing reconstruction using the same number of overall complex spectral data samples. On full size images, the Kriging reconstructions were significantly better than the

best optimized CS reconstruction using the spiral sampling geometry class. In test images where there is considerable variation in the scene, such as the urban images we explored, the inclusion of high-frequency samples in the spectral sampling geometry has a considerable impact on reconstruction quality.

We noted, however, that for specific scene types, when phase interpolation was included in the Spectral Statistical reconstruction, the detrimental effects of high-frequency reconstruction inaccuracies (where we sample at a much lower rate) result in lower SSIM values than the CS reconstructions. Here, optimal CS reconstructions performed better when scenes contained large regions that can be well approximated by piecewise constant models, such as for the rural sub images in our sub image data set. This leads us to recommend Spectral Statistical modeling and reconstruction of the magnitude spectra only.

We also observed that the CS reconstructions often failed to achieve any improvement over the initial guess during the reconstruction parameter optimization procedure. In many of the satellite image reconstructions optimal parameters included a Wavelet transform penalty value that was negative. As was mentioned in Chapter 2, a negative transform penalty will result in a reconstruction that is over-smoothed in small, well defined regions of the spatial image due to an over-emphasis on the total variation minimization term in the objective function. This is clearly evident in the CS reconstruction in Figure 4.15. In such instances it is clear that the optimization algorithms employed by

our method failed in providing any improvement over the initial value (e.g. the zero-filled spatial image reconstruction).

Finally, the computational complexity of most CS image reconstruction algorithms do not lend themselves to some practical applications due to the considerable amount of computational cost associated with solving the nested optimization paradigm required for general use. In the case of the fMRI study in Chapter 2, we were able to calculate well-defined bounds on the reconstruction parameters that provide a general solution to the specific image type we were exploring. Applying our optimal CS methods to any image requires the calculation of unique parameters for each image being processed, assuming that the images are significantly different from one another.

References

- [1] Z. Wang, A. C. Bovik, H. R. Sheikh, and E. P. Simoncelli, "Image quality assessment: from error visibility to structural similarity," in *IEEE Transactions on Image Processing*, vol. 13, pp. 600-612, 2004.
- [2] B. Wohlberg and P. Rodriguez, "An iteratively reweighted norm algorithm for minimization of total variation functionals," in *IEEE Signal Processing Letters*," vol. 14, pp. 948-951, 2007.
- [3] Stanford University Department of Statistics. WaveLab 850 Matlab software package. Retrieved June 12, 2008, Website:
http://www-stat.stanford.edu/~wavelab/Wavelab_850/index_wavelab850.html
- [4] M. Lusting, D. Donoho, and J.M. Pauly, "Sparse MRI: The application of

compressed sensing for rapid MR Imaging,” in *Magnetic Resonance in Medicine*, vol. 58, pp. 1182-1195, December 2007.

- [5] M. Lustig. (2006) Retrieved SparseMRI, a collection of Matlab functions, scripts, and demos of compressed sensing MRI. Retrieved Jun 12, 2008. Website:http://yoni.stanford.edu/cgi-bin/axs/ax.pl?http://www.stanford.edu/~mlustig/sparseMRI_v0.2.tar.gz

Chapter 5

Final Conclusions and Future Work

5.1 Final Conclusions

The dissertation is focused on providing quality image reconstructions from a limited number of Fourier samples. In particular, the dissertation also provides an optimization framework for comparing different methods in terms of the maximum image quality that can be achieved.

First, an optimized solution for four different sampling geometry classes was found to lead to significant increases in the image reconstruction quality of partial K-space samples using Compressive Sensing. The sampling geometry classes were specifically designed to compare deterministic sampling geometries that we characterized as providing fast fMRI acquisitions from random geometries that are supported by Compressive Sensing theory. The fast sampling geometries were obtained by either sampling a small, central portion of K-space over a spiral or by omitting phase encoded vectors in a dyadic manner. The random geometries were developed to add a level of incoherence between samples, and in one case, also reduce the number of phase encoded vectors scanned in the K-space acquisition process.

Our optimization technique provides both the best CS reconstruction parameters for a given image for each geometry, but also produces a range of acceptable parameter values resulting in reconstructions of sufficient quality. Using both of these results, we observed that the fast, deterministic sampling geometries result in consistently better reconstructions than those designed for use in CS applications. This research, which makes up a large portion of this dissertation, was not part of the proposal submitted to the committee in December, 2006. As we were introduced to more literature on the topic of Compressive Sensing, exploration of this application seemed like a good problem to explore in parallel as it seeks to find similar results to those provided by the Spectral Statistical approach that was formally proposed.

The new Spectral Statistical method for reconstructing remote sensing imagery was developed specifically as a flexible framework for estimating high and medium frequency components of the Fourier spectrum at independent Spectral sampling rates. This was accomplished by estimating individual statistical models that are optimized to best fit the magnitude and unwrapped phase spectra of non-overlapping, dyadic sampling blocks. Using Kriging, an optimized statistical interpolator, we observed that the magnitude and phase reconstructions produced higher quality magnitude and phase estimates than other widely accepted interpolators. Finally, the reconstructed images obtained from Kriging were shown to result in higher PSNR and mean SSIM index values than

those reconstructed using two selected optimized CS sampling geometry classes for an equal number of Fourier samples.

5.2 Future Work

Both of the spectral estimation techniques presented here are based on numerical optimization theory, which is becoming an important aspect in image processing applications. The scope of optimization is rather large, and could lead to further extension of the methods we have presented. In addition, we have limited our application to a single specific Fourier sampling application (K-space) and a representative collection of publicly available aerial images. Seeking data from other optical or electromagnetic Fourier sample platforms or various high-resolution imagery on which to apply our methods would provide an indication of how successful we were in designing portability into our approaches.

Finally, we mention some more specific areas that are noteworthy and should receive additional attention:

- Specifically to the problem of CS reconstructions of fMRI samples, it would be interesting to explore the optimization of sampling geometries over slices of various depths and provide an adaptive solution that is based on the combination of (i) the extent of the image containing tissue and (ii) the knowledge of the physiological structures that are common among

patients during a full brain scan. This could lead to feasible solutions for fast MRI acquisitions, especially for spatio-temporal applications.

- More generally, it would be interesting to explore how effectively the CS sampling geometries presented here are applicable to other ℓ_1 -norm minimization algorithms.
- The Spectral Statistical framework we developed here is intended to be extended in future studies. It would also be interesting to explore additional benefits from more complex Kriging approaches that have been shown to produce accurate data interpolation. These include, but are not limited to: Universal Kriging where localized spectra trends, specifically in unwrapped phase, are accounted for; Co-Kriging of samples from adjoining spectral blocks; and Bayesian Kriging where Monte-Carlo Markov Chains simulations are used to solve for the best statistical model parameters from a large number of observations.
- Another alternative is to explore non-dyadic Fourier partitioning geometries that are adaptively selected based on indicators from the full Fourier spectrum.
- Future work can also focus on the use of Chirp-Z transform methods to generate dense samples over different frequency domain regions. By generating more dense samples we can also consider the use of anisotropic models. Here, we note that for bounded objects, such the MRI images, we can interpolate by simply zero-padding. In this case, we can thus generate a very large number of discrete Frequency samples over very limited

discrete Frequency space regions and use them to allow for much more complex spectral statistical models.

- The Spectral Statistical model approach lends itself to applications in compression using quantization and entropy encoding. For example, the sampled spectral data of a given image can be stored along with the optimal covariance model parameters. This would reduce the amount of data required to be stored and/or transmitted and Kriging could then reconstruct the image for display or representation in the spatial domain.
- Spectral data reconstruction using Kriging also lends itself to the field of super-resolution image processing. The few experiments on magnitude spectra extrapolation attempted to simulate such a scenario. For super-resolution applications, we would need to simply first upsample the original data and then apply a low-pass filter to eliminate any higher frequency components introduced by the upsampling. Then, to produce high-frequency information from the low-frequency filtered data, we would need the critical extrapolation step that was demonstrated in this dissertation. Phase spectra would have to be considered for completeness.